UNIVERSITAT JAUME I
ESCUELA SUPERIOR DE TECNOLOGÍA Y CIENCIAS EXPERIMENTALES
DEPARTAMENTO DE QUÍMICA INORGÁNICA Y ORGÁNICA
ÁREA DE QUÍMICA INORGÁNICA

PREPARACIÓN Y ESTUDIO DE PELÍCULAS DELGADAS CON APLICACIONES FOTOVOLTAICAS

PREPARATION AND STUDY OF THIN FILMS FOR PHOTOVOLTAIC APPLICATIONS

TESIS DOCTORAL
Presentado por:
Teodor Krassimirov Todorov

Directores:

Purificación Escribano López
Juan Bautista Carda Castelló

Universitat JAUME I
Octubre de 2008, Castellón de la Plana,
ESPAÑA

Acknowledgements.

It would not be completely fair to say that this is my thesis. It is the work of so many people, that I cannot be sure I have mentioned all of them. Still, here I would like to thank everybody who has contributed in one way or another to this dissertation.

I begin by thanking my parents for their incessant care and support throughout three decades. Their dedication to my education is the biggest contribution to this thesis. To my sister who has been there for me anytime I needed her and to my grandparents who also contributed to my education by many means.

I am indebted to my wife for her love and understanding and for raising our two little kids sometimes alone, when work was taking me away for days and even months.

Switching to science, I would like to thank my professors at the University of Chemical Technology and Metallurgy. To Dr. Stoyan Stoyanov and the Ecology Department for making me what they called “engineer-ecologist”. To Dr. Vladimir Kozukharov for accepting me in the Erasmus program by which I started my work in Spain and for giving me his help and advice ever since.

I am grateful to my colleagues at Jaume-I University, especially the Solid State Chemisty Group. To my directors: Dr. Juan Carda, for accepting me in the team and for always giving me his full support in work and life, backing up even my bravest ideas; and Dr. Purificación Escribano for her dedication to convert me from a kid in the lab into a scientist with her discipline, knowledge and care under the program FPU (Formación de Profesorado Universitario). Thanks to Dr. Eloisa Cordoncillo for introducing me to the sol-gel and guiding me through TiO_2 synthesis. To Jose Miguel, Maruxa, Carlos, Inma, Rado, Dania, Teodora, Sandra, Sergio, Ezequiel, Javier, Mª Paz, Milena, Leo and the rest of the group for helping me, tolerating my temper and bringing joy in the office and the lab. Acknowledgements to Leo for his moral and technical support in finishing this dissertation. To the team of Servicios Centrales de Instrumentación Cientifica who have always been there to help me with my samples and comfort my soul – especially Javi, Gabriel, Lourdes, Chris, Manolo, Laura.

To Dr. Juan Bisquert for telling me that a solar cell can be made cheap and for giving me the opportunity to work with his group Física Aplicada. To all of them, especially Francisco Fabregat, Ivan Mora-Sero, German García and Jorge García-Cañadas with whom we explored all-solid TiO_2 cells.

I am grateful to Dr. Reiner Klenk for introducing me to the mysteries of the chalcopyrites and for offering me his invaluable expert advice and help in my first low-cost trials. To the team at Hahn-Metner-Insitut Berlin (now Helmholtz Zentrum Berlin): Roland, Paul, Christine, Carola, Michael, Rodrigo, Alex, Abdelhak, Ahmed, Thomas, Nick, Bojan and the rest who were helping me develop an electro deposition method for In_2S_3 buffers and make my first chalcopyrite cells.

I would like to thank Dr. William Shafarman and the team at the Institute of Energy Conversion, Delaware, for giving me the opportunity to work and learn with them. It was a short but highly productive and enriching visit thanks to Steve Hegedush, Brian McCandles, Greg Hanket, Rui, Kevin, John and the rest of the group who contributed despite their dense schedules to converting my films to absorbers and making solar cells.

I am grateful to Dr. Daniel Lincot for his incessant optimism and inspiring leadership and for accepting me in l'Institut de Recherche et Développement sur l'Energie Photovoltaïque (**IRDEP**). Thanks to Olivier Kerrec and his IRDEP team. Special thanks to Elisabeth Chassaing for her cordial care throughout my whole stay. To Patrick Panheleux, for his genuine dedication that converted my paints into photovoltaic absorbers by Rapid Thermal Anneal. To Carmen, Veronica, Jean-Francois, Gilles, Jean, Frederique, Negar, Valerie, Olivier, Audrey, Cedric, Ludovic, Philippe, Pierre-phillipe, Gregory, Victor, Edgardo, Gregory, Enrique and all the rest who participated in the last efforts of this thesis work that ended up with improved results.

In this multidisciplinary and multi-team work there are yet many more people whom I have not mentioned here, despite their contributions - either of help or advice. To all the ones I did and did not mention I want to say:

Thank you! Throughout my thesis I have always been a foreigner in distant lands and knowing that I could count on you has made me feel at home.

Finally, I would like to thank the Ministry of Education and Science for granting me the predoctoral scholarship FPU that made this work in Spain and abroad possible.

A mi familia.

¡Oh único dios, cuyos poderes
nadie más posee!
A todos los que están
en lo alto,
que vuelan con sus alas
tú subvienes a las necesidades.
Cuán excelsos son
tus designios,
¡Oh dios de la eternidad!

Extracto del himno, dedicado
al Dios del Sol, Aton.
(~1350 A.C.)

CONTENIDOS/ TABLE OF CONTENTS

Summary

Our modern world has reached the point when global environment and economy are starving for immediate and vast deployment of renewable energy sources. The Sun has the capacity to satisfy all our energy needs, yet photovoltaic production is still too expensive to allow this. Our work was motivated by the possibility to apply chemical routes in the fabrication of low-cost, thin-film solar cells, suitable for large-area production.

Solar cells are like complex organisms in which many materials systems interact with each other and all of them interact with light and electricity. This is why the creation of a successful device requires a multidisciplinary approach including physics, chemistry and engineering. Often applied aspects limit the possibilities to investigate fundamental principles as is done in pure Materials science. On the other hand, thin-film configuration often makes characterization much more difficult in comparison with bulk materials. Following our principle goal – to obtain useful films for photovoltaic cells - the study naturally expanded into an exploration of a large domain of materials and methods– from nanoparticulate oxides to pentanary chalcogenides and from sol-gel to electrodeposition. It is clear that exhaustive scientific investigation of all these cannot be done in a single thesis. Nonetheless, our effort was to carry out both fundamental studies and applied research of the systems we explored.

Part I, in Spanish, investigates nanocrystalline titanium dioxide dye-sensitized solar cells.

The work starts with sol-gel synthesis and deposition of TiO_2 films. The original goal was to develop an alternative route to the hydrothermal synthesis used for mesoporous TiO_2 films in dye-sensitized solar cells. We investigated direct deposition by spin-coating of TiO_2 sols and printing deposition of re-dispersed powders, synthesized by sol-gel. Nanocrystalline films with excellent uniformity were obtained, yet dye adsorption was very limited due to the dense nature of the layers. Polymer addition could not increase enough the open surface to allow sufficient dye adsorption. Nevertheless, our films exhibited excellent bactericidal effect and can be used for the fabrication of self-sanitizing tiles.

In the course of the study we understood that the biggest challenge that dye-sensitized cells pose is not the TiO_2 itself, but the liquid electrolyte used in high-performance devices. Such electrolyte is difficult to implement in large-area modules where electrical interconnection and chemical sealing is a challenge. We decided to investigate two alternative solid electrolytes. The first one was polyethileneglycol matrix used to support

I^-/I_3^- redox couple. Efficiencies reached 1.6% but cells were not stable. These results lead us to another route: an organic hole transporting material, PEDOT (Poly(3,4-ethylenedioxythiophene)). It was introduced by photoelectrodeposition, using dye excitation to initiate polymerization reaction. Photoelectrodeposition was carried out successfully. However, the material absorbed strongly in the visible region and did not allow sufficient illumination of the dye within the mesoporous layer. As a result, photocurrent density was very low.

These results and the discouraging reports in literature on the stability of solid dye cells made us search for an alternative technology. The chalcopyrite thin-film solar cell concept was found particularly attractive because it had demonstrated excellent efficiency and stability and did not require electrolyte.

Part II, in English, explores low-cost deposition methods for chalcopyrite thin-film solar cells.

The following materials were deposited by sol gel: $CuInS_2$, $Cu(In,Ga)S_2$ $Cu(In,Ga)Se_2$ and $Cu(In,Ga)(S,Se)_2$. In addition we developed a nanoparticle printing route by which $CuInS_2$ and indium-free Cu_2ZnSnS_4 were deposited.

The baseline sol-gel route was developed for $CuInS_2$ films. The Cu-In-O precursors were deposited by spin-coating and were subjected to sulfurization treatment. We obtained homogeneous and adhered chalcopyrite films that yielded promising initial device results – 1.8%. A systematic study of parameters such as Cu/In ratio, thermal treatment and sulfur content, yielded films with improved crystallinity.

This method was successfully applied to the transformation of amorphous Cu-In-Ga-O precursors to selenides and sulfoselenides, known to be among the most efficient chalcopyrite absorbers. Ga-incorporation is generally considered challenging because of the high stability of Ga_2O_3. Our precursors did not present this problem, probably because of the amorphous nature of the oxides. Three different treatment methods were explored: chalcogenation in tubular reactor with elemental sources, rapid thermal selenization and treatments with hydride gasses. Highly oriented films with excellent crystallinity and Ga-incorporation were obtained on glass substrates by use of elemental sources. We encountered difficulties when switching to Mo-coated glass substrates because of high molybdenum reactivity and delamination. Rapid thermal selenization produced very large planar crystals but Ga-incorporation was poor. Good adherence and GI-incorporation was achieved by treatments with hydride gasses. These devices yielded 3.1% efficiency.

Printing deposition methods are preferred by industry because of the possibility for easy up scale. We investigated nanoparticle paste printing for $CuInS_2$ and obtained highly oriented materials. Devices fabricated from these films have not been successful yet, probably due to pinholes and shunting.

This printing method was adapted to Cu_2ZnSnS_4. This material is particularly attractive candidate for future large-scale production because it does not contain toxic or rare elements (Se, In, Ga). Different elemental ratios were studied and homogeneous films with desired composition were obtained. We are looking forward to test these films in complete solar cells.

The “buffer” is an important layer for the completion of chalcopyrite devices. Currently a widely used buffer is CdS deposited by chemical bath deposition. Both the material and the method are undesirable for industrial production because of the high toxicity of large volumes of residual liquids. We developed an electro deposition route for a non-toxic buffer, In_2S_3, and obtained efficiencies up to 2/3 of efficiencies of the reference CdS cells. Optimization is expected to yield efficiencies equal to the CdS.

In the course of the study, an alternative printing method for $Cu(In,Ga)Se_2$ was found. Precursor nanoparticles were deposited and subjected to Rapid Thermal Anneal, yielding good crystllininty and Ga-incorporation. Devices with 7.5% efficiency were obtained.

This work explored different deposition methods for materials with application in TiO_2 sensitized solar cells and chalcopyrite photovoltaic devices. Some of the novel achievements of this thesis are:

- $CuInS_2$ and $Cu(In,Ga)(S,Se)_2$ deposition by sol-gel spin-coating.
- Nanoparticle printing method of highly oriented $CuInS_2$.
- Nanoparticle printing for indium-free and non-toxic Cu_2ZnSnS_4.
- Electro deposition method for Cd-free buffer layers for $CuInS_2$ solar cells.
- Nanoparticle printing method for $Cu(In,Ga)Se_2$.

ABBREVIATIONS AND SYMBOLS

α	absorption coefficient
AM	Atmospheric Mass
ATD/TG	Análisis Térmico Diferencial /Termogravimetry
CBD	Chemical Bath Deposition
CH	Chalcopyrite
CIGS	Copper Indium-Gallium Selenide
DEA	Diethanolamine
E	Energy
EDX	Energy Dispersive X-ray microanalysis
EEUU	Estados Unidos de America
EJ	Exa Joule (10e18 J)
eV	electron Volt
FWHM	Full Width at Half Maximum
HMI	Hahn-Meitner-Institut (Renamed Helmholtz-Zentrum-Berlin)
IRDEP	Institut de Recherche et Développement sur l'Énergie Photovoltaïque
ISET	International Solar Energy Technology
ITO	Indium-Tin Oxide
J	Joule
JCPDS	Joint Committee on Powder Diffraction Standards
Jsc	Short circuit current
MEA	Monoethanolamine
PEDOT	Poly(3,4-ethylenedioxythiophene)
PEG	Polyethylene glycol
PV	Photovoltaic
QE	Quantum efficiency
Rs	Series Resistance
Rsh	Shunt Resistance
RTP	Rapid Thermal Processing
SCIC	Servicios Centrales de Instrumentación Científica
SEM	Scanning Electron Microscopy
TCO	Transparent Conductive Oxide
TEA	Triethanolamine
TW	Terawatt
Voc	Open Circuit Voltage
WCED	World Commission of Environment and Development
Wp	Watt peak
XPS	X-Ray photoelectron spectroscopy
XRD	X-Ray Diffraction
ZJ	Zeta Joule (10e21 J)

OBJETIVOS DEL TRABAJO

PARTE I. PELÍCULAS NANOCRISTALINAS DE TiO_2 Y CÉLULAS FOTOVOLTAICAS DE COLORANTE

Preparación y estudio de películas nanocristalinas de TiO2 a través del método sol-gel.

1) Síntesis de TiO_2 (anatasa) nanocristalino utilizando el método sol-gel con diferentes componentes y condiciones de preparación.
2) Preparación películas nanocristalinas de TiO_2 sobre substratos de vidrio conductor a través de dos métodos: deposición de suspensiones de polvo y *spin-coating* de soles.
3) Estudio del efecto de los componentes iniciales y condiciones de preparación sobre el tamaño de los cristales y su estructura.

4) Preparación y estudio de células fotoelectroquímicas de películas de TiO_2 nanocristalino empleando nuevos electrolito sólidos a base de polietilenglicol.

5) Preparación y estudio de células fotoelectroquímicas de películas de TiO_2 nanocristalino empleando transportador de huecos orgánico depositado por fotoelectropolimerización.

PARTE II. MÉTODOS DE BAJO COSTE PARA CÉLULAS FOTOVOLTÁICAS DE CALCOPIRITAS

1)Desarrollo de capas de óxidos precursores de los sistemas Cu-In y su conversión en $CuInS_2$, $CuIn,GaS_2$ $Cu(In,Ga)Se_2$ and $Cu(In,Ga)(S,Se)_2$.

2) Desarrollo de método de deposición de Cu_2ZnSnS_4 a partir de nanopartículas.

3) Desarollo de método de electrodeposición de capas “bufer” sin cadmio para células de $CuInS_2$.

4) Desarrollo de método de deposición de $Cu(In,Ga)Se_2$ por impresión.

PARTE I.

PELÍCULAS NANOCRISTALINAS DE TiO_2 Y CÉLULAS FOTOVOLTAICAS DE COLORANTE

I-1) INTRODUCCIÓN

I-1.1) Energía y medio ambiente

El ritmo de la contaminación ambiental y el agotamiento de los recursos no renovables de nuestro planeta es alarmante, sin que se encuentre en la historia de la humanidad un precedente de tal magnitud. El calentamiento global por el efecto invernadero ya no es sólo una hipótesis, la desaparición de especies se produce diariamente y, la crisis mundial energética y económica por el déficit de petróleo y otros combustibles fósiles, está empezando de frenar el desarrollo de nuestra civilización.

La sostenibilidad del desarrollo global de la sociedad está íntimamente relacionada con la disponibilidad de fuentes de energía suficientes, su impacto medio-ambiental y con la relación consumo/restauración. En el año 1998, el consumo total anual fue 400.10^{18}J, que corresponde a un consumo de potencia continuo de 12.7 TW. Se estima que la demanda se doblará en el año 2050 y triplicará en el 2100 [1] . Este incremento en el consumo de energía será considerablemente superior a la energía total producida actualmente.

El consumo de energía no supondría ningún problema si durante los últimos 200 años la industrialización no hubiera empleado casi exclusivamente los combustibles fósiles para satisfacer sus necesidades energéticas [2]. En la Figura I-1.1 se representa el consumo de energía y las fuentes de las que se obtiene desde el año 1970 al 2002, haciendo una extrapolación hasta el año 2025. Estas previsiones están calculadas por el Departamento de Energía de los EE.UU. a partir de las tendencias actuales [3], pero sin considerar tres factores de gran importancia:

1) La concienciación ciudadana contra el cambio climático está creciendo.

2) El suministro de petróleo puede disminuir y su precio aumentar.

3) El precio de las energías renovables se puede reducir a través de avances tecnológicos.

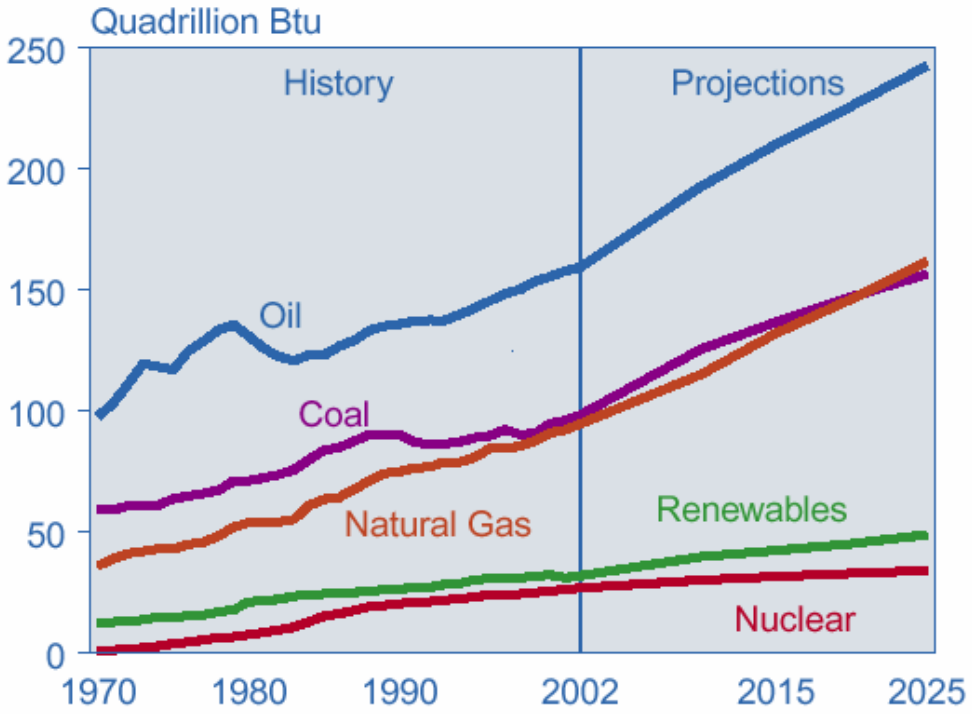

Figura I-1.1. Consumo y fuentes de energía y previsiones[3] sin considerar el potencial de las energías renovables y el creciente precio del petróleo.

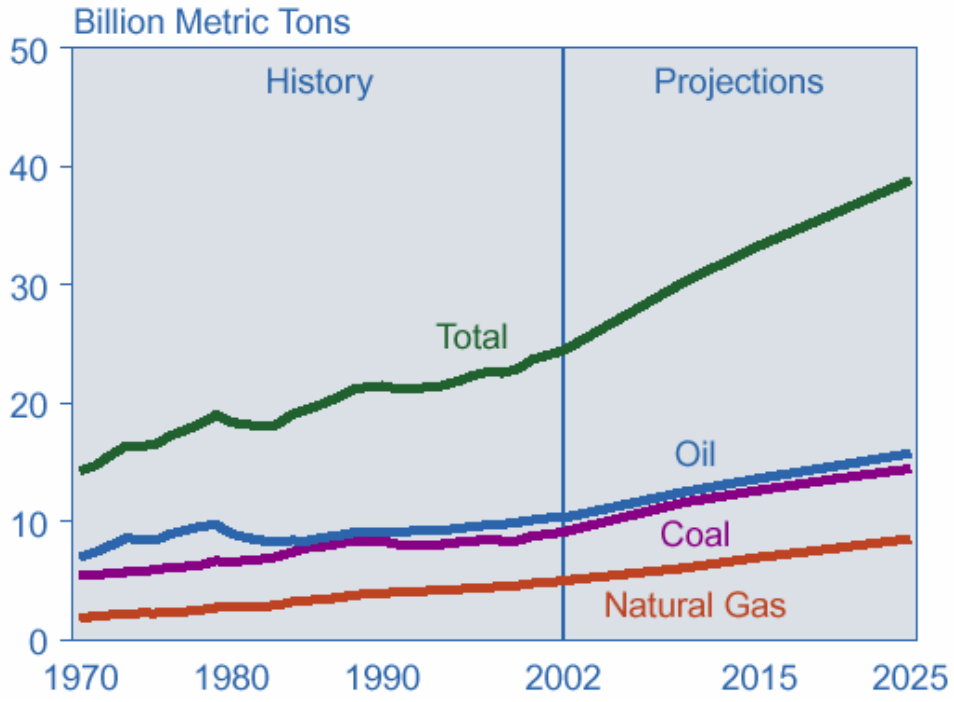

Figura I-1.2. Aumento de la concentración de CO_2 por los diferentes combustibles fósiles [3].

Este escenario hipotético en el cual las fuentes renovables están prácticamente ignoradas supondría un aumento progresivo en las emisiones de CO_2,(Figura I-1.2), CO, SO_2, NOx, cenizas, etc. tienen múltiples efectos negativos sobre el medio ambiente. El CO_2 ocupa el primer lugar en la lista de los gases con efecto invernadero del Protocolo de Kioto (Anexo A) y como fuentes principales de contaminación se indican la producción energética y los combustibles fósiles. Las emisiones globales han crecido 10000 veces en los dos últimos siglos. Se estima que en el año 2020, la concentración en la atmósfera se duplicará (Figura I-1.2), provocando un calentamiento global entre 1.5 y 4°C así como la subida del nivel del mar de aproximadamente 1m [4]. Las emisiones de SO_2 y NO_x provocan lluvias ácidas que contaminan las aguas y los suelos, que causan deforestación y extinción de especies.

La Comisión Mundial de Medio Ambiente y Desarrollo (WCED en abreviación inglesa) da la siguiente definición del *Desarrollo Sostenible*:

"El desarrollo es sostenible cuando responde adecuadamente a las necesidades de la generación de hoy sin poner en peligro la capacidad de las futuras generaciones para poder satisfacer igualmente sus necesidades".

La economía de hoy muchas veces se contrapone a este principio. En un sólo día se están quemando recursos no renovables cuya creación ha tenido lugar durante miles de años. Con el ritmo de explotación actual, las reservas conocidas de petróleo y el gas natural se podrían agotar en unas décadas [5], mientras que el carbón seguirá su destino un siglo más tarde.

El agotamiento del petróleo esta a punto de provocar una crisis económica con dimensiones gigantescas a corto plazo (dentro de unos 10-20 años). Cuando la producción de cualquier producto alcance su punto máximo, la crisis en el sector se considera inevitable [6,7]. Sin medidas radicales para migración de la producción energética actual a fuentes renovables, las consecuencias económicas para los países modernos serán devastadoras. Figura I-1.3, muestra la curva de la producción de crudo en los EEUU. Dicha producción alcanzó su máximo en 1970, provocando la celebre crisis de los años 70. Cuando la producción mundial alcance el suyo, la subida imparable del precio del petróleo provocará una crisis económica global y mucho mayor.

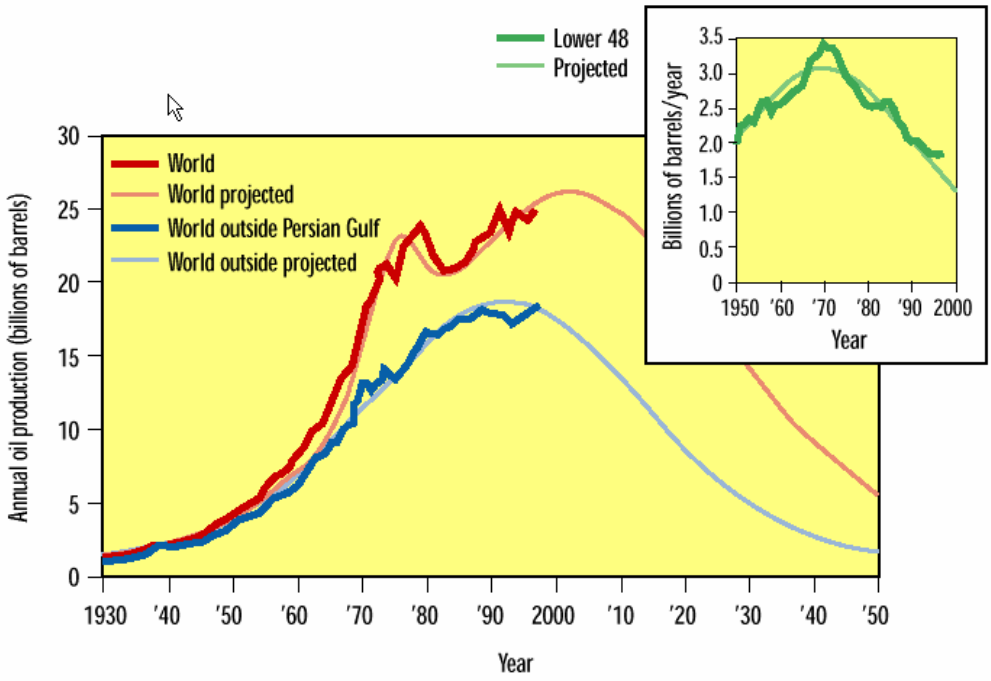

Figura I-1.3. La producción de crudo en los EEUU (arriba) y el mundo (abajo) [7].

La única forma en la que podemos enfrentar, incluso evitar las catástrofes ambiental y económica es sustituir lo más rápidamente posible los combustibles fósiles por fuentes de energía renovables.

I-1.2.) Capacidad de las fuentes* de energía renovables

Una migración significativa o completa a fuentes de energía renovables supone un gran reto que, requiere el esfuerzo mundial para emplear conjuntamente los recursos renovables disponibles. Considerando el enorme consumo energético actual (400.10^{18}J/año), es importante evaluar de manera práctica la posible contribución de las diferentes energías verdes – solar, eólica, biomasa, hidroeléctrica, marina y geotérmica. Su potencial aproximado y características más significativas son las siguientes [8, 9]:

* A pesar de su amplio uso en la literatura y los medios, por lo que se ha utilizado tambien en la presente tesis, el termino “fuentes de energía” es técnicamente incorrecto ya que se refiere a formas de energía o de maneras de convertirla.

Biomasa
A partir de ella podríamos obtener 7-10 TW, si se ulilizara toda la tierra agrícola del planeta sembrándola con “cosechas de energía”, o especies de rápido crecimiento. A pesar del enorme potencial de la biomasa hay que considerar que llos mismos territorios son imprescindibles para la alimentación de la creciente población terrestre. Al mismo tiempo, el uso de fertilizantes y laboriosos procesos industriales para fermentar y transformar la biomasa crea ciertas controversias medioambientales.

Energía eólica
Su potencial se estima en 2.1 TW. A parte de que esto puede proporcionar sólo una fracción del suministro global, los parques eólicos tienen algunas inconveniencias tales como la contaminación visual y acústica y pueden tener impacto serio en diversos ecosistemas, en particular de las aves.

Hidroeléctricas
Un uso intensivo a este recurso, instalando presas a todos los rios disponibles suministraría 1.5 TW adicionales. Evidentemente, la contribución potencial de la energía hidroeléctrica es aun menor a la eólica mientras que su impacto en los ecosistemas es considerablemente mayor, no sólo sumergiendo territorios terrestres de gran biodiversidad, sino interceptando los flujos naturales de alimentos y las rutas migratorias de todas las especies acuáticas presentes.

Energía de las mareas y olas
Esta fuente puede proporcionar aproximadamente 2 TW, similar a la energía eólica. Su impacto ambiental es importante por la variedad y complejidad de los ecosistemas en las zonas afectadas.

Energía geotérmica
La energía geotérmica tiene mayor potencial y aparentemente menor impacto medio ambiental pero requiere avances tecnológicos importantes antes de que pueda contribuir significativamente a la producción energética.

Energía solar
El Sol es el origen de casi todas las fuentes utilizables de energía en la tierra. Únicamente la geotérmica y la nuclear tienen un origen distinto) [6]. Las demás formas de energía de que disponemos proceden, directa o indirectamente, del sol. La energía eólica utiliza el viento, provocado por los efectos climáticos causados por la radiación solar y el movimiento de la tierra. La biomasa está formada por la fotosíntesis. Los

combustibles fósiles por su parte son productos de biomasa antigua, formados a lo largo de cientos de millones de años.
La energía total que llega a nuestro planeta en un año es 3 850 ZJ (10^{21}J o mil millones TWh)[10]. Para entender éste enorme potencial energético basta decir que, sólo una hora de iluminación solar trae a la superficie terrestre mas energía de la que hemos consumido en el año 2002 [11] y, en un año, el doble de la cantidad total que se podría extraer jamás de todos los recursos no renovables del planeta: carbón, petróleo, gas y uranio [12].

La energía solar fotovoltaica y térmica es la más cómoda de usar y con menos impacto ambiental en comparación con las demás fuentes renovables, por la posibilidad de integrar los conversores en la edificación y la construcción de infraestructuras. En la Figura I-1.4 se presenta la distribución de la radiación solar sobre la tierra.

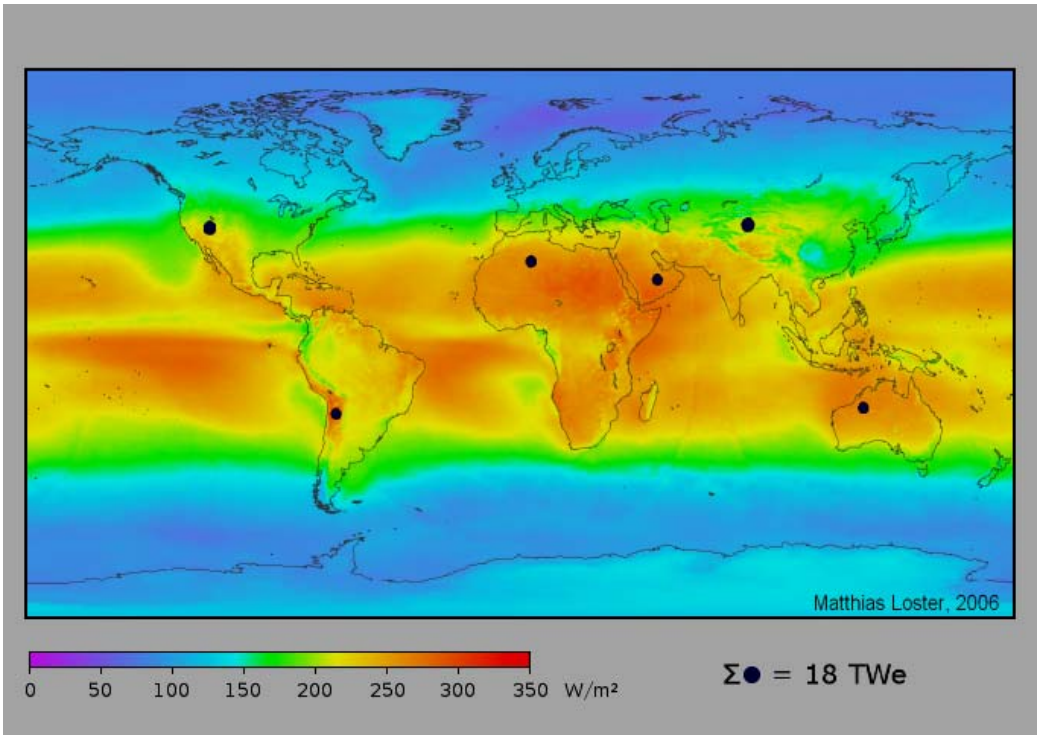

Figura I-1.4. Radiación solar media en watios por metro cuadrado [13]

Solamente instalando paneles solares sobre los tejados disponibles de las zonas edificadas de España (unos 600km^2 en total), [14] se pueden generar 90 GWh/año – un tercio del consumo eléctrico de todos los sectores de la economía y mas del 10% de la energía total consumida en España (aproximadamente 800 GWh/año) [15].

Pensando en términos globales, los desiertos ofrecen excelentes posibilidades de satisfacer las necesidades energéticas del planeta, como se muestra en la Tabla I-1.I. Recubriendo sólo la mitad de la superficie del desierto de Gobi con dispositivos fotovoltaicos, se puede generar la cantidad de energía que necesita la civilización humana (384 EJ ó 10^{18}J en el 2000).

Tabla I-1.I. Área y energía solar incidente en los mayores desiertos de la tierra.

DESIERTO	Area (10^3km^2)	kWh/m2.year
Sahara (Africa)	8600	2685
Sonora (Mexico)	310	1995
Negev (Israel)	1	1939
Thar (India)	200	2179
Gobi (China/Mongolia)	1300	1701
Great Sandy Desert (Australia)	400	2343

Al mismo tiempo las instalaciones fotovoltaicas en los desiertos permitirían poblar estos territorios con nuevas autosuficientes comunidades que dispondrían de energía abundante para cubrir sus necesidades, incluso para desalinizar agua para la irrigación [16].

A pesar del enorme potencial de la energía solar, es preciso abordar retos tecnológicos y científicos a muchos niveles para poder alcanzar una contribución importante. Ya que aún se desconocen los futuros avances de la ciencia y tecnología, la mayoría de las previsiones de la aportación de la energía solar son relativamente pesimistas. Como se puede ver en la Figura I-1.5, algunos expertos prevén a lo largo de varias décadas una contribución de la energía solar fotovoltaica térmica y fotovoltaico mucho menor que las demás fuentes, incluso de las renovables [17].

.

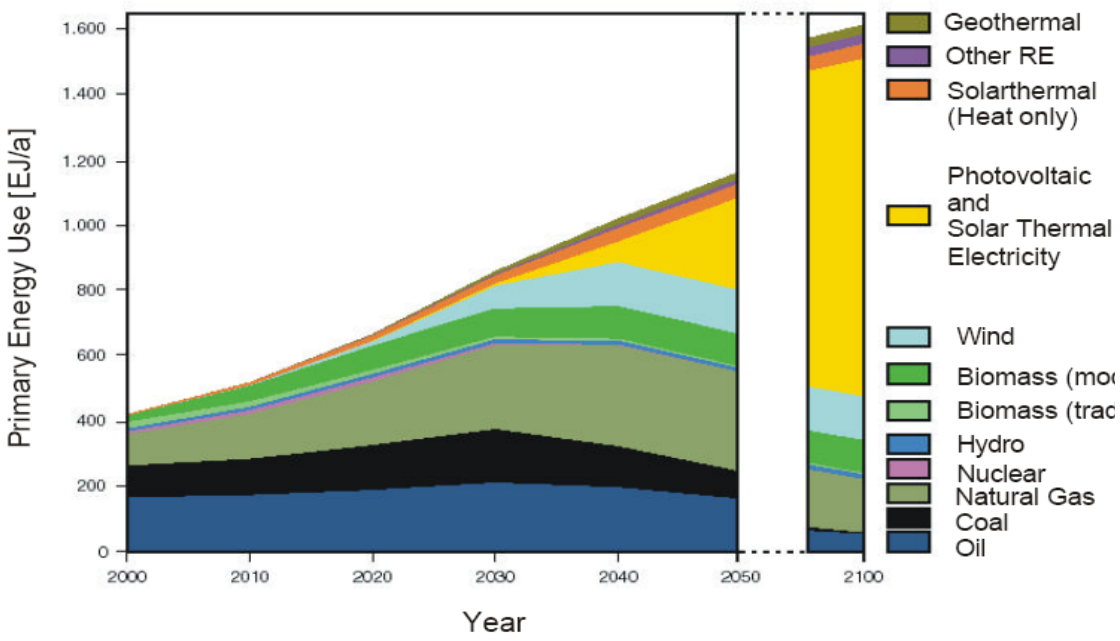

Figura I-1.5. Una previsión del suministro de diferentes tipos de energía durante el siglo 21 [17].

Estas estimaciones, a pesar de ser presentados con la buena voluntad de los autores como escenarios "optimistas" para estimular y promover la tecnología fotovoltaica, pueden estar alejados de la realidad. El desarrollo de la industria fotovoltaica se podría acelerar por una subida de los precios de los combustibles fósiles y/o por innovación y desarrollo de tecnologías fotovoltaicas baratas y aplicables a gran escala.

Con el propósito de movilizar la sociedad mundial a todos los niveles para responder adecuadamente a la necesidad inmediata de desarrollo de las tecnologías fotovoltaicas, el Dr. Daniel Lincot, presidente de la 23 Conferencia Europea de Fotovoltaica, Valencia 2008, ha realizado un llamamiento, firmado por la sociedad científica internacional. El documento intenta hacer llegar a la ciudadanía y los organismos gubernamentales que la energía fotovoltaica puede ser una solución clave para la producción energética mundial y que beneficiará a todas las poblaciones y futuras generaciones:

"Acelerar el desarrollo de la tecnología fotovoltaica a una gran escala y sin dilaciones se ha convertido en una necesidad absoluta. La fotovoltaica no es simplemente ciencia, ni tecnología clásica en desarrollo. Se puede considerar una misión pública y estratégica."

I-1.3) Tecnologías fotovoltaicas

A pesar de que el efecto fotovoltaico fue descubierto en 1839 por Bequerel y explicado por Einstein en 1904 (lo que le permitió conseguir el premio Nóbel), las primeras células fotovoltaicas con uso practico fueron creadas en los EE.UU., en los años 50 y, posteriormente desarrollados por los programas espaciales. Hoy contamos con numerosas tecnologías para producir módulos* fotovoltaicos. Algunas de ellas ya están comercializadas (Figura I-1.6), pero casi todas tienen un problema en común – el alto precio [18]. Los módulos actuales cuestan entre 3 y 6€/Wp [19]. Se considera que sin incentivos gubernamentales el precio debe bajar aproximadamente a 1 €/Wp para ser competitivo a los fuentes de energía tradicionales en el mercado actual.

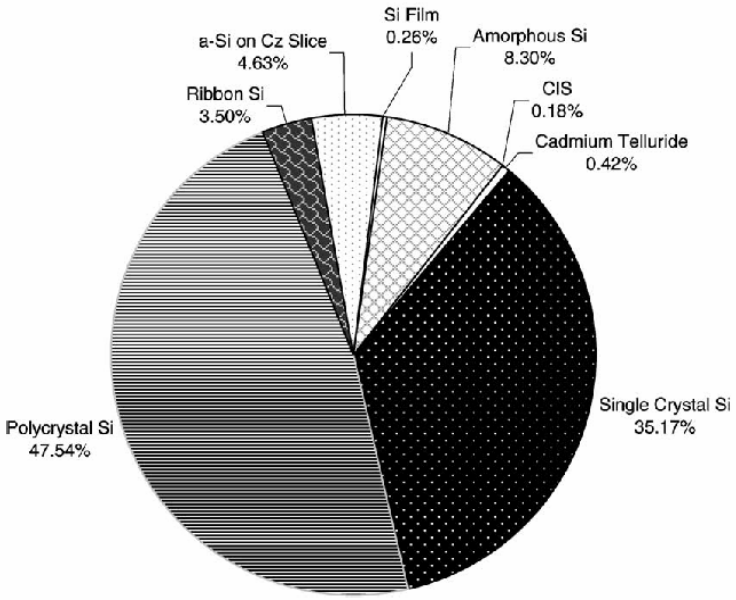

Figura I-1.6. El mercado fotovoltaico mundial [20].

La Figura I-1.6, [20], muestra la distribución de las diferentes tecnologías fotovoltáicas que existen en el mercado. La parte dominante pertenece al silicio mono y policristalino. Como veremos a continuación, muchas inconveniencias de la tecnología de los módulos de silicio pueden ser superadas por las tecnologías a base de capas delgadas que poseen un potencial prometedor no sólo para una producción a gran escala, sino para una reducción de costes importante.

* El módulo, o panel fotovoltaico, consiste en varias células interconectadas en serie y un acabado que permite su instalación directa.

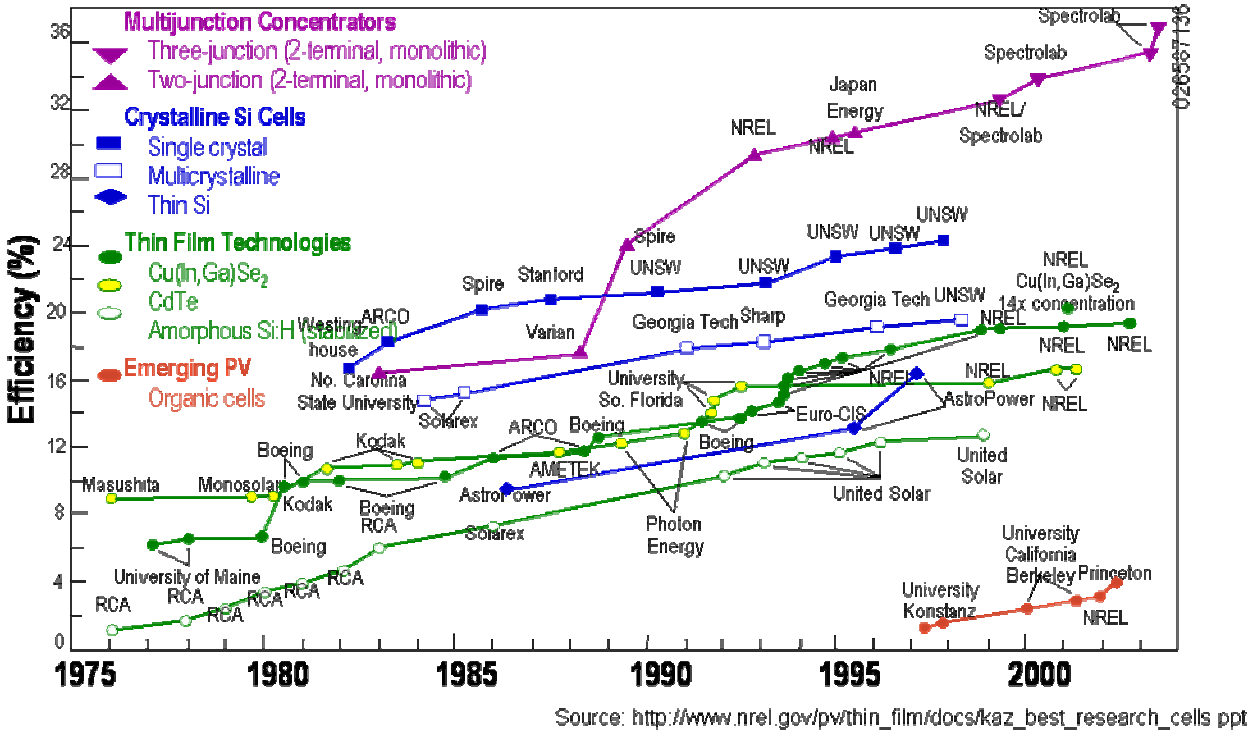

Figura I-1.7. Mapa del desarrollo de las diferentes tecnologías fotovoltaicas durante las últimas décadas [21].

Como se muestra en la Figura I-1.7, durante más de tres décadas, los esfuerzos de diferentes grupos han logrado un desarrollo de numerosas tecnologías fotovoltaicas. Algunas de ellas, como las del silicio cristalino están ya establecidas en el mercado, mientras que otras, como las de capas delgadas están empezando a demostrar su potencial.

La tecnología ideal para una producción del orden giga o incluso terawatios por año tendría los siguientes requisitos:

- Posibilidad de obtener grandes áreas a bajo coste.
- Alta eficiencia (superior a 10%) y
- Estabilidad durante explotación en condiciones atmosféricas (por los menos 10-20 años)
- Suministro suficiente de materias primas (evitar el uso de elementos escasos)
- Bajo consumo de energía para la fabricación (rápida recuperación de la energía invertida)
- Uso de materiales que no sean tóxicos o contaminantes.

Como en muchas otras industrias, es muy difícil conseguir todos éstos requisitos a la vez. No obstante, alcanzar varios, incluso todos es factible y esto es la meta de los miles de científicos que forman la creciente sociedad fotovoltaica mundial.

Silicio cristalino

En el 2008 la eficiencia record de una célula con éste material es de 24% y de módulo-20.1% [22]. Las eficiencias de módulos comerciales varia entre el 14 y el 17%. Estos conversores son muy estables y suelen tener garantía de explotación de 20 años.

Las mayores ventajas del silicio cristalino como material son su abundancia y la enorme base de conocimiento acumulado por la industria electrónica. Al mismo tiempo el silicio es un semiconductor de bandgap indirecto por lo que se necesita un grosor 50-100 veces mayor y/o diseños ópticos para conseguir una absorción de la luz solar comparable con la de los semiconductores de gap directo como son las calcopiritas.

El mayor grosor requiere, por su parte, materiales de altísima pureza (superior a 6n o 99.99999%) para evitar la recombinación de los portadores de carga [23]. Actualmente los residuos de la industria electrónica suministran la mayor parte de la materia prima para ésta tecnología, un material de grado electrónico con extrema pureza, del orden de 9n. La creciente demanda necesita un suministro independiente que redundaría en un aumento del precio que no sólo sería unas 50 veces mayor al Si metalúrgico, sino ineficiente de un punto de vista energético (anulando una gran parte de los beneficios medio ambientales). Hay que mencionar que se están investigando nuevas tecnologías de purificación que podrían producir silicio de “grado solar” a un precio más competitivo.

Otra desventaja de los módulos de silicio cristalino es su laboriosa fabricación ya que se realiza en numerosas etapas que requieren maquinaría robotizada (Tabla I-1.II).

La tecnología de los módulos de silicio cristalino es muy madura ya que todas las etapas de su fabricación han sido optimizadas durante décadas. Por eso no se puede esperar una reducción de coste drástica.

Muchas investigaciones tienen como objeto reducir el grosor de las obleas o sustituirlas por capas o laminas cristalinas. De momento no se ha podido realizar un procedimiento con mejor viabilidad económica y practica del silicio cristalino que el método tradicional.

Tabla I-1.II. Coste en Euro/m^2 de cada etapa en la fabricación de módulos de silicio cristalino [24].

ETAPA	Monocristalino	Policristalino
Purificación de silicio	38	38
Cristalización de lingote	115	35
Corte de obleas	77	77
Fabricación de célula	80	80
Ensamblaje de módulo	75	75
Laminado	75	75
Coste del módulo final	***476***	***406***
Coste relativo de potencia	3.4 Euro/Wp	3.38 Euro/Wp

Células cristalinas de alta eficiencia tipo III-V

Con este tipo de células han conseguido el record de eficiencia – 34%, utilizando estructura laminada de 3 células. Muy importante es el hecho que su eficiencia es aun mayor con altas intensidades de iluminación llegando a los 40%.

La fabricación de estas células requiere un crecimiento de materiales como GaAs, AlGaAs y InP crecidos epitaxialmente sobre monocristales de germanio de gran calidad, lo que hace que ésta tecnología fotovoltaica sea extremadamente cara, muy por encima de la del silicio.

No obstante por su alta eficiencia, la tecnología es idónea para aplicaciones en el espacio y sistemas concentradores que enfocan en células minúsculas la radiación de arreas mucho mayores, hasta 2000 veces la área de la célula [25]. Los sistemas concentradores podrían llegar a ser muy rentables con un diseño avanzado para obtenerlas en serie. No obstante, no funcionan bien con luz dispersa (cuando hay nubes por ejemplo) y se integran difícilmente en la construcción urbana por su mayor tamaño y necesidad de mantener orientación precisa hacia el sol.

Tecnologías de capas delgadas

La posibilidad de utilizar capas finas para módulos fotovoltaicos es muy atractiva por el enorme ahorro de materiales costosos y la simplificación del proceso de fabricación. Al mismo tiempo el aspecto homogéneo y elegante de estos módulos, así como la libertad de formas y diseños que permiten, los hacen muy atractivos para una integración arquitectónica.

Silicio Amorfo

Los primeros módulos comerciales de capa fina fueron de silicio amorfo. La eficiencia de células de este material ha alcanzado un valor record del 9.5 % (estabilizada). El rendimiento inicial puede ser mayor – alrededor del 15% [26] - pero una característica típica de éste material es su degradación bajo iluminación, conocida como efecto de Staebler-Wronski.

Normalmente la deposición se lleva al cabo en alto vacío utilizando técnicas asistidas por plasma.

Últimamente se han introducido diferentes alternativas como el silicio microcristalino y nanocristalino en estructuras similares que se deterioran menos por el efecto Staebler-Wronski, pero su producción es más costosa.

Telururo de Cadmio

Estas células han alcanzado una eficiencia del 16.5% y los módulos- 10.5% [27]. Su relativamente sencilla producción ha llevado a una rápida expansión en su producción durante los últimos años.

Una característica de estos dispositivos es la versión “superstrato”, i.e. el vidrio sobre cual se depositan las capas es la superficie que será iluminada. Se depositan capas de óxido conductor, CdS por baño químico y la capa de CdTe, normalmente por sublimación en espacio cerrado – un proceso fácilmente escalable. Un paso importante para la buena cristalización y acondicionamiento de la capa es el tratamiento posterior con la adición de un cloruro o cloro [28].

La presencia del cadmio en éste sistema es preocupante de punto de vista ambiental. Las componías productoras aseguran la completa ausencia de emisiones tanto durante la etapa de producción como durante la explotación de los módulos, terminando con un reciclaje centralizado por el propio productor [29]. A pesar de todo, es deseable sustituir un elemento ya prohibido en la industria electrónica [30].

Tecnologías a base de calcopiritas.

Células utilizando $Cu(In,Ga)Se_2$ como absorbente de la luz recientemente han alcanzado la eficiencia del 19.9% [31]. Por su alto rendimiento y estabilidad, ésta tecnología se considera muy prometedora para una producción de módulos fotovoltaicos a gran escala [32].

Considerando una producción futura a escala muy grande, se investigan intensamente métodos de deposición de bajo coste y vías para sustituir no sólo los elementos escasos y tóxicos. Si se consigue alcanzar éstas dos metas, se abrirá un camino viable para una industria fotovoltaica, capaz de responder a las necesidades globales.

La **Parte II** de la presente tesis está dedicada a métodos de deposición de bajo coste de diferentes calcopiritas y en ella se describe ésta tecnología en más detalle.

Tecnologías emergentes.

Durante la última década nuevos conceptos para el desarrollo de células fotovoltaicas a base de materiales nanocristalinos, polímetros, fullerenos y compósitos han atraido a muchos investigadores.

Células orgánicas han alcanzado eficiencias del 5.4% [27], pero no han sido estables. La célula de nanocristalina de colorante (de Graetzel) tiene eficiencia confirmada de 10.4% y sufre del mismo problema.

Es muy difícil predecir cuales de los avances de hoy a escala de laboratorio tendrán una aplicación práctica en el futuro. Un ejemplo de célula solar que no ha podido cumplir las expectativas de su inventor y de muchos de sus seguidores es la célula nanocristalina de Graetzel, a la cual está dedicada la primera parte de ésta tesis.

I-1.4) Célula fotovoltaica a base de TiO_2 nanocristalino

Llamada también célula fotovoltaica de colorante o célula fotoelectroquímica sensibilizada (Figura I-1.8), este dispositivo fue descubierto por M. Graetzel [33]. Por su considerable eficiencia de conversión fotoeléctrica (alrededor de 11%) y la posibilidad de emplear métodos sencillos y materiales de bajo coste para su fabricación, ésta célula era considerada una opción muy prometedora como futura fuente de energía fotovoltaica a gran escala.

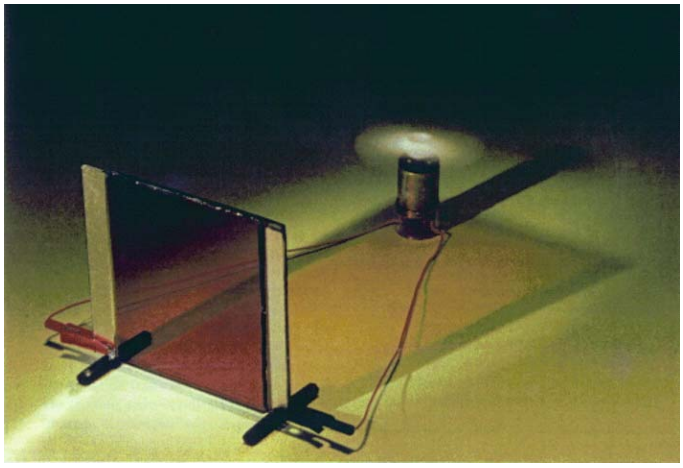

Figura I-1.8. Una célula de TiO_2 preparada por el grupo de M. Graetzel [34]

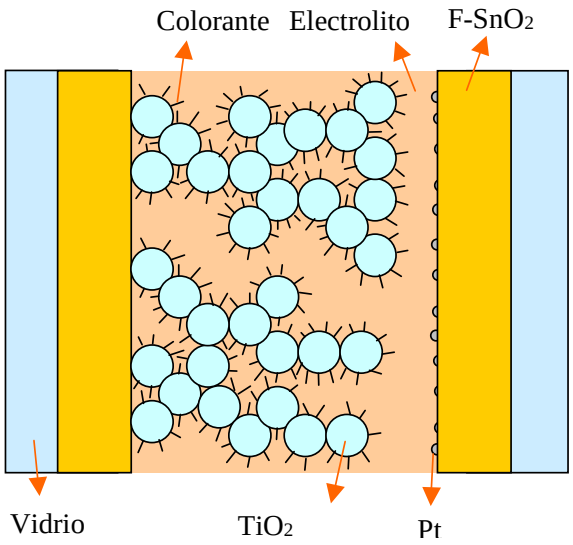

Figura I-1.9. Dibujo de la célula solar de colorante [a37].

La estructura de la célula está esquematizada en la Figura I-1.9. Los elementos principales son: electrodo mesoporoso, colorante, electrolito y contraelectrodo están descritos en mas detalle abajo.

Funcionamiento de la célula

El modo de conversión de la célula fotoelectroquímica de TiO_2 está esquematizado en la Figura I-1.10. El colorante, se excita al ser irradiado con luz visible y a continuación inyecta un electrón en la banda de conducción del dióxido de titanio. Para cerrar el circuito el complejo se regenera mediante la transferencia de electrones por un par redox en disolución – I_3^-/I^- que rescata los huecos da la banda de valencia del colorante y luego se reduce en el cátodo: $2e^-+I_3^-\rightarrow 3I^-$ [35, 36].

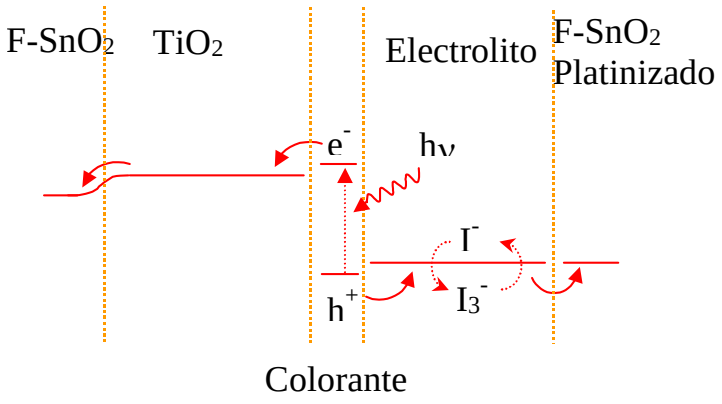

Figura I-1.10. Esquema del funcionamiento de la célula.

Los elementos de la célula poseen las siguientes características:

-Substrato. Normalmente se utiliza vidrio, a pesar de que los sustratos flexibles son de particular interés para la producción industrial [37] actualmente la empresa Konarka comercializa células fabricadas sobre substratos flexibles [38]. Técnicamente, la configuración de las células de TiO_2 en funcionamiento no son “substrato”, sino “superstrato” lo que significa que la parte iluminada de la célula es la lamina sobre cual está depositado el material. Esto proporciona iluminación óptima para evitar pérdidas ópticas.

-Capa de óxido conductor transparente. Para permitir recolección de la carga y al mismo tiempo la iluminación del dispositivo, se necesita que el contacto del lado iluminado sea a la vez transparente y conductor. La combinación de estas propiedades es difícil de conseguir y normalmente se tienen que utilizar óxidos semiconductores de banda ancha, dopados adecuadamente [28]. En las células de colorante, generalmente, se utiliza dióxido de estaño copado con flúor(SnO_2:F), pero se pueden utilizar otros materiales como el trióxido de indio, dopado con estaño.

-Capa de TiO_2 nanocristalino. La estructura nanométrica de este elemento principal de la célula, proporciona las condiciones clave de su funcionamiento: (i) un medio bifásico que permite no sólo transporte de electrones a través de la parte sólida, sino transporte de masas a través de la parte liquida [39] (ii)Una enorme área activa (del orden de 1000 veces más que el área de la célula) sobre cual se puede inmovilizar una capa molecular de colorante. El electrón se mueve a través de la masa de nanopartículas a través del fenómeno denominado percolación (salto del electrón de una partícula a otra) [40].

-Capa de colorante o sensibilizador. Cabe destacar que a pesar de las propiedades fotoactivas del dióxido de titanio (ver la siguiente sección), no es él, sino el colorante el material que absorbe la luz que genera la corriente eléctrica. Como veremos a continuación, es importante que el colorante esté colocado en la interfase entre el sólido TiO_2. El área abierta de la estructura mesoporosa permite adsorber suficiente cantidad de colorante para permitir una alta absorción óptica. Figura I-1.11 muestra tres de los colorantes utilizados en el grupo de M.Graerzel [41].

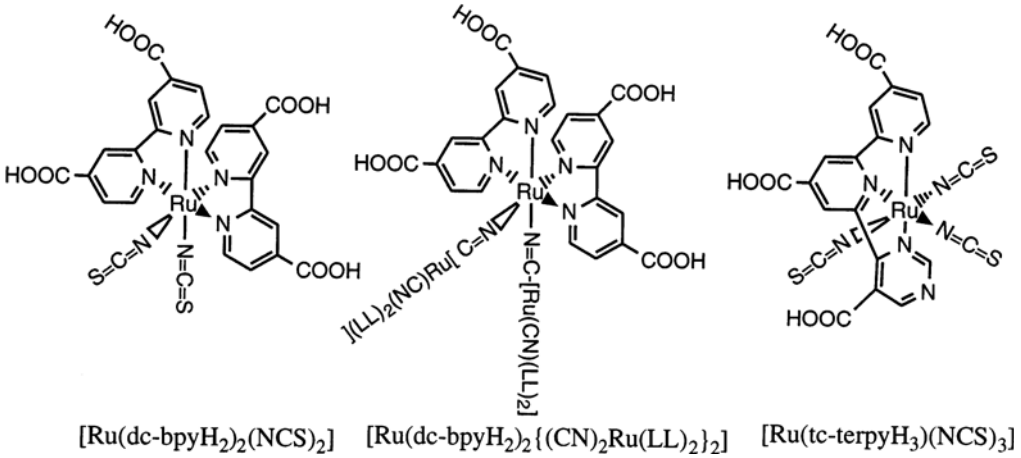

Figura I-1.11. Algunos ejemplos de colorantes utilizados en la célula de Graetzel [41]

Los grupos carboxílicos facilitan el anclaje a la superficie a través de esterificaciòn [41]. La elección de colorante no se limita a complejos de rutenio. Se puede utilizar amplia gama de compuestos, mientras que absorban la luz en el espectro deseado y se puedan inmovilizar a la superficie del TiO_2. Se han utilizado incluso extractos de frutas [42].

-Electrolito. Este elemento es uno de los factores limitantes del funcionamiento de la célula. Actúa en manera parecida a un semiconductor tipo-p transportando el hueco después de la separación de carga en la superficie del TiO_2. Las células de rendimiento record utilizan un par redox de iodo/ioduro en medio de disolvente con baja viscosidad, por ejemplo acetonitrilo [33], Para una aplicación a gran escala es muy importante sustituir el electrolito liquido por uno sólido porque el encapsulamiento de celulas separadas químicamente y colectadas eléctricamente (para conseguir una interconexión en serie) es tecnológicamente difícil. Ademas, la volatilidad de los disolventes líquidos limita el tiempo de vida del dispositivo.

-Contraelectrodo. Para catalizar la reduccion del triioduro: $2e^- + I_3^- \rightarrow 3I^-$ y reducir la resistencia de transferencia de carga, las células más eficientes utilizan cantidades minúsculas de platino (<10nm de grosor). También se puede utilizar carbono que da prestaciones parecidas [43]. La capa conductora no tiene por qué ser transparente, a pesar de que habitualmente se utiliza un óxido conductor igual que para el primer electrodo. Un contacto transparente ofrece la posibilidad atractiva de utilizar módulos semitransparentes para integraciones arquitectónicas.

A pesar de las ventajas de las células de colorante, entre cuales cabe citar la fácil producción, aceptable eficiencia y uso de materiales abundantes y no tóxicos, el uso de un electrolito líquido es una gran desventaja para su aplicación a gran escala. Para obtener una buena eficiencia es necesario tener un sellado fiable no sólo del módulo entero, sino entre cada una de las células. Como hemos dicho, es extremadamente difícil conseguir a la vez un sellado químico y un contacto eléctrico ya que la mas mínima imperfección resultaría en la destrucción electroquímica del módulo [44-46] . Por éstas razones es de gran interés conseguir una célula solida.

Los requisitos de un electrolito sólido son[44]:

- Tiene que ser apto de transferir los huecos del colorante sensibilizado después de que haya inyectado electrones en el TiO_2.
- Tiene que ser depositado dentro de la capa nanocristalina.

- Al ser introducido, tiene que dejar intacto al colorante. Esto limita la elección de agentes químicos, la temperatura de deposición y el régimen electroquímico de una posible deposición electroquímica.
- El compuesto tiene que ser transparente en el espectro visible para permitir que la luz llegue al colorante. Por el contrario tiene que poder efectuar una inyección electrónica eficiente y directa en el TiO_2.

.

Se están investigando las siguientes posibilidades:

- Semiconductores inorgánicos tipo-p. Se han utilizado con éxito compuestos de cobre (CuI [a49]. y CuSCN [47].). La eficiencia demostrada ha sido inferior a las células liquidas (1-3.8%) [48]. A esto hay que añadir su estabilidad inferior, especialmente en el caso del CuI. Por la dificultad de penetración dentro de la capa mesoporosa y cristalización indeseada, estos compuestos presentan dificultades adicionales.

- Otra alternativa ha sido el uso de polímeros estructurales (por ejemplo oxido de polietileno PEO) o geles para soporte del par redox I_3^-/ I^-. Células basadas en PEO han demostrado eficiencias del 3.6% [49]. Angunos trabajos indican eficiencias hasta los 8.1% con el uso de geles de metacrilatos pero no comentan sobre la estabilidad del dispositivo [50]. Muchos de estos sistemas tienen poca diferencia de las células liquidas en el sentido que son líquidos gelificados in-situ. Ofrecen ciertas ventajas como más fiabilidad con respecto a la pérdida de líquido y el aislamiento de las células individuales, pero siguen sin resolver los problemas de volatilidad del disolvente y la baja estabilidad de la célula.

En el presente trabajo hemos utilizado polietileno glicol (PEG) para el soporte del par redox I_3^-/ I^-.

- Una posibilidad muy atractiva es el uso de polímeros conductores de huecos orgánicos. Figura I-1.12 presenta el funcionamiento de un dispositivo de este tipo. Se estima que esto es un proceso de fases múltiples, en general un tiempo de regeneración un orden de magnitud menor que los sistemas redox [51].

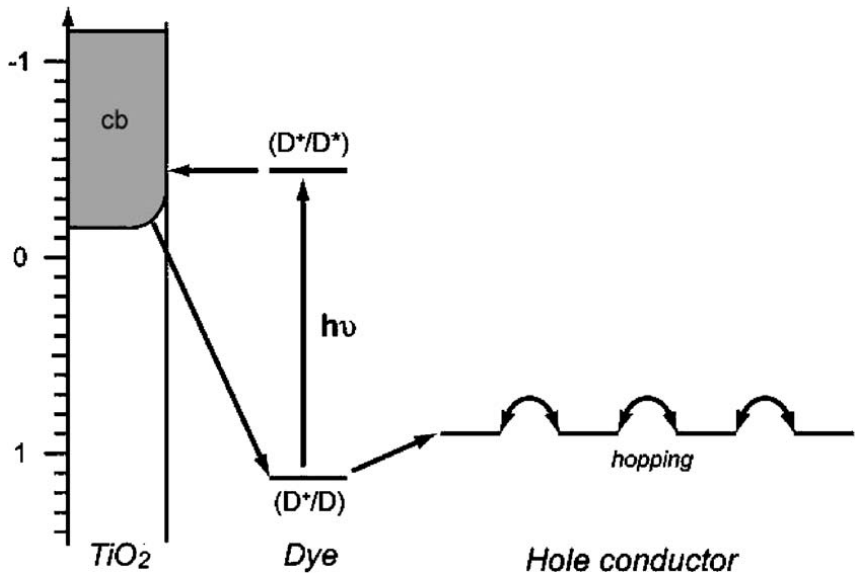

Figura I-1.12. Funcionamiento de un dispositivo con conductor de huecos organico.

Un polímetro conductor de huecos que ha atraído gran interés es el PEDOT (*Poly(3,4-ethylenedioxythiophene)* (Figura I-1.13), [52,53].

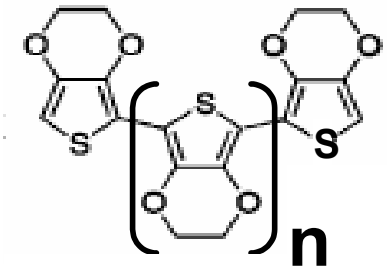

Figura I-1.13. PEDOT (*Poly(3,4-ethylenedioxythiophene)*

Este polímetro es el segundo material empleado como alternativa del electrolito liquido en el presente trabajo.

I-1.5) Dióxido de titanio – propiedades y vías de preparación de nanocristales

I-1.5.1) Fases cristalinas de TiO_2

El dióxido de titanio existe en tres modificaciones polimórficas: rutilo, anatasa y brookita (Tabla I-1.III), siendo las dos primeras (Figura I-1.14) estables y de origen natural, mientras que la tercera es una fase sintética metaestable [54]. La diferencia entre las estructuras de las dos fases más comunes es que en la anatasa los octaedros comparten vértices, mientras que en el rutilo comparten aristas.

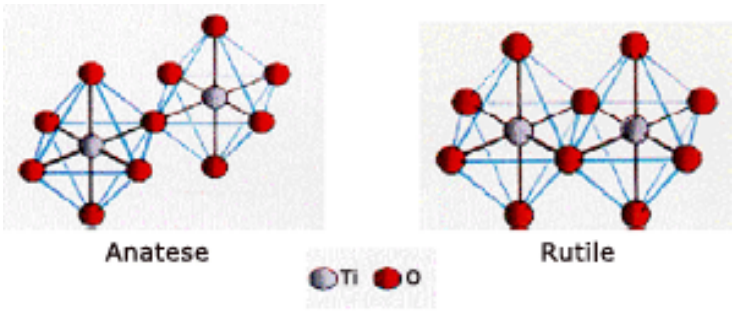

Figura I-1.14. Estructuras cristalinas del anatasa y el rutilo.

Tabla I-1.III. Datos cristalográficos de las formas polimorfitas del TiO_2.

	Rutilo TiO_2	Anatasa TiO_2	Brookita TiO_2
Peso molecular	79.890	79.890	79.890
Z	2	4	8
Sistema	Tetragonal	Tetragonal	Orthogonal
	Célula unidad		
a(Å)	4.5845	3.7842	9.184
b(Å)	4.5845	3.7842	5.447
c(Å)	2.9533	9.5146	5.145
Volúmen molar	18.693	20.156	19.377
Densidad	4.2743	3.895	4.123

De todas estas variedades alotrópicas del TiO_2, es la anatasa la que se utiliza en la mayoría de los casos para aplicaciones fotovoltaicas. Existen datos que la fase cristalina no es de importancia vital para el funcionamiento de la célula [55], Células con comparable eficiencia se han fabricado con la inclusión de rutilo de tamaño mayor

como dispersante de la luz [56] Óptimamente la diferencia entre las dos no es grande, ya que sus gaps de energía varían entre los 3 (anatasa) y 3.2 (rutilo) eV. Cabe destacar que la anatasa es la fase principal que se obtiene por el método hidrotermal (a temperaturas no superiores a 250ºC) y es la fase estable a temperatura ambiente. Para que se convierta en rutilo son necesarias temperaturas superiores, que provocarían un aumento del tamaño cristalino y reducción del área activa sobre cual está inmovilizado el colorante sensibilizador, que, como hemos visto, es un factor clave para el funcionamiento eficiente de la célula.

I-1.5.2) Otras propiedades del TiO_2: fotocataíticas, bactericidas, autolimpiables, antinieblas, antitumor, etc.

El motivo por el que el dióxido de titanio se usa como fotocatalizador es que la iluminación de la superficie del material origina la descomposición de un buen numero de sustancias orgánicas. Debido de que el dióxido de titanio es un semiconductor con ancha banda prohibida (alrededor de 3.0 eV), la luz ultravioleta se absorbe y excita a pares de electrones y huecos. Dichos electrones pueden reaccionar con oxígeno molecular para producir aniones superóxido (O_2^-), y los huecos reaccionan con agua, produciendo radicales hidróxilos ($^{\cdot}OH$) [57-61]. La presencia de estos dos tipos de especies, muy activas, puede originar la descomposición de compuestos orgánicos y, también, la destrucción de bacterias patógenas, virus y tumores[57].

Cabe destacar que dicho fenómeno ocurre con muy baja intensidad de la luz. Por eso no es necesaria la iluminación directa del sol. En una habitación con intensidad de luz media, 10μW/cm^{-2}, de la cual sólo ~ 1μW/cm^{-2} tiene longitud de honda adecuada para la activación del TiO_2, en unos 30-60min se efectúa la desinfección total o destrucción de una capa orgánica de un grosor de 1μm [58]. La luz artificial, como la común fluorescente, también provoca la activación del TiO_2 y la destrucción de patógenos y contaminantes. Este proceso se puede utilizar para la purificación del aire en las viviendas [58].

Un efecto, descubierto accidentalmente en el año 1995, pero importante para aplicaciones en superficies autolimpiables y antinieblas, es la alta hidrofilidad provocada bajo la iluminación de la luz ultravioleta. Los electrones formados por dicha separación de carga pueden reducir el Ti(IV) hasta Ti(III) y los huecos oxidar a los aniones O_2^-. En este proceso se expulsa un átomo de oxigeno, creando una vacante. Las moléculas de agua ocupan estas vacantes, suministrando grupos -OH que quedan adsorbidas en la superficie hidrófila. Bajo iluminación, el agua se extiende sobre toda la superficie.

Por todo ello, las películas nanocristalinas con enorme área activa de dióxido de titanio encuentran las siguientes aplicaciones:

- *Depuración de fluidos contaminados como aguas y gases residuales, aguas potables y aire.*

Dicha aplicación abarca un amplio campo, donde se puede emplear el efecto fotocatalitico de las películas nanocristalinas de dióxido de titanio. Algunos elementos dopantes como N, Fe, Pt, Cu, Ag, Mo, Zn pueden aumentar la velocidad del proceso de descomposición de las sustancias orgánicas [60]. Se han investigado las posibilidades de eliminación de contaminantes de orgánicos:
-alcanos y alquenos ;
-compuestos aromáticos;
-haluros de los alcanos, alquenos y aromáticos;
-compuestos orgánicos que contienen nitrógeno;
-hidrocarburos;
-ácidos orgánicos;
-pesticidas, herbicidas, surfactantes, colorantes;
Es de gran interés el uso del dióxido de titanio para la descomposición fotocatalitica de componentes tóxicos con bajas concentraciones permitidas. La eliminación de cianuros, tricloroetileno, percloroetileno, 4-clorofenol, tricloroetano, clorobencena, DDT, [61] etc. a través de los otros métodos ya conocidos es cara e incomoda.

-*Materiales para hospitales, edificios residenciales y de oficina:*
Baldosas para hospitales y quirófanos, azulejos exteriores e interiores, componentes de cocinas y aseos, superficies de muebles, superficies plásticas, persianas.
-*Materiales para carreteras*:
Recubrimientos del cristal para farolas, paredes de los túneles, pantallas aislantes acústicas, señales y reflectores.
-*Otros*:
Materiales para tiendas de campaña, ropa del hospital, pinturas autolavables, recubrimientos de coches, capas transparente UV-protectoras resistente al rayado, etc. [58].

Películas preparadas en el presente trabajo se han caracterizado por un laboratorio externo y han demostrado un aumento significativo de la actividad bactericida bajo iluminación.

I-1.6) Nanopartículas y métodos de síntesis

En las últimas décadas las nanopartículas han sido un campo científico muy popular. Conocidas también como *puntos cuánticos* o *partículas Q*, estas partículas coloidales tienen normalmente tamaños inferiores de 100 nm. En plan divulgativo, 30 g de partículas nanometricas, ordenadas en línea, formarían un hilo hasta la luna [62].

Muy importante para la célula solar de colorante es la enorme área efectiva que forma una película de nanopartículas. Por ejemplo, una película de 10 µm compuesta por nanopartículas de 10 nm tiene una área 1000 veces mayor que una superficie plana[22]. Así, la película mesoporosa (con tamaño del poro nanométrico) puede absorber sobre su superficie una cantidad suficiente de colorante en forma de capa monomolecular para captar la luz de la zona visible del espectro [63].

Cuando el tamaño de la partícula es más pequeño que el radio de Bohr del primer estado de excitación (normalmente por debajo de los 10 nm), se observan numerosos efectos cuánticos (confinamiento cuántico) [64, 65] que pueden dar lugar a propiedades diferentes de las partículas con mayor tamaño del mismo compuesto. Por ejemplo, el *bandgap* (ancho de banda) de los semiconductores aumenta, provocando un desplazamiento de la absorbancia hasta longitudes de onda menores[a66]. Un confinamiento cuántico fuerte implica que los nanocristales de un aislante, tenga varios niveles de energías discretos de valencia y conducción, parecidos a los de los átomos [66]. También se ha observado eficiencia quántica (ratio entre fotones absorbidos y electrones generados) mayor que 100% por la multiplicación de portadores en materiales nanocristalinos [66].

I-1.6.1) La síntesis hidrotermal

Con este método nanopartículas de TiO_2 se obtienen por hidrólisis en medio ácido de un precursor de titanio (generalmente un alcóxido, seguido del tratamiento térmico del producto de la hidrólisis en una bomba de presión a 220-280°C durante 12h [67].

A pesar de que se obtienen polvos muy homogéneos, este método requiere altas temperaturas y presión lo que encarece y complica el proceso.

I-1.6.2) El procesado sol-gel

El método sol-gel tiene características atractivas para la síntesis de óxidos y en particular, óxidos mixtos y materiales híbridos. Las más importantes de éstas características son la elevada pureza, la alta homogeneidad del material y la posibilidad de utilizar temperaturas relativamente bajas para obtener fases muy complejas. En todos estos aspectos, el método sol-gel es superior al método tradicional cerámico, donde la pureza, homogeneidad y reactividad de las fases sólidas es más baja.

Con el término sol-gel hoy se denomina una gran variedad de procedimientos, y prácticamente se suele utilizar para muchos métodos que utilizan una disolución para obtener material homogéneo que incluye en su estructura metal, incluso cuando no se forma como etapa intermediaria sol o gel. Por eso, en muchos de los casos es mas correcto el termino “química suave”.

El procedimiento sol-gel clásico fue desarrollado a base de reacciones de alcóxidos metálicos (principalmente de silicio, a pesar de que posteriormente fue adaptado a una gran variedad de metales) reúne los requisitos de etapas “sol” y “gel”. Las principales reacciones que dirigen éstas etapas son la hidrólisis y la condensación.

La mayoría de los métodos sol-gel incluyen algunas o todas de las siguientes etapas (Figura I-1.15):

Figura I-1.15 Diagrama del flujo del proceso sol-gel

En primer lugar se produce una homogeneización de los precursores en un disolvente hasta la obtención de una disolución que contenga los iones deseados para la formación del producto final. Los reactivos de partida que se emplean en la síntesis habitualmente son compuestos inorgánicos u orgánometalicos (alcóxidos de metales). Tras la dosificación de los precursores y la preparación de la disolución se procede a la obtención del sol. La definición de sol e una suspensión coloidal de partículas, a pesar de que no siempre ésta fase está presente.

Hidrólisis

La reacción implica el ataque de un grupo hidroxilo de la molécula del agua a un átomo metálico que conlleva la sustitución de un grupo OR(del alcóxido) por OH (del H_2O):

$$M(OR)_n + xH_2O \longrightarrow M(OH)_X(OR)_{n-x} + x\ ROH$$

Donde M puede ser: Si, Ti, Zr, Al, …R=alquílo.
En función de la cantidad de agua y del tipo de catálisis, la hidrólisis puede ser completa o parcial. La hidrólisis es completa cuando se reemplazan todos los grupos OR por OH:

$$M(OR)_n + n\ H_2O \longrightarrow M(OH)_n + n\ ROH$$

Condensación
Tras el proceso de hidrólisis se inicia el proceso de la condensación. Ésta puede darse a través de dos mecanismos que compiten entre sí: *oxolación* u *olación* [68]. La oxolación es la condensación a través de la formación de puentes de oxígeno:

$$\text{-M-OH+OH-M-} \longrightarrow \text{-M-O-M-} + H_2O$$

En cambio, la olación conlleva una condensación por formación de puentes hidroxo (-OH), entre los dos centros metálicos:

$$\text{-M-OR+OH-M-} \longrightarrow \text{-M-O-M-} + ROH$$

El conjunto de todas estas reacciones van a influir en la transformación del alcóxido metálico en una red macromolecular. La estructura y la morfología del material resultante dependerá, enormemente, de la contribución de cada una de estas reacciones. La combinación de las especies oxo-metálicas puede producir un

entramado tridimensional que afecta a todo el material, formando un gel. Sin embargo, dentro del gel pueden quedar retenidas moléculas del disolvente, subproductos de reacción o polímeros libres. Además, un gel no es el único producto que se puede obtener en estas reacciones de polimerización ya que se pueden alcanzar otros estados finales: formación de soles en donde existen estructuras polimerizadas pero que no alcanzan tamaños macroscópicos, precipitados en el caso de que las reacciones produzcan estructuras densas, polímeros poco solubles, etc. [68].
El control de estas reacciones para evitar una precipitación heterogénea se efectúa a través de parámetros como:

-*Relación agua/alcóxido metálico*.
En principio, con mayor proporción de agua, la velocidad de hidrólisis va a aumentar. Sin embargo, hay que tener en cuenta que la cantidad de agua puede influir la estructura final del material. Exceso de agua puede originar la formación de geles particulados o precipitados.

-*Uso de catalizadores.*
Los ácidos actúan protonando a los ligandos alcóxido de los precursores metálicos, que se encuentran cargados negativamente, transformándolos en mejores grupos salientes:

$$M\text{-}O\text{-}R \quad + \quad H^{+} \quad \longrightarrow \quad M\text{-}OH^{+}\text{-}R$$

Al eliminar la etapa de transferencia del protón del agua al grupo OR del alcóxido, se consigue acelerar la cinética de la reacción de hidrólisis. La condensación, en estas condiciones, se ve retardada con respecto a la hidrólisis, lo que permite separar estos dos procesos.

-*Uso de ligandos quelantes.* El uso de agentes quelantes tales como las β-dicetonas, los polialcoholes o ácidos carboxílicos permite reducir los procesos de condensación. La acetilacetona (acac) es una β-dicetona muy utilizada que se coordina fácilmente con los alcóxidos metálicos de acuerdo con la reacción:

$$M(OR)_n + x\ acacH \rightarrow M(OR)_{n-x}(acac)_x + x\ ROH$$

Las reacciones de hidrólisis y condensación de alcóxidos modificados con acac están gobernadas por dos parámetros: la relación de hidrólisis, $h=[H_2O]/[M]$, y la relación de complejación, [acac]/[M]. Los enlaces M-acac se hidrolizan más lentamente, previniendo los procesos de condensación en favor de la formación de especies pequeñas[68].

Finalmente, factores como el envejecimiento, secado y tratamiento térmico influyen el producto resultante.

En el presente trabajo se han utilizado ácido acético como catalizador, acac como quelante y ácido p-toluensulfonico como quelante y catalizador. Se ha estudiado la influencia del tratamiento térmico sobre el material obtenido.

I-1.6.3) Síntesis en llama

Esta técnica está comercializada por la empresa Degussa para la fabricación de polvo nanocristalino de TiO_2. Se emplean precursores volátiles metalorgánicos de Ti, los cuales se inyectan con el combustible en mecheros especiales. El tiempo de reacción es muy corto y la temperatura - más alta que la necesaria para la transformación del anatas en rutilo. El producto contiene aproximadamente 75% anatasa y 25% rutilo.

I-1.7) Métodos de deposición de capas por sol-gel

Las técnicas más comunes para deposición de capas delgadas a partir de soles son el *spin-coating* y el *dip-coating.* La técnica *doctor-blade* es adecuada para depositar películas a partir de suspensiones de polvo.

I-1.7.1) La técnica *spin-coating*

Llamada también recubrimiento por rotación o centrifugado, ésta técnica consiste en depositar unas gotas de la solución sobre el substrato a recubrir, que se somete a centrifugado para repartir homogéneamente el recubrimiento y eliminar el líquido sobrante. Los factores determinantes son la concentración del líquido y la velocidad de centrifugado.

Se puede generalmente dividir en cuatro etapas:

1) Deposición de la solución sobre el substrato (Fig. I-1.17). Se puede efectuar a través de una pipeta o dispositivo dosificador especial. Normalmente se suministra exceso del fluido que se reducirá en las siguientes etapas. Para muchas disoluciones es recomendable usar un filtro submicrométrico para eliminar las partículas que pueden provocar defectos en el recubrimiento.

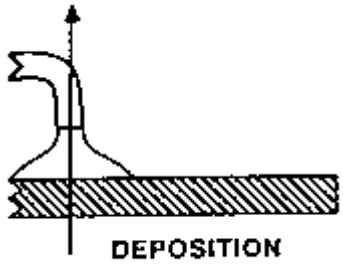

Figura I-1.17. Deposición de la disolución sobre el substrato.

2) Con *Spin-up* se denomina la etapa de aceleración del substrato hasta la velocidad deseada (Figura I-1.18).

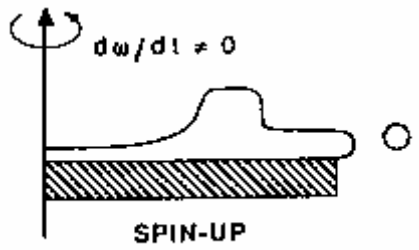

Figura I-1.18. La aceleración del substrato hasta la velocidad deseada.

Esta etapa se caracteriza por una agresiva expulsión del fluido por la rotación. La rotación puede provocar flujos espirales, los cuales desaparecen cuando la capa este suficientemente fina para girar simultáneamente con el substrato. Alcanzado la velocidad máxima, las fuerzas de la viscosidad y la aceleración giratoria se equilibran.

3) En la tercera etapa (*Spin-off*), el substrato está girando a una velocidad constante, siendo las fuerzas de viscosidad dominantes sobre el comportamiento del fluido. La capa se hace más fina gradualmente (fig I-1.19)

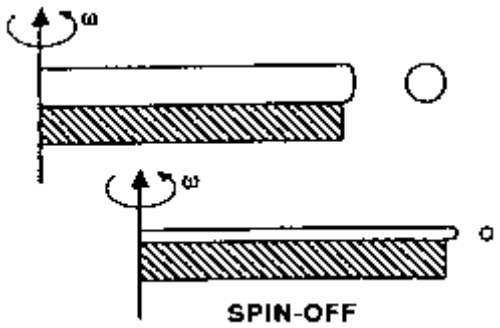

Figura I-1.19. El substrato está girando a la velocidad máxima.

4) En la cuarta etapa de *Evaporación*, el substrato sigue girando a velocidad constante, siendo la evaporación del solvente dominante sobre el comportamiento de la película (Figura I-1.20).

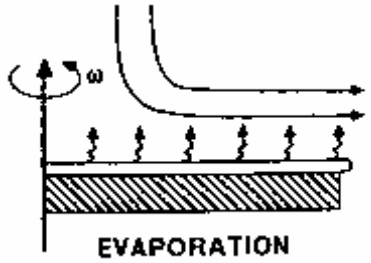

Figura I-1.20. La etapa de evaporación.

El grosor del fluido se reduce hasta el punto en el cual la viscosidad no permite un flujo significante. Desde este momento la evaporación del disolvente se convierte en el proceso principal. Prácticamente, la capa gelifica porque la eliminación del disolvente provoca un aumento en la viscosidad.

I-1.7.2) La técnica *dip-coating*

En el recubrimiento por inmersión *(dip-coating)*, el substrato se sumerge en una mezcla líquida con la formulación deseada. El espesor del recubrimiento depende de la concentración en el líquido, de la viscosidad y de la velocidad de extracción del substrato, factores que han de controlarse cuidadosamente para obtener recubrimientos homogéneos y reproducibles en cuanto a espesor, estructura y propiedades.
El proceso se puede dividir en cinco pasos [69]: El primero es la inmersión del substrato en la solución, seguido por elevación, deposición, drenaje y evaporación (Figura I-1.21).

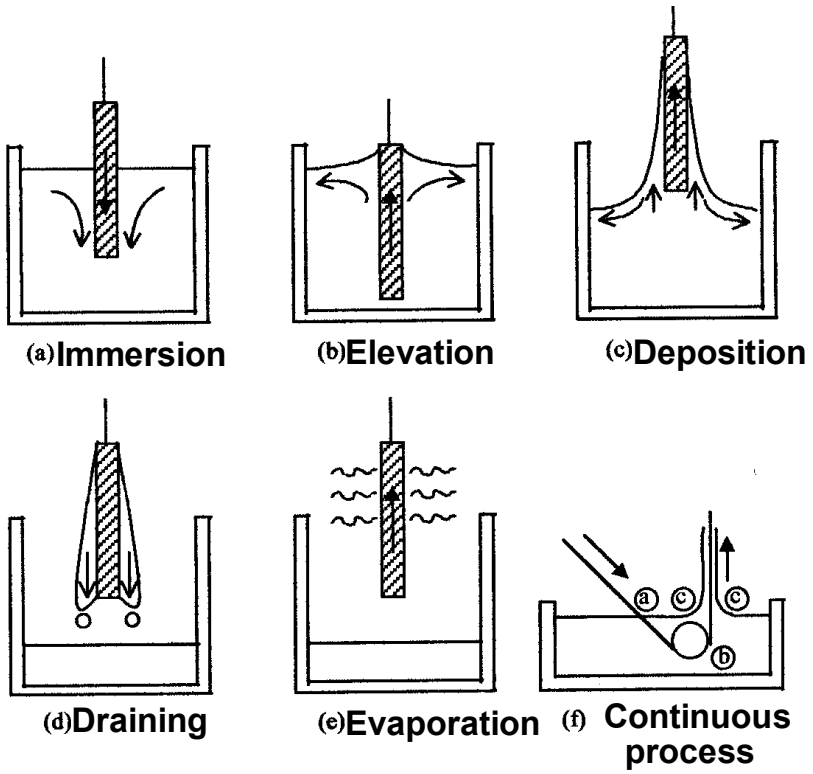

Figura I-1.21. El proceso “Dip Coating”.

I-1.7.3) La técnica *doctor-blade*

Ésta simple técnica se puede considerar un método de impresión y es fácilmente escalable (Figura I-1.22). Se utiliza frecuentemente para la deposición de capas a partir de suspensiones viscosas.

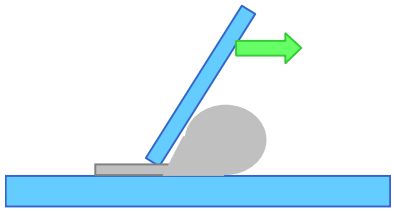

Figura I-1.22. La técnica doctor-blade.

Consiste en extender un líquido viscoso sobe la superficie del substrato empleando una varilla o hoja de metal o vidrio. En los ensayos de laboratorio, el grosor de la capa se puede controlar con cintas adhesivas, pegadas paralelamente sobre el substrato. Sobre ellos se desliza un elemento delimitador de grosor que puede ser una varilla de vidrio.

En el presente trabajo se han empleado las técnicas spin-coating y doctor-blade para depositar capas de sol-gel y suspensiones respectivamente. Después de un secado adecuado, cada muestra se ha sometido a un tratamiento térmico específico.

I-1.8) Técnicas instrumentales de caracterización y análisis

Los diferentes equipos que se han empleado en la caracterización de los materiales desarrollados se encuentran en las secciones del Servicio Central de Instrumentación Científica (SCIC) de la Universidad JAUME I.

Información más detallada sobre las técnicas y métodos empleados se puede encontrar en la introducción de la ***Parte II****.*

Análisis térmico diferencial y termogravimetría (ATD/TG)

Análisis térmico diferencial y termograviertría (ATD/TG) y espectroscopia de masas, mediante un equipo METTLER TOLEDO STAR^{e} acoplado a un espectrómetro de masas, BALZERS, modelo QUADSTAR™422. El análisis se ha llevado a cabo en flujo de aire y velocidad de calentamiento de 5°C en el intervalo 25-1000°C con una rampa de 1h a 400°C.

Difracción de rayos X (DRX)* en polvo

La caracterización estructural de los materiales sintetizados se ha realizado a través de un difractómetro de rayos X en polvo, mediante un equipo SIEMENS, modelo D5000, con una geometría Bragg-Bretano, provisto de cátodo de cobre y filtro de níquel y monocromador de grafito. Generalmente, las medidas se han llevado a cabo con voltaje de 40kV y 20mA, en el intervalo de 15 a 70º/2θ con un paso de 0.03º/2θ y con un tiempo de recogida de los impulsos de 1 s. Para la determinación del tamaño cristalino medio se ha utilizado la formula de Scherer utilizando como patrón externo de referencia el Si.

Los tamaños medios de los cristalitos se han calculado a través de la ecuación de Scherrer [70]:

$$t = \frac{0.9\lambda}{B \cos \theta_B}$$

$$B = \sqrt{\left(B_M^2 - B_S^2\right)}$$

* Hemos utilizado también la abreviación inglesa XRD (X-Ray Diffraction)

Donde t es el tamaño medio λ es la longitude de honda de los rayos X, θ_B el ángulo de Braga, B_M la anchura de medio pico de la muestra en radianes y B_S – la misma del patrón utilizado (Si).

Microscopía electrónica de barrido (MEB)[**] y microanálisis por dispersión de energías de rayos X (EDX)

Se han caracterizado micorestructuralmete todos los materiales obtenidos mediante Microscopía electrónica de barrido (MEB*)* a través de un microscopio electrónico de barrido LEO 440 (Oxford Instruments) equipado con un espectrómetro que mide la dispersión de energías de rayos-X. Las imágenes se han obtenido con una distancia del foco de 10 a 25 mm, voltaje de aceleración de 20kV y corriente de sonda 100pA. Los parámetros de medida del microanálisis han sido: voltaje 20kv, corriente de sonda 1nA, tiempo de medida 100s, velocidad de recuento 1.2 kcps. Las muestras se han colocado sobre un adhesivo de grafito adherido a un portamuestras de aluminio y se han sombreado con grafito.

-Propiedades ópticas

Las propiedades ópticas de las muestras se ha medido con espectrofotómetro Cary 500 Scan UV-Vis-NIR en el intervalo 250-1100 nm. Se ha utilizado la unidad de medida en transmitáncia. Como referencia se ha utilizado un vidrio sin recubrimiento.

[**] Hemos utilizado también la abreviación inglesa SEM (Scanning Electrón Microscopy)

I-2) PREPARACIÓN DE PELÍCULAS NANOCRISTALINAS DE TiO_2 POR EL MÉTODO SOL-GEL

I-2.1) Metodología

En la primera etapa de nuestro trabajo hemos utilizado el método sol-gel para preparar polvos y películas nanocristalinas Figura I-2.1. Las películas se han depositado por dos vías:

a) directamente por spin-coating y

b) a partir de polvos nanocristalinos, producidos por el método sol-gel y redispersados.

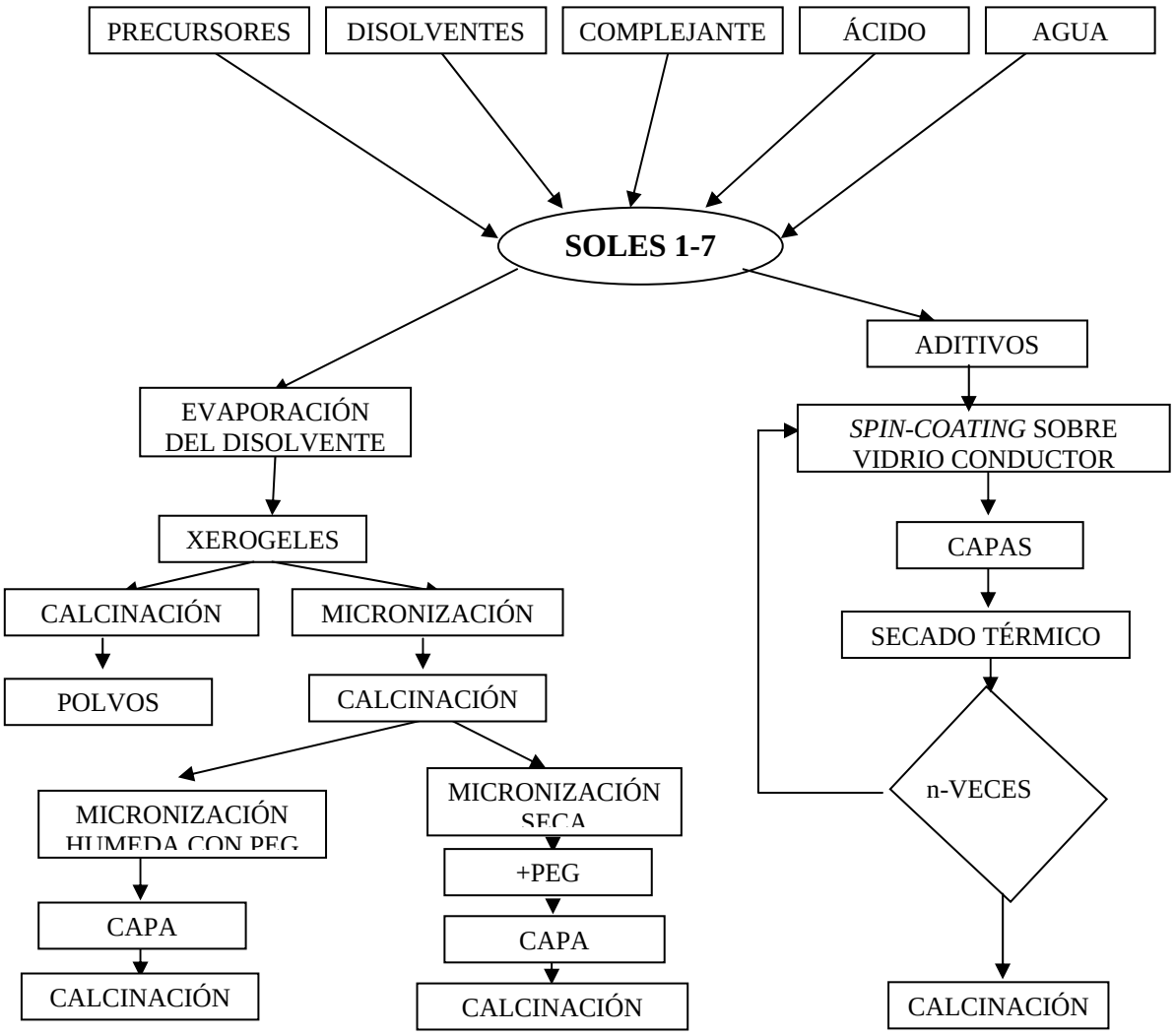

Figura I-2.1. Diagrama de flujo de la preparación de las películas.

Hemos utilizado varias secuencias de micronizado con el propósito de reducir el grado de sinterización entre las partículas durante el tratamiento térmico y finalmente – para poder dispersar los polvos en suspensiones.

Se han preparado 7soles de diferentes composiciones, empleando siempre el ratio molar: precursor / complejante / disolvente / agua / ácido: 1/1/9/10/0.2 (Tablas I-2.I-VII). En la muestra 2 se ha omitido la adición de agua. I-propóxido y n-butóxido de titanio (IV) se han utilizado como precursores del metal. Acetilacetona se ha usado como complejante en todos los casos para evitar la hidrólisis rápida del Ti(IV). La reacción de hidrólisis se ha catalizado con los ácidos acético y p-toluenesulfónico.

Se han usado los siguientes reactivos:
- i-propoxido de titanio, 98%, STREM CHEMICALS
- n-butoxido de titanio, 99%, ABCR
- acetilacetona (acac), 99.5%, PROBUS
- etanol, 99.8%, SCHARLAU
- i-propanol, 99.85%, FLUKA
- n-butanol, 99.89%, PROBUS
- ácido acético, 99.7%, PROBUS
- ácido p-toluensulfónico, 99%, ALFA AESAR
- Polietilenglicol

I-2.2) Preparación

Utilizando el razón molar indicado anteriormente, las cantidades de reactivos utilizados para la preparación de los soles se muestran en las Tablas I-2.I-VII.

Tablas I-2.I-VII. Composiciones:

I - SOL Nº1			
COMPUESTO	Tiempo de adición (min).	Cantidad. (mol)	Masa (g)
Etanol	0	0.342	15.79
AcAc	1	0.038	2.29
Ti $(OPr^i)_4$	5	0.038	11.02
H_2O	20	0.380	6.84
ácido acetico	20	0.0076	0.45

II - SOL Nº2			
COMPUESTO	Tiempo de adición (min).	Cantidad. (mol)	Masa (g)
i-propanol	0	0.342	20.58
AcAc	1	0.038	2.29
Ti $(OPr^i)_4$	5	0.038	11.02
H_2O	--	--	--
ácido acetico	20	0.0076	0.4577

III - SOL Nº3			
COMPUESTO	Tiempo de adición (min).	Cantidad. (mol)	Masa (g)
i-propanol	0	0.342	20.55
AcAc	1	0.038	2.29
Ti $(OBu^n)_4$	5	0.038	12.9
H_2O	20	0.380	6.84
ácido acetico	20	0.0076	0.45

IV - SOL Nº4			
COMPUESTO	Tiempo de adición (min).	Cantidad. (mol)	Masa (g)
Etanol	0	0.342	15.792
AcAc	1	0.038	2.293
Ti $(OBu^n)_4$	5	0.038	12.9
H_2O	20	0.380	6.84
ácido acetico	20	0.0076	0.45

V - SOL Nº5			
COMPUESTO	Tiempo de adición (min).	Cantidad. (mol)	Masa (g)
Etanol	0	0.342	15.79
AcAc	1	0.038	2.29
Ti $(OBu^n)_4$	5	0.038	11.02
H_2O	20	0.380	6.84
ácido p-toluensulfónico	20	0.0076	1.46

VI - SOL Nº6			
COMPUESTO	Tiempo de adición (min).	Cantidad. (mol)	Masa (g)
n-Butanol	0	0.342	25.34
AcAc	1	0.038	2.29
Ti $(OBu^n)_4$	5	0.038	12.9
H_2O	20	0.380	6.84
ácido acetico	20	0.0076	0.45

VII - SOL Nº7			
COMPUESTO	Tiempo de adición (min).	Cantidad. (mol)	Masa (g)
n-Butanol	0	0.342	25.34
AcAc	1	0.038	2.29
Ti $(OBu^n)_4$	5	0.038	12.9
H_2O	20	0.380	6.84
ácido p-toluensulfónico	20	0.0076	1.46

Síntesis

La síntesis de cada sol se llevó a cabo en un matraz de 200 ml. Después de añadir el alcohol y el complejante (acetilacetona), la mezcla se sometió a agitación magnética durante 5 minutos antes de incorporar el precursor de titanio. 20 minutos más tarde el agua, homogenizada con ácido se añadió gota a gota agitando vigorosamente. Después de 2 horas a temperatura ambiental, los soles se calentaron a 40 °C, manteniendo la agitación durante 24h.

Los soles se han dividido en dos partes para:
- deposición directa a través de *spin-coating*
- preparación de polvo.

Preparación de películas a través de *spin-coating*

Los soles se diluyeron con etanol (99.8%) para ajustar su densidad a 0.85 g/ml. La solución obtenida se depositó sobre vidrio conductor FTO (Vidrio, recubierto con una capa de óxido de estaño, dopado con flúor) con resistividad de hoja (*sheet resistance*)

10 Ω/□. Se utilizó un spin-coater de *CHEMAT TECHNOLOGY KW-4A* y velocidad de giro 4000 rpm durante 20 s. Después de cada ciclo de deposición las muestras se secaron a 100°C durante 5min y 250°C durante 30 min. La calcinación final se llevó a cabo a 450°C durante 1h.

Con el fin de aumentar la porosidad (observada por microscopía electrónica de barrido) de las capas obtenidas con la metodología anterior, se prepararon muestras a partir de soles, modificados con la adición de 20 o 40% de PEG con respecto al TiO_2.

Preparación de polvos y películas a partir de suspensiones.

Para obtener cada xerogel, el sol correspondiente se transfirió a un vaso de precipitados de 200 mL y colocó en un desecador durante 48 horas. Después se secó en aire hasta la formación de gel estable. Se completó el secado, poniendo las muestras en una estufa eléctrica a 60°C durante 48 horas.

La muestras así obtenidas se molturaron en un mortero de ágata y dividieron en dos partes:

- Una parte se calcinó directamente a temperaturas diferentes (300, 400, y 450°C) con una velocidad de calentamiento de 5 °C/min con objeto de obtener TiO_2.

- La otra parte se ha sometió a micronización vía húmeda (3 ciclos de 15 min) en molino vibratorio McCrone con cilindros de trabajo de ágata. A continuación las muestras se calcinaron durante 1 o 3 horas a 300, 400 o 450°C (velocidad de calentamiento 5 °C/min). Los polvos calcinados se micronizaron de nuevo vía húmeda durante 25 min, repitiendo el proceso 2 veces.

Se obtuvieron suspensiones de 20% TiO_2 en agua a partir de los polvos calcinados y micronizados con una adición de 8% PEG 20000 con el propósito de (i) aumentar la viscosidad para facilitar buena homogeneidad de la capa impresa y (ii) reducir el grado de sinterización, aumentando así la porosidad. Para mejor dispersión se empleó agitación ultrasónica. Las suspensiones se depositaron mediante la técnica *Doctor-blade* sobre substratos de vidrio conductor FTO (SnO_2:F). Las películas obtenidas se han calcinaron a 450°C de 1 a 3h con una velocidad de calentamiento de 5°C/min.

Figura 1-2.2 presenta una foto de los productos de los diferentes etapas del trabajo: sol, xerogel, polvo micronizado de anatasa, película, preparada por *doctor-blade* y películas de 5 capas sobre FTO antes y después de la sensibilización.

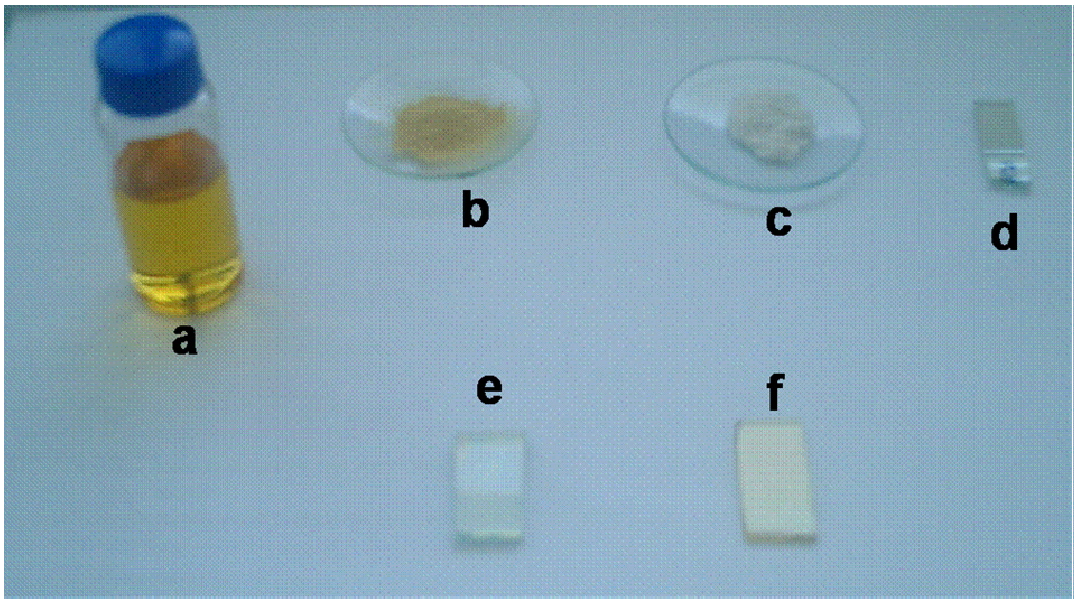

Figura I-2.2. Productos de los diferentes etapas del trabajo: sol (a), xerogel (b), nanopartículas micronizadas de anatasa (c), film obtenido por *doctor blade* a partir de las nanopartículas (d), film obtenido por *spin coating* del sol antes (e) y después de sensibilización (f).

I-2.3) Resultados y discusión

I-2.3.1) Análisis térmico diferencial y termogravimetría (ATD/TG).

Como se puede apreciar en Figura I-2.3. a y b, durante el tratamiento termico de los xerogeles, aproximadamente el 45% de la masa se pierde, debido a la evaporación de los compuestos volátiles y a la combustión de la materia orgánica.

En las muestras preparadas con ácido acético como catalizador, ésta pérdida ocurre casi completamente antes de alcanzar los 400°C (Fig. I-2.3a)). En el caso del ácido p-toluensulfónico, la combustión finaliza alrededor de 500°C (Fig. I-2.3b).

El pico exotérmico de la transformación de anatasa en rutilo se detecta a 790°C.

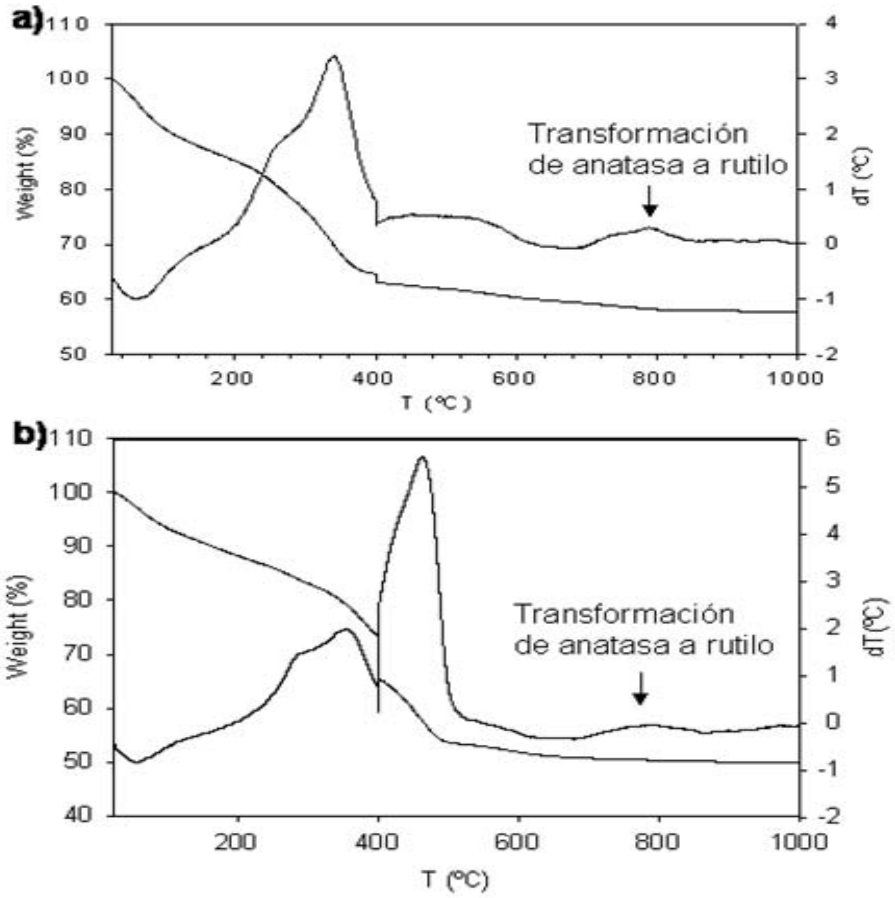

Figura I-2.3. Diagrama de ATD/TG de xerogel Nº 1, preparado con ácido acético (a) y de xerogel Nº 5, preparado con ácido p-toluensulfonico(b).

I-2.3.2) Difracción de rayos X (DRX)

La difracción de Rayos X revela que los xerogeles, así como las muestras calcinadas a 300°C, representan estructuras amorfas, pero tras la calcinación a 400 y a 450°C se detecta TiO_2 (fase anatasa). En la Figura I-2.4 se representan los difractogramas de los polvos calcinados a 450°C durante 1 hora con y sin micronización respectivamente. Los picos se asignan al polimorfo anatasa del TiO_2 JCPDS 21-1272.

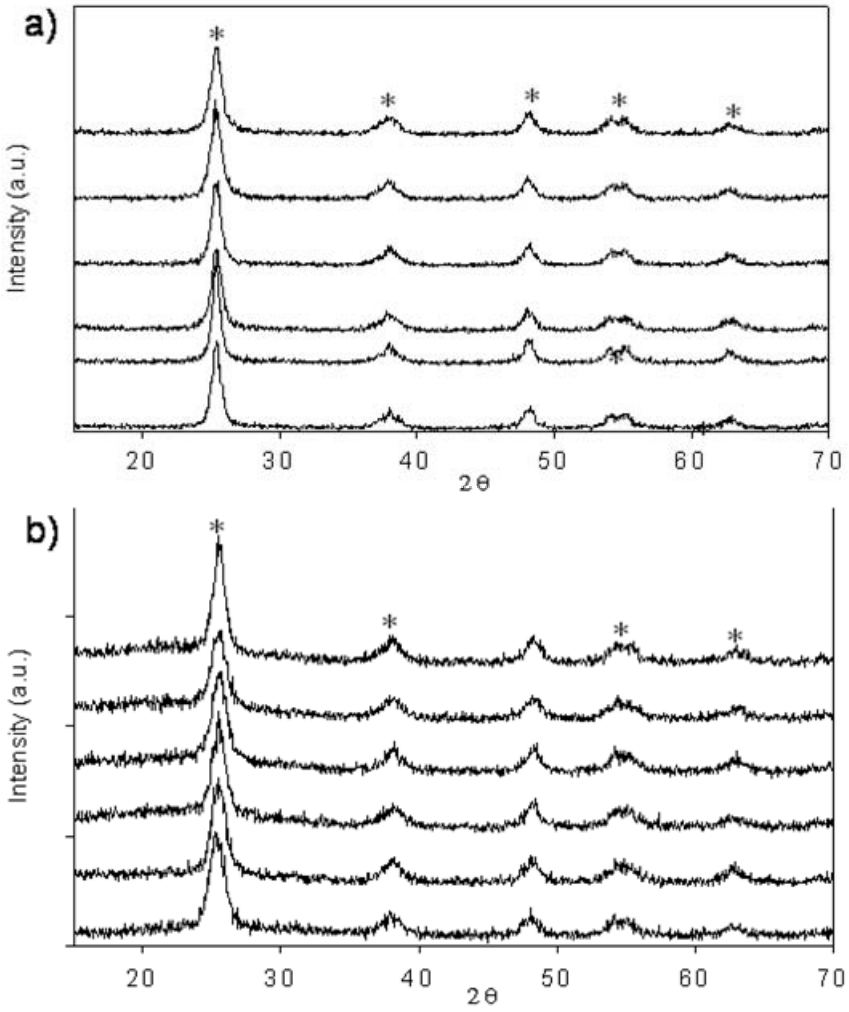

Figura I-2.4. DRX de polvos, calcinados a 450°C durante 1h sin micronización previa (a) y con (b) micronización previa.
*picos de TiO_2 anatasa, JCPDS 21-1272.

En la Figura I-2.5a se incluyen los difractogramas de películas depositadas sobre vidrio conductor por *doctor blade* a partir de polvos calcinados y micronizados y por *spin coating* de disoluciones(Figura I-2.5b). La principal diferencias con respecto a los representados en los difractogramas de polvos es la aparición de la fase de SnO_2 casiterita, JCPDS 41-1445, debido a la capa transparente conductora de SnO_2:F del substrato.

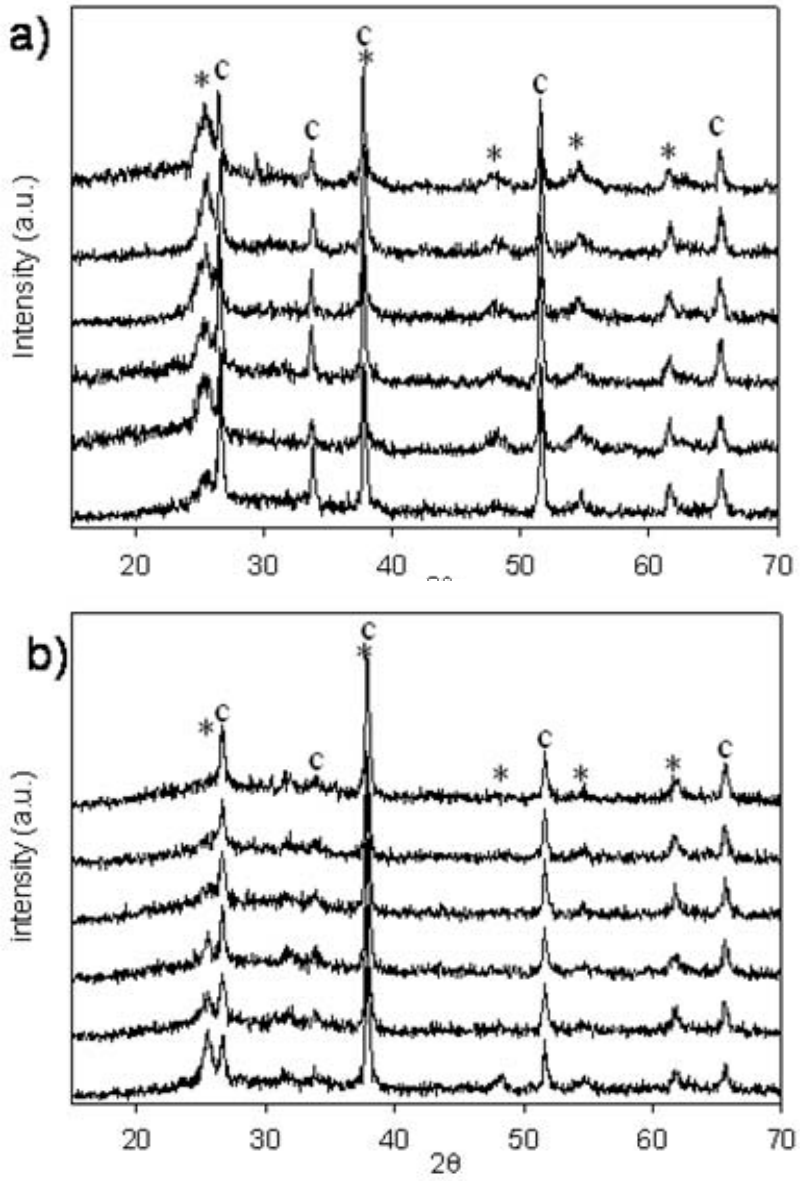

Figura I-2.5. DRX de películas, depositadas sobre vidrio conductor (SnO_2:F) a partir de polvos micronizados (a) y de soles por *spin-coating* (b) .
*picos de TiO_2 anatasa, JCPDS 21-1272, ^{c} SnO_2 cassiterita, JCPDS 41-1445.

Los tamaños de los cristales, calculados a partir de la anchura del pico principal (101) se muestran en la Tabla I-2.VIII.

Tabla I-2.VIII. Tamaños medios de los cristales obtenidos por los diferentes métodos y a partir de los soles indicados en la tabla (P=polvo, F=film, M=micronizado).

REFERENCIA DEL SOL (Tabla 1)	**Nº 1**	**Nº 2**	**Nº 3**	**Nº 4**	**Nº 5**	**Nº 6**	**Nº 7**
TIPO MUESTRA Y CONDICIONES	Tamaño medio (nm)						
P, calcinado a 400° C - 1h	16,9	20,1	15,7	16,1	11,1	15,3	12,0
P, calcinado a 450° C - 1h (figura 3)	18,4	18,2	22,0	17,9	18,4	18,0	15,7
P, M, calcinado a 450° C - 1h (figura 4)	12,6	11,2	11,0	10,7	10,3	12,8	10,0
P, M, calcinado a 450° C - 3h	16,1	12,9	11,7	--	10,6	--	10,7
F of M calcinado M P, calcinado a 450° C - 3h (figura 5)	15	11,9	12,1	--	10,5	13,4	10,3
F, 5 capas, directamente depositado(figura 6)	16,1	--	16,5	18	12,4	--	--

Los cristales obtenidos tienen tamaños medios entre 10 y 20 nm. Los nanocristales preparados con ácido p-toluensulfónico (N°5 y N°7) mostraron tamaños menores que las muestras para cuya preparación se ha empleado ácido acético. Se ha observado fuerte influencia de la temperatura de calcinación en las muestras calcinadas a 400 y 450°C, siendo los primeros más pequeños. El aumento del tiempo de calcinación de 1 a 3h ha contribuido menos al aumento del tamaño medio de los cristales en las muestras calcinadas a 450°C.

I-2.3.3) Microscopía electrónica de barrido (SEM).

Las micrografías por SEM (LEO 440, Oxford Instruments) revelaron que las muestras sin micronizar (Figura I-2.6) estaban formadas por aglomerados de granos de tamaño irregular entre 1 y 30μm con bordes agudos y lados lisos. Las muestras micronizadas (Figura I-2.7) consistían de aglomerados granulares con tamaño 0.5-10μm.

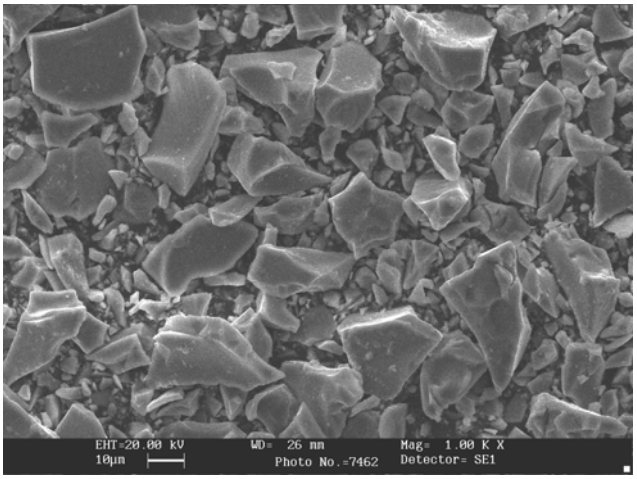

Figura I-2.6. Micrografía de aglomerados de titania obtenidos a partir de sol N5 sin aplicar micronización.

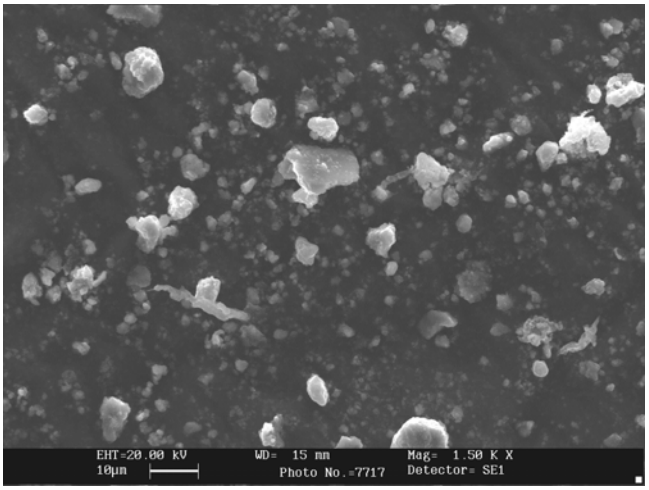

Figura I-2.7. Micrografía de aglomerados de titania obtenidos a partir de sol N5 aplicando micronización.

Imágenes de los cortes transversales de las películas muestran que las depositadas a partir de suspensión no presentaban una buena adhesión al substrato y un grosor de 30µm (Figura I-2.8), mientras que las capas obtenidas por spin-coating tenían una excelente adhesión y un grosor de 400nm (Figura I-2.9).

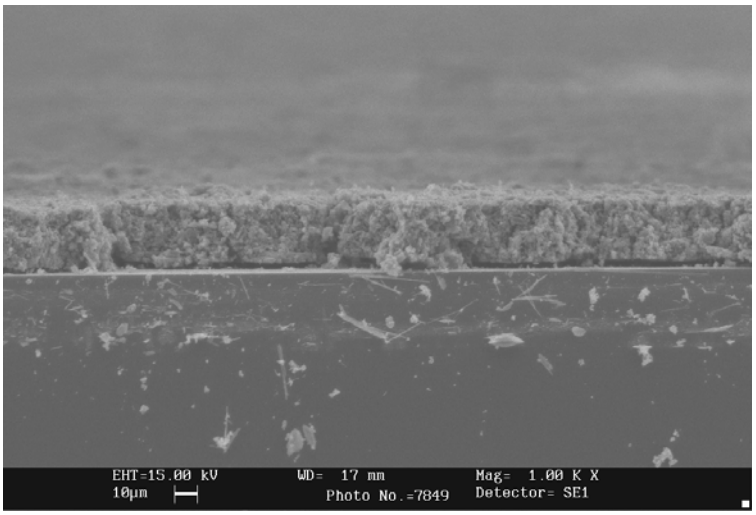

Figura I-2.8. Micrografía de película preparada a partir de suspensión de polvo nanocristalino

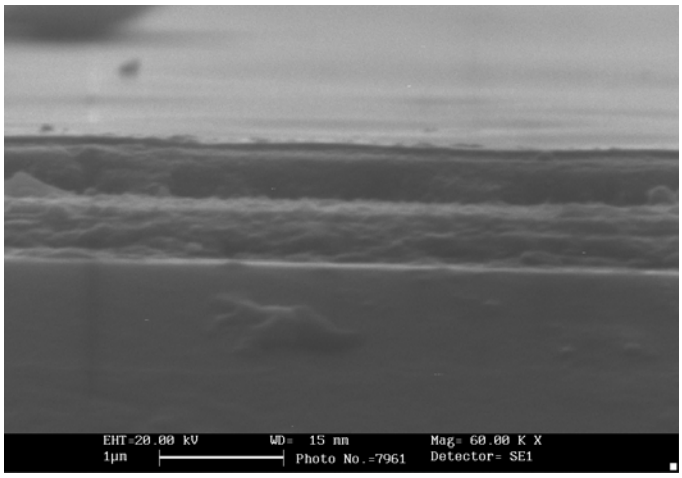

Figura I-2.9. Micrografía SEM de una película de 5 capas obtenida por spin-coating.

Las muestras preparadas a partir de soles puros son lisas (I-2.10), mientras que las modificadas por la adición de PEG 20000 presentan porosidad en forma de grietas micrométricas cuya densidad aumenta proporcionalmente con el contenido de PEG (Figuras I-2.11-12) .

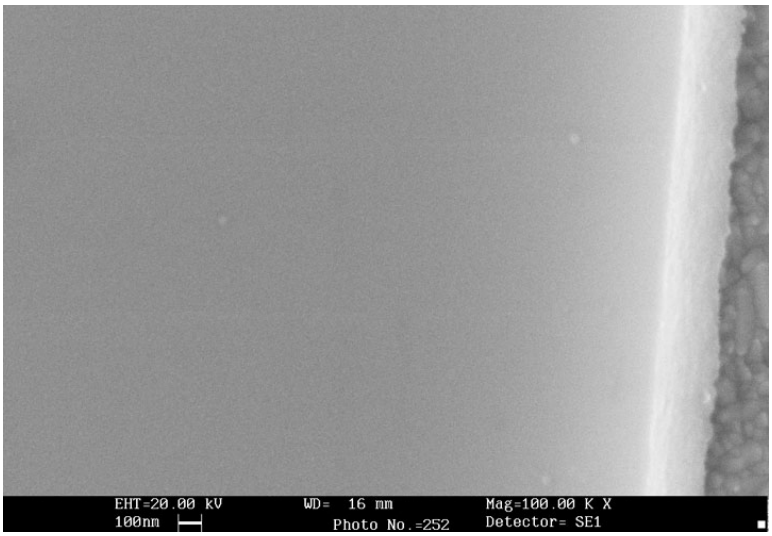

Figura I-2.10. Micrografía SEM de la superficie de una película obtenida por spin-coating de sol N°7 sin adición de PEG.

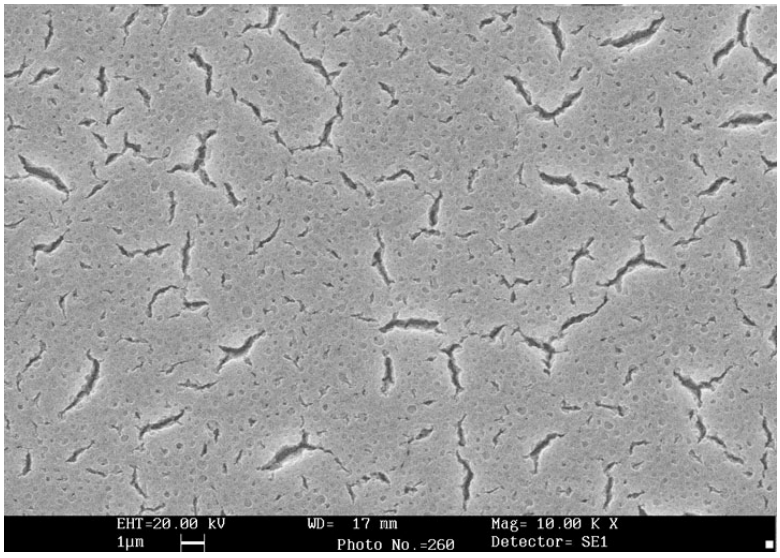

Figura 1.11. Micrografía SEM de la superficie de una película obtenida por spin-coating de sol N°7 con adición de 20% PEG.

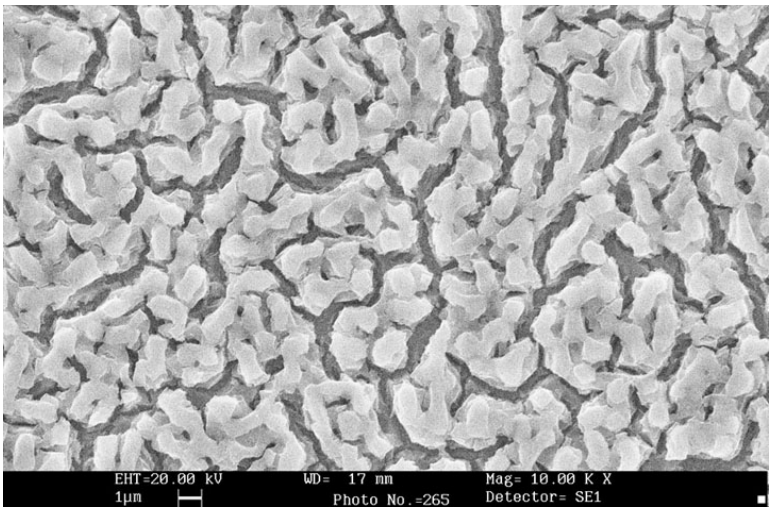

Figura 1.12. Micrografía SEM de la superficie de una película obtenida por spin-coating de sol N°7 con adición de 40% PEG.

I-2.3.4) Microscopía electrónica de transmisión. (TEM)

La imagen de TEM (figura I-2.13) de xerogel N°7, calcinado a 400°C durante 1 hora muestra la forma esférica de los nanocristales y su distribución de tamaño uniforme, la cual corresponde bien al tamaño medio calculado (12nm).

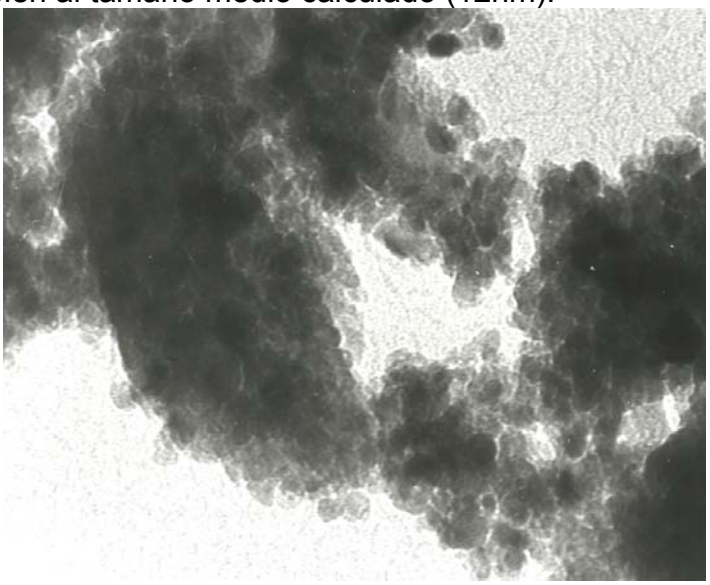

Figura I-2.13. Imagen de TEM del polvo de anatasa, preparado a partir de sol N°7.

I-2.3.5) Propiedades ópticas

Las películas preparadas a partir de suspensiones eran opacas, mientras que las obtenidas por spin-coating eran transparentes y su absorbancia se ha medido con un espectrómetro Cary 500 Scan (Figura I-2.14).

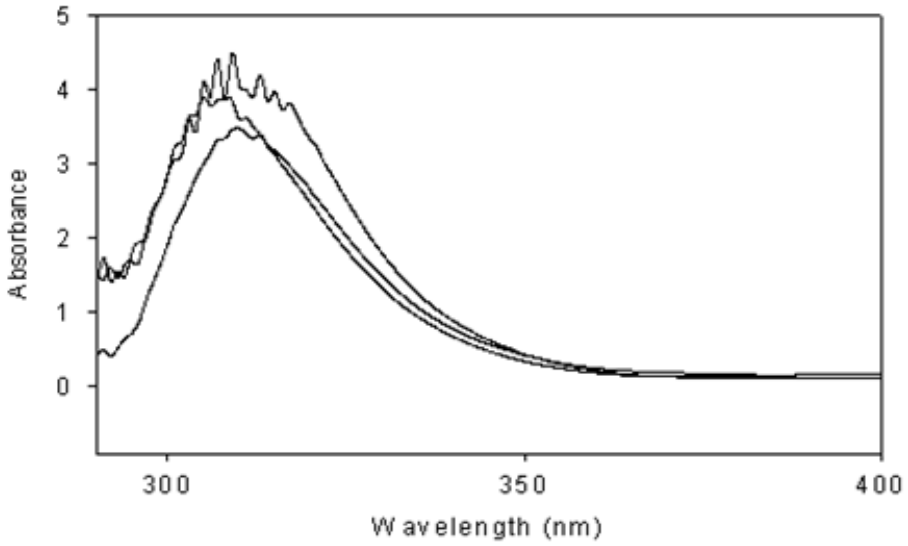

Figura I-2.14. Absorbancia en la región ultravioleta de muestras de 5 capas obtenidas por *spin-coating.*

Las colas de las bandas de absorción están desplazadas hacia longitudes de honda menores, correspondiendo un band gap de aproximadamente 3.4 eV cuando el del dióxido de titanio microcristalino varía entre 3 y 3.2 eV. Como hemos comentado, desplazamientos de éste tipo son efectos característicos de nanopartículas de tamaño menor.

I-2.3.6) Propiedades fotoeléctricas

Las medidas de fotocorriente en cortocircuito (J_{cc}) y el fotovoltaje de circuito abierto (V_{ca}) se han efectuado con potenciostato *Autolab* en una célula electroquímica de tres electrodos. Como electrolito ha utilizado una disolución acuosa ajustada a pH 2 con ácido sulfúrico. La fuente de luz ha sido una lámpara de Xenón de 150 W con la luz ultravioleta filtrada por debajo de 320nm.

Los datos obtenidos (Tabla I-2.9) muestran que los films preparados a través de *spin-coating* tenían mayor fotovoltaje (0.6V) y fotocorrientes hasta 47.4μA/sm, un orden de magnitud mayor que las películas depositadas a partir de suspensiones cuyo voltaje también ha sido más bajo. De las películas preparadas de soles, las de 5 capas tenían mejor respuesta que las de una sola capa.

Tabla I-2.IX. Propiedades fotoeléctricas de las películas obtenidas.

Característica	**Sol N°**	**Capas**	**V_{ca} (V)**	**J_{cc} (μA/cm^2)**
Películas, depositadas por *Doctor blade*	1	1	-0.37	2.9
		1	-0.32	1.7
	5	1	-0.40	3.29
Películas, depositadas por *Spin-coating*	1	1	-0.54	27.5
	3	1	-0.49	21.6
	5	1	-0.60	22.9
	1	5	-0.54	39.5
	3	5	-0.59	36.1
	4	5	-0.60	47.4

La iluminación por las dos caras ha proporcionado resultados muy similares, por lo que se puede concluir que la menor eficiencia en las capas depositadas de suspensiones no es debida al mayor grosor y la consecuente filtración de luz por las mismas.

Las películas con mejores propiedades eléctricas se han sometido a pruebas preliminares para comprobar su capacidad para aplicación directa en células fotovoltaicas, sumergiendo los electrodos en una disolución de colorante (Ruthenium 535 de Solaronix, 3.10-4M en etanol puro) durante 24h. Al cabo de este tiempo se han lavado con etanol.

No se ha observado un cambio visible de la coloración, por lo que se ha concluido que no pueden ser utilizados con éxito en células de colorante. Se ha decidido emplear otros métodos para la preparación de electrodos para células fotovoltaicas.

I-2.3.7) Pruebas de la actividad bactericida

Se han depositado películas sobre azulejos cerámicos blancos (mate y brillo) del sol Nº1 por *spin-coating*, siguiendo el mismo procedimiento descrito anteriormente.

La actividad bactericida se ha evaluado por el laboratorio de microbiología de Dr. Galiano. El estudia ha sido subvencionado por la empresa ESMALTES S.A.

El estudio se ha llevado al cabo con cepa *Escherichia coli* ATTC 35218 según Norme Francaise FT-72-190, utilizando como fuente de iluminación dos tubos fluorescentes Phillips TLD 36W.

Se ha concluido que las muestras obtenidas tienen una actividad bactericida muy superior que las muestras de referencia sin recubrimiento (Figura I-2.15.)

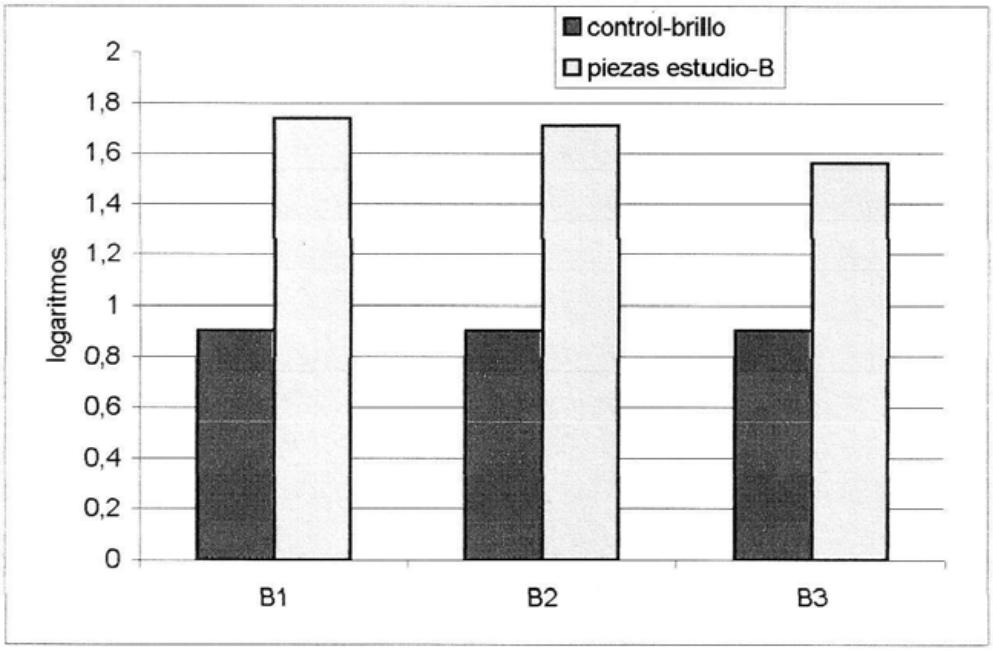

Figura I-2.15. Logaritmo del ratio entre bacterias colocadas y recuperadas en las piezas de estudio recubiertas con TiO_2 y las piezas de control, mostrando el alto poder bactericida de las primeras.

Los detalles del procedimiento y los resultados están especificados en el informe oficial que se recoge en el **Anexo 1**.

I-2.4) Conclusiones

- Se prepararon películas y polvos nanocristalinos de anatasa a través de las técnicas *Doctor-blade* y *Spin-coating*.

- El proceso de micronización vía húmeda y la temperatura de calcinación fueron importantes para obtener óptimos tamaños de los nanocristales.

- El uso de ácido p-toluensulfónico dio lugar a cristales con menor tamaño en comparación con las películas preparadas con ácido acético.

- La duración del tratamiento térmico no mostró una influencia significante sobre el tamaño cristalino medio.

- A pesar de los esfuerzos de disminuir los tamaños de los aglomeraciones de los nanocristales obtenidos, no se pudo reducir suficientemente para formar contactos eléctricos buenos y las capas depositadas a partir de suspensiones tuvieron una adhesión insuficiente al substrato y consecuentemente, una baja respuesta fotoeléctrica.

- Las películas obtenidas por spin-coating mostraron mejores propiedades fotoeléctricas.

- Las películas con mejores propiedades fotoeléctricas no mostraron una adsorción de colorante satisfactoria para su uso en células fotovoltaicas sensibilizadas.

- Las películas depositadas por spin-coating tuvieron una actividad bactericida muy elevada por lo que se pueden utilizar como recubrimientos en azulejos cerámicos auto-desinfectantes.

I-3) PREPARACIÓN DE CÉLULAS FOTOVOLTAICAS DE COLORANTE CON ELECTROLITO SÓLIDO A BASE DE POLIETILENGLICOL

Debido a la absorción insatisfactoria de colorante por las películas que hemos comentado anteriormente, para la elaboración de células fotoeléctricas de colorante con electrolito sólido se recurrió a la utilización de polvo nanocristalino comercial Degussa P-25.

I-3.1) Preparación

Se utilizó el mismo procedimiento y proporciones descritos arribe: 0.4g H_2O, 0,1g TiO_2, añadiendo 0.04g PEG 20000. Se obtuvieron células fotovoltaicas sustituyendo el electrolito líquido tradicional con un nuevo sólido a base de polímero estructural (PEG-20000). El procedimiento se muestra en la Figura I-3.1.

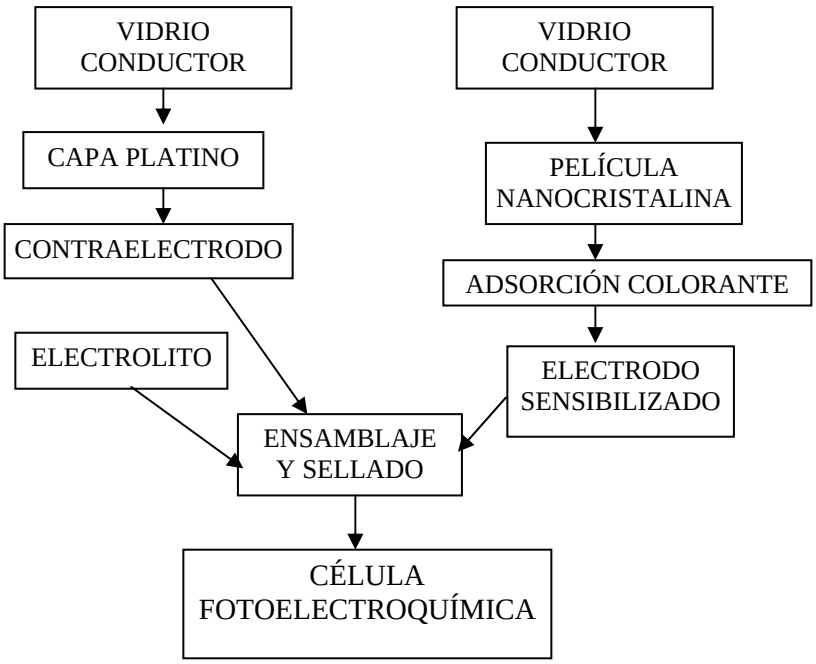

Figura I-3.1. Procedimiento empleado en la elaboración de células fotoelectroquímicas

Preparación de los electrodos

Los electrodos nanocristalinos, Figura I-3.2, se obtuvieron a través de la técnica "doctor-blade". Sobre substratos de vidrio conductor (Hardford, resistencia de hoja 8Ω/cuadrado) se depositó una suspensión acuosa de un 10% de TiO_2 (Degussa P-25), previamente molturado y dispersado con ultrasonidos, y polietilenglicol (PEG 20000). Las muestras se sinterizaron a 500°C durante 1 hora en aire. La sensibilización se consiguió sumergiendo los electrodos en una disolución de colorante (Ruthenium 535 de Solaronix, 3.10-4M en etanol puro) durante 24h. Al cabo de este tiempo se lavaron con etanol.

Preparación de los contraelectrodos

Los contraelectrodos (Figura I-3.2) se prepararon a partir de una disolución de ácido hexacloroplatinico (H_2PtCl_6) que se ha aplicado mediante "spin-coating" a 1500rpm sobre substratos de vidrio conductor, seguido por la calcinación a 500°C durante 1 hora.

Figura I-3.2. Par de contraelectrodo y electrodo sensibilizado.

Los componentes del electrolito se muestran en la Tabla I-3.I y fueron disueltos en 5 mL de acetona.

Tabla I-3.I. Composiciones de los electrolitos sólidos.

Referencia	Razón molar LiI:I_2	LiI (g)	I_2(g)	PEG(g)	CÉLULA:
E40	10:1	0,4	0,076	1,21	G15
E41	20:1	0,4	0,038	1,21	G16
E42	5:1	0,4	0,152	1,21	G17
E50	10:1	0,6	0,114	1,21	G18
E51	20:1	0,6	0,057	1,21	G19
E52	5:1	0,6	0,228	1,21	G20

Ensamblaje de las células

Las células completas (figura I-3.3) se ensamblaron de dos maneras, cuya diferencia básica era el proceso de secado del electrolito. En ambos casos los electrodos de TiO_2 sensibilizado previamente se impregnó con electrolito diluido (1ml en 4ml de acetona) para asegurar una buena penetración en los poros. Después de secarse, una gota de la disolución concentrada del electrolito se depositó con pipeta. El primer método (A) implicó la evaporación completa del disolvente antes del montaje de la célula (a 60°C durante 30 minutos), mientras que en el segundo (B), el disolvente fue evaporado después del montaje de la célula (a 45°C durante 24h). El grosor de la capa del electrolito que resultó después de colocar el contraelectrodo, en el caso (A) se estima a 0.04mm por la cantidad del polímetro depositado entre los electrodos, mientras que en el caso (B) es del orden del grosor de la capa mesoporosa. Todas las células solares de colorante tenían áreas activas de aproximadamente 1cm^2.

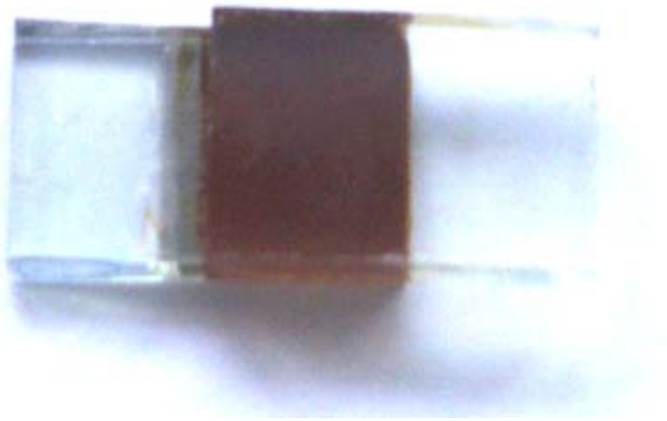

Figura I-3.3. Una célula completa.

Las medidas eléctricas se realizaron con un potenciostato PGSTAT20 de Autolab, equipado con módulo del análisis de la impedancia. La fuente de luz era una lámpara comercial de halógeno de 50W.

I-3.2) Resultados y discusión

Estructura

El grosor del film (aproximadamente 5,5µm) se determinó mediante microscopia electrónica de barrido de su sección transversal (Figura I-3.4 a y b). No se observó una diferencia aparente del material original Degussa antes y después de la calcinación 450ºC. Las medidas de difracción de rayos X tampoco evidenciaron cambios en el tamaño de las partículas y de la fase cristalina de Degussa P-25, durante del proceso de calcinación.

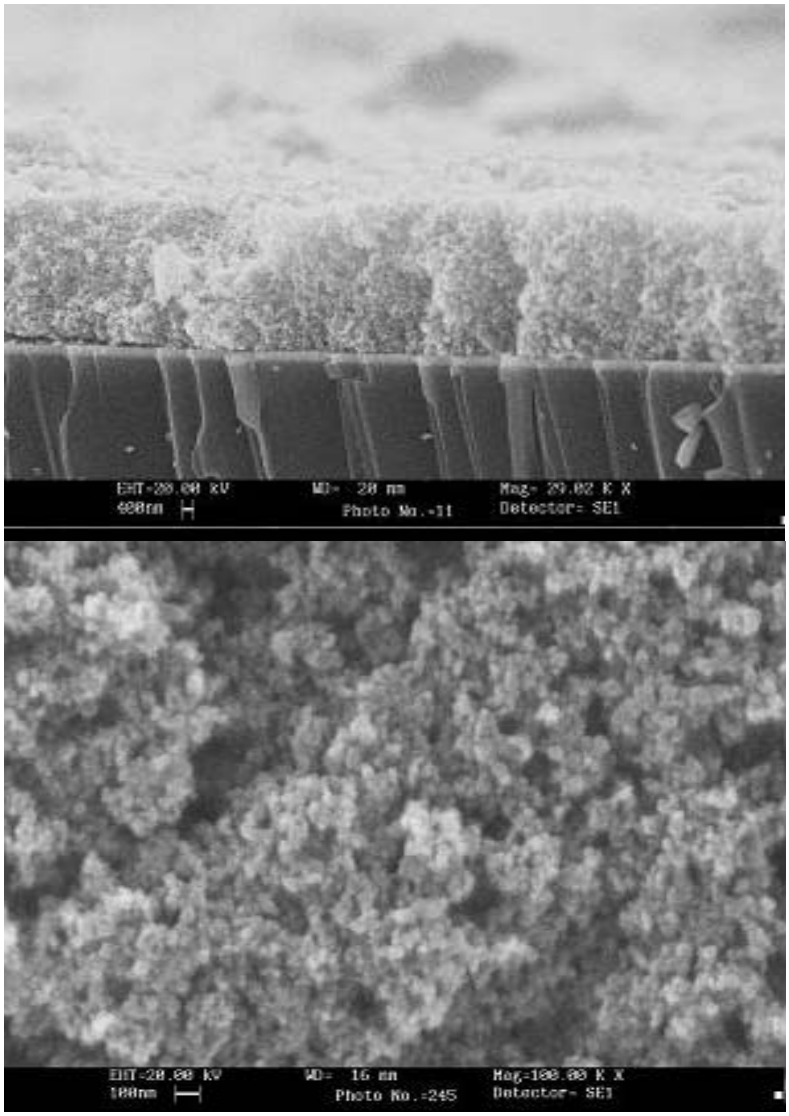

Figura I-3.4. Micrografía SEM de una película nanocristalina preparada a partir de Degussa P-25 (a). y nanoestructura de la película(b).

Voltametría

Los parámetros de las células fotovoltaicas se han determinado a través las curvas corriente-voltaje. Información más detallada sobre estos parámetros se encuentra en la introducción de la **Parte II**.

Todas las muestras mostraron respuesta fotoeléctrica (Tabla I-3.II).
Con el método de ensamblaje B (Figura I-3.5) se obtienen células con mejor calidad. El aumento de la relación LiI:I_2 de 10:1 a 10:2 resulta en una disminución del fotovoltaje y de la fotocorriente por efectos de recombinación, los cuales ocurren dentro de la capa nanocristalina, a pesar de que los electrolitos con relación 10:2 tienen más alta conductividad (Este efecto lo comentaremos en los resultados de impedancia). Por eso en las células preparadas a través del método A (con peor calidad, capa más gruesa de electrolito, y su peor penetración en la película nanocristalina) la eficiencia aumenta con el contenido de I_2 aunque es mucho más baja que en las células B.

Tabla I-3.II: Eficiencia de algunas células, preparadas a través de los métodos de secado A y B.

Dye Cell	Voc (V)	Jsc (mA cm-2)	Fill Factor (%)	ηmax (%)
B10	**0,60**	**0,46**	**58**	**1,61**
B30	**0,53**	**0,38**	**72**	**1,45**
G15	0,52	0,27	48	0,68
G16	0,47	0,15	58	0,41
G17	0,49	0,38	44	0,82
G18	0,50	0,15	80	0,53
G19	0,51	0,08	85	0,34
G20	0,49	0,19	66	0,61

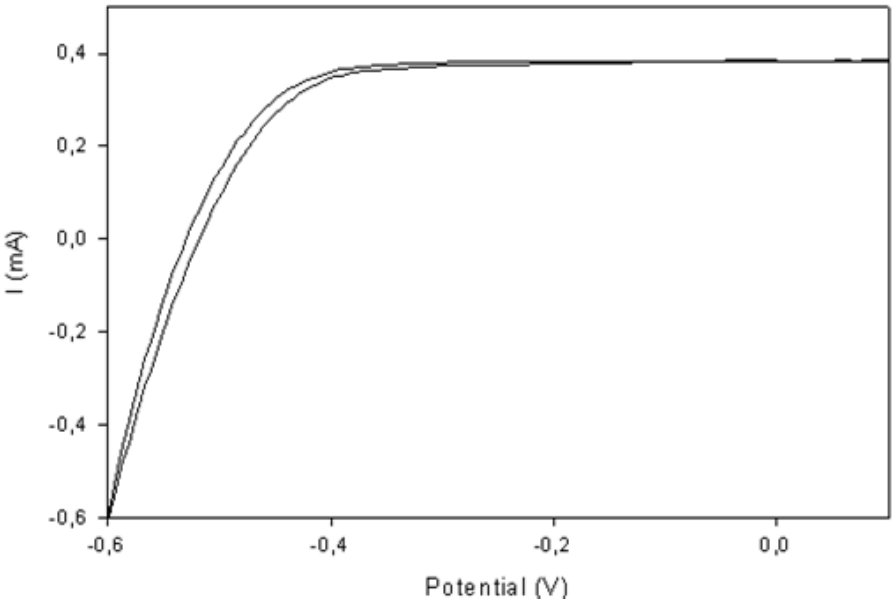

Figura I-3.5. Voltametría de célula B30, hecha a través del método B.

I-3.3) Conclusiones

- Poletilenglicol se utilizó como polímero estructural en electrolitos sólidos en células fotovoltaicas de TiO_2 nanoporoso, consiguiendo respuesta fotovoltaica. utilizado en este trabajo es un posible polímero estructural en electrolitos sólidos para células fotoeléctricas de TiO2 nanoporoso.

- Los diferentes métodos de montaje tuvieron gran importancia para obtener un buen contacto triple entre el TiO2, colorante y el electrolito sólido.

- El coeficiente de difusión no influyó significativamente en la eficiencia de las células, cuyo valor máximo ha sido el 1.6%.

- No obstante ello, estas células fueron insuficientemente estables con el tiempo, llegando a una degradación completa de sus propiedades a lo largo de varios meses.

- Consecuentemente, en la tercera parte se decidió reemplazar el electrolito redox por un transportador de huecos orgánico.

I-4) PREPARACIÓN DE CÉLULA FOTOVOLTAICA NANOCRISTALINA SÓLIDA CON POLÍMERO TRANSPORTADOR DE HUECOS SINTETIZADO POR FOTOELECTRODEPOSICIÓN

Debido a la baja estabilidad de las células fotoelectroquímicas sólidas con PEG preparadas en la sección anterior, en la ésta sección de nuestra investigación, sustituimos el electrolito redox por el polímero poly(3,4-ethylenedioxythiophene) (PEDOT), conocido como un transportado de huecos estable[52,53].

I-4.1) Preparación

Deposición de capa densa bloqueadora de TiO_2 a través de spray-pirolisis.

Para evitar el contacto entre el polímetro conductor y la superficie del FTO, que resultaría en corto cirquito, los substratos de FTO se recubrieron con una capa densa de TiO_2.
Los substratos de FTO se lavaron con etanol utilizando ultrasonidos y calentado hasta 400°C sobre una plancha de cobre montada sobre una placa calentadora de alta temperatura. La disolución precursora se preparó disolviendo 10% de i-propóxido de titanio y 10% de acetilacetona en i-propanol. Dicha disolución se pulverizó sobre los substratos calientes en 8 pulsos de 1s utilizando un aerógrafo manual y N_2 con presión de 1atm como gas propulsor.

Síntesis de las nanopartículas y preparación del electrodo nanocristalino

1.2 mol de isopropóxido de titanio, disuelto con 1.2 mol isopropanol se añadió gota a gota a 170mL ácido acético de 25%, agitando enérgicamente. El precipitado, formado inicialmente, se redispersó, después de calentar la mezcla en un baño de aceite a 80°C. La disolución viscosa se mantuvo agitada a esta temperatura durante 3-4h, hasta que el volumen se ha reducido a 120ml. El sol blanco se transferió a una bomba de presión con recipiente de teflón y se colocó en una autoclave a 230°C durante 12h. El precipitado obtenido se re-dispersó utilizando ultrasonidos y concentró en rotavapor hasta una concentración de aproximadamente 10-15% de TiO_2. La pasta obtenida se depositó mediante la técnica *doctor-blade* sobre la capa densa de TiO_2 y calcinó a 450°C durante 30min (velocidad de calentamiento 10°C/min).

La sensibilización se efectuó sumergiendo los electrodos en una disolución de colorante (Ruthenium 535 de Solaronix, 3.10^{-4}M en etanol puro) durante 24h. Al cabo de este tiempo se lavaron con etanol.

Fotoelectropolimerización de PEDOT (Poly(3,4-ethylenedioxythiophene) sobre el electrodo mesoporoso sensibilizado

Se ha decidido sintetizar el PEDOT a través de fotoelectropolimerización utilizando el efecto de excitación del colorante. La iluminación del electrodo sensibilizado permitiría iniciar la polimerización desde la superficie de las nanopartículas lo que permitiría una orientación óptima de las cadenas del transportador de huecos (Figura I-4.1). Al mismo tiempo la fotoactivación permitiría llevar al cabo la reacción a potenciales más bajos que los que puedan descomponer el colorante [52].

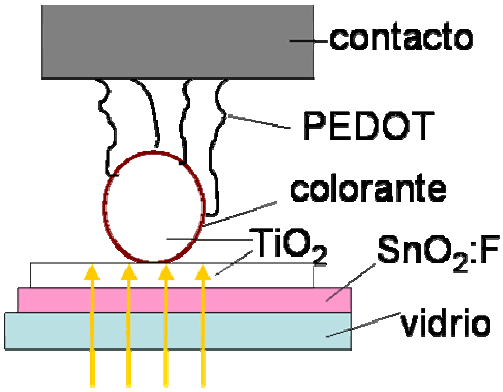

Figura I-4.1. Esquema de un dispositivo utilizando PEDOT.

Se preparó una disolución 0.05 M de bis-EDOT, (*bis-*(*3,4-ethylenedioxythiophene)*) y 0.1M $LiClO_4$ en carbonato de propileno y se colocó en una célula de tres electrodos. La disolución se desgasificó burbujeando N_2 durante 15 min y se mantuvo en atmósfera de N_2 durante todo el proceso. Se utilizó lámina de platino como contraelectrodo y Ag/AgCl/KCl, conectado mediante un puente como referencia.

La electrodeposición fue fotoasistida por iluminación con lámpara de Xe, filtrando la luz de λ<520nm para evitar la activación del TiO_2 y la descomposición fotocatalítica de los demás componentes (Figura I-4.2). Se aplicó potencial constante de 0.4V durante 30 minutos.

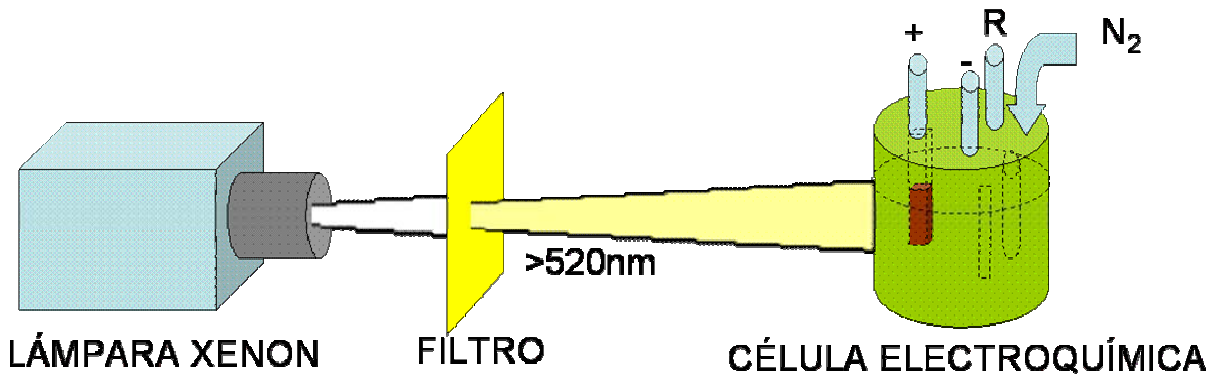

Figura I-4.2. Esquema del experimento.

Después de completar la fotoelectrodeposición, el electrodo se ha lavado con acetonitrilo y se depositó una capa de oro a través de sputtering y pintó con laca de plata para completar la célula fotovoltaica.

En algunos casos se ha utilizó impregnación con líquido iónico - una solución de 0.2M Lithium *bis*-(trifluoromethanesulfone) imide y 0.2M 4-*tert*butylpiridine 1-ethyl-3-methylimidazolium (*bis*-(trifluoromethanesulfone)imide para mejorar los parámetros de la célula antes de formar el contacto base.

El comportamiento fotoeléctrico de las células se estudió empleando con potenciostato *Autolab.* Como fuente de luz se utilizó una lámpara de Xenón de 150 W con la luz ultravioleta filtrada por debajo de 520nm.

I-4.2) Resultados y discusión

Figura I-4.3 muestra el cambio de la corriente eléctrica con el tiempo durante la fotoelectropolimerización, aplicando el potencial constante de 0.4 V. Con el inicio de la iluminación se observa una subida inmediata de la corriente que después, a lo largo de 5 min disminuye hasta un valor bajo. Esta evolución se puede explicar con la poca transparencia de nuestro polímetro, observada visualmente.

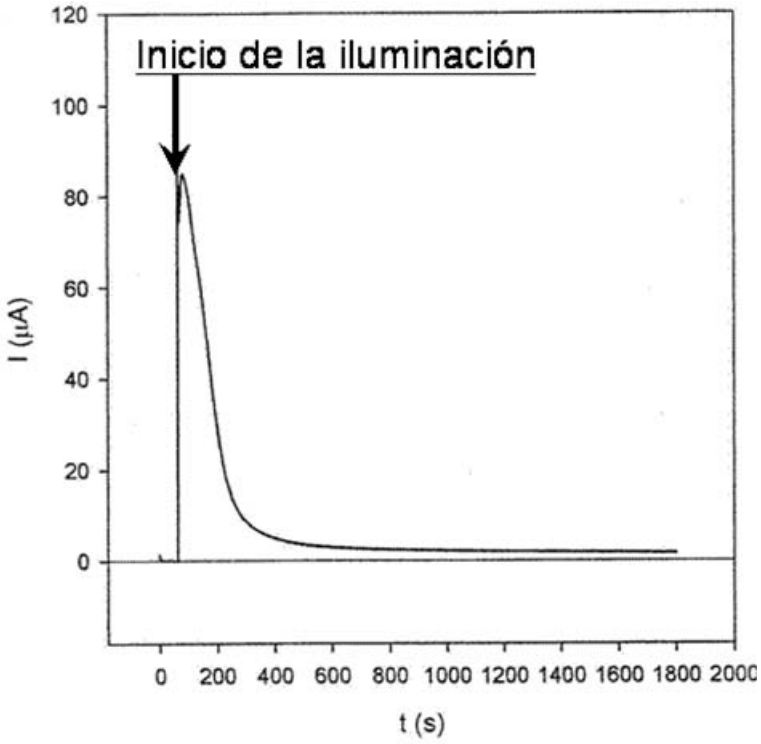

Figura I-4.3. Fotoelectropolimerización de bis-EDOT sobre el electrodo sensibilizado.

Durante la reacción, el electrodo rápido adquirió una coloración negra, debida al polímetro que se está depositando en los mesoporos. La resultante elevada absorción de luz reduce a continuación la reacción fotoasistida, cuya velocidad esta muy baja y casi constante al final del proceso.

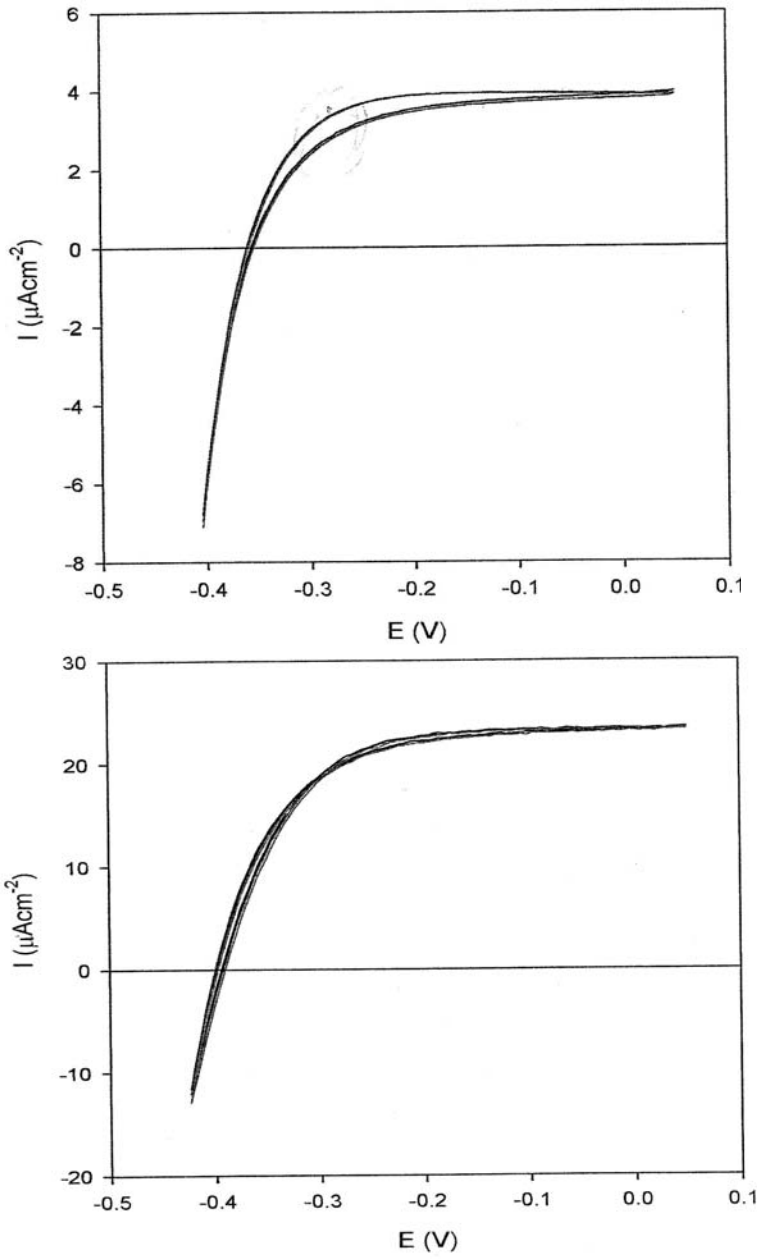

Figura I-4.4. Voltamogramas de células, iluminadas con 100 y 500W/m^2.

Figura I-4.4 a y b muestra dos voltamogramas de una célula hechas con iluminación de 100 y 500(W/m^2). A diferencia de las células de electrolito líquido, cuya eficiencia es más baja cuando la densidad luminosa es elevada, en nuestro caso tenemos rendimiento comparable, incluso en algunos casos mayor eficiencia con altas intensidades de la luz (Tabla I-4.I). Comportamiento parecido se observó con células de tipo III-V, utilizados en sistemas concentradores, cuyos rendimientos aumentan con mayor concentración debido a elevada fotoconducción del material.

Tabla I-4.I. Parámetros y características de algunas células

Grosor del TiO_2	**Polímero**	**Contra-electrodo**	**ilumin. (W/m^2)**	**Voc (mV)**	**Isc ($\mu A/cm^2$)**	**η(%)**	**FF (%)**
2	PEDOT	Au-Ag-cable Cu	100	360	3.9	0.0086	0.62
			500	392	23.3	0.011	0.61
4	PEDOT	Au-Ag-Cu	500	187	7	0.0007	0.28
2	PEDOT+ Liq. Iónico	Hilo de carbono	1000	240	75.97	0.0063	0.34
			500	221	42.34	0.0066	0.36
2	PEDOT+ Liq. Iónico	FTO	1000	260	70.32	0.0068	0.37
			500	236	39.22	0.0071	0.38

De acuerdo con informes previos [52], intentamos mejorar la corriente de la célula empleando líquidos iónicos. En nuestro caso el efecto sobre la eficiencia no fue positivo. A pesar de que se aumentó la fotocorriente, el voltaje y el fill factor disminuyeron.

Debido a la elevada recombinación, el aumento del grosor de 2 a 4 µm disminuye aproximadamente dos veces el fotovoltaje y el *fill-factor* y 3-4 veces la fotocorriente, resultando muy baja su eficiencia.

I-4.3) Conclusiones

- Se llevó a cabo la fotoelectropolimerización de PEDOT sobre electrodos mesoporosos sensibilizados de TiO_2 que ha sido limitada por la alta absorción del polímero.

- Las células fotovoltaicas obtenidas mostraron baja eficiencia fotoeléctrica posiblemente por la misma razón.

- La utilización de líquido iónico para activar la respuesta fotoeléctrica no produjo mayor eficiencia.

1.5) CONCLUSIONES DE LA PARTE I

- Se depositaron películas de dióxido de titanio nanocristalino por el método sol-gel e impresión de nanopartículas.

- Las películas nanocristalinas de TiO_2 obtenidas por el método sol-gel tuvieron una morfología densa que no permitió una buena adsorción del colorante. No obstante, las mismas mostraron excelentes propiedades bactericidas y pueden ser utilizadas en azulejos auto-desinfectantes.

- Para células fotovoltaicas se ha sintetizado TiO_2 por la vía hidrotermal.

- Las células preparadas con polímero estructural PEG han tenido respuesta fotoeléctrica inicial prometedora, pero no han sido estables con el tiempo.

- Las células preparadas con transportador de huecos orgánico (PEDOT) dieron respuestas de corrientes muy bajas, posiblemente por la baja transparencia del polímetro. El rendimiento no se pudo incrementar con el uso de un líquido iónico.

- El factor limitante en ambos casos no fue el dióxido de titanio, sino el electrolito.

Considerando el objetivo principal de la tesis, i.e. investigar la deposición de películas con aplicaciones fotovoltaicas, se ha tomado la decisión de estudiar otro tipo de célula, que haya mayor estabilidad y que no necesite electrolito líquido.

La Parte II describe nuestro trabajo en el campo de las calcopiritas.

PART II.

LOW-COST APPROACHES TO THIN-FILM CHALCOGENIDE PHOTOVOLTAIC MATERIALS

OBJECTIVES OF PART II

The principle goal of our work was to obtain films for photovoltaic devices by low-cost methods, suitable for large-scale photovoltaic production. Based on this aim, throughout the **Part II** of the study, the following specific objectives were defined:

1) Development of a sol-gel route for the deposition of oxide precursors of the Cu-In and Cu-In-Ga systems and their conversion by subsequent chalcogenation to the following chalcopyrites: $CuInS_2$, $CuIn,GaS_2$ $Cu(In,Ga)Se_2$ and $Cu(In,Ga)(S,Se)_2$.

2) Development of a nanoparticle printing routes for $CuInS_2$ and indium-free absorbers of the type Cu_2ZnSnS_4.

3) Development of an electro deposition process for Cd-free buffer layers.

4) Development of an alternative nanoparticle printing route for $Cu(In,Ga)Se_2$.

II-1) INTRODUCTION TO PART II

II-1.1) Development of chalcopyrite photovoltaics

This photovoltaic system has been considered one of the most promising solar cell technologies for cost-effective power generation [1]. There are many reasons for this. On one hand this technology has demonstrated high and stable efficiency- about 20% [2], close to that of crystalline silicone. On the other, the inherent advantages of thin-film processing, in contrast to bulk crystalline materials, permits quick upscale of the deposition process to high-throughput, large area deposition. Another big advantage of thin-film technologies is the possibility to replace the individual cell processing and soldering procedure of silicone wafers with simple scribing. This can provide straightforward monolithic interconnection of individual cells and results in high module output voltage and reduced series resistance losses. Several companies have already started pilot production of large-area modules, yielding efficiency above 12%. The record of 13.4% full-scale module belongs to Showa Shell [3].

The history of this technology starts with the synthesis of $CuInSe_2$ by Hahn in 1953 [4]. The first photovoltaic device was fabricated from a single crystal with 12% efficiency in 1974 [5]. Boeing Corporation developed the first efficient (10%) thin-film devices in the early 80-s by use of a process based on three-source coevaporation [6]. With some modifications (multistage instead of two-stage regime) it is still the record-performance process used today both for cells and modules. In 1987 Arco Solar increased this efficiency to 14% [7]. The same company under the name Siemens Solar (later Shell Solar) produced the first commercial chalcopyrite photovoltaic module in1998 [8]. Today numerous companies, employing various processes, materials and substrates are involved in intense development work to scale up their pilot facilities to large-scale production. Some of them use vacuum-based techniques such as sputtering or coevaporation: Wurth Solar, Avancis, Showa Shell, Miosole, HelioVolt, Global Solar, Sulfurcell, etc. At the same time there are already companies which introduce at the industrial level novel low-cost vacuum-free approaches. Institut de Recherche et Développement sur l'Énergie Photovoltaïque (IRDEP) and Solopower use electro deposition. International Solar Electric Technology (ISET) and Nanosolar employ nanoparticle suspension printing.

Quick growth of production volumes is envisioned in the near future as many of the processes have reached maturity and large production facilities are under construction. Three main issues still have to be addressed by researchers:

- Lower processing costs and higher efficiency by vacuum-free deposition routes.
- Replacement of toxic elements such as selenium and cadmium employed by current technology.
- Replacement of rare elements such as indium and gallium with more abundant alternatives.

If these issues are properly addressed, the chalcopyrite photovoltaic technology has unlimited potential to supply our civilization with cheap and abundant renewable energy.

Within this thesis work we have investigated different strategies to respond to these challenges.

II-1.2) Device structure and operation

While there is a large variety of processes and materials used for the fabrication of chalcopyrite devices, the main features of these solar cells are similar (Figure II-1.1).

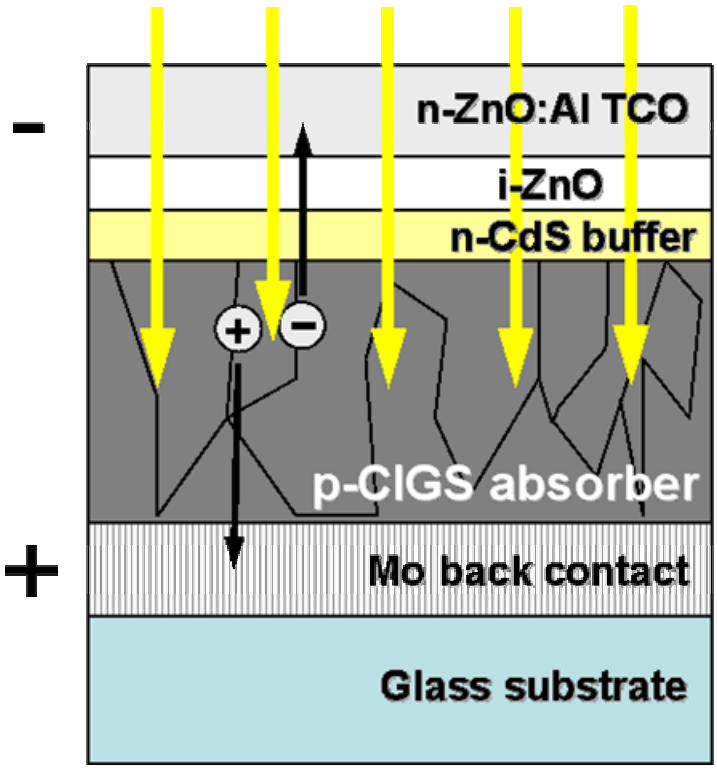

Figure II-1.1. Structure of a record-performance chalcopyrite device.

This structure includes 5 principal elements which in record performing devices are:

- **Substrate** – soda lime glass, providing adequate surface for the deposition of all active layers
- **Back contact** - sputtered molybdenum layer
- **Absorber** – p-type chalcopyrite Cu(In,Ga)Se_2
- **Buffer** – n-type CdS
- **Transparent conductive oxide** – Al-doped ZnO (often preceded by a thinner isolating ZnO).

In contrast to the CdTe solar cells, which are built in superstrate configuration (i.e. by depositing all layers on transparent material that is intended to face the illuminated side), the general process for chalcopyrite devices employs the substrate version. Several research efforts have demonstrated the feasibility of superstrate version of Cu(In,Ga)Se_2 cells but the efficiency was substantially lower than substrate devices [9]. Although superstrate-type solar cells can potentially be used as the top cell of tandem (multi-junction) devices and thereby lowering manufacturing costs, the efficiencies of these cells still remain in the 10–12% range [10].

The main advantage of the substrate junction is the possibility to grow the absorber at higher temperature without damaging the p-n junction. Its subsequent formation is easily achieved by a variety of routes at low temperature. Subjecting the junction to temperatures above 200ºC can have negative impact on performance.

A brief review of the principal cell elements is given below.

II-1.3.1) Substrate

The best-studied substrate is soda lime glass. It was originally used because of its low cost, chemical inertness and thermal stability. Soon it was found out that very small amounts of sodium diffusing from the glass into the absorber have beneficial effect on its electronic properties. Advanced processes use sodium diffusion barrier and later deposit controlled amount of sodium compound in order to achieve better control on Na-incorporation [11].

Flexible substrates are of particular interest from industrial point of view because of the possibility of using roll-to-roll processing. Different materials such as metal and

polymeric foils have been used. There are several requirements to the substrate which make it difficult to find an optimal flexible substrate [12]:

• Vacuum compatibility. The substrate should not degas during the various vacuum deposition steps, especially during CIGS deposition, when the substrate must be heated. This requirement is not valid for low-cost, vacuum-free deposition methods.

• Thermal stability. Generally, efficient devices are grown at temperatures exceeding 400ºC, while record performance CIGS is deposited at temperatures about 550ºC. Polymeric foils are not suitable for temperatures above 450ºC.

• Suitable coefficient of thermal expansion (CTE). It should match the one of the absorber (7-11 ppm/K) as closely as possible, otherwise poor adhesion or molybdenum cracking may be observed. While titanium and steel foils have similar CTE (8.6 and 11ppm/K respectively), the values for aluminum (23ppm/K) and many polymers are very high and result in absorber delamination.

• Chemical inertness. The substrate should not be damaged while exposed to the different aggressive processing environments, in particular to Se environment at high temperature during the absorber formation and in the chemical bath used for buffer deposition. In addition, it should not release impurities that may deteriorate the electronic properties of the cell, except when this is explicitly desired (such as in the case of Na diffusing from the soda lime glass). In some cases a diffusion barrier can be deposited in order to meet this requirement.

• Sufficient humidity barrier. Because long-term atmospheric exposure (especially at high temperature and humidity) may damage the modules, the substrate must provide reliable atmospheric protection.

• Surface smoothness. Substrate roughness, especially at micrometric scale may result in shunting the front and back contact. At the same time, isolation scribing required for module interconnection cannot be performed successfully on rough substrates.

• Cost, energy consumption, availability, weight. These general requirements apply to all module elements, especially if large-scale deployment is envisioned.

II-1.3.2) Back contact

The most widely used back contact for chalcopyrite devices is sputtered molybdenum layer. It has several advantages such as:

- Low reactivity with chalcogens during absorber deposition
- Coefficient of thermal expansion close to the absorber
- High hardness, permitting mechanical scribing of the subsequent layers for module interconnection without damaging the contact.

Often a thin layer of $MoSe_2$ forms during the high temperature treatments of the buffer. This phenomenon is normally not detrimental for cell performance.

In some cases, when a metallic foil is used, it is possible to omit the back contact deposition and cut single cells which are then interconnected in series similarly to silicon solar cells. Nevertheless, impurities that could diffuse from the foil may require a deposition of an additional diffusion barrier. Such interconnections are used by some companies employing low-cost processing such as ISET and Nanosolar. However, one of the biggest advantages of thin-film modules is the easy monolithic series interconnection on a single large substrate. This is why ongoing research efforts on flexible substrates are focused on non-conductive (polymeric and inorganic) materials or reliable isolation of metallic foils. Subsequent deposition of molybdenum film provides the classical configuration back contact.

Another type of back contact, especially interesting for the fabrication of semi-transparent or stacked junction devices is the transparent back contact. Employing transparent conductive oxides, SnO:F and ITO (indium-tin oxide), device efficiencies of 13.7 and 15.2% were reached [13].

II-1.3.3) Absorber layer

This is the most important layer of the chalcopyrite device and has been a subject to a vast array of research activities, resulting in numerous modifications and improvements. As already mentioned, record performance has been achieved with $Cu(In,Ga)Se_2$, although many other materials are being investigated.

In all cases the absorber formation is based on delivery of the constituting elements by a vacuum or atmospheric pressure technique, accompanied or followed by high-temperature treatment resulting in crystalline material.

Low-cost atmospheric pressure approaches for absorber formation are one of the major objectives of this thesis.

Another challenge for CIGS technology related to large-scale production is the substitution of the scarce and toxic elements such as In, Ga and Se with environmentally friendly and abundant alternatives. An example of a promising material is Cu_2ZnSnS_4 which was successfully deposited by a low-cost method in this work.

These issues are discussed in detail in the following sections.

II-1.3.4) Buffer layer

Serving also as the n-partner in the p-n hetero junction, this layer is crucial for cell performance. It is very thin (10-60nm) and has to provide complete coverage of the absorber.

While there are numerous and sometimes controversial reports on how the buffer contributes to device efficiency enhancement [14, 15], there is a general agreement that it chemically modifies the absorber surface and, in addition, provides protection of the absorber surface during ZnO sputtering.

Record performing devices employ CdS buffer layers deposited by chemical bath deposition. Both the material itself and its formation route are undesirable for industrial production. Apart from being a relatively slow, precisely controlled batch process, CBD has the following inherent disadvantages: a need for fresh solution for each cycle, poor material utilization and necessity to manage large amounts of residual liquids.

Intense research efforts by many teams have yielded fundamental understanding and successful alternatives of CdS, in most cases by use of zinc or indium sulfide based materials [16-27]. Good results in large-scale experiments have been achieved with methods alternative to CBD, such as atomic layer deposition (ALD), metal organic chemical vapor deposition (MOCVD), ion layer gas reaction (ILGAR), sputtering and thermal evaporation [19]. However, most of these methods still need to be approved in industry.

Within this thesis we have developed an electro deposition process for In_2S_3 buffer deposition [28]. All materials and deposition conditions were selected taking into account environmental, economic and technological aspects of a potential transfer to

large volume industrial production. Different bath compositions and electro deposition parameters were studied. The obtained films exhibited complete substrate coverage, confirmed by SEM and XPS. In/S ratio close to 2/3 was obtained. XPS measurements detected the presence of indium hydroxide, transforming into oxide upon anneal at 200ºC. Maximum photoelectric conversion efficiency of 7.1% was obtained, limited mainly by a low fill factor (51%). Further process optimization is expected to lead to efficiencies comparable to CdS buffers. So far, open-circuit voltages as high as 660mV were demonstrated. For further information, please see **Chapter II-7.**

II-1.3.5) Transparent conductive front contact

This principal layer of the solar cell structure is both important and challenging due to the trade-off between electrical and optical requirements. From electrical point of view it has to be sufficiently conductive in order to reduce efficiency losses and provide ohmic contact to the buffer layer, in order to collect the charge of the whole device. From optical point of view it must be highly transparent to allow maximum illumination of the active layers.

Finding materials which are able to comply with both requirements is not an easy task. For instance, metals are highly conductive but are not transparent while most transparent and easily processed materials such as plastics and glass are isolating. Only certain metal oxides, known as Transparent Conducting Oxides (TCO-s) and some polymers such as polyanilines, polypyrroles, polythiophenes, polyphenylenes, poly(p-phenylene vinylene)s and especially PEDOT, Poly(3,4-ethylenedioxythiophene [29]. In addition to the limited choice of materials, their properties are subject to very precise control of oxygen content and doping levels in order to obtain the desired high transparency and conductivity.

TCO-s are preferred for solar cell application because of their long-term stability under illumination, including low-wavelength radiation that can damage most polymers. The group includes some oxides of groups III(Sn, Al, Ga, In) and VIII (Cd, Zn, Cu). These materials are in fact semiconductors with very high energy gap (usually above 3eV) which guarantee high optical transmission in the region of cell operation. Generally, the resistivity values of these compounds is very high so they have to be doped in order to move the Fermi level towards the conduction band an increase the concentration of electrons [30].

For solar cell applications, the properties of the TCO usually have to meet the following requirements:

- Low sheet resistance (less than 10Ω/□) in order to minimize the final series resistance of the device.
- High transmittance (more than 90% in the 400-900nm spectral range which would allow high photon flux towards the window material and the absorber.
- Good adherence to the preceding layers.

Chalcopyrite cells in most cases use aluminum-doped ZnO although in some indium-doped tin oxide (ITO) or Sn_2O:F are used. These materials are n-type due to oxygen vacancies and this guarantees electrical matching with the n-type buffer layer.

Typical deposition technique is sputtering from ceramic targets. Precise control of oxygen content is necessary in order to achieve optimal conductivity and transparency. Other deposition techniques which still are being investigated are laser ablation, spraying, and solution growth and sol-gel. A big limitation to low-cost techniques such as sol-gel is that they usually require high temperature in order to obtain good conductivity [31]. At the same time, the low thermal stability of the p-n junction in chalcopyrite devices makes it impossible to deposit the TCO-s at temperatures much above 200ºC.

II-1.4) Monolithic series interconnection and module fabrication

As already mentioned, one advantage of thin film devices is the possibility to achieve series interconnection by simple scribing procedures without the necessity to solder individual cells.

As shown on Figure II-1.2, the first patterning step is carried out on the molybdenum back contact. Since molybdenum is a hard metal, laser scribing is preferred.

Patterning 2 is done mechanically after deposition of the elements of the p-n junction (absorber and buffer). This scribe is done above the molybdenum and aims opening of contact surface for the subsequent deposition of the conductive ZnO:Al layer.

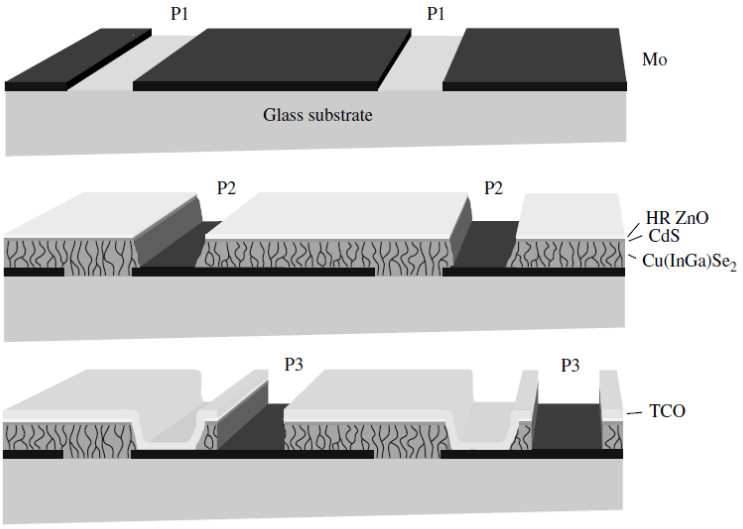

Figure II-1.2. Scheme of the patterning steps necessary for monolithic module series interconnection [1].

Patterning 3 is again mechanical and forms individual cells. The zones above all scribes are sacrificial, i.e. they do not contribute to the current generation. This is why the area of the scribes should be minimized in order to increase device performance.

The overall production process depends mostly on the absorber formation technique, while the rest of the processing steps of many of the pilot production lines are similar.

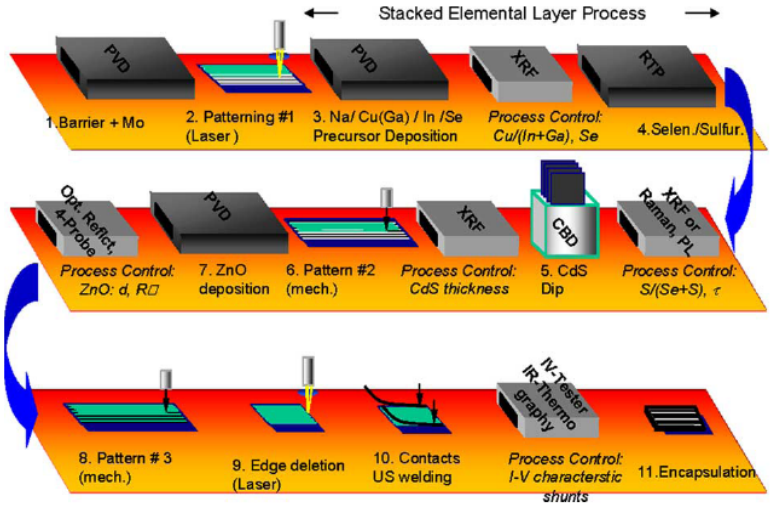

Figure II-1.3. Manufacturing steps in a module production plant employing the Siemens sequential process [32].

Figure II-1.3 shows a scheme of such a production line, employing a sequential process by which the precursors for chalcopyrite formation are first deposited and then subjected to high-temperature selenization. The rest of the steps form device elements described above. Because process failure at any step may result in defected module, quality control at each level is of vital importance.

After forming the interconnected module, contact grids are placed by ultrasonic welding and the structure is encapsulated, usually by EVA (ethylene vinyl acetate) and cover glass. Glass is the preferred surface protection cover because of its excellent atmospheric stability, humidity barrier and light transmission. If low-weight applications are desired, polymeric foils or resins can be used. Long term exposure UV-containing light requires highly resistant polymers, such as TEFLON-based or special blends with UV-protection component.

II-1.5) Basic concepts and device operation

Before giving a brief review of some physics concepts we have to point out that all significant advances in the efficiency of chalcopyrite photovoltaic cells have been achieved on an empirical basis and in spite of poor understanding of the electronic mechanisms and electronic defects that control device behavior [1]. Complex models using elaborate physics apparatus have been developed in order to explain some of the phenomena observed, yet these are sometimes contradictory and not within the scope of the present work.

The *charge carriers* in a semiconductor can be divided in two functionally different groups: majority and minority carriers. In an n-type material the majority i.e. predominant carriers are the *electrons* while the *holes* are the majority carriers on a p-type semiconductor. On the other hand, the minority carriers in p-type material are electrons and in n-type materials - holes. Minority carriers are the ones that determine device performance.

The heart of the device operation is the *p-n junction*, (Figure II-1.4) produced by contacting a p-type and n-type semiconductor. Driven by affinity to equilibrate the total charge of the device, electrons from the n-type material diffuse across the junction into the p-type side and, vice versa, holes diffuse into the n-type material. Electrons and holes within this region recombine, leaving it devoid of any free or mobile charges

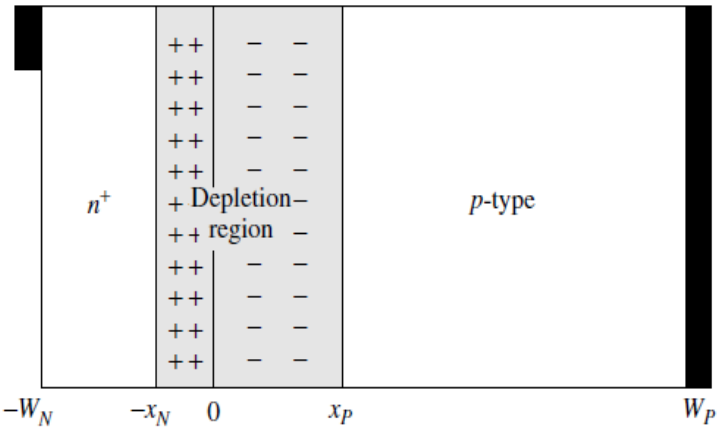

Figure II-1.4. A simple scheme of the p-n junction: free carriers have diffused across the junction (x = 0) leaving a space-charge or depletion region practically devoid of any free or mobile charges [8].

This leads to the accumulation of negative charge on the p-side (ionized acceptors) and a positive charge at the n-side (ionized donors). The region where these effects occur is called *space charge* or *depletion* region and leads to the formation of a strong electric field which counteracts the carrier diffusion across the p-n junction leading the system to an equilibrium state.

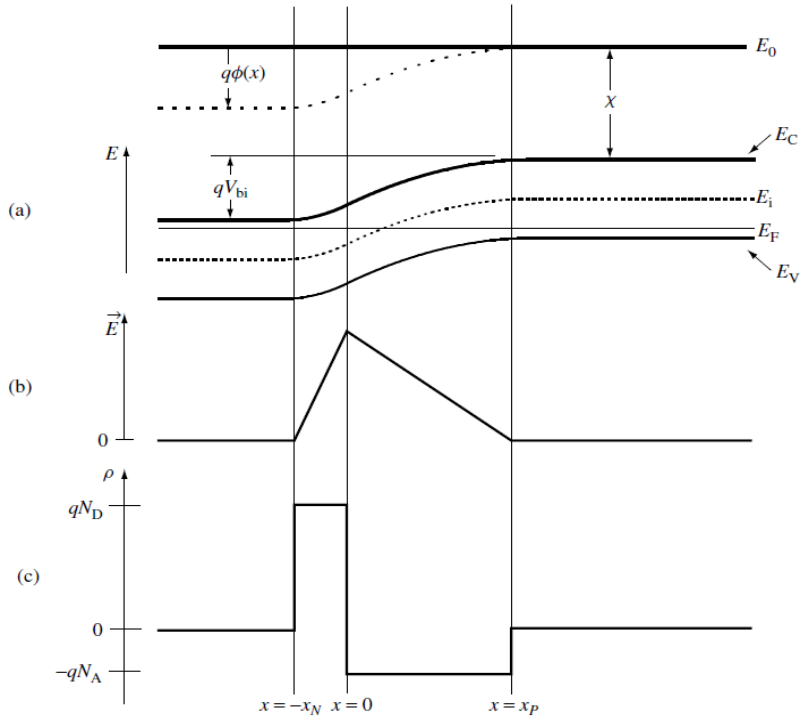

Figure II-1.5. Equilibrium conditions in a homo-junction solar cell: energy bands (a); electric field (b); and charge density(c).

As a consequence to the local exchange of charges, the Fermi energies *(E_f)* of the materials equilibrate. Because the valence and conductions bands (*Ev* and *Ec* respectively) have to be parallel in their flat zones to the vacuum level (*Eo)*, a band bending is observed in the space-charge region (Figure II-1.5).

In order to obtain photo generated current, it is important to achieve charge separation before the electrons and holes recombine. The electric field generated by the junction region is the driving force for this separation when the electron-hole pairs are generated within the space-charge region (Figure II-1.6).

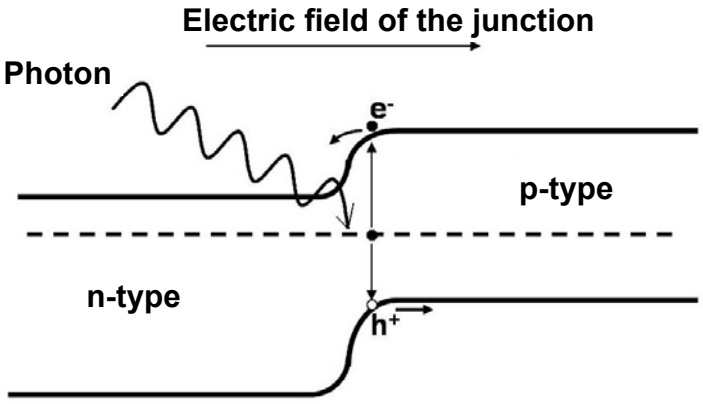

Figure II-1.6. Scheme of electron-hole generation upon photon absorption

The electric field opposes the migration of electrons from the n-type to the p-type material but favors the migration of the electrons created in the p-side to the n-side. This effect drives minority carriers (holes and electrons) across the junction contributing in both cases to the final current. Practically, all electron-hole pairs generated by light absorption within the space-charge region can be separated. The charge movement created by the electric field is called “drift”.

The rest of the charge carriers, generated by light absorption outside of the space charge region must remain separated for a sufficient period of time in order to migrate to the space-charge region. The undesirable in this case *recombination* of the carriers releases energy and can be either thermal, releasing heat, or optical, releasing photons. This last feature is the principle of operation of light emitting diodes (LED-s). The time before electron-hole pairs recombine is called *lifetime* and it corresponds to the *lifetime* of the *minority carriers*. Direct-band gap semiconductors generally have very short (0,01μs) in comparison with indirect gap materials.

With regard to the semiconductor material, there are two types of junction. A *homo-junction* is a junction formed by the same material with different type (usually by suitable doping agent in-diffusion). Usually, the upper layer (called emitter) is thinner than the bottom layer (called base) which is the principle light absorber. A *hetero-junction* is the one formed by two different materials, which is the case of the CdS/chalcopyrite device. A band diagram of this device is shown in figure II-8 Some reports have claimed the formation of homojunction by in-diffusion of Cd-ions, yet the evidence for this is limited [b33]. If the theory is correct, this would require the junction to be very close to the CdS/chalcopyrite interface in order to minimize recombination of carriers generated near the interface [30, 33]. The band diagram of a complete chalcopyrite device is given in Figure II-1.7.

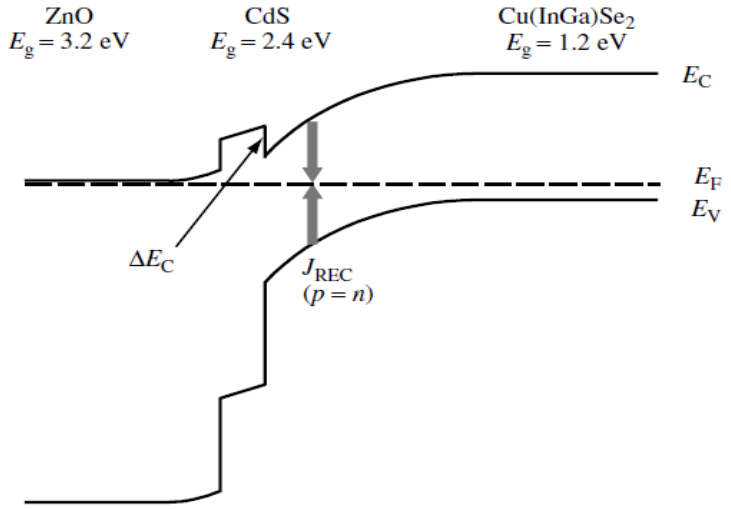

Figure II-1.7. Band diagram of a ZnO/CdS/Cu(In,Ga)Se2 device at 0V in the dark. The maximum recombination current is indicated by J_{REC} [30].

The recombination rate is given by the equation:

$$R = \frac{np}{\tau(n+p)}$$

Where *n* is the concentration of electrons, *p* the concentration of holes and τ the carrier lifetime [34] The maximum of the recombination rate lies in the space charge region of the chalcopyrite where p=n. In Figure II-8, the recombination current density is indicated by J_{rec}.

The conduction band offset ΔE is important for cell performance. As seen in the graph, a “spike” is observed, meaning that the conduction band minimum of the Cu(InGa)Se_2 is lower than the one of CdS. Although a small spike helps create type inversion at the interface, reducing recombination, models of current transport have shown that a spike larger than 0.5eV would impede collection of photogenerated electrons in Cu(InGa)Se_2 and sharply reduce the short-circuit current *Jsc* and the fill factor *FF* [34]. On the other hand, a “cliff” or a negative ΔE would lead to lack of type inversion at the interface and the interface state recombination will limit the open circuit voltage *Voc*. These cell parameters are described in the following section.

II-1.6) Photovoltaic device properties

All devices prepared in the present work were characterized by one of the simplest but also the most important and conclusive diagnostic technique for solar cells – the current-voltage measurement. This measurement can give information about the functional device properties: efficiency, open circuit voltage and short circuit current.

The *current-voltage curve (J-V curve)*[*] of a solar cell in the dark resembles the J-V curve of a diode describer by the Shockley equation:

$$J = J_{Osc}\left(e^{\frac{qV}{nkT}} - 1 \right)$$

Where J is the diode current, J_{osc} is the reverse bias saturation current, V - the voltage applied, q - the elementary charge (the magnitude of charge of an electron), n – diode ideality factor, k - Boltzmann's constant and T- the absolute temperature of the p-n junction in K.

Under illumination the curve remains identical, but displaced by the value of the photogenerated current J_L.

$$J = J_{0sc}\left[e^{\left(\frac{qV}{nkT}\right)} - 1 \right] - J_L$$

The *open circuit voltage Voc* is one of the most important cell characteristics and is the maximum voltage that can be measured between cell terminals when the current J=0. By substituting this value in the previous equation we obtain:

$$V_{oc} = \frac{nkT}{q} \ln\left(\frac{J_L}{J_{0sc}} + 1 \right)$$

Record performance CIGS devices have Voc in the range of 700mV.

S*hort-circuit current* J_{sc} (or the current which passes through the cell when the applied voltage V=0) is another important cell characteristic. In the ideal case, all photons with

[*] Many sources use the indication "I-V" instead of "J-V". Usually, *"I"* indicates the current, while *"J"* indicates the current density.

energy larger than the band gap of the absorber can be converted in current. The real *Jsc* depends on an array of factors such as light intensity and spectrum, recombination, optical and electrical properties of the absorber, reflection, band alignment, etc. High efficiency CIGS devices have Jsc in the range of 35mA/cm^3 [35, 36] out of the 42.8 mA/cm^2 available for their band gap of 1.12 eV [1].

A typical J-V curve of a solar cell is presented in Figure II-1.8. As shown, for each point the output power P=I.V and the Vsc and Jsc do not correspond to the actual voltage and current at normal operation. The point where the product of current and voltage is maximum (graphically represented by inscribed rectangle with maximum area) corresponds to the maximum output power P_{max}.

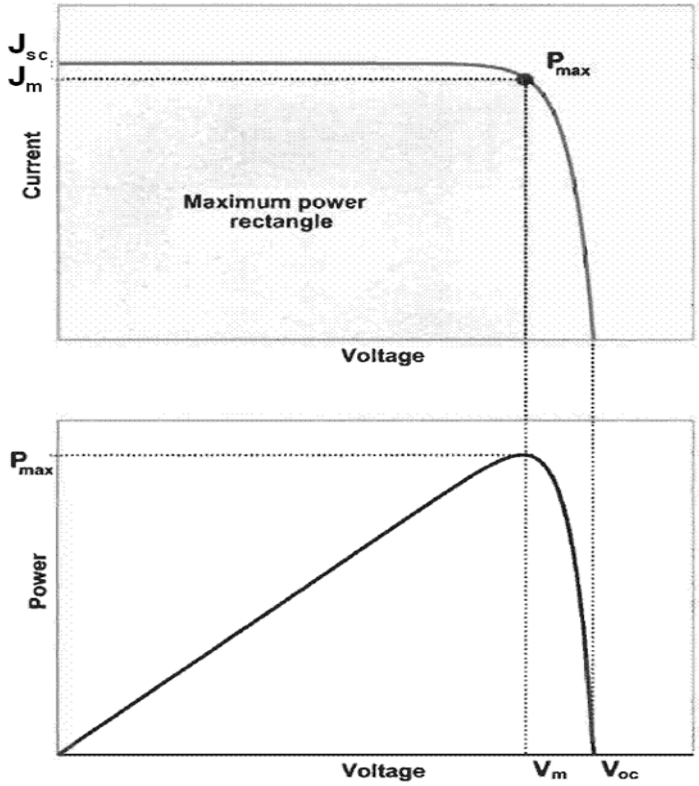

Figure II-1.8. Typical J-V curve of a solar cell and corresponding power output [8].

Fill factor FF is the ratio between the theoretical maximal obtainable power (power at maximum voltage and current) and the measured maximum power P_{max}.

$$FF = \frac{J_m V_m}{J_{sc} V_{oc}} = \frac{P_{\max}}{I_{sc} V_{oc}}$$

The device efficiency is the percentage of the maximum output power and the incident power or: η=100.Pmax/Pilum. It can be expressed by the other cell parameters discussed in this section:

$$\eta = \frac{FF.V_{oc}.J_{sc}}{P_{ilum}}.100$$

The J-V curve can also give information about two parameters of vital importance for optimal cell operation - the *series resistance* R_s and the *parallel (or shunt) resistance* R_{sh}, indicated in the equivalent circuit of a solar cell , Figure II-1.9.

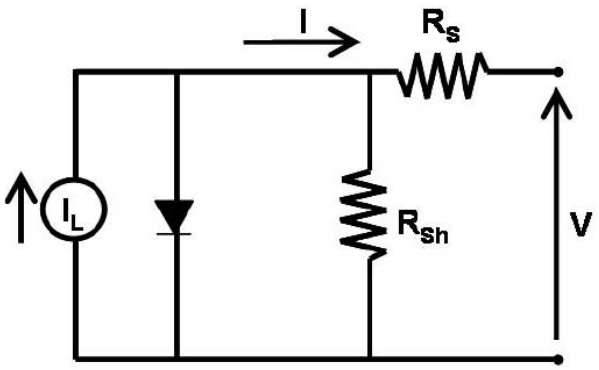

Figure II-1.9. Equivalent circuit of a solar cell showing the parallel and series resistance.

The series resistance can be viewed as the sum of most undesirable resistance components such as the current resistance through the buffer and the absorber plus all contact resistances. It can be calculated from the slope of the J-V curve in the point of intersection with the x-axis.

$$\left(\frac{dJ}{dV}\right)^{-1}_{\lim J \to 0}$$

The series resistance R_s must be minimized because high values of this parameter would lead to lower fill factor and, in consequence, lower efficiency. In a cell with an

area of 1cm^2 the series resistance should be 0.5Ω or less in order to achieve high performance.

The shunt resistance R_{sh} reflects mainly recombination losses and can be calculated from the slope of the J-V curve at the point of intersection with y-axis:

$$\left(\frac{dJ}{dV}\right)^{-1}_{\lim V \to 0}$$

Low values of shunt resistance would allow part of the current to run through the loop indicated in the equivalent circuit as a resistance, which corresponds to current losses due to recombination. Normally, low values of R_{sh} are a consequence of poor p-n junction formation [30].

In summary, in order to fabricate a high-efficiency device, i.e. a solar cell not only with high V_{oc} and J_{sc} but also with a high *FF*, two of the important requisites are low series resistance *Rs* and high parallel resistance *Rsh*.

Another measure of device quality is the *Quantum Efficiency (QE)* or *Spectral response*. It indicates the ratio between incident photons n_f and photogenerated electrons (holes) n_e which contribute to the final current:

$$QE = \frac{n_e}{n_f}$$

The current can be also described by the following equation where q is the electron charge and t-time:

$$J = \frac{n_e q}{t}$$

At the same time, the incident radiation power P can be expressed by the equation:

$$P = \frac{n_f . h\nu}{t}$$

Where hν is the photon energy. Combining above equations y substituting ν=c/λ, the quantum efficiency can be determined by the equation:

$$QE = \frac{n_e}{n_f} = \frac{hc}{q}\frac{J}{P}\frac{1}{\lambda}$$

Quantum efficiency measurements are usually carried out by irradiating the sample with monochromatic laser with known power (calibrated by use of a reference solar cell) [30].

II-1.7) Solar radiation and absorber requirements

For optimal harvesting of solar energy, the absorber material has to be optimally selected with regards to the spectral distribution of solar radiation (Figure II-1.10). In space, the spectrum of solar radiation is similar to the black body model at 5767K. At terrestrial surface, atmospheric absorption and reflectance reduce the amount of incident radiation. A standardized unit for the atmospheric effect is the Air Mass (AM). Its value indicates the secant of the angle of incidence of solar radiation (hence the optical path through atmosphere). As an example, AM1 is the spectrum of solar radiation at 90º. Standardized AM spectra are used for calibration of simulation and measurement equipment.

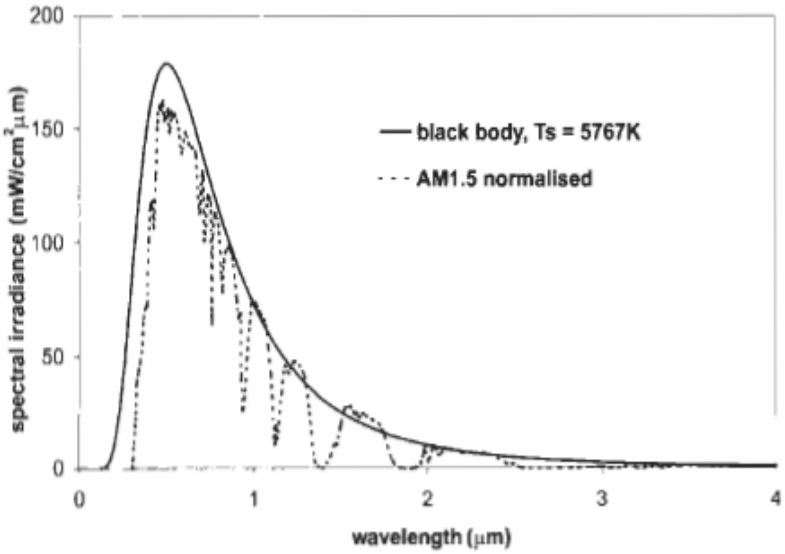

Figure II-1.10.The black-body spectrum of solar radiation and the terrestrial AM1.5 spectrum [8].

In order to be absorbed efficiently by a semiconductor, the light must have sufficient path through it. Then, almost the totality of incident photons with energy higher than its band gap can be absorbed and, in the ideal case, converted to electrical current. This can be achieved either by providing sufficient thickness of the semiconductor layer or by the use of efficient light-trapping schemes such a patterned back reflector. The necessary optical path to achieve high light harvesting is determined by the absorption coefficient α:

$$\alpha = \frac{\ln I_0 / I}{t}$$

Where I_0 and I are the intensities of the incident and transmitted radiation, respectively, and t is the film thickness. Figure II-11 represents the absorption coefficients of selected semiconductors in function of photon energy.

One of the inherent advantages of thin-film chalcopyrites, is their extremely high absorption coefficient (above 10^4/cm) allowing efficient light inclusion to be achieved with layers thinner than 1 micron (Figure II-1.11) whereas the thickness of crystalline silicon without special light trapping must be 100-200 micron in order to absorb the same fraction.

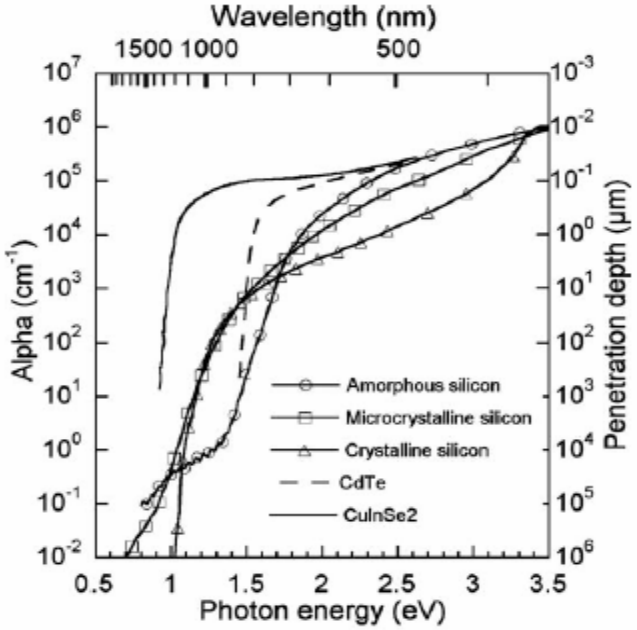

Figure II-1.11. Absorption coefficient and penetration depths (1/α) of the several thin-film absorber materials [8].

This high absorption coefficient is due to the fact that chalcopyrite is a direct band gap semiconductor, i.e. the top of the valence band and the bottom of the conduction band lie at the Γ point of the first Brillouin zone, (at zero wave vector k=0). In contrast, silicon has at least two orders lower absorption coefficient as it is an indirect gap semiconductor, i.e. the minima of the conduction band lie at another point of the first Brillouin zone, with a different value of the wave vector $\boldsymbol{k}$ [8].

The absorption coefficient for a direct band gap material can be related to the photon energy by the Tauc equation:

$$\alpha h\nu = k(h\nu - E_G)^{1/2}$$

Where *k* is constant, hν is the photon energy and E_G is the band gap energy. The band gap is measured by plotting a $(\alpha h\nu)^2$ versus hν. The extrapolation of the straight line in the graph to $(\alpha h\nu)^2=0$ gives the value of the energy band gap. We have used this dependence for band gap determination.

As mentioned in the previous section, higher power output is equivalent to a higher product of voltage and current. Unfortunately, the trade-off between higher voltage and higher current is present again when it comes down to optical properties.

In order words, to obtain higher current, a higher number of photons have to be absorbed and converted into electrons. With little deviation from the ideal case, a large fraction of photons with energy higher than the gap can be converted to electrons (Figure II-1.12). This means that, generally, higher current can be generated by a semiconductor with a lower band-gap.

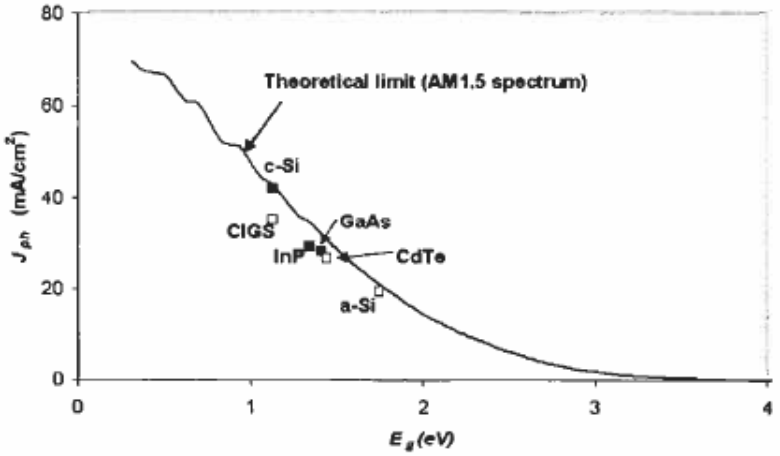

Figure II-1.12. The theoretical limit on photogenerated current at AM1.5 photon flux, compared with the best measured values [8].

The relation between semiconductor band gap and maximum voltage is exactly the opposite (Figure II-1.13). Higher energy photons are capable of generating higher voltage and in the typical case where each photon generates only one electron, the excess energy is lost.

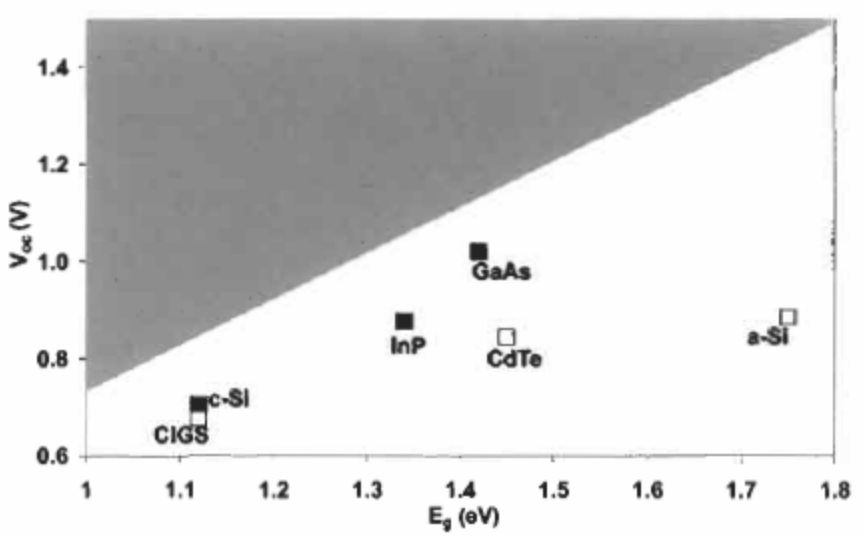

Figure II-1.13. Theoretical Shockley-Queisser limit on open circuit voltage: values exceeding this limit lie in the shaded area of the graph [8].

As a result, the optimum choice of the band gap would require one to consider both the possible current and voltage with respect to the solar spectrum. As seen in Figure II-1.14, the maximum theoretical efficiency values are found between 1 and 1.5 eV. These values are given for terrestrial surface at AM1.5 global spectrum. For space applications (black body spectrum), the optimal band gap is approximately 1.5 eV.

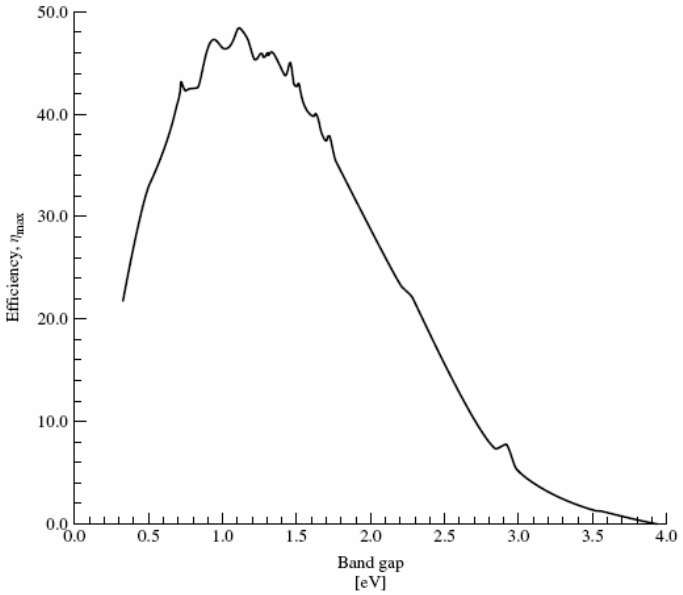

Figure II-1.14. Theoretical maximum efficiency as a function of semiconductor band gap for AM1.5 global spectrum [1].

It is generally agreed that higher voltage cells are preferable for module manufacturing because of the following advantages [37] :

- Reduction in the number of necessary scribes for the monolithic interconnection
- Lower current density would allow reduction in the thickness of the top and bottom electrodes.
- The temperature coefficient of maximum power output is reduced

Such higher voltage can be obtained with higher band gap semiconductor such as $CuInS_2$ (1.5eV). Nevertheless, the experimental results have not surpassed 13% while the record performing $Cu(In,Ga)Se_2$ chalcopyrite absorbers have already yielded 20% with rather lower band gaps - 1.14eV [38]. As discussed above, there are additional factors that can influence device performance and for both types of materials and there are no optical limitations to achieve efficiencies above 30%.

Even higher theoretical efficiency can be achieved by use of “tandem” or stacked solar cell structures. Such devices include more than one p-n junctions with absorbers of different band gap. Concentrated sunlight thermodynamically can be converted even more efficiently – reaching 40%. The theoretical efficiency of triple tandem solar cells at high concentrations is above 60% [39] Multipe-junction concept is widely used in thin-film silicon photovoltaics and concentrator III-V devices. The last have already surpassed 40% efficiency by use of high concentration ratio (above 500sun).

At the moment, no efficient chalcopyrite devices employ multiple junctions. Building a chalcopyrite tandem cell in monolithic configuration similar to III-V devices is a big challenge mainly because the p-n junction formed after the buffer deposition has very low tolerance to temperatures above 200ºC. Instead, schemes of mechanically stacked cells are being investigated [41]. $CuGaSe_2$ is considered a promising material for the top cell absorber [42].

Concentrator systems that currently hold the record efficiency are very expensive, because high precision is necessary to achieve high concentration ratio. These systems employ two-stage mirrors and/or lenses and robust metallic tracking structures with precise electronic control. At the same time, they are difficult to integrate architectonically because of the volume required for their operation.

The possibility to avoid high concentration by low-cost, large-area modules offers many advantages such as easy integration, maintenance-free operation, little space requirements, elegant aspect, etc. Module efficiencies of 7-10% are sufficient for mass

deployment, despite the fact that they require three times more area in order to produce the same output as advanced concentrator systems.

Both concentrator and flat-panel photovoltaics have their niches and together can contribute to satisfying the vast demand of renewable energy. The area available for building integration will remain practically unlimited within the next decades, and at the same time specially designed solar farms would require higher efficiency per area. Within the global effort to supply cheap solar power, thin-film chalcopyrites are excellent absorber materials for future large-scale module deployment.

II-1.8) Chalcopyrite materials

The name of this group of tetragonal crystalline materials belongs to the oldest and best known representative – $CuFeS_2$. Unfortunately, no efficient devices have been fabricated with it. Various elements can substitute each of the three constituents and furthermore different chalcopyrites can form solid solutions permitting a vast number of combinations.

The ternary chalcopyrite compounds A^{I}-B^{III}-C^{VI}_2 (A=Cu, Ag; B=Al, Ga, In, Tl and X= S, Se) are similar to their isoelectronic II-VI binary analogues (ZnS for example). On the other hand, these derive from the tetrahedrally bonded class IV semiconductors (Figure II-1.15) [43]. Double unit cells are shown for (a) diamond Si, (b) zincblende ZnS, and (d) Cu-Au ordered $CuInS_2$, in comparison with the single unit cell of chalcopyrite $CuInS_2$. In the diamond structure of the class IV semiconductors each atom is bonded to four neighboring atoms occupying the corners of a regular tetrahedron (Figure II-1.15a). The zincblende structure (Figure II-1.14b) can be regarded as a superlattice structure of diamond, where one sublattice is occupied by cations and the other by anions. The chalcopyrite structure is derived from the zincblende by preserving the anion positions and replacing the single-type cations with two types of cations in alternating order – one of lower (A) and one of higher valence (B) as shown in Figure II-1.14c. The unequal strength of the A-X and II-X bonds leads to tetragonal distortion, i.e. the lattice constant *a* is not exactly half of the constant *c*, i.e. $c/2a \neq 1$. [44, 45]

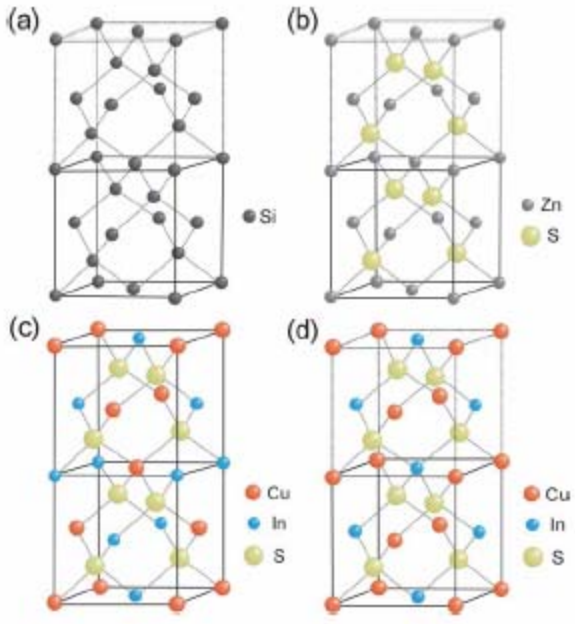

Fig. II-1.15. Structures of (a) diamond Si, (b) zincblende ZnS, (c) chalcopyrite $CuInS_2$, and (d) Cu-Au ordered $CuInS_2$ [43].

One of the undesirable polymorphic modifications of chalcopyrite is the Cu-Au ordering (Figure II-1.15d). In the case of $CuInSe_2$ and $CuInS_2$ polytypes the formation energies and the band structures are very close resulting in band gap difference of only 46 and 30 meV [44, 45]. Although this theory suggests that cell performance should not be affected by the presence of Cu-Au ordering, the experiment has shown that Cu-Au is detrimental for thin-film photovoltaic devices. The presence of Cu-Au in the film is correlated with worsening of the structural features, i.e. decrease of grain size and increase in density of extended defects in grain [46]. Severely deteriorated solar cell properties, especially open circuit voltage, is found in samples containing even small amount of Cu-Au ordered phase [47, 48].

Raman scattering is widely used for the detection of Cu-Au ordering which is difficult or impossible to distinguish by X-ray diffraction. It was found that the Raman spectrum of $CuInS_2$ is characterized by the presence of a dominant A-1 mode at about $290cm^{-1}$ [48]. The spectral characteristics of this line proved to be very sensitive to the structural quality of the CuInS2 layer, being the full width at half maximum (FWHM) of the A^{-1} line representative of crystal quality. Increased FWHM can be related to an additional peak at 305 cm^{-1} [48, 49] that may correspond to Cu-Au ordered phase. This ordering may be also present in other materials such as $CuInSe_2$ [50].

The band gap energies of chalcopyrites are often related to the lattice constant ***a*** or, in a more advanced approximation, to the average lattice constant **2/3a+c/6** (Figure II-1.16) [51].

For preliminary rough evaluation of a new material, one can use the lattice constant of isostructural and isovalent phases, determined either from analysis of the X-ray diffraction data, or from more general considerations about the atomic size. The energy band formation in a crystal is due to a splitting of the energy levels of the atoms because of their interaction. The larger the lattice constant and the smaller the interaction between the atoms, the smaller is the splitting and also the band gap width.

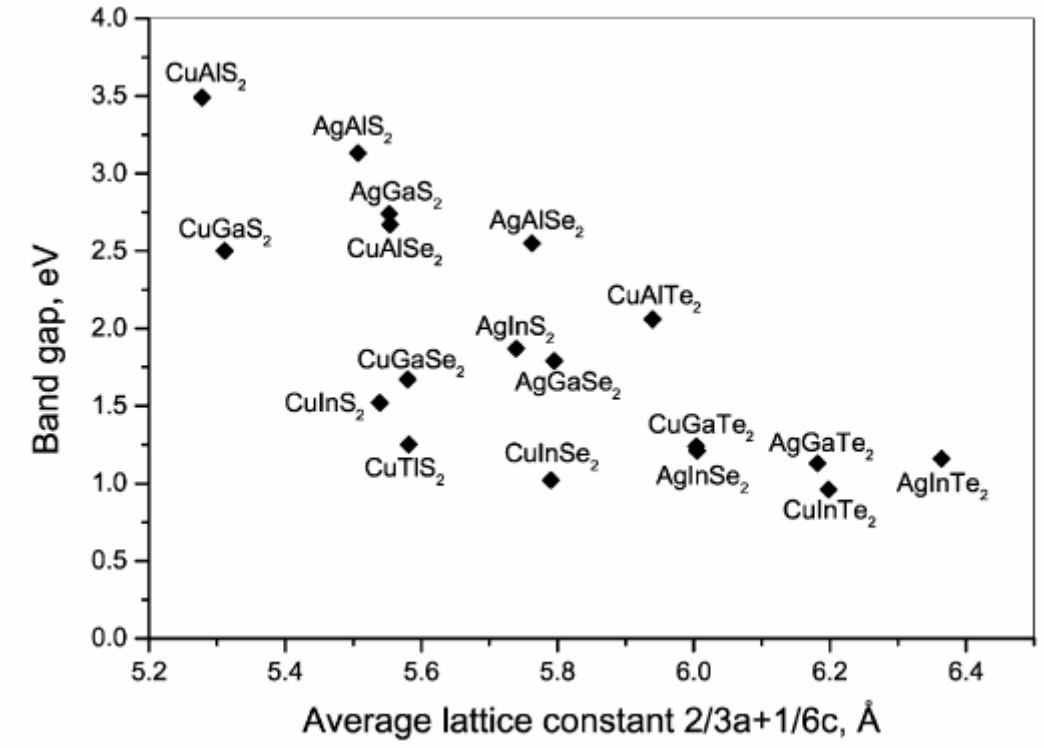

Figure II-1.16. Correlation between average lattice constants and band gap energies of isovalent isostructural materials [51].

A practical example of this dependence is the possibility to tune the band gap by the introduction of isovalent atoms with different size. For instance, the band gap of $CuInSe_2$ (approximately 1 eV) can be increased either by substituting In atoms with smaller Ga atoms or by substituting Se atoms with smaller S atoms [51].

All principal chalcopyrites that are currently used industrially as photovoltaic absorbers ($Cu(In,Ga)Se_2$, $Cu(In,Ga)(S,Se)_2$ and $CuInS_2$) have increased band gap in comparison with the pioneer material $CuInSe_2$ because of Ga and/or S incorporation.

II-1.9) Materials considerations in view of future terawatt production: abundance and safety

While developing higher efficiency photovoltaic technologies, it is important to estimate whether our resources are sufficient to permit these technologies to achieve their goal. The goal, of course, is significant contribution to global energy production and reduction of carbon dioxide emissions. In order to do so, photovoltaic technology must face unprecedented upscale, reaching a staggering volume - terawatt peak (TWp) within decades. This transfers to hundreds of thousands of square kilometers of installed photovoltaic modules. When reaching such levels, it is natural to ask if our materials reserves, especially of rare elements such as Indium and Gallium would be sufficient. At the same time, health and environmental concerns always arise when toxic elements (e.g. Cd and Se) are used in large-scale industry. These concerns must be properly addressed at an early stage, considering the urgent need for photovoltaic production.

There are controversial data about In and Ga reserves. Figure II-3x presents data on materials US Geological Survey, based on current mining and refinement processes employing high grade raw materials [52, 53].

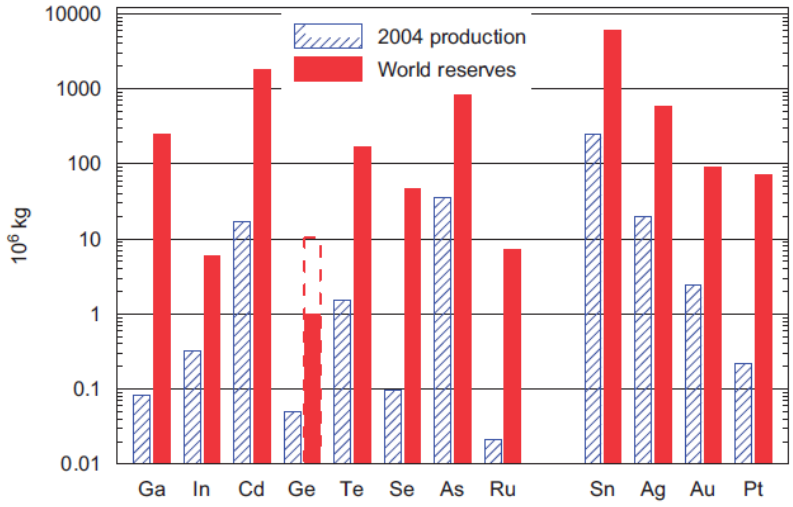

Figure II-1.17. Estimated 2004 annual production levels and material reserves according to the pessimistic first source [52].

According to this study, the world reserves of indium deposits (not considering low-grade sources) would allow the production of only a small fraction of the required

capacity (0.02TW), as shown in Figure II-1.18 [52, 53]. The authors claim that indium availability would be a major limiting factor for the contribution of $Cu(In,Ga)Se_2$ photovoltaic technology. In addition, Indium is used by other growing technologies, such as Flat-panel displays.

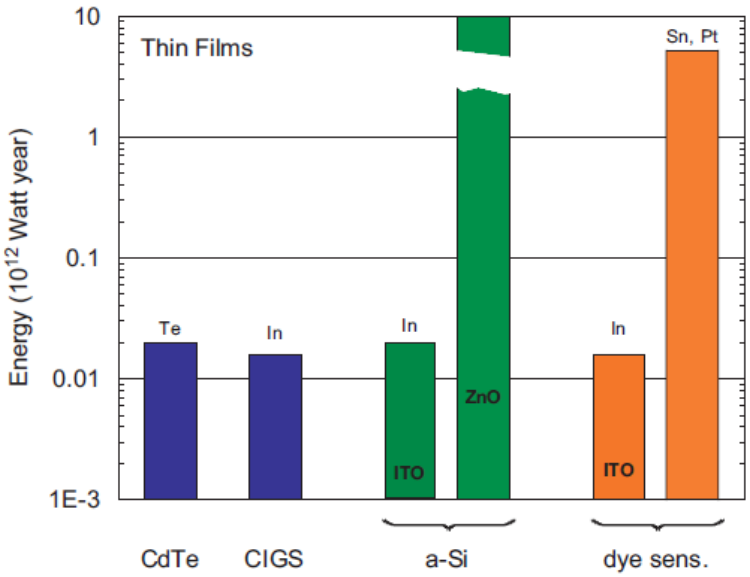

Figure II-1.18. Potential energy limits imposed for four different thin film photovoltaic technologies, according to the pessimistic source.

Other authors [54] give a radically different estimation. They point out that the abundance of Indium in the earth's crust is estimated to be 0.05 ppm for the continental and 0.072 ppm for the oceanic crust, which is higher than the concentration of silver. Considering that silver is currently produced at a rate of 20 000 t/year in comparison with only 400t/year for indium, there is no danger for indium shortage for the long term. There is a clear controversy with the above data for world reserves of indium, as in the pessimistic source they are less than half of the yearly production of silver.

The authors of the second and more realistic scenario [54] show that the reason for low indium production is the low demand and current state of technology. They explain that for primarily economic reasons, "Indium was originally only extracted from zinc and lead concentrates containing at least 500 ppm indium (and coming from ores containing about 50 ppm of indium). Due to improvements in the extraction technology, combined with the economics of higher prices, Indium is now recovered as a bye-product of a wider range of base metals including tin, copper, and other polymetallic deposits. Indium is also now being extracted and recovered from base metal concentrates containing as little as 100 ppm." The big challenge here, especially in the short run, is to build sufficient refining capacities to satisfy the growing demand.

The development of advanced refinement facilities would be also driven by another exponentially growing indium consumer – flat panel display industry.

The same source [54] also gives an optimistic prognosis about the Ga-supply: “Similar to Indium, Gallium is the result of an extraction process. There are no primary Gallium mines. Gallium is extracted from bauxite as part of the bauxite-alumina-aluminum refining flow, which most commonly utilizes the Bayer liquor process. By all accounts, bauxite is plentiful in the earth’s crust and is widely distributed geographically and politically. Similar to Indium, this contributes to stability of supply of Gallium feedstock. Interestingly, only a small portion (less than 10%) of the potentially available Gallium in the bauxite is actually extracted. Hence, the existing flow of bauxite processing offers tremendous capacity increases. Historically, the low extraction volume was limited more by the relatively small demand and economics of relatively low prices. For all practical purposes, gallium output is limited only by facilities investment and capacities.”

Although optimistic, these scenarios would require new large-scale technologies that have yet to be established. At the same time it is unclear what the production costs and environmental impact of refining such vast volumes of low-grade raw materials would be.

An alternative to the use of rare materials having uncertain supply and high cost is the use of more abundant materials.

An example of a promising alternative material that has already demonstrated reasonably efficient devices is the kesterite-type Cu_2ZnSnS_4 [55]. Cu_2ZnSnS_4 is composed of abundant and non-toxic elements and can be considered a strong candidate for future terawatt production.

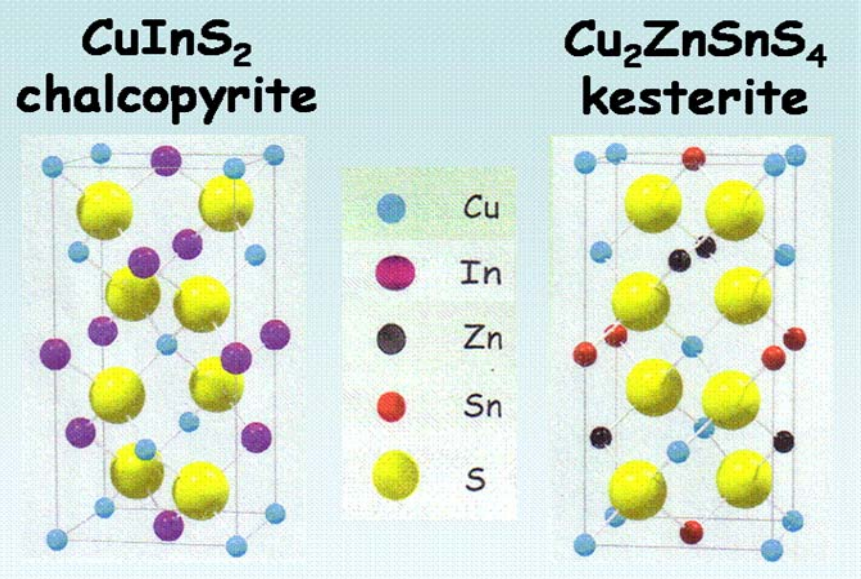

Figure II-1.19. Structures of Chalcopyrite and Kesterite

The kesterite structure can be derived from the $CuInS_2$ structure by substituting half of the Indium atoms with Zn and the other half with Sn (Figure II-1.19). [56] Within our work we have developed a novel low-cost method for Cu_2ZnSnS_4 deposition based on printing of nanoparticle suspensions.

II-1.10) Some specifics of advanced $CuInS_2$ processing

While state of art devices aim to increase the band gap of $CuInSe_2$ by Ga and/or Sulfur doping, the inherent band gap of $CuInS_2$ is about 1.5eV. This value is considered optimal for solar energy conversion permitting conversion efficiencies beyond (25%) [57].

Another important advantage of this material is the lower toxicity of sulfur in comparison with selenium which makes it environmentally safer.

The first device employing this material was reported in 1977 [58]. The first thin-film device with efficiency exceeding 10% was based on the co-evaporation approach [59]. A much more scalable two-stage process based on sulfurization of sputtered metallic precursors was developed in 1996, yielding efficiencies above 10% [60]. The introduction of Rapid Thermal Processing during the sulfurization of the metallic precursors not only shortened the reaction times from 1 h to 3 minutes, but increased device efficiency up to 11.4% [61] a scheme of this process is presented in figure II-1.20. The processing steps are similar to the CIGS sequential processes with the difference that $CuInS_2$ can be grown Cu-rich and therefore large-grained in a single step (low melting point Cu-S phases act as a fluxing agent). The highly conductive Cu-S phases are and then etched to remove excess copper. This is a technological advantage because Cu-rich CIGS cannot be conditioned for photovoltaic applications by simple etching.

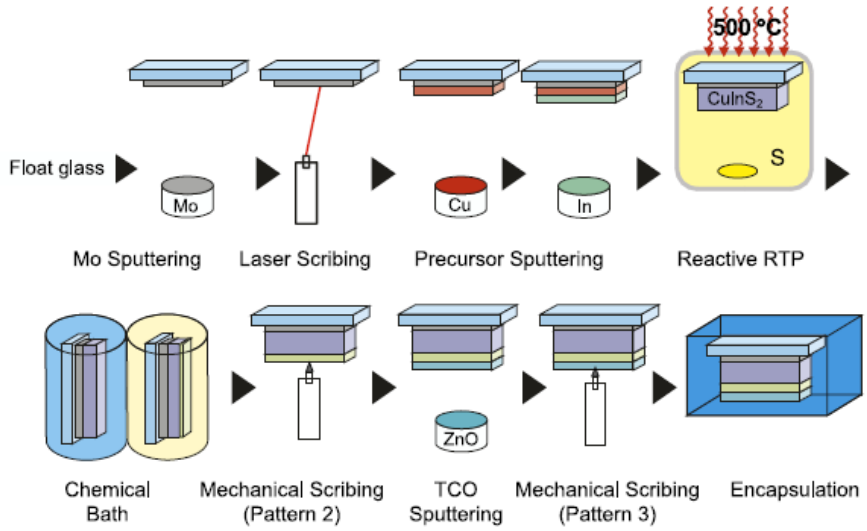

Figure II-1.20. Baseline process for manufacturing $CuInS_2$-based modules at Hahn-Meitner Institut [62]

.

The two-stage process developed at Hahn-Meitner-Insitutut, Berlin (Figure II-1.20), [62] is already applied in pilot production of large-area modules (125x65cm) by the company Sulfurcell with steadily growing efficiency - 7.6% in 2007, outperforming amorphous silicon modules in field tests. [63]

II-1.11) Some specifics of advanced $Cu(InGa)Se_2$ (CIGS) processing

There are two principal techniques by which commercial $Cu(InGa)Se_2$ are currently produced: coevaporation and sequential processes. The growth of high-quality crystalline material here is challenging because, unlike the case of $CuInS_2$, final composition must be Cu-poor. While co-evaporation approaches can have a Cu-rich stage followed by an In-rich one, the sequential processes use copper-poor precursors. Another difference from the previous absorber is the fact that very small amounts of sodium (in the range of 0.1%) are highly beneficial not only for improved crystal growth, but also for the electronic properties of the absorber.

Record performance $Cu(In,Ga)Se_2$-based devices are deposited by co-evaporation. This process is advantageous for growing excellent quality materials because of the possibility to control elemental fluxes and conveniently employ both Cu-rich growth conditions and In-rich final composition. The first successful development of this type was the Boeing 2-stage process which starts with Cu-rich and ends with Cu poor fluxes. The concept was further developed in more advanced multistage processes (Figure II-1.21).

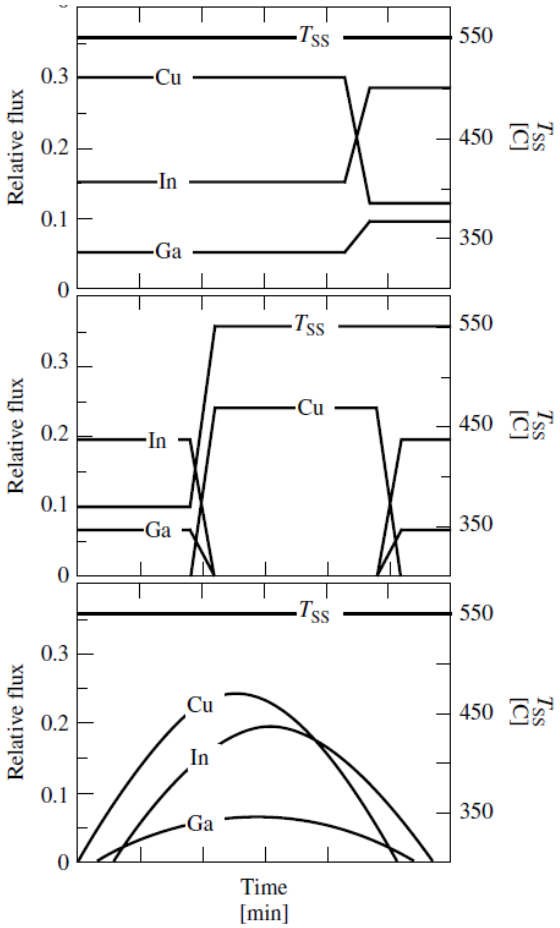

Figure II-1.21. Relative metal fluxes and substrate temperature for different coevaporation processes [1].

Variations of these techniques aim for improved nucleation and film smoothness. An attractive feature of the coevaporation methods is the process flexibility, demonstrated by the high efficiency achieved by diverse methods. Yet, precise control of composition uniformity over large area is challenging because elemental fluxes are sensitive to very small temperature differences.

An example of in-line coevaporation system is shown in Figure II-1.22. The development of large-scale high-throughput coevaporation equipment is a challenging task and the cost for module fabrication by coevaporation is expected to be higher than most alternative methods.

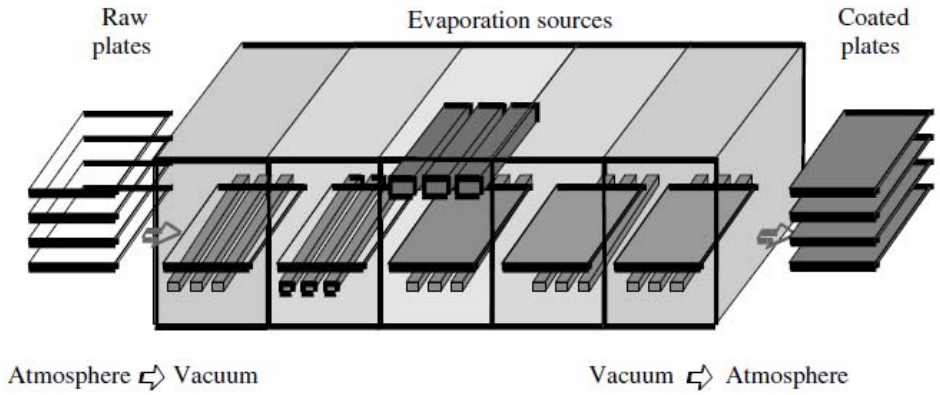

Figure II-1.22. A scheme of In-line coevaporation system for Cu(InGa)Se_2 with linear evaporation sources at ZSW, Stuttgart [1].

Treatments of stacked precursors (Figure II-1.23) have also resulted in high efficiency devices. The treatment can be either rapid thermal anneal [64,65] or in precisely controlled hydride gas atmosphere [66, 67]:

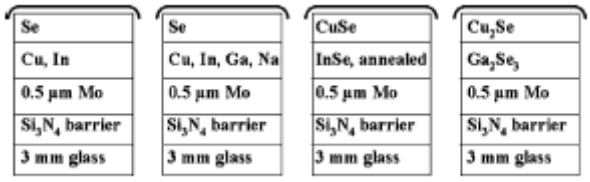

Figure II-1.23. Some examples of stacked elemental layers [64].

One important element in the growth of high-quality $CuInSe_2$ and Cu(In,Ga)Se_2 is the presence of sodium. This effect was discovered serendipitously. Devices fabricated on sodium-free glasses failed to match the efficiency of the ones previously fabricated on low-cost sodium containing glass. It is estimated that the optimal sodium content is only about 0.1% - approximately the amount that diffuses from the glass and through the molybdemum layer into the final film [69].

The effect of sodium is manifold. On one hand it influences absorber growth. $Na_2(Se)_n$ phases concentrate at the surface of the growing absorber (Figure II-1.24) and act as Se-trapping agent with low melting point, resulting in excellent growth medium.

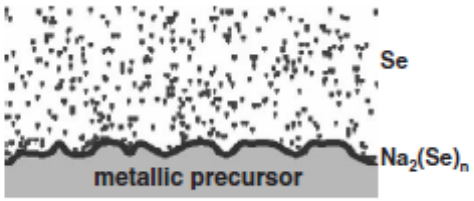

Figure II-1.24. Principle of $Na_2(Se)_n$ action[68]

On the other hand, sodium doping is very important for the electronic properties of the absorber. There are many, often controversial, explanations of this effect, but generally it is considered that Na is concentrated at the grain boundaries where its effect is mostly manifested. The believed contribution is passivation of defects (e.g. hole traps) at the grain boundaries. Nevertheless, influence of intra-granular Na cannot be ruled out completely [69].

II-1.12) Low-cost approaches to chalcopyrite deposition

Vacuum-based techniques such as sputtering and coevaporation have demonstrated high efficiency, but when it comes to large-scale production, these technologies have the following disadvantages:

- High initial cost of manufacturing equipment. This includes vacuum chambers, load-lock sections, vacuum pumps, etc.
- Low throughput. Most of these techniques are “line of sight”, i.e. each substrate must be exposed to the materials sources and coated individually. Processing times by vacuum technology are relatively long (typically from 10 min. to more than an hour for each layer), which results in low manufacturing rates.
- Difficult control of stoichiometry over large area. When several elements are evaporated or sputtered, minor deviations in the deposition uniformity may result in modification of elemental ratios that can be detrimental for device performance.

Non-vacuum techniques can generally address most of these challenges:

- The capital cost of the facilities is significantly lower than vacuum equipment
- Throughput can be as high as newspaper printing.
- The uniformity of final stoichiometry, especially metal ratio is predetermined by the initial composition when a solution or paste is used.

Despite these advantages, each low-cost method presents some challenges:

Spray-pyrolisis is a relatively low materials utilization technique. It is a slow process with some similarities to vacuum coating in terms of throughput. At the same time the use of aerosols requires special safety and environmental precautions. This method has been used for the deposition of $CuInS_2$ 71-73 as well as oxides that were later treated in chalcogen vapor to form $CuInSe_2$[72, 72] or CdS [73].

Electro deposition has the advantage of being industrially established process for large-area coating. Materials utilization can be close to 100%. Extensive work on chalcopyrite electrodepostion has yielded fundamental understanding of the process and high-performance devices [73-81].Some difficulties may be present in co-electrodeposition of several elements, as their redox potentials may be different. Co-

electrodeposition of gallium-containing materials is particularly difficult, although solutions have been proposed [82]. Electro deposition is already used in the pilot industrial facilities of companies like IRDEP and SoloPower.

Solution coating or sol-gel is one of the main techniques used in this work [83-86]. It has the advantage of simple compositional control and high flexibility in this aspect. Drawbacks include relatively low "critical thickness" or the thickness that can be achieved without cracking. Usually it is less than 300 nm which requires several coatings in order to reach the thickness required for and absorber in solar cells. A common disadvantage of this and the paste-coating method described bellow may be the use of organic substances. There is a tradeoff between residual carbon elimination by atmospheric anneal and oxidation of the materials. These drawbacks are addressed by a novel approach that uses hydrazinates [87] yielding high-purity materials and efficient devices (above 10%). Despite of this, there are some concerns about toxicity and flammability of hydrazine. Spin coating is a laboratory technique that can transfer to other industrial techniques such as dip-coating or ink-jet printing, generally requiring low viscosity fluid.

Paste-coating or printing is a very straight-forward approach that can be up-scaled to large area deposition with almost no intermediate optimization. The general approach is to use nanoparticle suspensions [88, 89] although solution-based pastes with ethylcellulose viscosity enhancer have also been reported [90]. Efficiencies above 13% have been reported [91]. This technique is used by companies like ISET and Nanosolar to print CIGS on flexible foils and glass [92, 93], yet module efficiencies are still much lower. A major drawback of paste coating is the need to use binding or viscosity-enhancing agents in order to deposit uniform layers [89-91]. These additives may produce carbon contamination and reduced crystal growth.

Table II-1.I. Materials for chalcopyrite devices and deposition methods

Method	$CuInS_2$	$Cu(InGa)Se_2$ $Cu(InGa)(SSe)_2$	In-free (Cu_2ZnSnS_4)	In-free buffers
Co-evaporation	+	+	+	+
Sputtering	+	+	+	-
Spray pyrolisis	+	-	+	+
Electro deposition	+	+	+	Our work*
Sol-gel spin-coating	Our work*	Our work*	Our work	-
Paste coating (printing)	Our work	Our work	Our work*	-

*The first report on such deposition.

Table II-1.I. summarizes the approaches developed in our work in comparison with previous art.

We were the first to publish spin-coating of $CuInS_2$ and $Cu(In,Ga)(S,Se)_2$ absorbers [83-85], electro deposition of In_2S_3 buffers for $CuInS_2$ solar cells [94] and printing of Cu_2ZnSnS_4 from nanoparticle suspensions [95].

In addition, this dissertation reports for the first time a method for printing highly oriented $CuInS_2$ films and a novel $Cu(In,Ga)Se_2$ coating technique which does not require the use of special binding agents. Promising device efficiencies of 7.5% were obtained.

II-1.13) Characterization techniques

X-ray diffraction

This technique is based on elastic scattering of X-rays by atoms. When these atoms are ordered in a regular form, the regular resultant waves cancel each other, adding only in few specific directions determined by the Bragg's law:

$$2d\sin\theta = n\lambda$$

where *d* is the interatomic distance, θ the scattering angle. The intensity registered at specific angles gives information about the crystalline lattice.

In our work the crystal structure of the films was determined by X-ray powder diffraction (XRD) with a SIEMENS D5000D diffractometer equipped with a Cu-K_α radiation source and "SIEMENS DIFFRACT PLUS" software which also determined diffraction peak positions and intensities. Data were collected by step-scanning from 20 to 60 $^{o}2\theta$ with a step size of 0.05 $^{o}2\theta$ and 1s counting time per step. The instrument was calibrated using an external Si standard which served also as a reference for average crystalline size determination.

The average crystalline size was calculated by use of the Scherrer formula [96]:

$$t = \frac{0.9\lambda}{B\cos\theta_B}$$

$$B = \sqrt{\left(B_M^2 - B_S^2\right)}$$

Where t is the crystalline size, λ is the wavelength of the X-ray used, θ_B the Bragg angle, B_M the full width at half maximum of the measured peak in radians and B_S the full width at half maximum of the peak of the standard used (Si).

Scanning electron microscopy (SEM)

Scanning electron microscopy uses high energy electron beam instead of light in order to obtain images of the sample. The electrons, impacting in a scanning mode, interact

with atoms from the sample producing signals that contain information about sample morphology, composition and other related properties.

An important tool integrated in this technique is the energy dispersive X-ray microanalysis (EDX). A detector registers X-rays emitted form the sample due to interaction with high-energy electrons and generates specific pattern for each element. The data provides information about semi-quantitative composition.

Unless otherwise specified, film morphology and composition were determined by Scanning Electron Microscopy (SEM) using *Leica Leo 440* equipped with a spectrometer for energy dispersive X-ray microanalysis(EDX) using the following operating parameters: acceleration voltage 20 kV, measuring time 100s, working distance 25 mm, counting rate 1.2 kcps. The samples for microstructure and microanalysis determination were introduced using an aluminum holder with graphite adhesive tape. The thickness of the films was estimated from micrographs of film cross sections.

Thermo gravimetry and differential thermal analysis (TG/DTA)

This characterization technique measures mass loss during thermal treatment in air or inert atmosphere. It provides important information of many phenomena accompanying thermal treatments, such as solvent loss, combustion reactions and phase transformations.

Differential thermal analysis/Thermogravimetry of precursor solutions was carried out in with Mettler-Toledo using platinum crucible air flux and heating rate of 5ºC/min.

X-Ray fluorescence

This technique employs high energy X-rays which expel electrons form the inner orbits of atoms of the analyzed sample. The places of the expelled electrons are occupied by electrons from higher orbitals. These transitions emit photons with characteristic energies equal to the energy difference of the higher and lower state. Energy dispersive techniques use detectors that measure the energy of detected photons. The spectra obtained are element-specific with peaks proportional to content and after calibration with reference samples can be used for composition analysis.

In our work we used *Fischerscope Xray Xan* controlled by the *WinFTM* software running under Windows. Calibration was carried out using co-evaporated reference films and measurement time was 2 min.

X-Ray photoelectron spectroscopy (XPS)

This is a highly sensitive qualitative or semi-quantitative surface chemical analysis technique used to estimate elemental composition, chemical state and electronic state of elements in the superficial layer (less than 10 nm) of materials. X-rays generate emission of electrons from the core orbitals. The kinetic energy and number of these electrons are measured. The kinetic energy is used to calculate the binding energy of the electrons.

Unless otherwise specified, in our work film composition was studied by X-ray photoelectron spectroscopy (XPS) depth profiling under the following conditions: The measurements were carried out in an ultra-high-vacuum evaporation chamber connected to an ESCALAB 210 multi-analysis system (base pressure $1.0x10^{-10}$ mbar) from Thermo VG Scientific. Photoelectrons were excited with the Mg-Kα line (1253.6 eV). The sample was successively sputtered by using an Ar ion gun until the film was removed from the sputtered area, allowing us to analyze the homogeneity of the sample.

Raman spectroscopy

Raman spectroscopy is based on inelastic scattering of monochromatic light that is usually generated by a lased source. Inelastic scattering means that the frequency of photons changes upon absorption and reemission from the sample. The shift in frequency can provide information about vibrational, rotational and low frequency transitions in molecules [97].

In our work we used Raman spectroscopy mainly to determine the presence of Cu-Au phase which, as already explained in the introduction, is detrimental for device performance.

Unless otherwise specified, MicroRaman spectra were recorded on HORIBA Jobin Yvon LabRamHR800L high resolution spectrometer with He-Ne laser line (λ= 632.81 nm). To avoid thermal effects of the laser beam on the films, intensity was adjusted to

an excitation power of 20 μW. The acquisition time is 180 s. Spectra fitting was done with LabSpec© software supplied with the apparatus.

Optical measurements

The optical transmission of the films was measured with a Cary 500 Scan UV-Vis-NIR spectrophotometer. The data were registered from 400 to 1100 nm using an uncoated glass as a reference.

The absorption coefficient was determined by the formula:

$$\alpha = \frac{\ln I_0 / I}{t}$$

Where I_0 and I are the intensities of the incident and transmitted radiation, respectively, and t is the film thickness, determined by scanning electron microscopy.

The band gap of the materials direct band gap materials was determined by plotting a $(\alpha h\nu)^2$ versus $h\nu$. The extrapolation of the straight line in the graph to $(\alpha h\nu)^2=0$ gives the value of the energy band gap. This method is based on Tauc equation, described in detail above.

II-2. DEVELOPMENT OF A SOL-GEL ROUTE TO $CuInS_2$

II-2.1) BACKGROUND AND PRINCIPLE OF THE METHOD

As already described above, $CuInS_2$ is an attractive material because of its inherently optimal band gap of 1.5% , flexible processing conditions, and lower toxicity of sulfur in comparison with selenium.

At the time we carried out our work, very few reports on low-cost methods for $CuInS_2$ deposition existed, mostly based on spray-pyrolisis [70]. Within this thesis we developed a new solution spin-coating method which was published in 2006 [83]. The present section includes this work.

The principle of the process was based on two previous works – deposition of copper oxides by sol-gel [98] and the report of Kapur on $CuInSe_2$ films by nanoparticle oxide reduction and selenization with H_2 as H_2Se respectively [91]. Our idea was to form in-situ the oxide precursors that were to be converted later to sulphides.

More recently, in 2008, other authors published almost identical method for $CuInS_2$ deposition without mentioning our work [99]. The same group also reported paste-coating of $CuInS_2$ nanoparticles [100].

The principle of our method is presented in Figure II-2.1.
The substrates are coated with triethanolamine-ethanol solutions of Cu(II) and In(III) acetates and subjected to a reduction- sulfurization treatment with ethanol-saturated nitrogen and elemental sulfur.

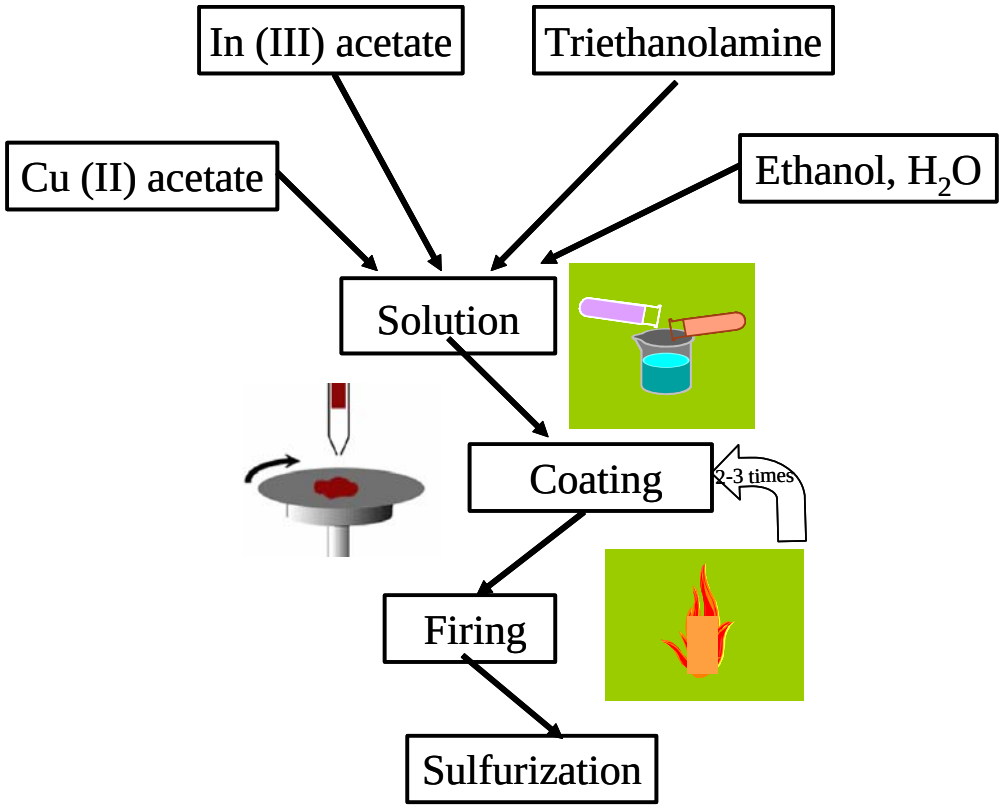

Figure II-2.1. Flow diagram of the process

Figure II-2.2. shows a scheme of the sulfurization reactor employed in the study. The use of elemental sulfur vapor is safer than the use of H_2S gas. Instead of H_2 we used ethanol-enriched nitrogen to provide reducing atmosphere.

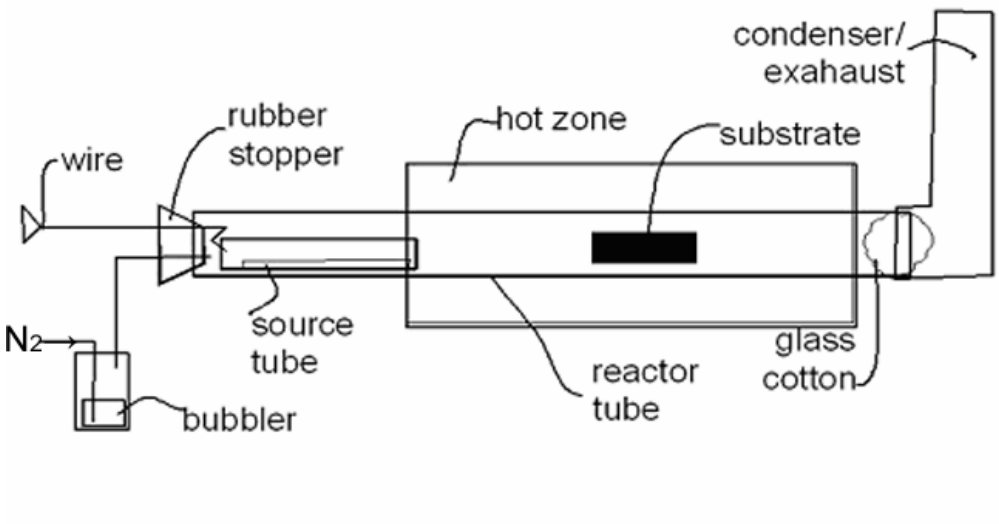

Figure II-2.2. Scheme of the sulfurization reactor employed

Previous work on soft-chemistry methods for copper-oxide film deposition reports the use of mono- and diethanolamine copper (II) acetate complexes [98]. While smaller crystal size was obtained with diethanolamine, the reasons for this were not discussed. Two possible explanations could be the better chelating ability of diethanolamine and the fact that the rate constant of the reduction of Cu(II)-amine complexes was found to increase in the order mono-, di-, triethanolamine (TEA) [101]. The authors explain this with the increasing ionicity (α^2) of the Cu-amine bond from primary to secondary to ternary amine. Hence it would be even easier to reduce the Cu^{2+} ion in a tertiary amine. Other authors also report that Cu (I) may be present in TEA complexes of this metal because some of the alcohol functions on the ligands may be oxidized, possibly to aldehyde [102]. Following this rationale, we decided to use TEA as a polydentate ligand. Furthermore, its indium (III) complex has demonstrated to be effective for the synthesis of mesoporous oxide structures [103]. This chelating agent is already widely used in industry for being cheap, abundant and environmentally tolerable [104].
In order to avoid a separate treatment and to favor the reduction reactions during the atmospheric pressure sulfurization process, we introduced ethanol vapor as a reducing agent in the N_2 carrier gas.
The whole process is carried out at atmospheric pressure without the use of toxic or inflammable gases, thus reducing the health hazards as well as the materials and equipment costs. Although we have used the spin-coating technique, any standard coating method, such as spraying, printing or dipping can be used, achieving almost complete material utilization.

II-2.2. Experimental

Reagents

All reagents used for the deposition were analytical grade: copper (II) acetate monohydrate, $Cu(CH_3COO)_2{\cdot}H_2O$, (98%, Aldrich); indium (III) acetate, $In(CH_3COO)_3$, (99.99%, Aldrich); triethanolamine (Tris-(2-hydroxyethyl)-amine) (TEA), (99%, Riedel-de Haen); ethanol, CH_3CH_2OH, (99.8%, Scharlau); sulfur, S (99.5%, J.P. Baker).

Preparation of the coating solution

Copper (II) acetate monohydrate and indium (III) acetate were dissolved into a TEA/water/ethanol solution. The Cu:In:TEA:H_2O:ethanol ratio was 1:1:5:4:26.
The mixture was first stirred for 4h at 60°C and then for 24h at room temperature. The obtained transparent deep-blue solution was used directly (samples A and B) or diluted with ethanol to deposit thinner layers (sample D).

Film deposition

Glass slides (Menzel-glaser) were used as substrates. Prior to deposition, the substrates were ultrasonically cleaned in a water-detergent solution, then washed with distilled deionized water and ethanol.
The samples were spin-coated (Chemat Technology KW-4A coater) at 2000 rpm for 1min, preceded by spin-up at 500 rpm for 2 sec. The obtained transparent films were heat-treated consecutively on two separate hot-plates. The first one was maintained at 250°C to eliminate the solvents and to initiate precursor decomposition, upon which the films turned reddish-brown. The second plate was adjusted using an infrared thermometer (Scantemp ST80XB) so that the surface of the films was maintained at 350-360°C. During the 5-minute process the samples turned transparent with a slightly brownish hue. The coating cycle was repeated 1 to 3 times for concentrated solutions (samples A1,2,3 and B1,2,3 respectively) and 8 times for the solution diluted with an equal volume of ethanol (sample D).

Sulfurization

The samples were subjected to a novel one-step reduction-sulfurization process using ethanol-saturated nitrogen gas and elemental sulfur. The reactor (Figure II-2.2) consisted of a 50 cm-long borosilicate-glass tube inserted in a tubular oven. A glass bubbler filled with ethanol was connected to the inlet pipe. The sulfur source consisted of a smaller diameter 15 cm glass tube, which position could be adjusted inside the wider tube. The outlet of the reactor was plugged with glass cotton. The hot gases which might otherwise corrode the metal parts of the oven were guided away through an exhaust tube made of aluminum foil on which most of the residual sulfur condensed. The treatments were performed under a fume hood.
In a typical experiment, the source tube was loaded with 2g of precipitated sulfur distributed along 10 cm and set at the beginning of the hot zone of the tubular oven. The samples were heated at a rate of 20°C/min up to the maximum temperature -- 450°C for samples A, 500°C for samples B and 550°C for samples C and D -- in a flow of ethanol-saturated N_2 (about 0.5 L/min). During the heating, the material at the end of the sulfur source melted, initiating slow evaporation. Five minutes after the maximum temperature was reached, the sulfur source was moved manually about 1cm at one-minute intervals for 10 minutes into the hot zone. At the end of this intense sulfurization treatment, the reactor was withdrawn from the oven, letting the sulfur source cool down for 1 minute before removing the samples from the hot zone.
In order to study the reducing effect of ethanol a 3-layered sample was subjected to identical treatment at 500°C in a clean glass tube without a sulfur source.

The sulfurization treatment conditions of the films are summarized in Table oo2. The procedure was performed only once after the deposition of all precursor layers, except for sample E, which was sulfurized a total of 3 times after the deposition of each layer.

Solar cells were fabricated completed at Hahn-Meitner-Institut-Berlin, employing their baseline process, including KCN etching, chemically deposited CdS and i-ZnO/ZnO:Al window and Ni:Al grids.

Table II-2.I. Film processing conditions and average crystal size, calculated by the Scherrer Equation.

Sample Ref.	**Number of layers**	**Sulfurization temperature (°C)**	***Average crystal size by XRD (nm)***
A1	1	450	*36*
A2	2	450	*48*
A3	3	450	*34*
B1	1	500	*39*
B2	2	500	*56*
B3	3	500	*61*
C	3	550	*33*
D	8 (diluted)	550	*61*
E	*3*	*450 (3 times)*	*68*

II-2.3) Results and discussion

X-ray diffraction

The XRD of all films pretreated in air can be assigned to an amorphous material, although a small peak in the diffraction patterns of the reddish-brown samples obtained after the first firing at 250°C could be attributed to elemental copper. This peak disappears as films turn transparent during the heat-treatment at 350°C.
These results suggest that the reduction of Cu (II) to Cu(I) is initiated in the precursor solution as already mentioned in the introduction part. The oxidation of the organic material during the heat treatment leads to the reduction of copper to elemental state at 250°C that in the next firing at 350°C generates amorphous material. The color change to transparent with a very slight brownish hue suggests that the Cu^0 is oxidized to Cu(I) [105]. Hence it can be concluded that prior to sulfurization the films are composed

mainly of Cu(I) and In(III) amorphous oxides, although the presence of small amount of Cu(II) cannot be excluded [72].

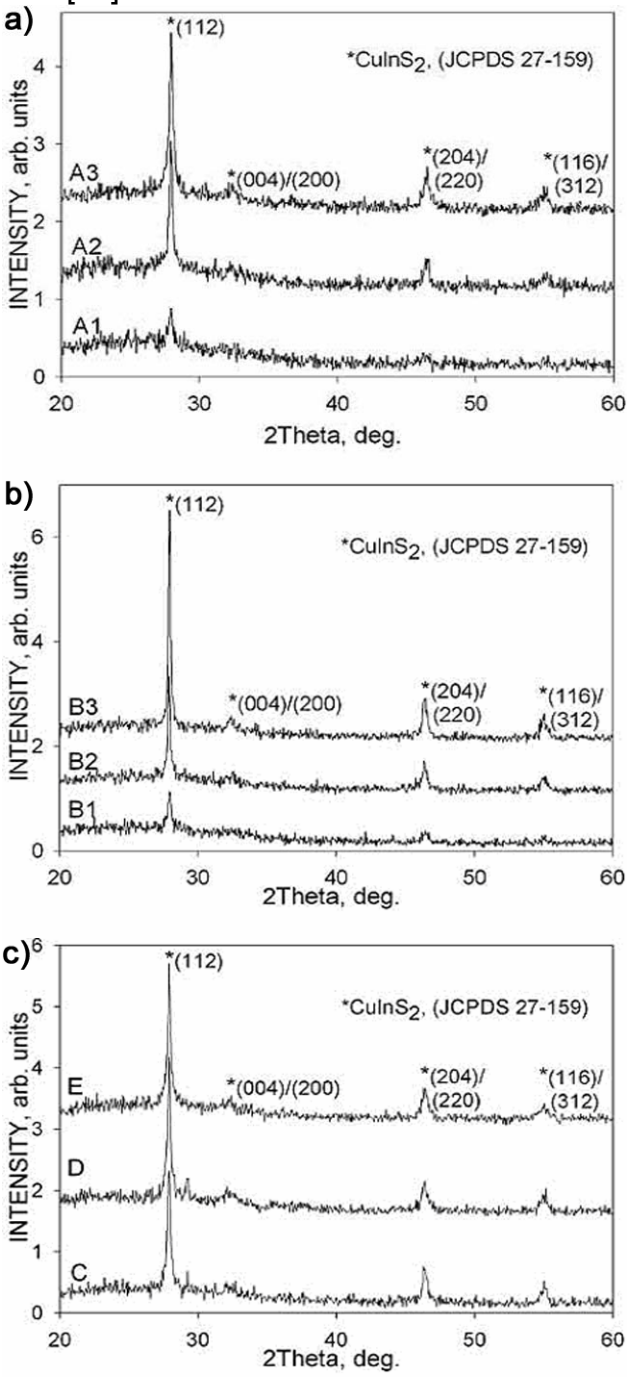

Figure II-2.3**.** XRD of films prepared at different conditions. (a) A1, A2 and A3 of 1, 2 and 3 layers respectively, sulfurized at 450ºC, (b) B1, B2, B3, of 1, 2 and 3 layers respectively, sulfurized at 500 ºC, (c) C (3-layered) and D (8-layered) – at 550 ºC and E – at 450 ºC after each coating cycle.

The reducing effect of ethanol vapor during the next sulfurization step is demonstrated by repeating the treatment process at 500°C only in a flow of ethanol-saturated N_2 with no sulfur addition. The XRD results indicate the presence of metallic copper and In_2O_3.
Thus it can be inferred that the proposed synthesis route can lead to the formation of Cu(I) through the reduction of Cu(II) complexes in solution, during the oxidation of the organic material and/or ethanol.
Figure II-2.3 (a, b and c) presents the diffractograms of thin-film samples after sulfurization under different conditions.
The diffraction data can be summarized as follows:
The diffraction peaks can be assigned to the $CuInS_2$ crystalline structure, space group I-42d, with a preferred (112)-plane orientation, according to the JCPDS 27-159 file. In the spectra of 1A and 1II-layered films, (Fig.2a and 2b, respectively), only (112) and (204)/(220) diffraction peaks are visible. For the rest of the samples, peaks at (004)/(200) and (116)/(312) are also observed.
Peak intensities increase with film thickness and with temperature increases from 450 to 500°C. Contrary to our expectations, higher treatment temperatures have a much smaller effect on the intensities of the diffraction peaks what would be expected from their improved crystallinity. This might indicate that at sulfurization temperatures as low as 450ºC the crystal quality is comparable to that of the films treated at 550ºC. On the other hand, a higher temperature reduces the full width at half maximum (FWHM) of the (112) peak, indicating a grain-size increase.
The particle size *(D)* was determined with Scherrer's equation [96] for the (112) peak. The calculated average particle sizes ranged from 36 to 68nm (Table II-2.I). It could be inferred that, apart from sample A3, the average crystal size of the thin-film samples grows with the number of layers and is also influenced by the sulfurization temperature (comparing samples A and B). The observed exception may be due to the very small fluctuations of the sulfur partial pressure in the beginning of the treatment and the multiple phase transformations occurring during this period [106]. The 8-layered sample D, prepared from a diluted solution and sulfurized at 550ºC had a larger size (61nm) than a typical 3-layered sample C treated at the same conditions (33nm), demonstrating the effect of the deposition procedure, probably causing difference in the diffusion rate of the sulfur. Maximum particle size (68nm) was obtained when each layer was sulfurized individually (sample E).
Further investigation is in progress in order to optimize the sulfurization treatment and achieve larger grain size which is preferable for photovoltaic applications.

X-ray photoelectron spectroscopy

XPS spectra of a 3-layered film sulfurized at 500ºC was taken at different sputtering depth up to about 600nm (Figure ff13). The results should be considered within the known limitations associated with depth profiling techniques using ion beam sputtering [107]. Considering the difficulty of an accurate quantitative analysis [108, 109], the data only represents the distribution behavior of the elements in the bulk of the film.

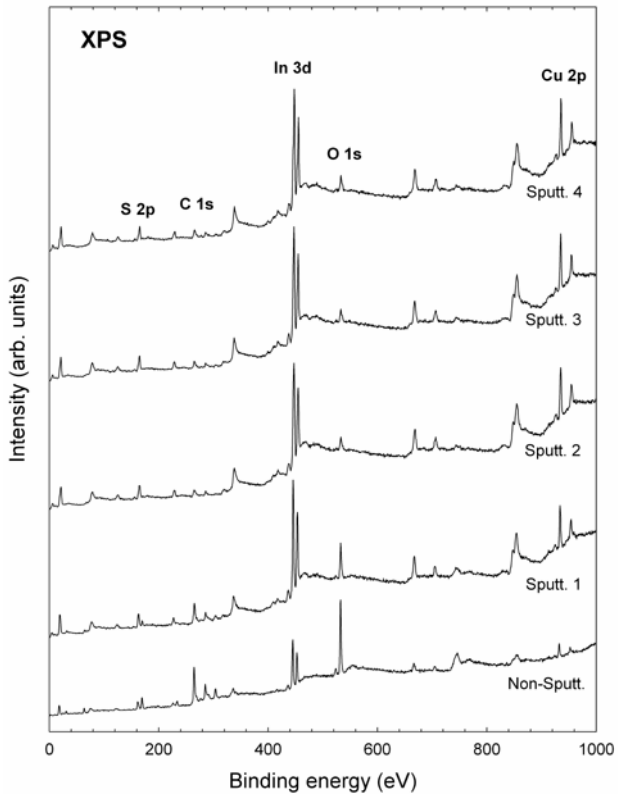

Figure II-2.4**.** XPS spectra of a 3-layered film sulfurized at 500°C up to a depth of approximately 600nm taken before sputtering and after each of the four sputtering steps.

As can be seen in Figure II-2.4, after removing the surface layers, including the area shaded by the larger grains (sputtering 2), a homogeneous distribution of the elements in the film is observed, which is almost stoichiometric according the EDX results. Copper loss from film surface was confirmed also by EDX analysis of this specific sample, and may be due to volatilization of copper sulfides during the various phase transformations accompanying sulfurization treatment, as we already commented. Low carbon and oxygen impurities on sample surface were detected which could not be avoided during the characterization [109]. The fact, that these elements are almost

absent after the second sputtering step, indicates that they are not inherent to the sample.

Scanning electron microscopy

The surface of the amorphous oxide films before sulfurization was so smooth that no defects or defined crystallites could be observed by SEM. From cross-section images which resolution was very poor because of the limits of the technique, it was estimated that the crystallite size of the oxide precursor is about 10-12nm.
Surface morphology and cross-section of the sulfurized films are shown on (Figure II-2.5 a,b). It can be observed that the films are dense and adhered to the substrate. Except for sample E (not shown), in which sulfuration process was applied after each coating cycle, no delamination upon fracturing can be detected by SEM. This, considering also the surface free of cracks and pinholes, is an indication of sufficient adherence to the substrate [72].

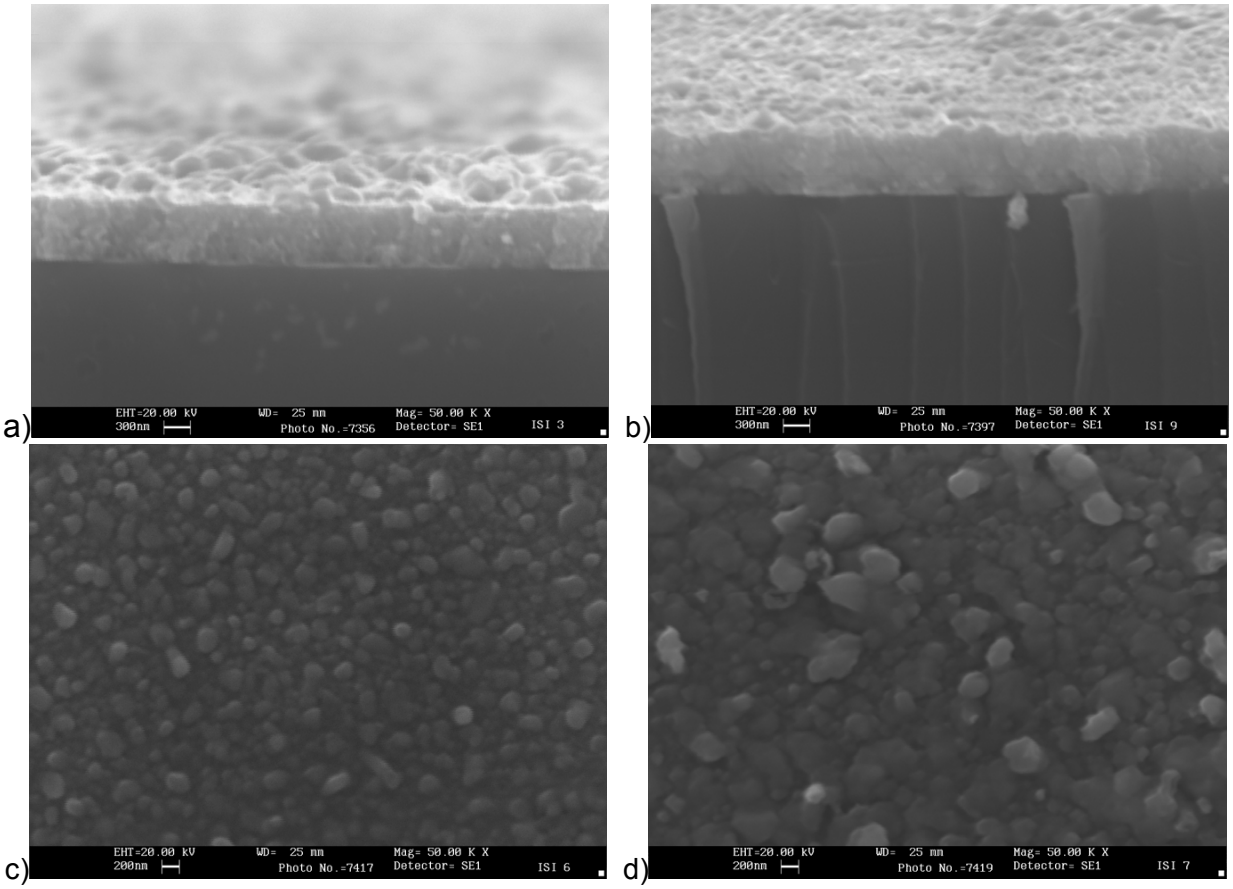

Figure II-2.5. Micrographs of the cross-sections of samples A3 (a) and D (b) and morphology of film B1 (c) and B2 (d) surfaces.

All films had a dense bottom layer and an irregular surface of embedded grains ranging from 100 to 800nm, depending on the deposition procedure and not on the sulfurization process. As can be seen, the size of these grains is about an order bigger than the average crystallite size obtained by XRD. There are two possible reasons for this: the grains are agglomerates of smaller particles or formation of larger crystals at the surface is caused by preferential consumption of sulfur vapor in the beginning of the process before it is able to diffuse in depth. When concentrated solution was employed, the grains were larger in the samples with more layers (Figure II-2.5c,d). Sample D, prepared from a diluted solution (8 layers) exhibited a smoother surface (Figure II-2.5 b). Upon rupture, the bottom layer revealed particles or agglomerates of irregular shape and size with a prevailingly vertical orientation, which might indicate partial columnar growth.

The thickness of the dense layer of each sample was determined from the micrographs of the cross-sections. Thickness of up to 300, 600 or 900 nm was achieved with a single sulfurization treatment of 1, 2 or 3-layered films respectively.

The film surface composition was determined by energy dispersive X-ray analysis (EDX). A ratio close to 1:1 of Cu to In was obtained in films, prepared at 500 ºC although high reproducibility of this ratio was obtained only in bulk (determined by EDX spot analysis of film cross section) while the surface composition in repeated experiments could show slight Cu-deficiency. Apart from the 8-layered sample D, all films, whether prepared at lower or higher temperatures had indium-rich surfaces. We attribute this copper loss to volatilization of some species during the several phase transformations which occur during the sulfurization treatment [106].The obtained results were further related to the optical band gap of the samples (figure 7).

As already mentioned, further investigation is in progress in order to optimize sulfurization treatment and achieve both larger grain size and better control on surface composition.

Optical properties

Figure 5 displays the room-temperature transmission spectra for all obtained thin-films. The data were recorded in the wavelength range of 400 to1100 nm.

From these graphs it can be concluded, that even in one-layered films (A1 and B1), a significant part of the visible spectrum is absorbed (Figure II-2.6). Film C, having 3 layers, shows a higher absorption than film D, which is of similar thickness but was obtained from a diluted solution and 8 coating cycles. The optical transmission of typical 3-layered films was less than 5% in the visible spectrum, sufficiently low for photovoltaic applications.

The optical band gaps of the films were determined using the transmission data together with film thickness determined by SEM. $(\alpha E)^2$ was plotted against E, where α is the absorption coefficient and E is the corresponding photon energy $h\nu$, as seen in Figure II-2.7.

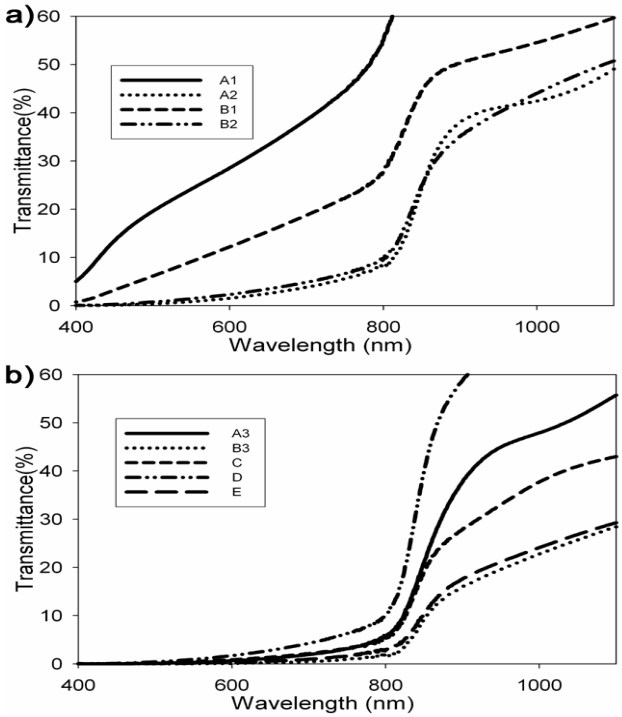

Figure II-2.6**.** Optical transmittance spectra of (a) 1 and 2-layered films; (b) 3-layered films.

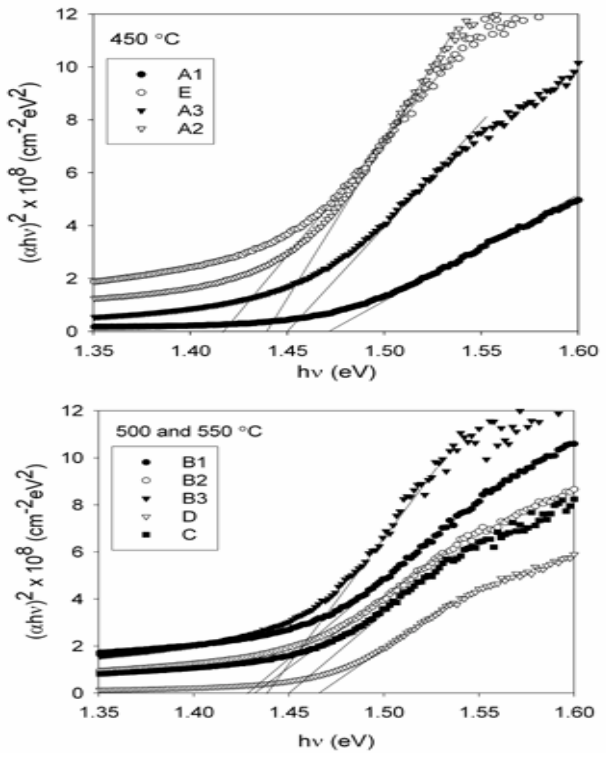

Figure II-2.7. Plot of $(\alpha E)^2$ vs. *E:* (a) Samples sulfurized at 450°C; (b) Samples sulfurized at 500 and 550°C.

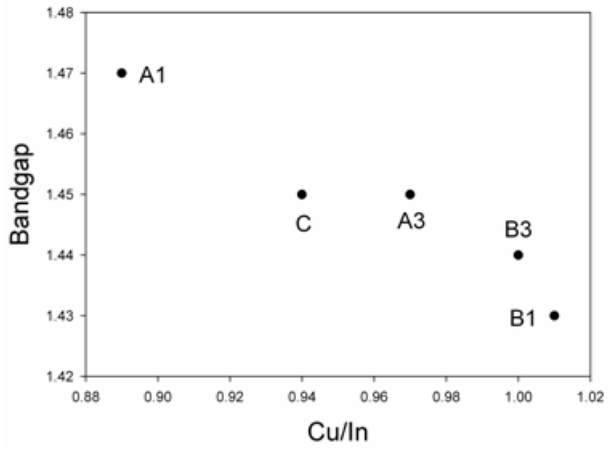

Figure II-2.8**.** Relationship between film surface composition and optical bandgap.

The obtained values range from 1.42 to 1.47eV, being slightly lower than those of monocrystalline $CuInS_2$ (~1.53eV) but adequate for photovoltaic applications and comparable to those obtained by other deposition methods [110]. Although a study of intentionally varied Cu/In ratio is given in the next chapter, here on the properties of the films will be published elsewhere, the limited copper loss during the sulfurization treatment can be related to the optical bandgap value. This is represented in Fig. II-2.8,

in which the Cu/In ratio decrease leads to a bandgap increase. This trend has already been reported by other authors [111]. It can be summarized that the bandgap values increase when the particle size and the Cu/In ratio decreases. As observed in other semiconductor systems, the optical absorption blue-shift is associated with quantum confinement effects [112,113].

Device results

Preliminary tests of our films in complete photovoltaic devices were carried out at Hahn-Meitner Institute.

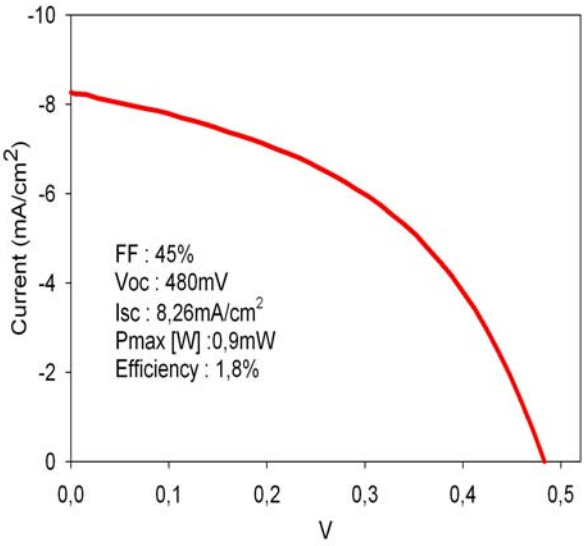

Figure II-2.9. J-V of a device with $CuInS_2$ absorber prepared by route II-3

Our first successful device employed route similar to B-3 (Figure II-2.9). While the open circuit voltage was relatively good, the fill factor and short circuit current were low. This was attributed to the small grain size of the material.

II-2.4. Conclusions

- Single-phase compact $CuInS_2$ films have been deposited successfully at atmospheric pressure by coating a precursor layer from solution and subjecting it to a novel reduction-sulfurization technique.

- Films with high optical absorption and a bandgap adequate for photovoltaic applications were prepared by using this simple and inexpensive equipment.

- No toxic or inflammable gases were used.

- Further treatment and precursor composition optimization is required in order to increase grain size

The next section describes three approaches used for improving crystalline quality.

II-3) STUDY OF DIFFERENT ROUTES TO INCREASE GRAIN SIZE OF OUR $CuInS_2$

II-3.1) Introduction

In the previous section II-2, we developed a method for deposition of compact $CuInS_2$ films from triethanolamine complexes of Cu(II) and In(III). Single-phase, chemically pure and optically adequate coatings were obtained, although the grain size remained too small for photovoltaic applications.

In this section we describe the study of several process modifications which lead to improved crystalline quality:

-Variation of solution composition
Different ammines used to complex precursor metals. Based on other reports of CuOx films which used diethanolamine and monoethanolamine, [98] we expected difference in grain size of the resultant films when substituting triethanolamine with diethanolamine and ethanolamine.

-Variation of Cu/In ratio.
As described in the introduction, one of the biggest technological advantages of $CuInS_2$ in comparison with CIGS is the possibility to grow Cu-rich materials which result in increased grain sized and high-efficiency devices [114,115]. The effect of copper excess is explained by the formation of Cu_xS phases with low melting point which facilitate excellent media for large crystal growth. Another inherent advantage of the process is that at the end, the Cu-rich phase is segregated on the top and is easily etched chemically (KCN treatment).

-Variation of thermal treatment
Another well-known approach used for the fabrication of device-quality $CuInS_2$ is the so-called Rapid Thermal Treatment (RTP) [114]. The advantage of RTP is a very quick temperature increase (in the order of 500ºC/min) which allows reaching favorable high-temperature reaction conditions without allowing intermediate reactions and undesirable phase formations during the ramp-up.

-Variation of sulfur concentration
Being the major factor for oxide conversion to sulfide, sulfur amount in the reactor was varied in order to study its effect.

In the course of the study it was found that the last three of the above parameters were the most important for obtaining materials with improved quality. At the same time, the type of ammine affected the intermediate amorphous oxide morphology and had little effect on the final chalcopyrite film.

II-3.2) Experimental

Sample preparation

The reagents were identical to the indicated in the previous section, except for the monoethanolamine and diethanolamine:
copper (II) acetate monohydrate, $Cu(CH_3COO)_2xH2O$, (98%, Aldrich); indium (III) acetate, $In(CH_3COO)_3$, (99.99%, Aldrich); mono-, di- and triethanolamine (MEA, DEA and TEA), (Riedel-de Haen); ethanol, (99.8%, Scharlau); sulfur, S (99.5%, J.P. Baker).

Copper (II) acetate monohydrate and indium (III) acetate were dissolved into the amine/alcohol/water solution. In the case of MEA and DEA water proved to decrease stability and was omitted. The In:amine ratio was kept 1:5 while the Cu/In was varied in the range 0.9-1.8. The samples were spin-coated (Chemat Technology KW-4A coater) on glass slides (Menzel-glaser) at 2000 rpm for 1min and heat-treated in air at 250 and 350°C for 5 min. The oxide precursor films were sulfurized at 500 or 550°C at atmospheric pressure with elemental sulfur vapor and N_2 carrier gas, with or without the addition of ethanol as a reducing agent. Typical sulfur concentration in the treatment gas was achieved as described in previous sections, adjusting the position of a source tube within the reactor tube. The influence of higher sulfur concentration (especially during the heating ramp) was studied by introducing 1g of sulfur directly into the reactor tube. Three different heating regimes were used: 20 °C /min, 50 °C /min and direct insertion in preheated oven. Yet another treatment employed was a 3-ramp process – 10, 15 and 20 min ramps at 400, 530 and 550ºC respectively. In order to avoid a separate treatment and to favor the reduction reactions during the atmospheric pressure sulfurization process, our original method employed ethanol vapor as a reducing agent in the N_2 carrier gas. In the present work, we carried out parallel treatments without ethanol addition.

The exact preparation conditions of each sample are specified in Table II-3.I. within the XRD section, together with results on grain size and optical properties.

Characterization of the films

Differential thermal analysis/Thermogravimetry of precursor solutions was carried out in with Mettler-Toledo using platinum crucible air flux and heating rate of 5ºC/min. Before the analysis, the solutions were let to dry in the air at room temperature for 1 h.

Film morphology and composition were determined by Scanning Electron Microscopy (SEM) using a scanning electron microscope (Leica Leo 440) equipped with a spectrometer for energy dispersive X-ray microanalysis(EDX) using the following operating parameters: acceleration voltage 20 kV, measuring time 100s, working distance 25 mm, counting rate 1.2 kcps. The samples for microstructure and microanalysis determination were introduced using an aluminum holder with graphite adhesive tape. The thickness of the films was estimated from micrographs of film cross sections.

The optical transmission of the films was measured with a Cary 500 Scan UV-Vis-NIR spectrophotometer. The data were registered from 400 to 1100 nm with uncoated glass as a reference.

Raman measurements were performed in backscattering configuration in a DILOR XY spectrometer with a liquid-nitrogen-cooled CCD detector and excitation through a X50 microscope objective lens, using the 514.5 nm line of an Ar^+ laser and a spectral resolution of about 2.5 cm^{-1}. Power at the sample was kept lower than 3 mW.

Table II-3.I. Preparation conditions, average crystal sizes, calculated by Scherrer's equation, and optical bandgap, determined from transmission spectra.

Sample	**Cu/In ratio**	**Complexing agent**	**Treatment conditions**			**Size (nm)**	***Optical Bandgap (eV)***
			Tmax °C	**Ramp °C**/min	**Sulfur**		
A500	1.8	TEA	500	20	Normal	86	*1.37*
B500	1.5	TEA	500	20	Normal	61	*1.38*
C500	1.2	TEA	500	20	Normal	65	*1.43*
D500	1	TEA	500	20	Normal	55	*1.43*
E500	0.9	TEA	500	20	Normal	45	*1.45*
A550	1.8	TEA	550	20	Normal	56	*1.36*
B550	1.5	TEA	550	20	Normal	50	*1.38*
C550	1.2	TEA	550	20	Normal	53	*1.39*
D550	1	TEA	550	20	Normal	56	*1.44*
E550	0.9	TEA	550	20	Normal	42	*1.45*
MC50	1.2	MEA	500	20	Normal	58	*1.45*
MD50	1	MEA	500	20	Normal	45	*1.42*
DC50	1.2	DEA	500	20	Normal	44	*1.46*
DD50	1	DEA	500	20	Normal	46	*1.45*
T2E	1.5	DEA	550	50	High	114	*1.48*
204D	1.5	DEA	550	direct	High	184	-
3STD	*1.5*	*DEA*	*550*	*3-stage*	*High*	*164*	-

II-3.3) Results and discussion

Thermal differential analysis/Thermogravimetry (DTA/TG)

DTA/TG showed mass reduction down to about 20% of the precursor mass, previously dried in ambient conditions for solvent removal. Steep decrease of the mass was observed below 250°C and is associated with the elimination of unbound amines and other species, the remaining material with respect of the original mass being 43% for MEA, 54% for DEA and 64% for TEA. The relative mass difference at this point with respect to the final 20% can be related to the mass of the complexion agents used (MEA<DEA<TEA). This could indicate that the metal complexes stable at this temperature are formed by similar ratio of amine to metal valence bonds, roughly estimated as 1. Complete combustion was observed upon reaching 440°C (MEA), 460°C (DEA) or 480°C (TEA), the first exothermal peaks starting to ascend at about 350°C.

It is arguable if this bulk analysis is valid for thin layers which specific reactive area is several orders of magnitude higher, i.e. it is possible that complete combustion is achieved at lower temperatures. On the other hand, the molybdenum substrates, commonly used for chalcopyrite solar cells, may oxidize at high temperatures. This is why we used a maximum air pretreatment temperature of 350°C. In the previous section XPS analysis indicated that no carbon contamination was found in the sulfurized film.

X-ray diffraction

The XRD patterns of all films pretreated in air at 250 and 350°C can be assigned to amorphous material. The predominant phase in all sulfurized samples (Figure II-3.1) is $CuInS_2$, space group I-42d with a preferred (112)-plane orientation according to JCPDS 27-159 file. We could not establish relationship between phase formation and the presence or absence of ethanol vapor in the treatment gas, which reducing effect was observed in a previous section. An increase in main-peak height was observed with higher Cu/In ratios.

Contrary to our expectations, the higher sulfurization temperature of 550°C did not improve crystal quality as the peak intensities in these samples are lower than those of samples treated at 500°C. This effect could be related to the intermediate formation of different phases such as In_2S_3 which has been reported to be the cause of poor film quality obtained by sulfurization of metal layers at 600°C [116]. It should be noted that such results are in discrepancy with state of art treatment procedures, which obtain best

film quality at about 550ºC [117]. Nevertheless, these methods use high heating rates and sulfur-rich atmosphere.

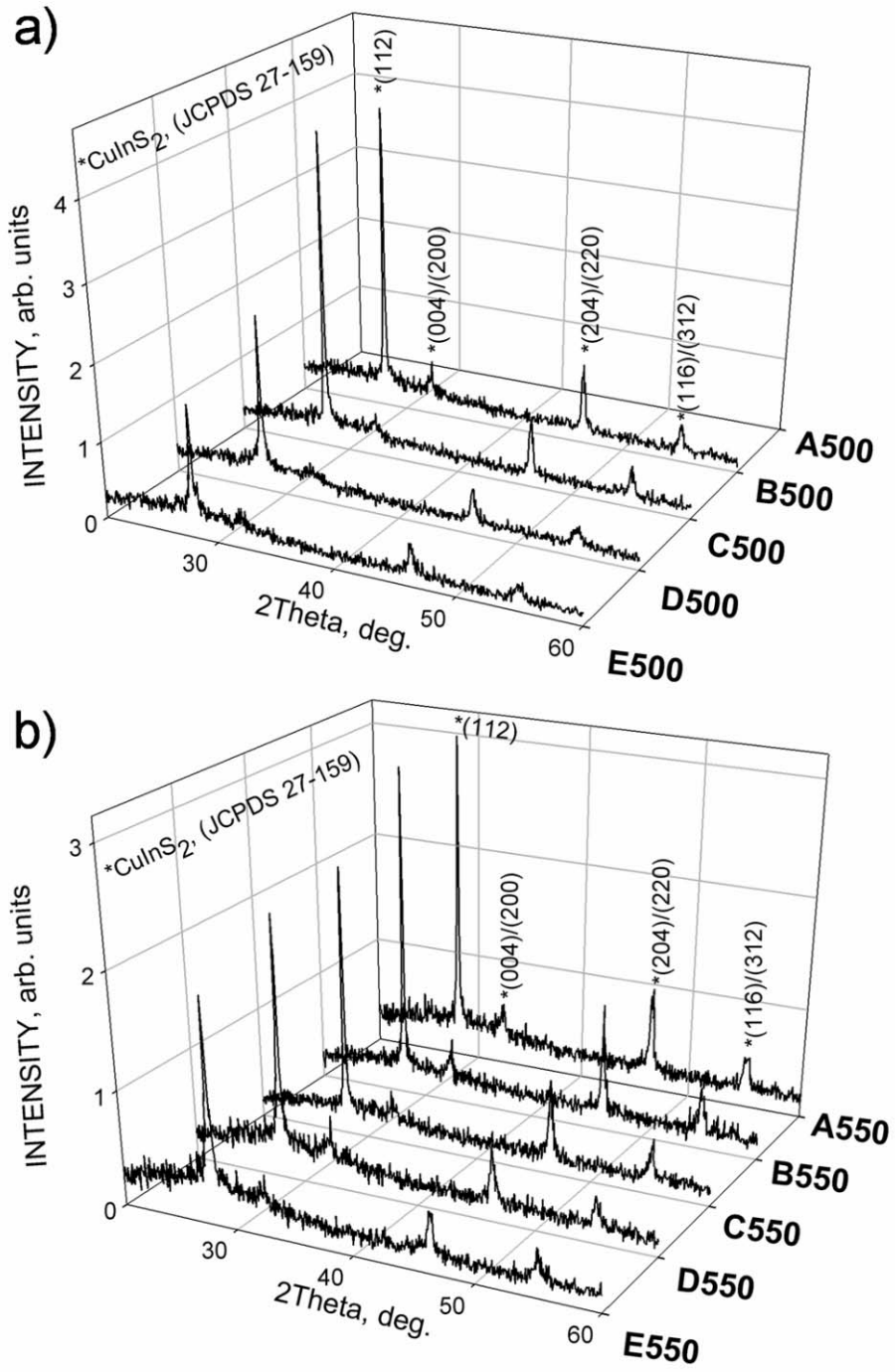

Figure II-3.1. XRD patterns of films with different Cu/In ratios treated at 500 and 550ºC.

When we investigated the influence of the heating ramp and sulfur excess, especially during the ramp-up, the results were consistent with these reports [117]. Larger crystalline size (determined by Scherrer's equation for the (112) peak), was obtained with higher heating rates, sulfur-rich atmosphere and Cu-excess (Samples T2E and 204D, Table II-3.I). Neither of these factors alone could yield significant crystallite size increase, but all three had to be present together. At the same time the different complexing agents and solvents played secondary role, TEA (sample C500) yielding slightly larger crystallites than DEA and MEA (DC50 and MC50).

The 3-ramp thermal process was introduced after observing by EDX small copper loss in samples B. As we were unable to find information in literature on volatilization of copper sulfides, we suspected the formation of some volatile specie in the presence of ethanol vapor. The purpose of each ramp was as follows: 400ºC-completion of the sulfurization process; 530ºC-intermediate crystal growth at lower volatilization rate; 550ºC-final crystal growth. A significant increase in crystal size (164nm, sample **3STD**) was observed. Nevertheless, the largest crystal size obtained in this work (184nm, sample 204**D**) was produced at higher heating rates by direct insertion of the reactor in the tubular oven preheated at 550ºC. We expect that the use of Rapid Thermal Annealing equipment, permitting even higher heating rates will lead to further increase in grain size [86].

Scanning electron microscopy

Air-pretreatment

Films using different complexing agents preannealed in air, before sulfurization showed difference in morphology. Smallest particle size (less than 20 nm) is achieved with TEA (Fig2-a), in good agreement with our preliminary assumptions. Similarly to reported studies of spin-coated copper oxide films using MEA and DEA copper(II) acetate complexes [98] , in our case MEA yielded larger grain sized Cu-In-O films than DEA (Fig 2-b,c). Some possible explanations for the grain size difference could be the better chelating ability of diethanolamine and the fact that the rate constant of the reduction of Cu(II)-amine complexes was found to increase in the order mono- < di- < triethanolamine (TEA) [101]. The authors explain this with the increasing ionicity (α^2) of the Cu-amine bond from primary to secondary to ternary amine. Hence it would be even easier to reduce the Cu^{2+} ion in a tertiary amine. Other authors report that Cu(I) may be present in TEA complexes of this metal because some of the alcohol functions on the ligands may be oxidized, possibly to aldehyde [102]. Another issue to be taken into account is the "anomalous basicity" that some amines exhibit, i.e. although their basicity

measured in gas phase increases in the order NH_3<RNH_2<R_2NH<R_3N, this order is reversed in solution. The authors [119] explain this effect by the decreasing energy of solvation of the conjugated ammonium ion related to electronic (inductive) effects, that in our case would result in a decreasing basicity: MEA>diethanolamine (DEA)>TEA. This may be the reason for enhanced hydrolysis leading to larger particles in the case of DEA and especially MEA with the presence of some interlayer voids, as observed in the SEM images.

Sulfurized samples

Most sulfurized samples were void free and had a dense bottom layer and larger crystals on the top, especially in the case of Cu-rich samples. The size of these crystals was larger in samples with higher Cu-content and their composition was Cu_2S, as determined by EDX spot-analysis. Whiskers and rod-like formations of the same composition were also found in highly Cu-rich samples. Analysis of film cross section indicated increased copper concentration near the surface, a typical phenomenon in Cu-rich films.

As seen in Fig. 2 (d) and (e), at a heating rate of 20°C/min, copper excess did not lead to the formation of large crystallites. Voids observed in the preannealed MEA films were present in a higher extent in the sulfurized films.

In all other cases, the difference in morphology found in the pre-annealed oxides prepared with different complexing agents was not found to influence significantly the aspect of the sulfurized films.

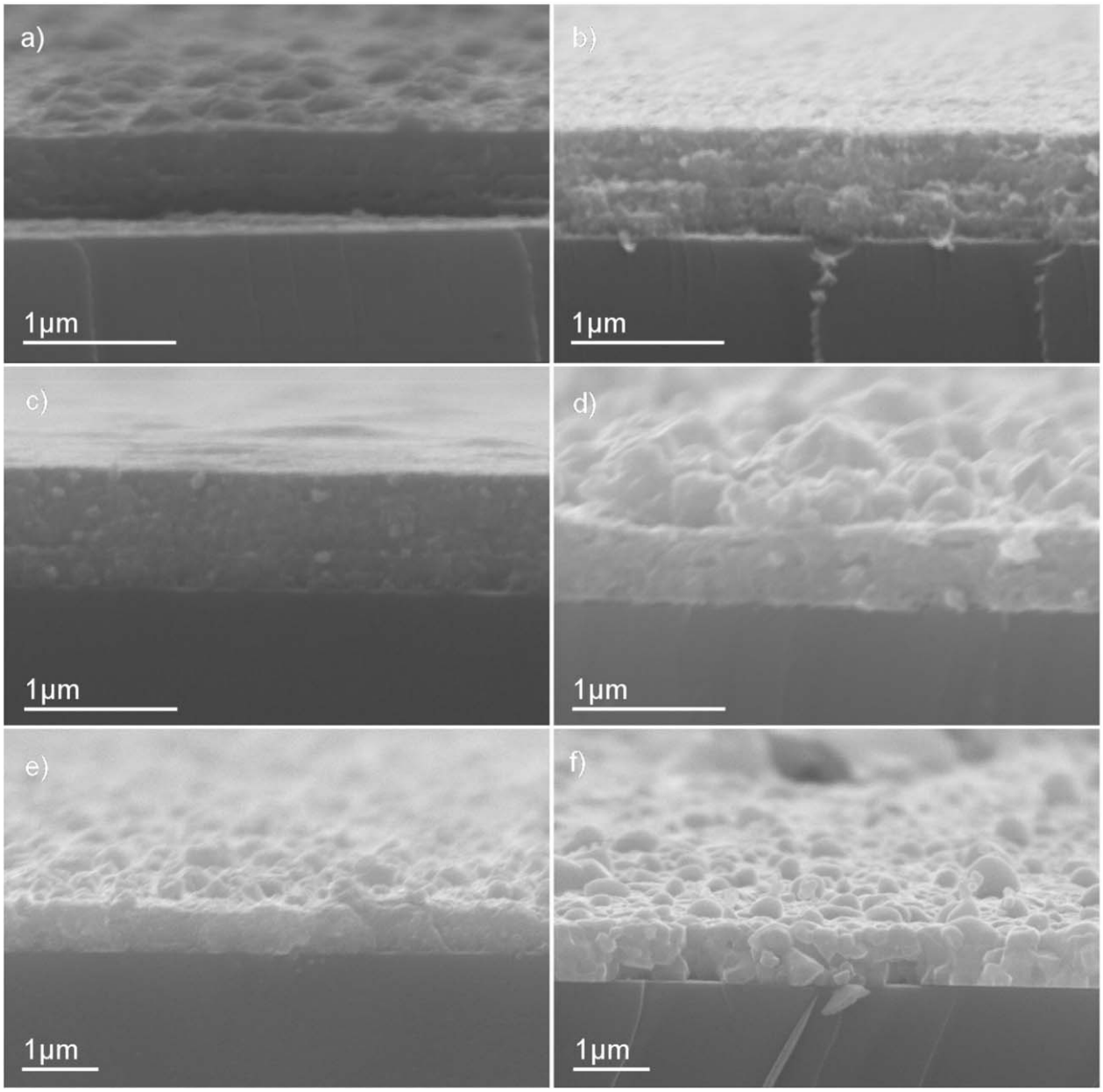

Figure II-3.2. Micrographs of oxide precursor samples, using MEA(a), DEA(b), TEA(c), copper-rich samples with MEA(d) and DEA(e) sulfurized at 20 °C/min and a DEA sample, sulfurized at 50°C/min (f).

In agreement with the results of XRD measurements, higher heating rates lead to improved morphology with large densely packed crystallites (Fig. II-3.2f).

Three-stage process yielded surface morphology different from the rest of the treatments (Figure II-3.3). Platelet –like formations were probably due to undesirable intermediate phases that were formed at lower temperature during the different ramps.

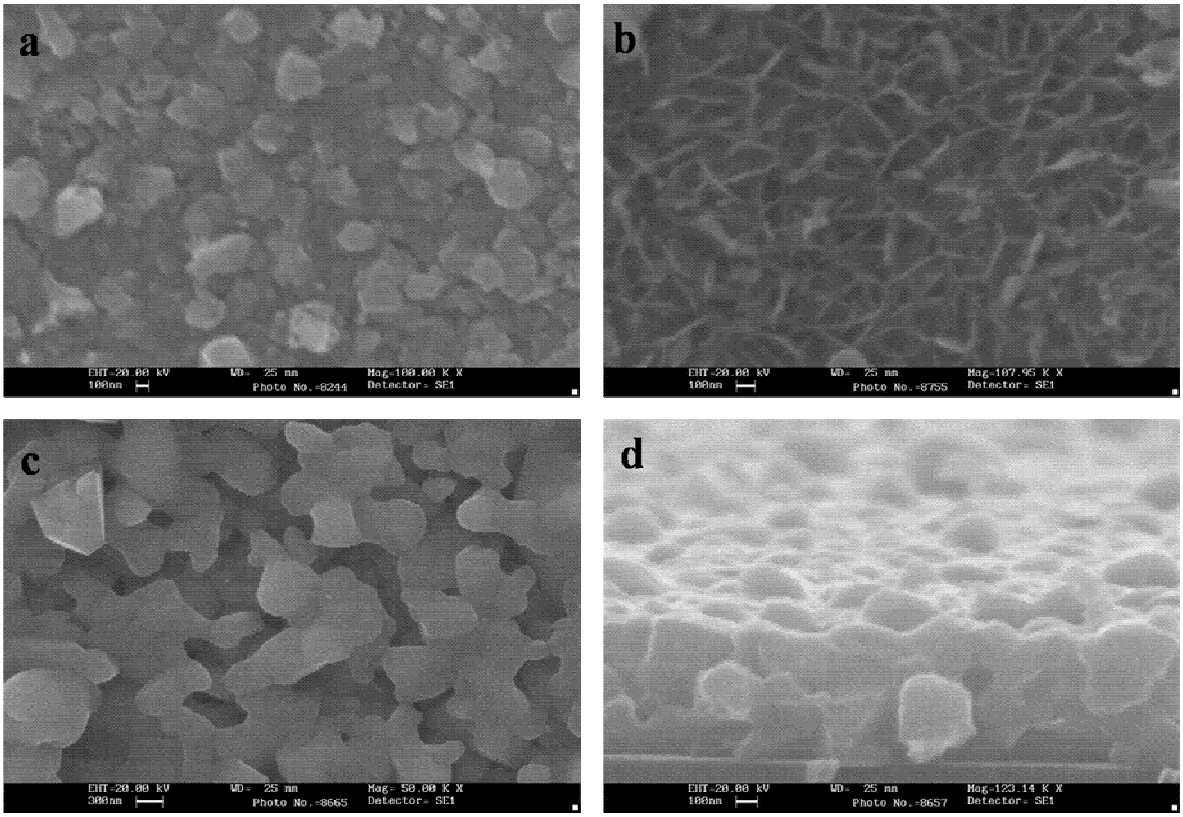

Figure II-3.3. Micrographs of films pretreated at different heating rates: 20K/min (a), 3-ramp process (b), 50K/min (c), (d).

Raman measurements

As discussed in the Introduction, Raman scattering is widely used for the detection of Cu-Au ordering with the same tetrahedral anionic sublattice as chalcopyrite but different Cu / In cation ordering. The presence of Cu-Au in the film is correlated with worsening of the structural features, i.e. decrease of grain size and increase in density of extended defects in grain [48, 49]. Although the C-Au initially forms as the dominating ordering independently from stoichiometry and doping of the starting precursors, its transformation into the chalcopyrite one is, in contrast, strongly dependent on the precursor composition (favoured by high Cu/In ratio) and requires high temperatures.

Two samples were selected to study the influence of treatment temperature: C500 and C550, (Cu/In=1.2, treated at 20ºC/min up to 500 and 550ºC respectively). The third sample, T2E, showed best morphology by SEM as well as large grain size by XRD (Cu/In=1.5, heated at 50ºC/min).

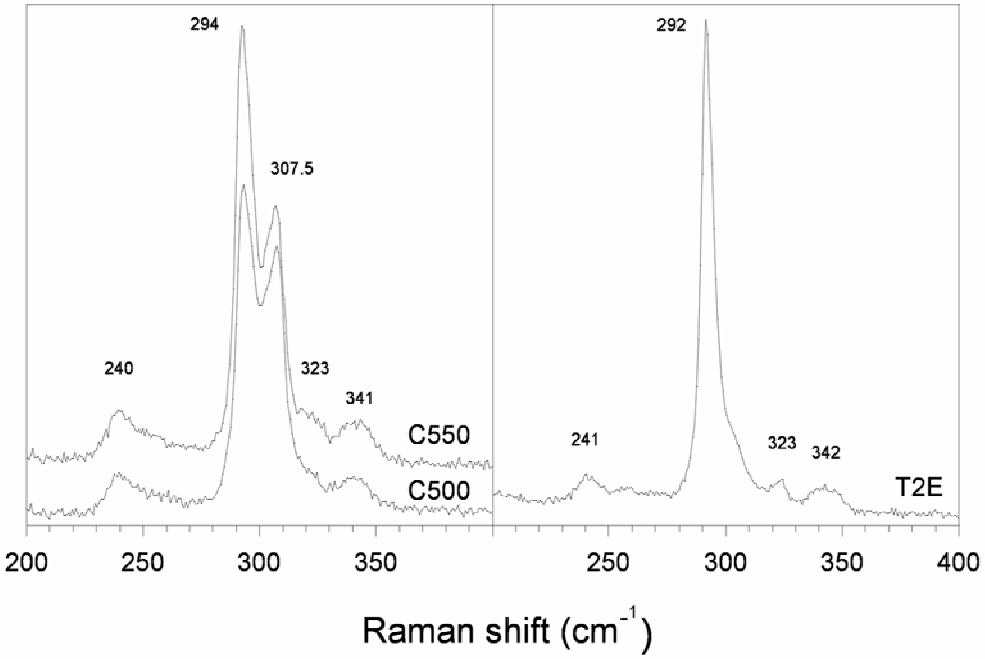

Figure II-3.4. Raman spectra of samples treated at different temperatures (C500 and C550) and higher heating rate (T2E).

Figure II-3.4 presents Raman spectra of these samples in the region 200-400 cm^{-1}. A peak at $\approx$ 307.5 cm^{-1} indicating CA ordering is seen in C500 and C550 samples with intensity comparable to that of the CH phase. However, the Raman spectrum of the T2E film shows almost exclusively the A_1 peak of CH phase at 292 cm^{-1}, [48, 49] together with other peaks belonging also to CH phase. Only a shoulder at $\approx$ 304 cm^{-1} is detected in the region of the A_1 mode of the Cu-Au phase. The almost complete disappearance of the Cu-Au phase in sample T2E is consistent with the improved crystallite size of the sample observed by X-ray diffraction and the optical properties discussed bellow. It can be expected that further treatment optimization will lead to complete elimination of the Cu-Au phase.

Optical properties

All samples prepared in this work had low transmission in the visible range, typically below 3% (Figure II-3.5 a) which is satisfactory for a photovoltaic absorber.

The optical band gaps of the films were determined by use of the transmission data together with film thickness determined by SEM by plotting $(\alpha E)^2$ vs. E, where α is the absorption coefficient and E is the corresponding photon energy $h\nu$ (Figure II-3.5 b). All measured values (Table 1 within the XRD section) exhibited values between 1.39 and 1.48eV that are comparable to those obtained by other deposition methods, and are close to the optimal for photovoltaic energy conversion. Lower heating rates yielded lower optical band gaps (1.39-1.46eV at 20ºC/min, in comparison with 1.48eV at 50ºC/min, sample T2E).

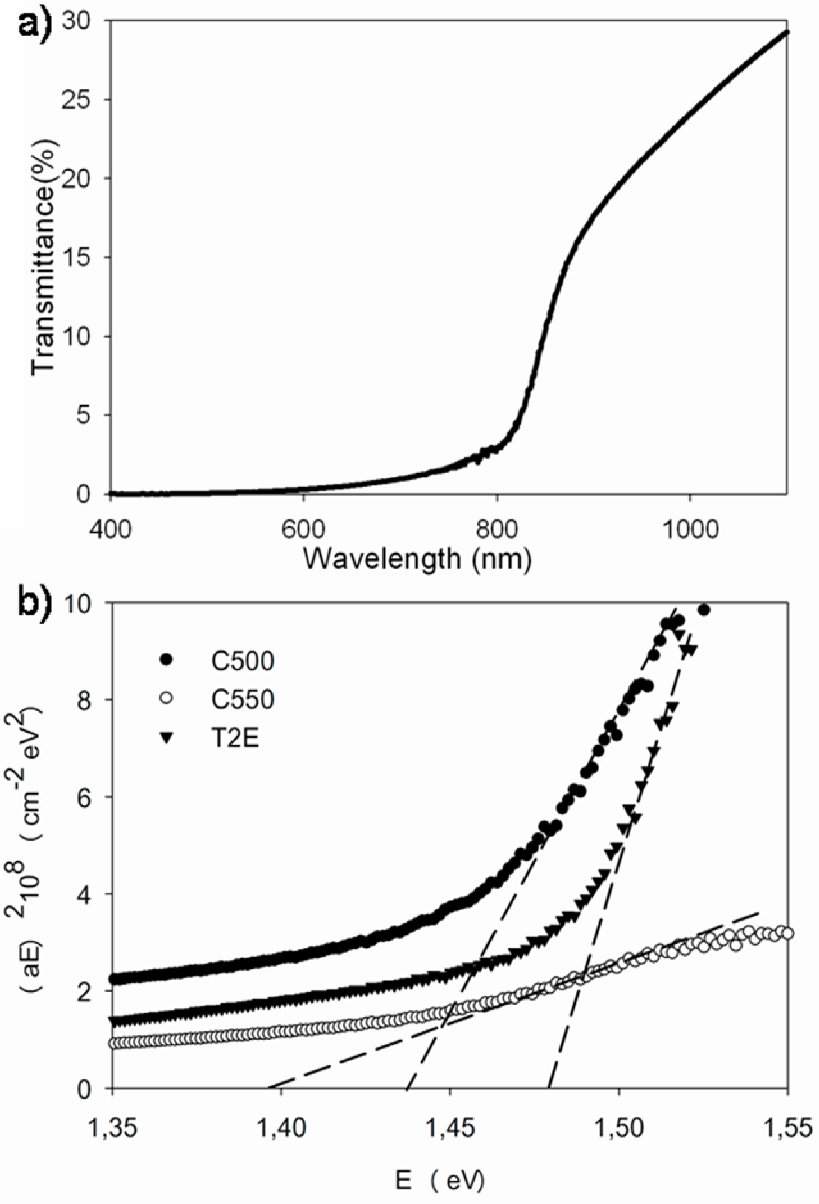

Figure II-3.5. Typical optical transmission spectra (a) and a plot of $(\alpha E)^2$ vs. E of samples C500, C550 and T2E (b).

The plots of samples C500, C550 and T2E, studied also by Raman spectroscopy (Figure II-3.5 b) show clear inverse dependence between the content of Cu-Au ordering and the value of the optical bandgap. The fact that some record performance devices were fabricated from devices with $CuInS_2$ bandgap 1.5eV or above [61] could be related to better material quality. The closest value obtained in this work (1.48eV) belonged to sample T2E which also had lowest content of Cu-Au phase and best morphology.

II-3.4) Conclusions

- Different deposition and treatment parameters of an atmospheric pressure $CuInS_2$ film deposition method were studied.

- Different oxide precursor layers were obtained by varying the complexing agents (MEA, DEA and TEA) with smallest particle size obtained in the case of TEA and largest in the case of MEA.

- The type of oxide precursor had little effect on the sulfurized film.

- Largest crystallite size, lowest content of secondary Cu-Au phases and bandgap closest to state-of-art devices was achieved with high heating rates, sulfur-rich atmosphere and Cu-excess.

B.4) DEPOSITION OF HIGHLY ORIENTED $CuInS_2$ BY NANOPASTE PRINTING

II-4.1) Introduction

Considering the possibility to deposit in one step the desired layer by a simple and scalable technique we developed a printing route to $CuInS_2$. Nanoparticle suspensions were deposited by doctor-blade technique, similarly to TiO_2.

We chose to use binary nanoparticles as precursor, prepared by a non-aqueous route. The aqueous precursor synthesis route chosen by others [88] lead to oxide contamination and in both cases difficulties in layer densification were encountered.

In order to minimize contamination with oxide and hydroxide species we developed a non-aqueous synthesis route for the binary precursor materials. Metal salts were reacted directly with elemental sulfur or tiourea in ethyleneglycol to obtain homogeneous and dispersible nanoparticles.

II-4.2) Experimental

Synthesis of In_2S_3 nanoparticles

In a set of preliminary experiments we found that ethyleneglycol is a suitable solvent of sulfur at high temperature.
To 1.5 mmol indium acetate and 75 g of Ethyleneglycol in a round-bottom flask, 2 g of TEA were added as a complexing agent to facilitate dissolution. The flask was placed at an oil bath and the mixture was stirred at 140ºC until dissolution. 2.25mmol elemental sulfur were added and the temperature was maintained at 170ºC for 90 min.
The precipitate was separated by centrifugation and washed with ethanol.

Synthesis of CuS nanoparticles

Identical procedure as the one used for In_2S_3 yielded very large crystals, as determined by SEM. In this case we chose a lower temperature route using thiourea as a sulfur precursor because elemental sulfur would not dissolve bellow 100ºC.

In a round-bottom flask, 2mmol copper acetate was dissolved in 75 ml ethyleneglycol at room temperature. 2.5mmol thiourea were added and the flask was immersed in an oil bath at 80ºC for 90 min.
The precipitate was separated by centrifugation and washed with ethanol.

Printing pastes

First, binary suspensions in ethyleneglycol were formed with solid contents:
A-In: In_2S_3 – 7% and
II-Cu: CuS – 11%
Different blends of these pastes were used for printing. A baseline composition (ref.1289) included: A-In: 0.160 g, II-Cu: 0.052 and ethyleneglycol: 0.525 g. Composition close to stoichiometric, although slightly cu-rich (Cu/In=1.1) was found by EDX. For the rest of the samples Cu-rich blends were used (between 40 and 50% more II-Cu in comparison with 1289).

The films were printed by the doctor-blade technique, dried on a hot plate at 100ºC and sulfurized in a tubular oven at 550 for 10 min in the presence of elemental sulfur vapor as described in section II-2.

II-4.3) Results

Homogenous, generally crack-free films were obtained without the addition of binders.

X-ray diffraction

Precursor powders and films were amorphous while the thermally treated samples were highly crystalline. Figure II-4.1a shows the diffraction patterns of sample 1289 with near stoichiometric ratio. The symmetric mode indicated highly oriented (112) film. The minor presence of non-oriented crystals was localized at the surface, as indicated a grazing-incidence (theta=2º) pattern.

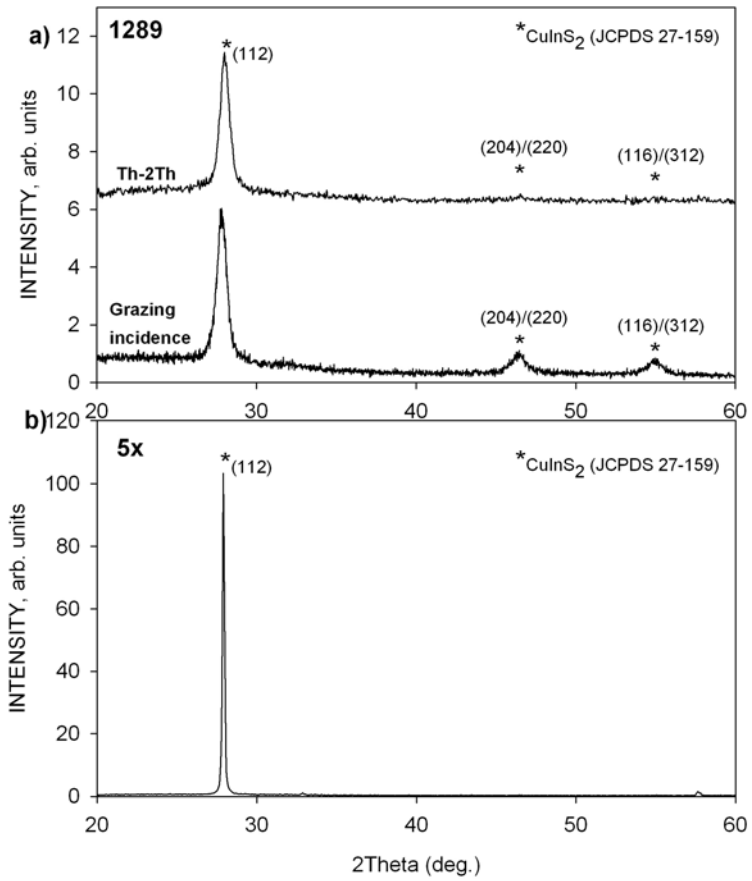

Figure II-4.1. X-ray diffraction patterns of close-to-stoichiometric sample 1289 and the Cu-rich 5x with intensity one order of magnitude higher.

Crystalline size determined by the Scherrer equation indicated that the average size of sample 1289 is 12nm, while the Cu-rich samples had average size in the range of 90-150nm. As shown in Figure II-4.1b, the peak in this case is an order of magnitude higher than in the near-stoichiometric composition case 1289. This effect can be attributed to the beneficial effect of excess Cu_xS phases during growth, as already discussed in the previous sections.

Scanning electron microscopy

Figure II-4.2 shows surface images of a Cu-rich sample. At high magnification the surface is smooth although at low magnification, domains of about 20 micrometer size can be distinguished, resembling separate crystallizations.

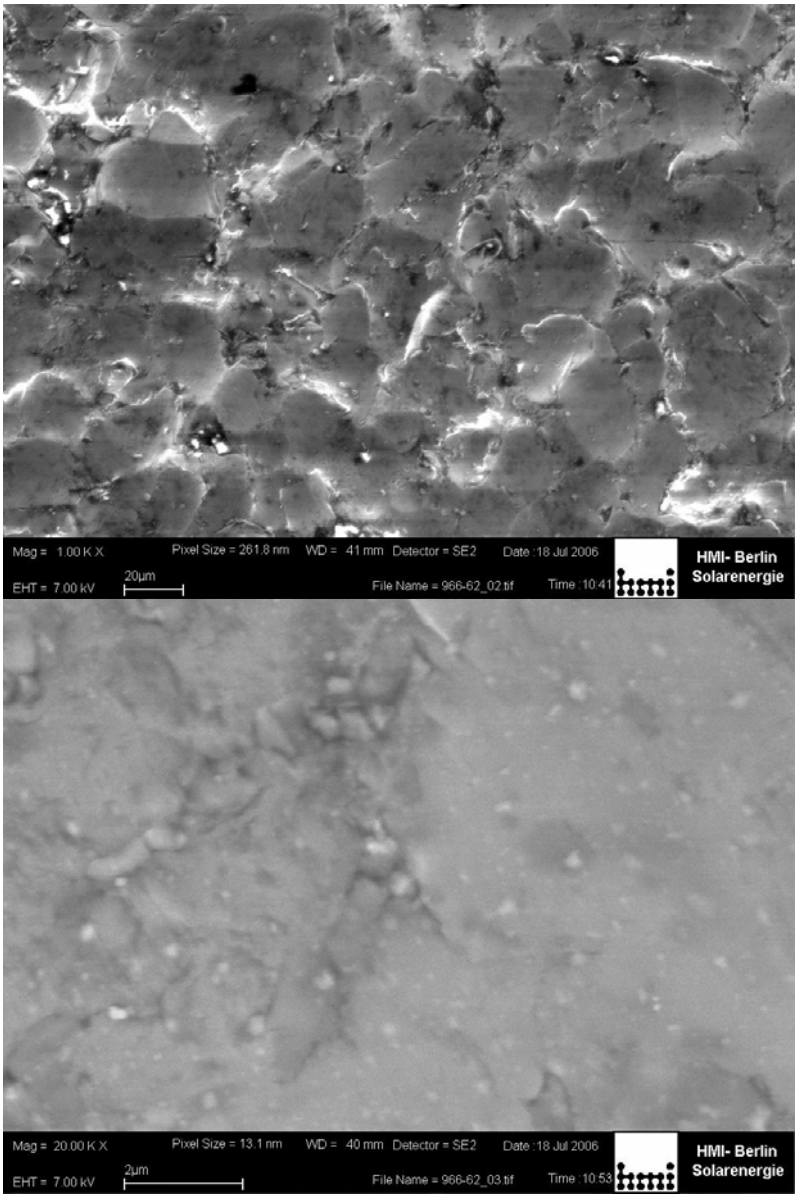

Figure II-4.2. SEM micrograph of a Cu-rich sample at low and high magnification

Further characterization of the samples is necessary in order to study these interesting phenomena.

Electrical characterization:

Solar cells were completed at Hahn-Meitner Institut-Berlin, employing their baseline process, including KCN etching, chemically deposited CdS and i-ZnO/ZnO:Al window and Ni:Al grids.

Solar cells did not yield significant photo voltage and photo current. This is probably due to shunting because of pin holes in the absorber. Optimization of the printing process is expected to resolve this problem.

II-4.4) Conclusions

- Exceptionally highly oriented (112) $CuInS_2$ films were deposited by simple paste-coating and sulfurization anneal from binaries blends.
- No photovoltaic devices could be obtained with this material, probably because of shunting.
- Further investigation of the process is expected to provide more information on this interesting crystallization.

II-5) DEPOSITION OF $CuInSe_2$, $CuIn(S,Se)_2$ and $Cu(In,Ga)(S,Se)_2$

II-5.1) Introduction

Despite the significant progress in terms of crystalline quality of $CuInS_2$ achieved in sections II-2 and II-3, no increase in device efficiency was observed. While there may be a number of reasons for this, the most probable of them are shunting because of microscopic defects in the layers and the existence of traces of Cu-Au ordered phases which, as we already discussed, are harmful for device performance.

At this point we reconsidered our general strategy. The most advanced $CuInS_2$ process (sputtering of metallic layers and rapid thermal selenization) [62] was yielding efficiency that, after decades of optimization, was just enough to allow module fabrication. There was little probability that our low-cost method even at optimal conditions would be able to surpass this technology. A decision was made that it was more rational to start research with selenide materials as they had demonstrated much higher efficiencies in general.

As mentioned in the introduction, record-performance chalcopyrite devices include Ga because of its beneficial effect on the band gap and electronic properties of $CuInSe_2$. There is also growing interest in pentanary chalcopyrites due to the possibility of tuning their optical and electric properties in a wide range [120,121].

The preparation procedure (Figure II-5.1) was similar to the one employed in sections II-2 and B -3. Gallium was introduced by means of acetylacetonate. It was found that these samples required higher temperature (390ºC) in order to eliminate completely carbon residue as concluded from visually observed discoloration. This can be attributed to the presence of acetylacetonate. Atomic ratios were selected in accordance with existing data of high-performance devices – Cu-poor films, Cu/(In+Ga)=0.92 with ratio of Ga/(In+Ga) =0.3.

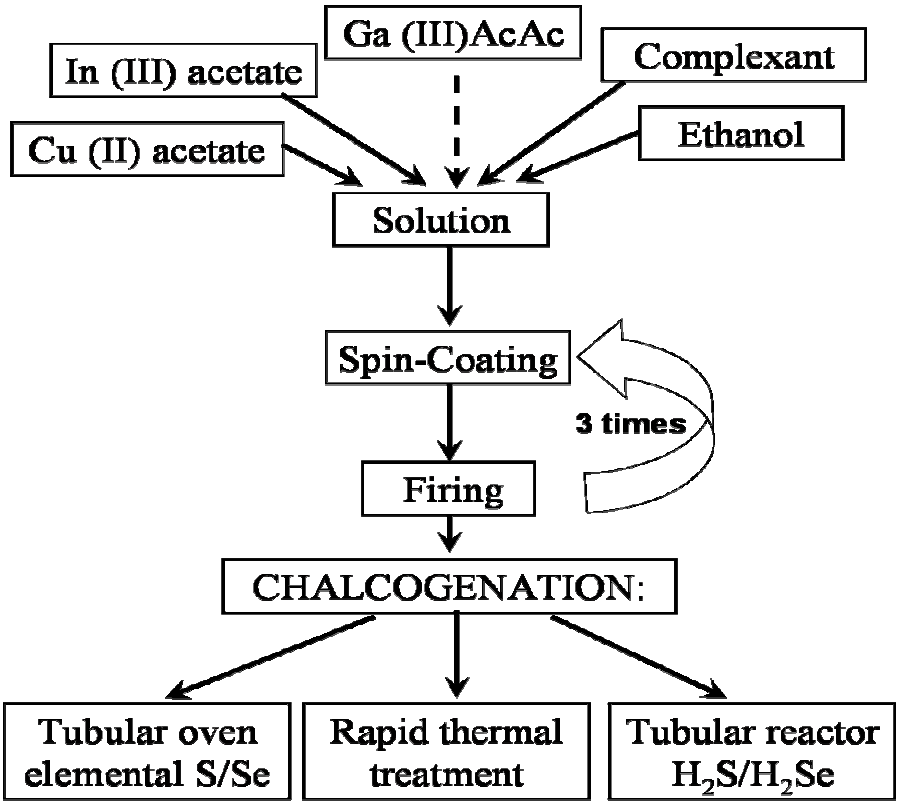

Figure II-5.1. Scheme of the different routes for selenide and sulfoselenide films.

II-5.2) Experimental

Sample Preparation

The precursor solutions were prepared by forming copper, indium, and in some cases, gallium diethanolamine (DEA) complexes in ethanol solution. Typically, 3 mmol of the complexing agent were dissolved in 1.2g of ethanol to which copper (II) acetate monohydrate, indium (III) acetate and gallium (III) acetylacetonate were added, using ratios indicated in Table II-5.I. The amount of indium remained constant at 0.666 mmol. The substrates were spin-coated at 1500 rpm and heated at 390°C for 4 minutes. This process was repeated three times to obtain the correct thickness of precursor layer, as discussed in a previous study [84]. The chalcogenizations of the precursors were carried out using elemental selenium or sulfur at a maximum temperature of 550°C in a 5% H_2/N_2 gaseous mixture.

Sample DR was subjected to Rapid Thermal Treatment (RTP) by halogen radiation from above at 500ºC/min up to 550ºC with no ramp. Nominal temperature was measured on the bottom side of a graphite holder and may be lower than the real temperature of the film. A brief description of all prepared samples is presented in Table II-5.I.

Table II-5.I. Sample description

Sample	Cu/(In+Ga)	Ga/(In+Ga)	Treatment	Details
A3	1.7	-	S	500°C to 550°C
B3	1.7	0.3	S	500°C to 550°C
C1	0.92	-	Se / S	500°C - 550°C / 500°C - 550°C
C2	0.92	-	Se	500°C - 550°C
D1	0.92	0.3	Se / S	500°C - 550°C / 500°C - 550°C
D2	0.92	0.3	Se	500°C - 550°C
DR	0.92	0.3	RTP Se	500 K/min. to 550ºC
D	0.92		H_2Se	450ºC
E	0.92	0.3	H_2Se	450ºC
F	0.92	0.3	H_2Se/H_2S	450º/550ºC

II-5.3) Results and discussion

Pre-treatment

Thermal analysis of precursor material in air indicated a main combustion reaction starting at about 350°C. Exothermal peaks were smaller in Cu-rich samples, reaching maximum at about 430ºC. The peaks of In-rich samples were higher both in intensity and temperature, about 440ºC. The peaks of Ga-containing samples were even more exothermic and shifted to higher temperatures - 450ºC. These increasing values can be related to higher amount of residual carbon eliminated during the thermal pretreatment, especially in the presence of acetylacetonate. Nevertheless, the combustion of these materials in a thin-film form may take place at lower temperatures.

X-ray diffraction

Air-pretreated films had amorphous nature while the XRD patterns of all chalcogenated samples can be assigned to chalcopyrite materials.

Sulfurized Cu-rich samples (groups A and B) showed $CuInS_2$ structure. No shift of the $CuInS_2$ peak was detected in Ga-added sample B3 by XRD indicating poor Ga incorporation in the crystal, in contrast with other treatments of $Cu(In,Ga)S_2$ films where such shift was observed [122, 123]. Small peaks related to CuS can be found in all Cu-rich samples (Figure II-5.1a).

Selenized samples C2 and D2 (Figure 1b) showed improved crystallinity and preferred (112) orientation. Ga-added sample D2 presented good Ga incorporation in the form of $Cu(Ga_{0.3},In_{0.7})Se_2$ phase.

Rapid thermal treated sample DR exhibited $CuInSe_2$ spectra with little or no Ga incorporation. This may be attributed to immobilization of Ga in stable oxide at high temperature before selenization was complete.

Double treatment (selenization plus sulfurization) yielded different spectra depending on Ga-presence (Figure II-5.1c). Cu-In precursor C1 formed two peaks belonging to $CuInS_2$ and $CuInSe_2$. Cu-In-Ga sample D1 exhibits a peak at 28.00º 2θ, which may be attributed to a pentanary compound with significant substitution of selenium by sulfur [124], as well as to higher gallium content.

Samples treated with H_2Se gas showed excellent Ga-incorporation as inferred by the displacement of the main (112) peak (Figure II-5.2).

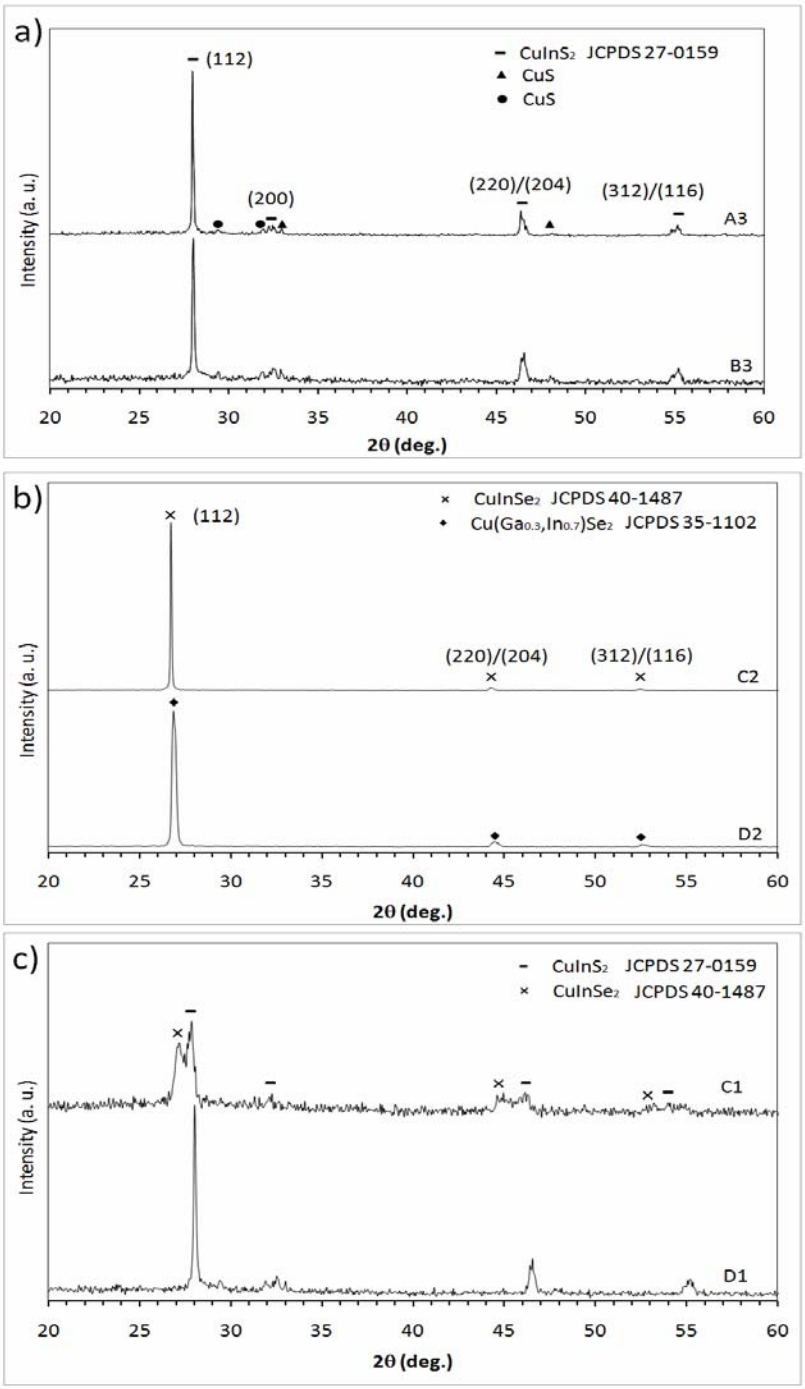

Figure II-5.1. XRD patterns of samples prepared in this work: Cu-rich sulfurized (a), Cu-poor selenized (b) and Cu-poor double-treated samples (c).

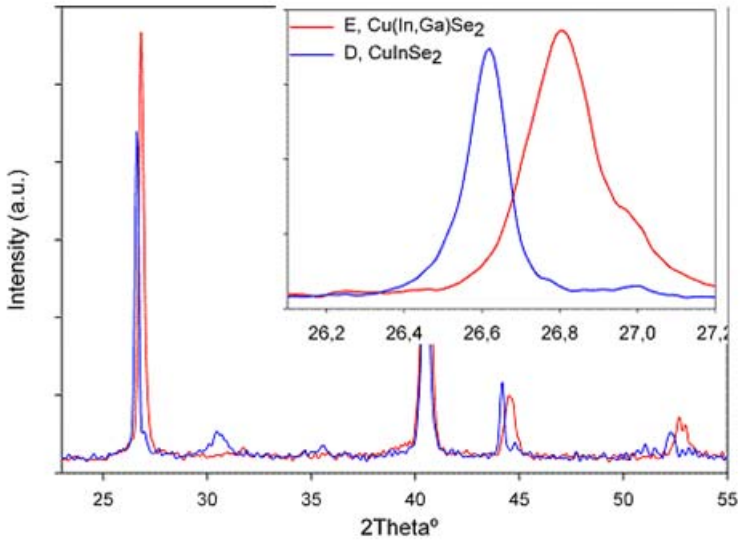

Figure II-5.2. XRD patterns of samples treated with hydride gases.

Scanning electron microscopy

Figure II-5.3presents SEM micrographs of chalcogenized films. The surface is free of pinholes. As expected, Cu-rich samples (groups A and B) formed CuS segregations on top (a). Planar crystals were observed on the surface of Cu-poor selenized sample D2 (b) with slightly lower Ga-content than the matrix.

Double-treated sample D1 (c) formed isolated Cu-rich crystals on top and smaller embedded $Cu(In,Ga)(S,Se)_2$ crystals. Three layers originating from the precursor layers can be distinguished in the cross section (d) with a total thickness of 1.2μm. EDX showed that the bottom layer has a relatively higher Ga content which is typical for similar layers [125].

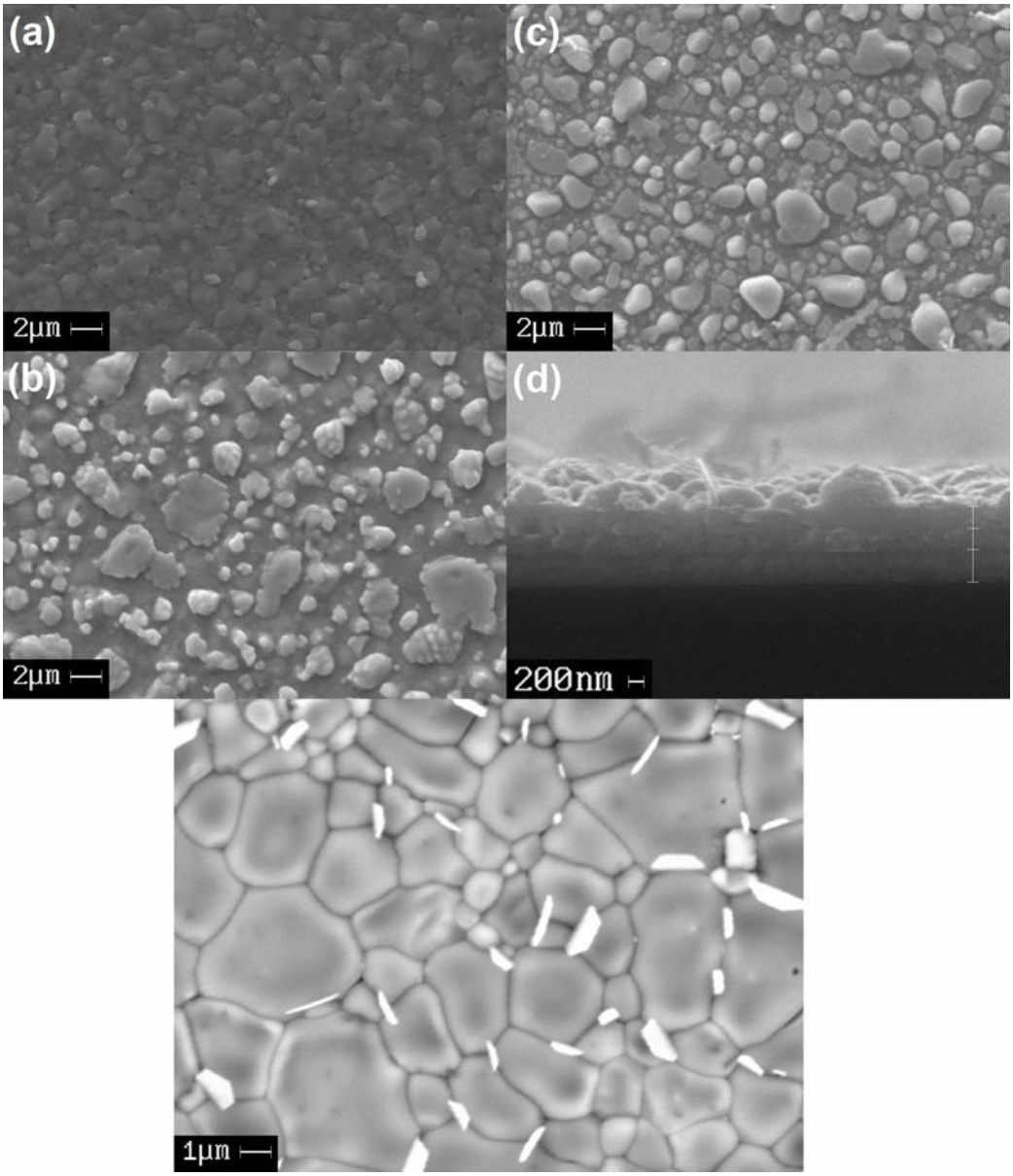

Figure II-5.3. SEM micrographs of chalcogenized films: Sulfurized sample A3 (a), selenized sample D2 (b), double–treated sample D1 (c, d) and rapid thermal-treated sample DR (e).

Rapid thermal selenization of sample DR (e) yielded very large densely packed planar crystals, up to 5 times film thickness. Poor Ga-incorporation was found in these by EDX analysis and was confirmed by XRD. Such large crystals have been reported with electrodeposited $CuInSe_2$ films [126].

Treatments with hydride gases yielded smaller grained, uniform films (Figure II-5.4).

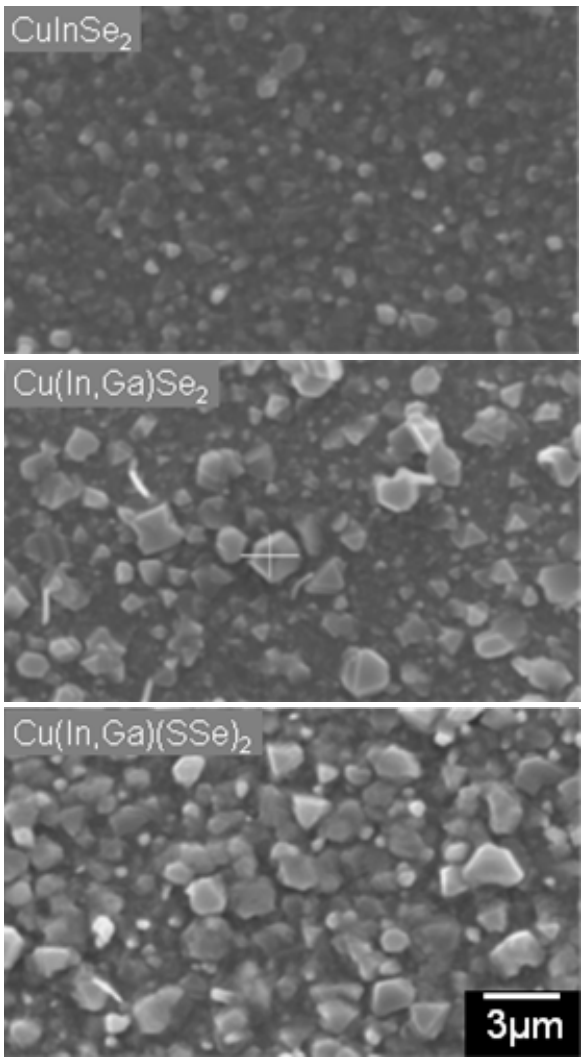

Figure II-5.4. SEM images of samples treated with hydride gases

EDX analysis of hydride-treated films showed minor Cu-loss and good incorporation of both selenium and sulphur (Table II-5.II)

Table II-5.II. EDX analysis of precursors and hydride gas treated samples

SAMPLE	Cu/(In+Ga)	Ga/(In+Ga)	Se%	S%
D-Precursor Cu-In-O	0.92	-	-	-
Precursor Cu-In-Ga-O	0.92	0.30	-	-
B: $CuIn(S,Se)_2$	0.82	-	27	28
E: $Cu(Ga,In)Se_2$	0.83	0.24	52	-
F: $Cu(In,Ga)(SSe)_2$	0.89	0.21	27	31

Optical properties

A typical optical transmission spectrum of a sample treated in tubular oven is presented in Figure II-5.5. The transmission in the visible range was almost 0.

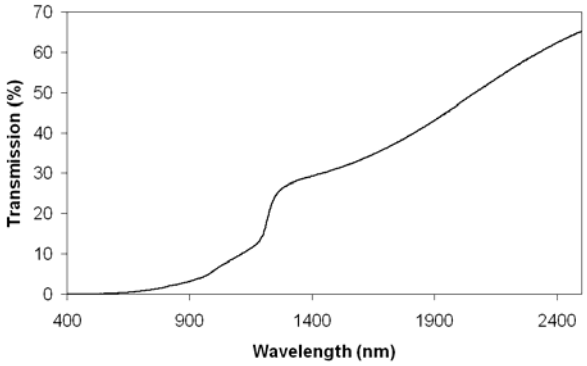

Figure II-5.5 . Typical transmission spectra of a film treated in tubular oven (sample C2).

The plots $(\alpha h\nu)^2$ versus $h\nu$ for the chalcogenized samples are presented in Figure II-5.6. Band gaps between 1.18 and 1.63 eV were found. Sulfurized Ga-added sample B3 showed 1.50 eV, typical for Ga-free $CuInS_2$. Selenized samples showed lower band gaps of 1.18 eV yet slightly higher than normally observed with $CuInSe_2$. Additional sulfurization treatment increased this value to 1.35 eV in sample C1. This confirms the effective incorporation of sulfur in the film. Ga-incorporation in $Cu(In,Ga)Se_2$ sample D2 is evidenced by increased gap of 1.23 eV. $Cu(In,Ga)(S,Se)_2$ sample D1 showed highest band gap of 1.63 eV, as expected from the influence of both sulfur and gallium presence.

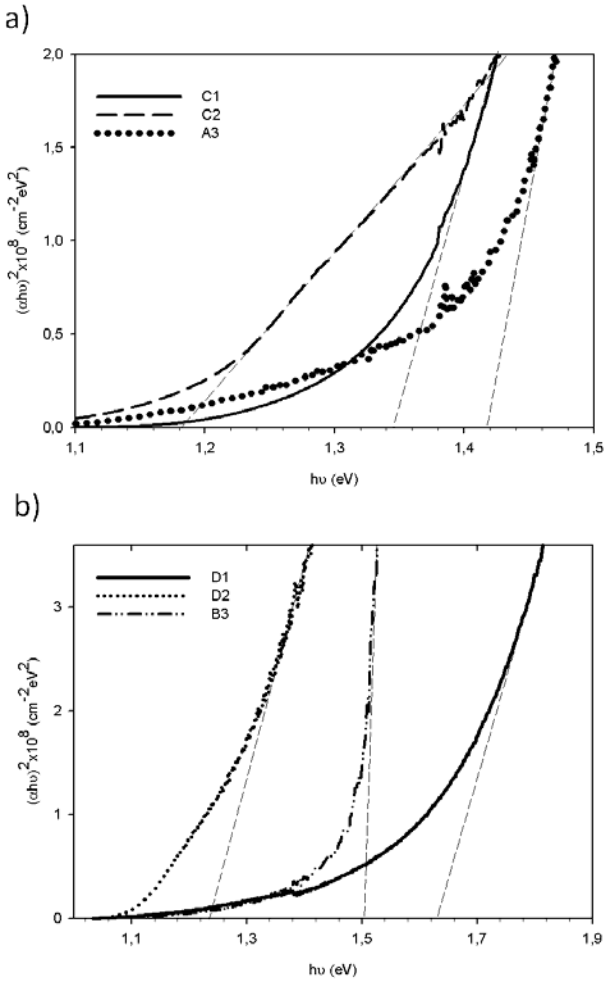

Figure II-5.6. Plots of $(\alpha E)^2$ vs E: Samples without gallium content (a) and with gallium content (b).

Solar cell properties.

Deposition was repeated on molybdenum-coated glass substrates for solar cell fabrication.

Treatments developed in tubular oven proved to be too aggressive for the molybdenum underlayer. Severe damage and delamination of both the molybdenum and the absorber were observed.

Operational devices were fabricated from samples treated with hydride gasses by the baseline process of the Institute of Energy Conversion in Delaware. It included CdS/i-ZnO/ITO/Metal grid deposition.

Table II-5.III. Photovoltaic parameters of cells prepared from hydride-gas treated absorbers.

Cell	Absorber - %Ga/(In+Ga)	Voc	Jsc	FF	Eff.
II-1	CIS	0,326	17,8	35,2	2,1
E-3	CIGS - 30%	0,260	20,6	37,9	2,0
P-1	CIGS - 20%	0,389	19,5	33,3	2,5
O-5	CIGSSe -20%	0,328	21,9	35,1	2,5
F-2	**CIGSSe - 30%**	**0,460**	**18,8**	**35,6**	**3,1**

Table II-5.III presents the data of solar cells obtained. Maximum efficiency was achieved with absorber F-2 – 3.1% with Voc 460mV, Jsc 18.8mA/cm^2 and FF 35.6% (Figure II-5.7). The low fill factor was of particular concern and its cause was further investigated using quantum efficiency measurements.

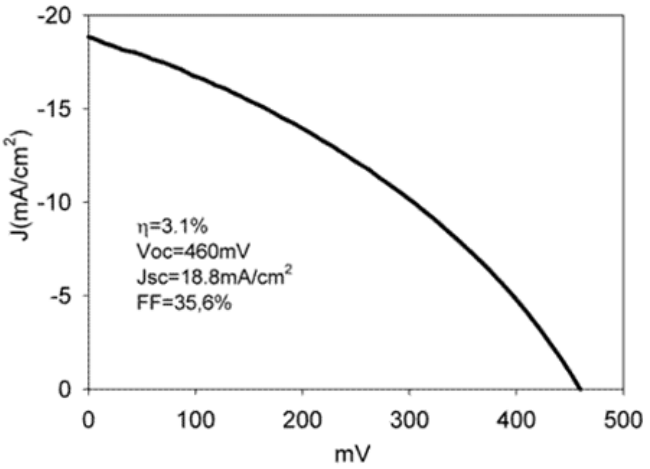

Figure II-5.7. J-V curve of a solar cell prepared from F-2 absorber.

Figure II-5.8 shows the spectral response spectrum of F-2 cell. The data below 600 nm are not representative and are attributed to heavy doping of the CdS layer that would result in a very high photoconductivity and instrumental error. Because chalcopyrite is very stable, it cannot leach sufficient copper to produce this effect. The reason for these results may be the presence of copper binary phases at the surface of the sample. As already discussed in the introduction, copper binaries can be detrimental to device performance. In this case, an intermediate etching step before buffer deposition may improve cell performance.

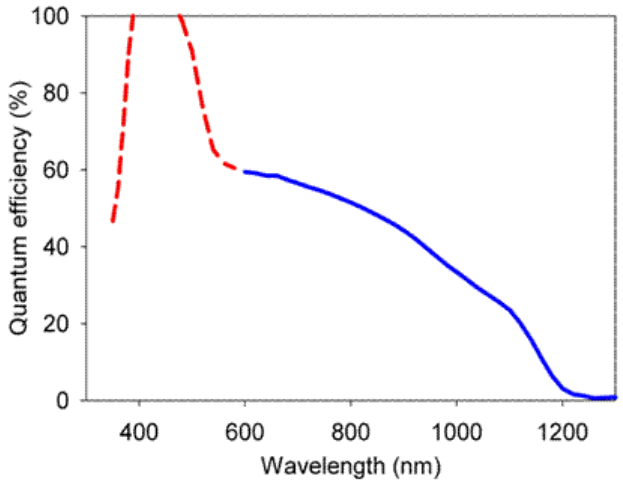

Figure II-5.8. Spectral response of a solar cell prepared from F-2 absorber with apparatus anomaly at lower wavelength attributed to heavy Cu-doping of CdS.

II-5.4) Conclusions

- Cu-In-Ga-O precursors deposited by a soft-chemistry method showed Ga-incorporation upon selenization and double treatment of selenization + sulfurization.

- No Ga-incorporation was found in sulfurized Cu-rich precursors.

- Rapid thermal anneal produced very large planar $CuInSe_2$ crystals.

- Band gaps in the range of 1.18 and 1.62 eV correlate well with the results of XRD and SEM.

- Solar cells prepared from absorbers treated with hydride gases yielded maximum efficiency of 3.1 %. A possible limiting factor may be the presence of Cu binaries at the surface, provoking heavy doping of the CdS layer.

II-6) PRINTING DEPOSITION OF Cu_2ZnSnS_4 FILMS

II-6.1) Introduction

As discussed in the introduction, CZTS (Cu_2ZnSnS_4) has emerged as a promising photovoltaic absorber material, free of scarce and toxic elements [127-130]. Solar cells based on CZTS have yielded conversion efficiencies as high as 5.74% and further increases are expected [130].

The development of low-cost deposition techniques for this material and the possibility of large-volume photovoltaic production have attracted the interest of several research groups. Diverse vacuum-free deposition routes have been reported: spray-pyrolisis [131,132], photochemical deposition [133], sol-gel [134], electro deposition [135].

The present work investigates the synthesis of quaternary precursors by a soft-chemistry method and their deposition by a printing technique. The process is a modification of the one used for $CuInS_2$ in section II-4. Chalcogenide nanoparticle-based deposition techniques have been used for $Cu(In,Ga)Se_2$ (CIGS) films [88, 136]. The aqueous precursor synthesis route chosen by [88] led to oxide contamination and in both cases difficulties in layer densification were encountered.

In order to minimize contamination with oxide and hydroxide species we developed a non-aqueous synthesis route for the CZTS precursor material. Metal salts were reacted directly with elemental sulfur in ethyleneglycol to obtain homogeneous and dispersible nanoparticles.

II-6.2) Experimental part

Reagents

All reagents used for the synthesis were analytical grade: zinc acetate dihydrate (99.999%, Aldrich), tin (II) chloride dehydrate (99.99%, Aldrich), copper (II) acetate monohydrate (98+%, Aldrich), sulfur S (pure, Baker), ethylene glycol (99%, Baker), triethanolamine (99%, Riedel-de-Haen), Mowiol™ (polyvinyl alcohol 98%, Aldrich).

Sample preparation

The synthesis of quaternary precursor powders was carried out in 50 ml glass bottles inserted in oil bath at 170ºC under magnetic stirring. Elemental sulfur was dissolved in 35 ml ethyleneglycol. The metal precursors were dissolved separately in 10 ml ethyleneglycol with 15 mmol of triethanolamine and added dropwise to the sulfur solution. The elemental ratios were varied and calculated for 1 mmol of product (Table II-6.I). After 3 hours of reaction the obtained materials were separated by centrifugation and washed with absolute ethanol. Coating suspensions were prepared by redispersing 7-12% of powder. To some samples 3% of Mowiol™ was added as a binder.

Films were printed on soda-lime glass substrates by sliding a glass rod over 50µm thick spacers. After drying in air at 150ºC, thermal treatments were carried out at a heating rate of 50 K/min or direct insertion in a tubular oven at 550ºC for 10 minutes in nitrogen gas saturated with ethanol vapor using a setup similar to the one described in section II-2.2. A sulfur source was maintained at 200ºC at the reactor inlet except in the case when sulfur loss was studied.

Characterization

The crystal structure of the films was determined by X-ray powder diffraction (XRD) with a SIEMENS D5000D diffractometer with theta-2theta geometry equipped with a Cu-Kα radiation source.

Film morphology and composition were determined by Scanning Electron Microscopy (SEM) using a scanning electron microscope (Leica Leo 440) equipped with a spectrometer for energy dispersive X-ray microanalysis (EDX). The thickness of the films was estimated from micrographs of film cross sections.

Optical measurements were carried out with Carry-500 Scan UV-Vis-NIR spectrophotometer.

II-6.3) Results and discussion

The elemental amounts used for the synthesis are presented in Table II-6.I. The composition of the resultant product determined by EDX was used as a feedback for composition tuning.

Table II-6.I. Elemental amounts used for the synthesis and EDX data of obtained product.

Reference	mmol used				Product elemental ratios by EDX*		
	Cu	Zn	Sn	S	Cu/Zn+Sn	Zn/Sn	S/metals
A	1	0.5	0.5	4	1.3	3.5	0.8
B	1	0.5	0.5	8	0.9	1.2	1.1
C	1	0.5	0.5	12	1.0	1.2	1.0
D	1.2	0.5	0.63	12	1.1	1.0	0.9
E	0.8	0.5	0.63	12	1.0	1.0	0.8
F	1	0.5	0.63	12	0.7	0.9	1.1

*These ratios calculated from semi-quantitative EDX data with 10% error.

Stoichiometric amounts of metallic salts used in sample A led to Sn-deficient materials. This was attributed to the strong affinity of copper species to sulfur and led us to investigate the effect of sulfur/metal ratio. Sulfur excess in samples B and C resulted in improved, but not complete, Sn utilization. The slightly Cu-poor and Zn-rich composition of sample B is close to the one of state of the art CZTS solar cells [130]. In order to obtain Zn/Sn ratios close to 1, a small excess of Sn salt had to be used in samples D, E and F. The lack of direct correlation between the amount of some elements in the starting solutions and in the obtained precursor powders (copper and sulphur in particular) can be attributed only partially to the measurement error. This difference is most probably due to species remaining in solution. We found that excess sulphur was bound in solution after the reaction, probably in thio-compounds. Copper may also form stable complexes with triethanolamine and remain in solution. These effects and the factors that may trigger them (for instance minor temperature fluctuations) require further investigation.

All films prepared without binder addition exhibited visual cracks after thermal treatment and did not adhere well to the substrate. In contrast, the films prepared with Mowiol™ were crack-free (except for the copper-rich sample D) and had better adherence. Polymer addition helps avoid crack generation and propagation in the layers during the drying and heating steps by efficiently binding nanoparticles together.

X-ray diffraction

The XRD patterns of as-synthesized powders can be assigned to mainly amorphous material (Figure II-6.1d) although small peaks were detected without indicating indisputably a specific phase.

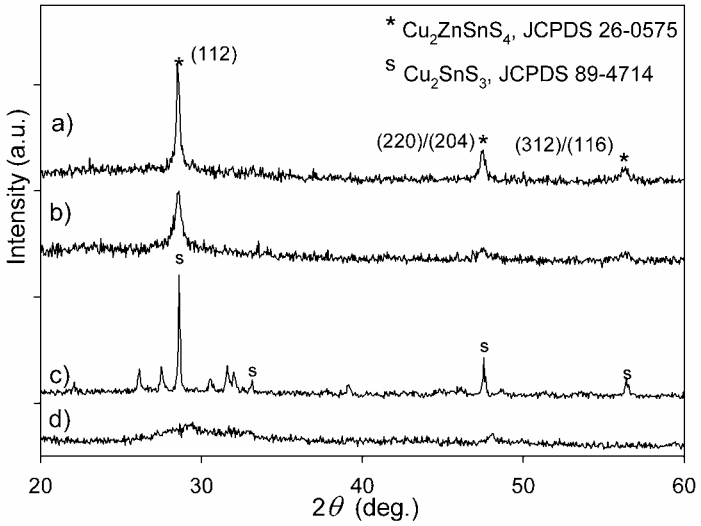

Figure II-6.1. X-ray diffraction patterns of samples prepared from composition B: binder-free sulfurized (a), with binder sulfurized (b), heat treated without sulfur addition (c) and precursor powder (d).

Sulfurized films showed crystalline nature. While little effect of the heating ramp was observed, the addition of sulfur vapor to the treatment gas was crucial for obtaining clean XRD patterns (Figure II-6.1).

When a sulfur source was used during the thermal treatment, all peaks in the XRD patterns could be assigned to kesterite Cu_2ZnSnS_4, JCPDS 26-0575 (Figure II-6.1a). Because materials in thin-film form usually do not complete the presumption of random orientation required for precise powder diffraction data analysis and because other phases such as Cu_2SnS_3 have very similar lattice constants, XRD could not confirm stannite absence. Instead, the lack of evidence for other phases together with the near-stoichiometric composition by EDX suggests that sulfurized films were composed of predominant Cu_2ZnSnS_4 phase.

The addition of Mowiol™ led to decreased peak height and increased peak width at half-maximum, indicating inferior crystallinity in comparison with the samples in which no binder was added, probably due to carbon contamination upon thermolysis of the polymer (Figure II-6.1b).

When no sulfur source was connected to the reactor, the sulfur loss during the treatment observed by EDX analysis was accompanied by the formation of Cu_2SnS_3 (Figure II-6.1c). The foreign peaks observed in the pattern can be ascribed to copper

sulfides which are not identified separately because of the large number of overlapping patterns.

Scanning Electron Microscopy

As-synthesized precursors comprised round-shaped nanoparticles of about 200nm with homogeneous size distribution (Figure II-6.2 a).

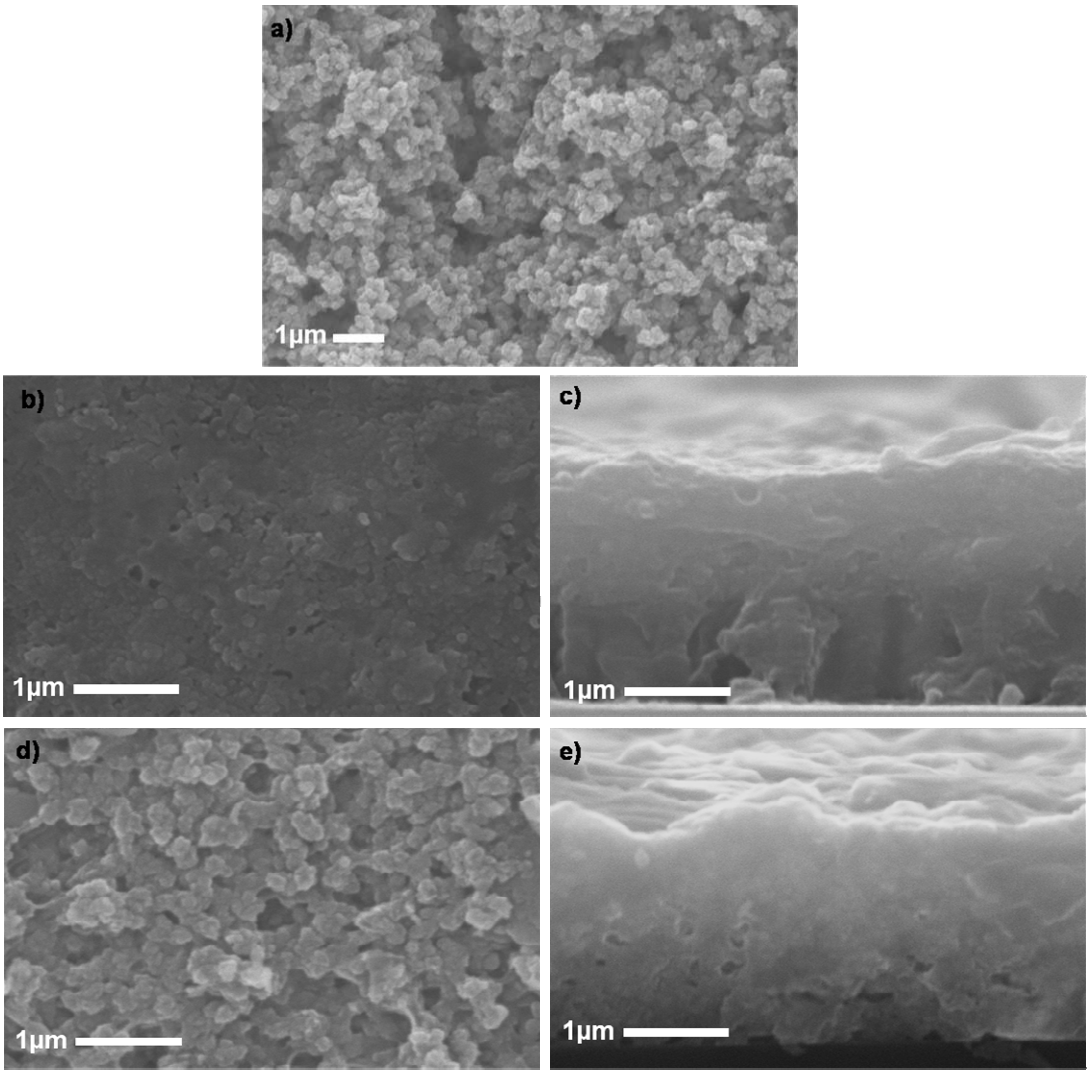

Figure II-6.2. SEM micrographs of as prepared powder (a) and surface views and cross sections of films prepared with binder after sulfurization treatment: Cu-poor/Zn-rich precursor B (b and c), stoichiometric precursor E (d and e).

As already mentioned, the films prepared without binder addition exhibited large cracks that make them useless for photovoltaic application. Curiously, large cracks were also observed in Cu-rich samples with binder addition.

Films prepared from Cu-poor/Zn-rich precursor B (Figure II-6.2 b) exhibited smoother surfaces than the stoichiometric precursor E (Figure II-6.2 d).

Precursor B was segregated in two layers (Figure II-6.2b). The bottom one, richer in Zn, formed larger columnar grains. Previous works [129] reported large grains with Zn-rich composition. We attempted to prepare more Zn-rich samples, but cracking upon anneal was observed even with binder addition. In E-type samples the compositional difference in cross section was smaller or absent although difference in morphology was observed, with the bottom part consisting of partially sintered grains. More Cu-poor samples of precursor F yielded smoother surfaces and smooth, glass-like cross sections (not shown).

Surface EDX analysis of sulfurized samples indicated sulfur-rich composition (S/metal=1.2-1.4). Close to the glass interface this ratio was between 1-1.2. Small peaks of carbon were visible in all spectra. Minor carbon contamination is due to binder thermolysis in non-oxidizing atmosphere but cannot be measured precisely by EDX. We did not observe carbon segregation as formed by other printing compositions, employed for CIGS [90].

Optical properties

Optical transmission (Figure II-6.3a) reaches 50% at a wavelength of 2500nm and is practically zero below 800nm for samples E and F; 500nm for samples B and C. Binder-free samples (not shown) had almost 80% transparency at 2500nm and about 0,5% (due to cracking) at 500nm. The 30% decrease in transmission in films with binder is probably due to carbon content which did not change the overall shape of the curve. A rather long band transition is observed in most cases.

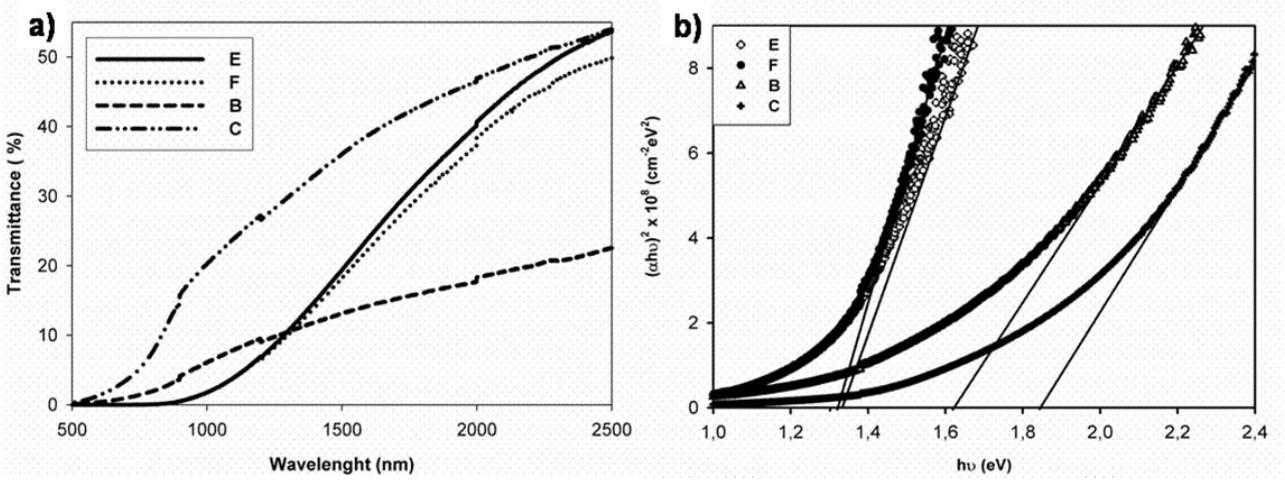

Figure II-6.3. Optical properties of crack-free films prepared with binder addition from compositions E, F, B and C: transmission (a) and $(E\alpha)^2$ vs. E (b).

The band gaps were calculated from these spectra by plotting $(\alpha E)^2$ vs. E where α is the absorption coefficient and E the photon energy (Figure II-6.3 b). Approximately 1.32eV were found for both stoichiometric F and Cu-poor E precursors. The Cu-poor/Zn-rich B yielded 1.63eV and C - 1.85eV. These values are below or above the1.45-1.51eV reported for Cu_2ZnSnS_4 by other authors [129,131]. Such a band gap shift can be related to the formation of solid solutions with different Zn-content. The incorporation of ZnS (with gap above 3.5eV) has resulted in a large shift of the band gap of other materials such as CuInS2 [138].

II-6.4) Conclusions

- Quaternary nanoparticle suspensions were used to print Cu_2ZnSnS_4 films.
- Binder addition was necessary in order to obtain crack-free films. This resulted in certain carbon content which decreased the crystallinity and optical transmission by 30% at lower energies.
- Bandgap values of 1.32-1.85eV were obtained.
- Optimization of deposition and treatment parameters may result in carbon-free layers with improved crystallinity.
- The possibility to tune the band gap in a wide range may be useful for device applications.

II-7) ELECTRO DEPOSITED In2S3 BUFFER LAYERS FOR CuInS2 SOLAR CELLS

Summary:

As discussed in the introduction, the buffer layer is an important element of the chalcopyrite device. Motivated to replace the toxic cadmium and the chemical bath deposition methods used in record performing devices, we developed an electro deposition of In_2S_3 buffer layers [94].

All materials and deposition conditions were selected taking into account environmental, economic and technological aspects of a potential transfer to large volume industrial production. Different bath compositions and electro deposition parameters were studied. The obtained films exhibited complete substrate coverage, confirmed by SEM and XPS. In/S ratio close to 2/3 was obtained. XPS measurements detected the presence of indium hydroxide, transforming into oxide upon anneal at 200ºC. Maximum photoelectric conversion efficiency of 7.1% was obtained, limited mainly by a low fill factor (51%). Further process optimization is expected to lead to efficiencies comparable to CdS buffers. So far, open-circuit voltages as high as 660mV were demonstrated.

II-7.1) Introduction

After several decades of intensive research, thin-film chalcopyrite photovoltaic technologies have evolved to become a competitive alternative of crystalline silicon. During the recent years multiple manufacturing challenges have been successfully overcome in several pilot production plants. Currently, as this promising technology is at the gates of large-scale production, it is crucial to adapt all processing steps to high throughput and contaminant-free manufacturing. While deposition of most of the layers, such as the back contact, absorber and window, have already been adapted to inline and environmentally safe handling, this is not entirely the case with the buffer layers, typically CdS films, deposited by chemical bath deposition (CBD). Both the material itself and its formation route are undesirable for industrial production. Apart from being a relatively slow, precisely controlled batch process, CBD has the following inherent disadvantages: need of fresh solution for each cycle, poor material utilization and necessity to manage large amounts of residual liquids.

Extensive research efforts by many teams worldwide have yielded fundamental understanding as well as some successful alternatives of CdS, in most cases using zinc or indium sulfide based materials [24, 139-144]. Good results in lab-scale experiments have been achieved with methods alternative to CBD, such as atomic layer deposition (ALD), metal organic chemical vapor deposition (MOCVD), ion layer gas reaction (ILGAR), sputtering and thermal evaporation [140]. However, most of these methods still need to be approved in the industry. In view of the risk involved in replacing the industrially established process of buffer layer deposition, we have selected for this work a method which is close to it, yet avoids its main disadvantages.

Electro deposition is a widely used industrial process for large area coating, both in batch and in line systems [145]. In addition, electro deposition permits the preferential growth of the buffer layer on defected areas with higher conductivity such as pinholes, thus reducing the probability of shunting. Very few attempts to electro deposit buffer layers on $CuInS_2$ have been reported [146,147]. In the first one, CdS was used, together with a high-temperature organic solvent which is difficult to apply in large-scale production. The second one (ZnSe) demonstrated junction formation, but no device performance. Successful electro deposition of In_2S_3 films on molybdenum substrates was reported as well [148]. The method uses high concentration (1M) Na_2SO_3 as a sulfur source and required precise control of the pH. The obtained films exhibited high oxygen content and In/S ratio obtained in this work was close to 1 while the stoichiometric one for In_2S_3 is 2/3. Although oxygen contamination is frequent in many successful Cd-free buffer layers, no conclusive data exists on whether this is beneficial for the performance of the solar cell. After reproducing the method, we found that large amounts of the active SO_2 were volatilized in our open setup and the pH rapidly changed, making it difficult to use the same solution for multiple depositions. In a search for a method which better copes with the objectives of our work, we adapted another process, already used for $CuInS_2$ electro deposition [149]. Using concentrations of several millimoles and $Na_2S_2O_3$ as a colloidal sulfur source, this method proved robust, environmentally friendly and permits multiple depositions from the same bath.

Electro deposition, uniformity, and reproducibility are largely dependent on the interrelated hydrodynamic and electrochemical processes in the deposition solution. Significant fundamental and industrial research efforts have been focused on this issue [145, 150]. A common industrial approach is injecting gas into the deposition bath. Unfortunately, bubbles can create pinholes in very thin coatings such as buffer layers, causing device failure. Other approaches include complex stirring or jet systems, difficult to implement in small-scale laboratory experiments.

We improved the uniformity of our electro deposited of In_2S_3 buffers by designing a simple stirring apparatus. Different industrial solutions for a potential large-area module deposition are also available [145].

Because of the difficulty to use potentiostatic conditions in industrial production over large areas, we decided to employ a two-electrode configuration and constant current conditions. Although the efficiency obtained has not yet surpassed 2/3 of the reference cells with CdS buffers, we believe these first results are encouraging.

II-7.2) Experimental

The electro deposition was carried out in two-electrode cell configuration using an aqueous solution of $Na_2S_2O_3x5H_2O$ (spectroscopic grade, Fluka), $InCl_3$ (99.999%, Chempur) and HCl (puriss. P.A.). The bath temperature and the concentrations of the three components were varied. Various substrates were used: graphite sheet, Mo-coated and ITO-coated glass or $CuInS_2$/Mo/glass structures prepared by HMI (Hahn-Meitner-Institut) baseline process [151] or the commercial process of Sulfurcell GMBH, both based on sequential sputtering and sulfurization. The substrates were mounted on a TEFLON sample holder with graphite contacts (interelectrode distance of 1.5 cm). Platinum sheet was used as a counter electrode. A custom-made constant current power supply (1-20 mA) was used for all depositions while the electrochemistry of the process was studied in a three-electrode cell configuration using an Autolab potentiostat. Table II-7.I presents some of the bath compositions.

Table II-7.II. Concentrations chosen in the present study and best device photovoltage obtained.

Reference:	In (mM)	HCl (mM)	S/In	Best Voc
A	3	3	7	645
B	3	9	7	630
C	3	1	7	440
D	3	3	21	190
E	1.5	3	14	590
F	3	3	2	660

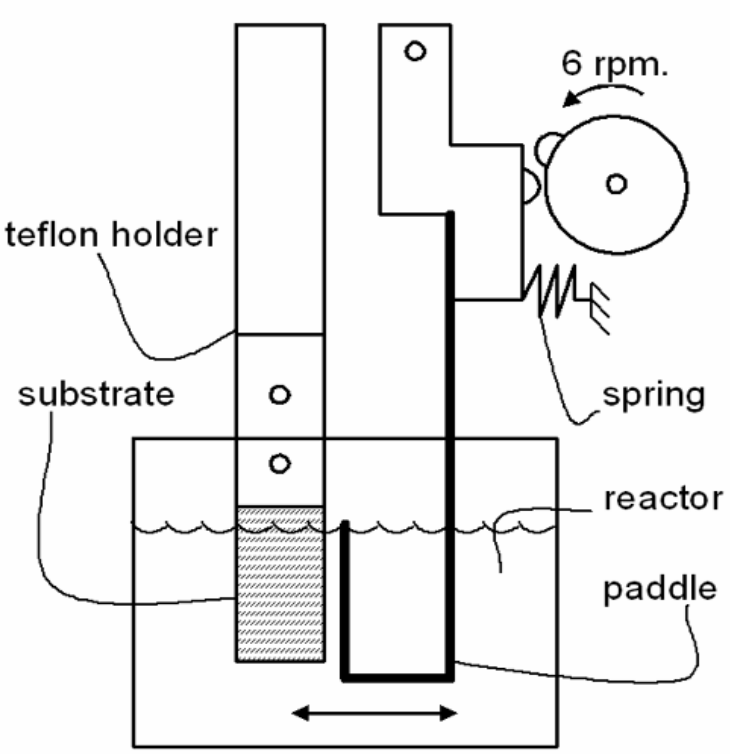

Figure II-7.1. Setup of the deposition reactor.

Different stirring regimes were explored: natural convection, magnetic stirrer and stirring pulses provided at 3 or 10 sec. intervals by means of the apparatus presented in Figure II-7.1. A wheel with a bump is driven by a constant speed motor (6 rpm). The bump displaces a pendulum mechanism terminating with a u-shaped polyethylene strip working paddle, oscillating between the electrodes. Figure II-7.2 stir shows the uniformity of deposition. When no stirring was present (A), there was a vertical gradient in thickness (determined visually by interference colors which were very bright due to the molybdenum reflectivity). When magnetic stirring was applied (B), the gradient was diagonal due to the liquid vortex. Short stirring pulses (3 sec) did not provide suitable electrochemical conditions for deposition (C) while 10-sec pulses resulted in improved uniformity (D).

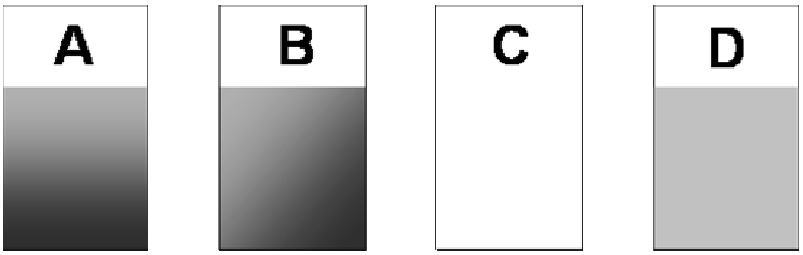

Figure II-7.2 Optimization of the stirring procedure: A- no stirring; B- magnetic stirring; C-stirring pulses at 3 sec; D- Stirring pulses at 10 sec.

Solar cells were fabricated with films on HMI $CuInS_2$ baseline structures [151] completed with i-ZnO/ZnO:Al window and Ni:Al grids. Preliminary studies were carried out on small substrates cut from Sulfurcell minimodule structures and completed without metallization grids.

The samples were characterized by scanning electron microscopy (SEM). Surface characterization was performed in the Hahn-Meitner-Institute "CISSY" ($CuInS_2$-diagnostic using Synchrotron radiation) end station, consisting of several interconnected UHV chambers and an attached glove box for sample preparation [152]. A CLAM 4 electron analyser (Thermo VG Scientific) was used for x-ray excited photoelectron (XPS) and x-ray excited Auger (XAES) electron spectroscopy . Al Kα (1486.6 eV) radiation from a SPECS XR 50 x-ray gun served as excitation source.
Cells performance was evaluated from quantum efficiency and J-V measurements under simulated AM 1.5 illumination (Steuernagel Xenon-Arc lamp simulator with filtering system, calibrated by use of a silicon reference cell). The same simulator was used for the light-soaking procedure, carried out for 30 min at AM 1.5. Homebuilt quantum efficiency measurement setup was used, calibrated by Hamamatsu cell calibrated by ISE Freiburg.

II-7.3) Results

Deposition bath

Shortly after dissolving the reagents, a whitish colloid solution formed. As previously reported [149], the $Na_2S_2O_3$ is decomposed after the addition of HCl according to the reaction:

$$S_2O_3^{2-} + H^+ \rightarrow S + HSO_3^-$$

The colloidal sulfur is consumed to form sulfide through the subsequent electrochemical reaction. Obviously, the concentration of active sulfur species in solution and, consequently, the sulfur contents in the film are dependent on the HCl concentration. The authors reported both higher sulfur and indium content in films with HCl concentration of $1.2x10^{-3}$%. At the same time the In/Cu ratio decreased at higher $Na_2S_2O_3$ concentration. Although the authors did not discuss this phenomenon and abstained from reporting the exact concentration of the reagents used, we observed higher tendency to aggregation of the sulfur colloids at high $Na_2S_2O_3$ concentration (0.2M). This would effectively decrease the activity of the sulfur species at the substrate surface and lead to lower sulfur content in the film. Based on the above observations, in the present study we chose the set of concentrations indicated in Table 1. The maximum photo voltage after device completion was used as a primary diagnostic tool for the quality of the film. The results confirmed the hypothesis that higher $Na_2S_2O_3$ and lower HCl content have negative impact on film properties.

Based on the above rationale, consistent with these preliminary results we chose the reverse engineering approach, limiting the present work to composition A which initially yielded best overall response. This does not discard the possibility to achieve good results with other compositions, especially type F which has lowest S/In ratio and yielded highest photo voltage. Further studies of the reaction chemistry, film structure and composition could yield better understanding of the mechanisms involved, leading also to improved device performance.

Electrochemical deposition

As mentioned in the introduction section, we opted for using constant current deposition conditions because this method is preferable for industrial applications over large substrates. Nevertheless, it is well known that the applied potential is of vital importance to the electrochemical reactions and, in consequence, to the composition and microstructure of the obtained films (the reduction potential of the In^{3+} to In^0 being -0.338V/NHE). The use of the contact area of the substrate to calculate an exact applied current is a method with a relatively low precision, especially in samples which are partially submerged. Furthermore, changes in the concentration of the reagents would lead to strong variations of the solution conductivity, changing the current/potential dependence. Because of these facts, for each deposition we adjusted the constant current with respect of an initial external voltage applied between the electrodes.

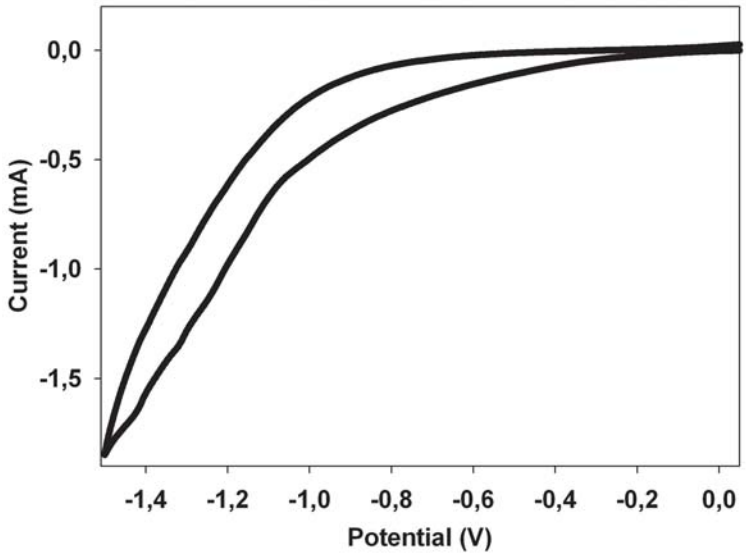

Figure II-7.3. Voltammetry plot of the electrochemical process using two-electrode configuration, composition A and graphite substrate at 70ºC.

Cyclic voltammetry was carried out with composition A at 70ºC in three-electrode cell configuration. Increased current densities, indicating an electrochemical reaction, were observed at 0.6V vs. Ag/AgCl reference electrode. The experiment was repeated using two-electrode configuration, finding the equivalent point at about 1.25V (Figure II-7.3). The deposition of all samples was carried out at constant current, which was adjusted manually for several seconds until this potential value was stabilized, before turning the stirring apparatus on.

The above conditions proved adequate, as at potentials higher than 1.6 V, the molybdenum film delaminated and at lower than 1.2V no deposition occurred. The observed delamination cannot be attributed to an electrochemical reaction of the molybdenum layer as it cannot be reduced by negative potentials further from its zero oxidation state. One possible explanation could be mechanical disintegration because of the formation of hydrogen bubbles within the layer due to water electrolysis at higher voltages.

Reference [149] reports lower reproducibility of the deposits of $CuInS_2$ at 70ºC than at room temperature. Although we observed a similar problem with reproducibility in the case of In_2S_3, our attempts to carry out the depositions at room temperature and 40ºC were unsuccessful. We expect that a more precise thermal and hydrodynamic control would result in superior reproducibility.

Scanning Electron Microscopy

Figure II-7.4 shows the surface and cross section of a film deposited on a molybdenum-coated glass from solution A. Complete substrate coverage with no pinholes is observed.

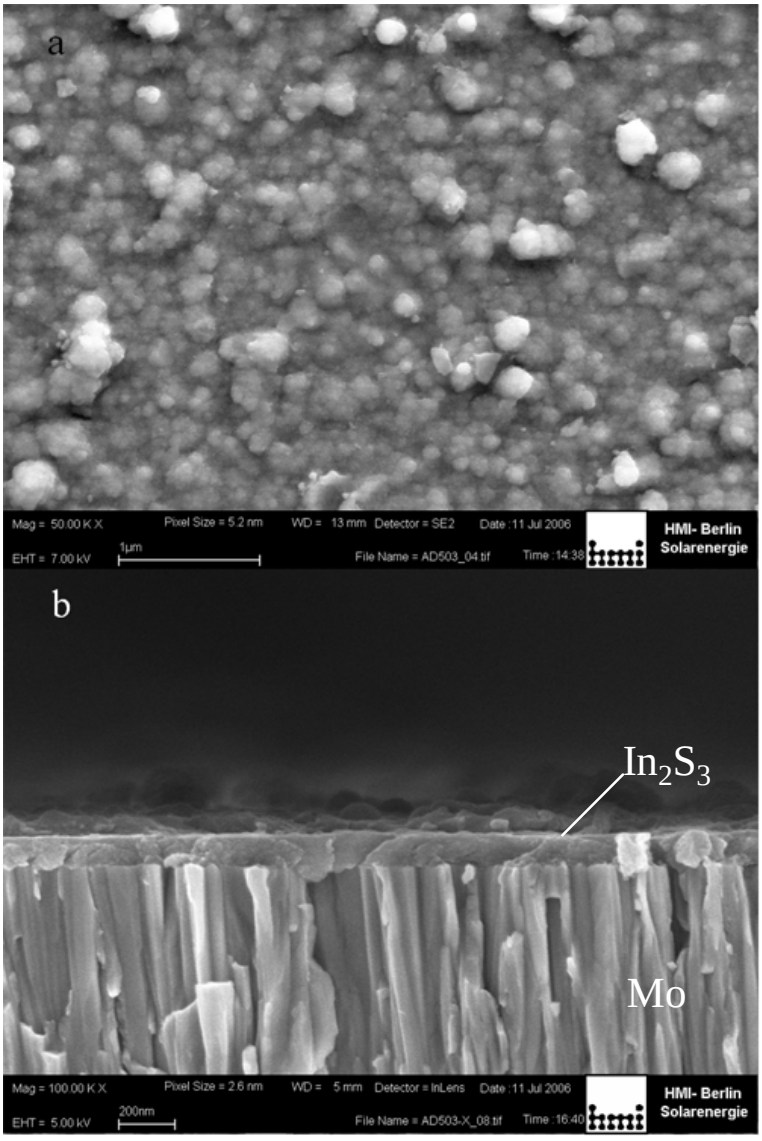

Figure II-7.4. Micrographs of the surface and cross section of a film deposited for 10 minutes on a molybdenum coated glass from solution A.

The film cross section shows well adhering films without voids, consisting of particles which size is close to or below the image resolution (about 10 nm).

The 10 minute deposition time yielded a thickness of 120 nm, about twice that necessary for a buffer layer. For device fabrication, a deposition time of 5 minutes was used, yielding at the same time smoother surfaces.

EDX analysis was carried out on films deposited from solution A on graphite substrates, because the main peaks of sulfur and molybdenum coincide. In/S ratio close to the stoichiometric 2/3 was found. Certain but difficult to quantify oxygen content was detected as well. As will be discussed within the XPS results, this is due to the presence of hydroxide species.

X-Ray Photoelectron Spectroscopy

XPS analysis was carried out on samples deposited on Glass/Mo/$CuInS_2$ structures from solution A. Good reproducibility in film composition was observed. In order to study the effect of low temperature anneal on film composition, after the first measurement, the sample was heat treated for 10 minutes at 200ºC without breaking the ultra high vacuum. By use of a computer controlled manipulator, the measurement was repeated at the exact initial sample position. The XPS spectra of a film before and after anneal are presented in Figure II-7.5a. No copper peaks are observed, indicating complete coverage of the absorber layer.

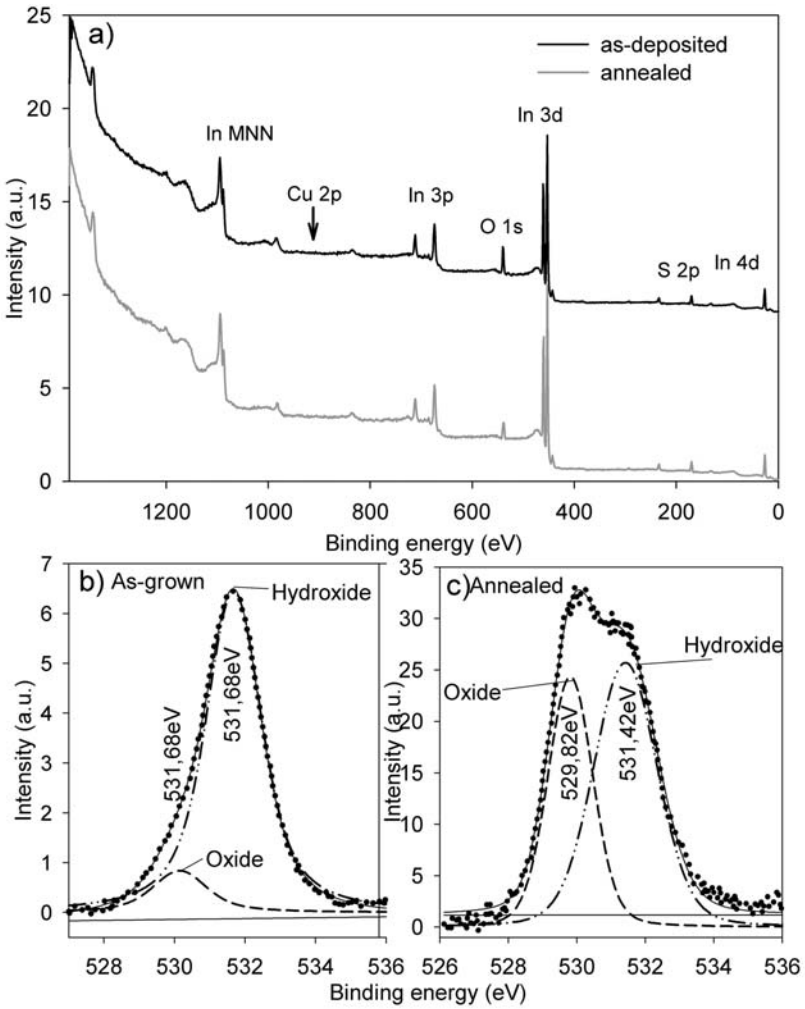

Figure II-7.5. XPS spectra of a sample deposited from solution A: overview (a) and spectral difference of O 1s peak of as-deposited (b) and annealed (c) sample.

Similarly to previous XPS studies of hydroxide-containing buffer layers such as Zn(O,OH) where the samples are heated or irradiated with synchrotron radiation[153,153], we observed the contributions of at least two peaks of the O1S, i.e. from oxide and hydroxide both before and after anneal. While the untreated samples exhibit a dominant higher energy component ascribed to hydroxide (Figure II-7.5b), heat treatment leads to an increase in the lower energy component attributed to the presence of oxide (Figure II-7.5c).

Device properties

Air annealing the complete cell proved to be beneficial, incrementing the Voc by up to 130mV. It is unclear whether the transformation from hydroxide to oxide observed by XPS is a major factor.

Table II-7.II. Parameters of a cell with a buffer layer deposited from solution A.

Sample	Voc (mV)	Jsc (mA/cm^2)	FF (%)	η (%)
As deposited	570	21.6	43	5.3
Air annealed at 200ºC, 10min	610	23.1	50	7.0
Light soaked after anneal	614	22.9	51	7.1

The maximum conversion efficiency was 7.1% (AM 1.5, 0.5cm^2 total area), obtained with composition A on HMI $CuInS_2$/Mo/glass substrate, completed with i-ZnO/ZnO:Al window and Ni:Al grids (Table II-7.II), Figure II-7.6. Both air anneal and light soaking proved to be beneficial for the fill factor, although its value of 51% is still severely limiting cell performance. Further optimization of solution composition and film thickness is expected to improve this value. The high photo current densities are confirmed by quantum efficiency measurements which demonstrated an excellent response over the full spectral range (Fig. II-7.7).

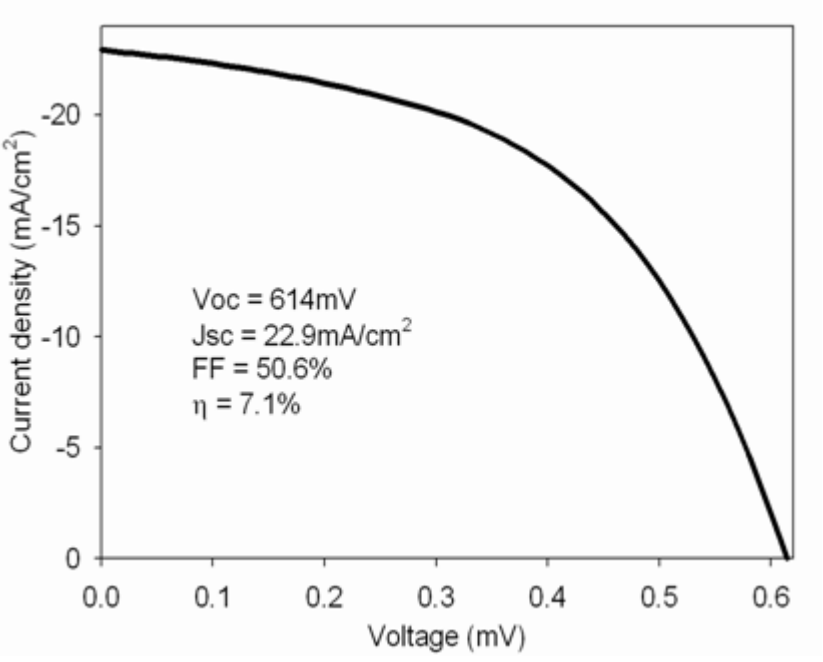

Figure II-7.6. J-V curve of $CuInS_2$ solar cell with electrodeposited In_2S_3 buffer.

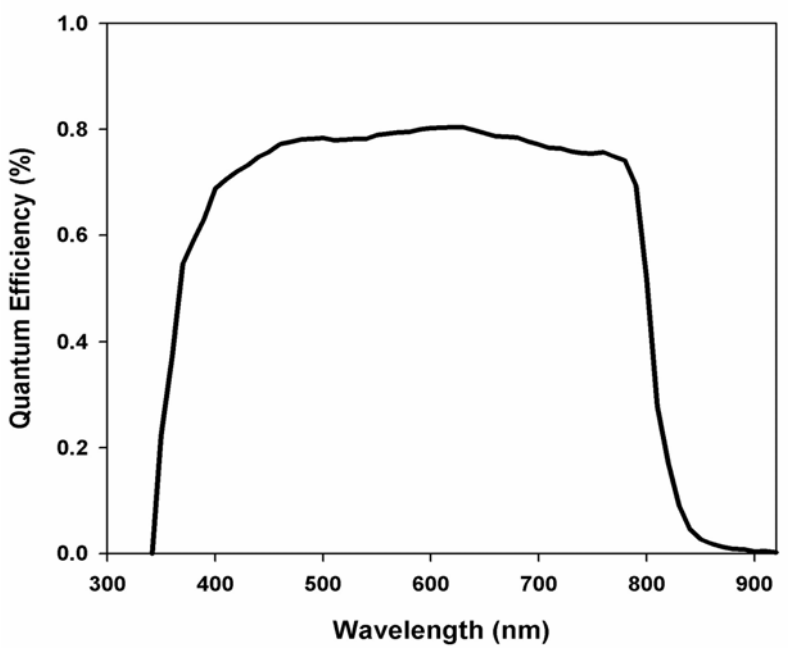

Figure II-7.7. Quantum efficiency of a 7.1% efficient solar cell.

The quantum efficiency observed is very similar to the one reported in other works on In_2S_3-buffered cells [139]. The optical properties of In_xS layers deposited by other methods (for instance CBD) are well known [155]. In particular, the fairly moderate absorption above the band gap due to the fact that the fundamental gap is indirect, can be related to the good blue response of In_xS-buffered cells.

II-7.4) Conclusions

- Successful one-step electro deposition of In_2S_3 buffer layers for $CuInS_2$ solar cells was carried out using materials and methods which can be applied in industrial production avoiding the main inconveniencies of chemical bath deposition and posing no environmental hazard.

- The obtained films exhibited good substrate coverage and microstructure.

- Open circuit photovoltage as high as 660mV an excellent photo current densities were obtained but cell performance was limited by the low fill factor.

- Judging from the strong dependence of film thickness and bath composition on cell parameters, we believe that these can be further optimized and the conversion efficiency improved.

II-8) DEVELOPMENT OF INKS FOR CIGS PRINTING

II-8.1) Introduction

As we mentioned in the Introduction, record performance devices employ Cu(In,Ga)Se_2 (CIGS). In previous sections we deposited CIGS films by sol-gel spin-coating. Significant Ga-incorporation was achieved by treatments in tubular oven and with hydride gasses. Unfortunately, results with the industrially attractive Rapid Thermal Processing were not satisfactory. On the other hand, paste coating (printing) has advantage over spin-coating in terms of throughput, scalability and simplicity of equipment.

The present chapter provides some results of a new printing approach for one-step CIGS printing that yields excellent Ga-incorporation by RTP. Absorbers were “doctor-bladed” on molybdenum-coated glass substrate and subjected to RTP. Homogeneous layers of well-crystallized quaternary phase were obtained. So far 7.5% efficient devices have been achieved. The work was developed in collaboration with IRDEP (Institut de Recherche et Développement sur l'Énergie Photovoltaïque).

Due to confidentiality issues parts from this section were removed. Further information is available to evaluators upon request.

II-8.2) Experimental

Precursors were prepared in the form of powder and redispersed to form printable pastes.

Table II-8.I. Precursor composition.

Ref.	X-ray Fluorescence			EDX		
	Cu/ (In+Ga)	Ga/ (In+Ga)	Se (%)	Cu/ (In+Ga)	Ga/ (In+Ga)	Se (%)
F5	1,17	0.24	56,0	1,3	0.26	41,9
F6	Cu	-	54,4	Cu	-	42,1
F7	0,00	0.25	58,7	0	23,9	51,1
F44	1.1	0.3	55.0	-	-	-
FTA	0.87	0.21	55.1	-	-	-
FTB	0.81	0.21	57	-	-	-
FTC	*0.95*	*0.2*	*55*	-	-	-

Film deposition

Molybdenum-coated glass substrates were “doctor-bladed” by use of 50μm thick scotch tape and a glass rod. The substrates were then transferred to a home-made setup, consisting of graphite wafer mounted on a hot plate, typically preheated to 350ºC and immediately covered by a glass-bell equipped with a safety extraction system designed to neutralize any possible selenium emissions through a KOH filled bubbler system. The rapid thermal treatment was carried out in a commercial RTP oven at approximately 550 ºC, with average heating rate of 500ºC/min.

Solar cells were completed by chemically deposited CdS and sputtered i-ZnO/ZnO:Al window.

II-8.3) Results and discussion

Analysis of annealed samples

The composition of the samples pretreated in air at 350ºC did not show significant deviation from initial composition, except for minor (about 5%) selenium loss (Table II-8.II.)

Rapid thermal anneal in atmosphere containing 6 mg selenium lead to increased selenium content, to a total of up to 70% measured by XRF. High Se content in the absorber was not confirmed by EDX and this could be an indication that it is due mainly to the formation of Mo_xSe at the bottom of the film, as observed by Scanning electron microscopy.

Table II-8.II. Composition of samples after air pretreatment at 350ºC and RTP, and best cell parameters for the corresponding sample.

Film/ Treatment	**Prec**	**Cu/ (In+Ga)**	**Ga/ (In+Ga)**	**(%)Se/ (Se+Me)**	**Rsh (Ω)**	**Rs (Ω)**	**Voc (mV)**	**Jsc (mA/ cm^2)**	**FF (%)**	***η (%)***
F10-3 350ºC	*F5*	*1.11*	*0.20*	*51*	-	-	-	-	-	**-**
F10-3 RTP	F5	0.93	0.17	68	1464	44	492	21	52	***5.4***
F371 350ºC	*F5*	*1.07*	*0.20*	*47.9*						
F37-2 RTP	F5	1.14	0.19	56.4	812	65	388	15	46	***2.7***
F462 350ºC	*F44*	*1.44*	*0.28*	*51*						
F462/4 RTP	F44	1.38	0.26	56	2388	55	448	16	54	***3.9***
AA8 RTP	FTA	0.90	0.16	68						
AAX	FTA	-	-	-	2668	23	451	26	62	***7.2***
AD2 RTP	FTA	-	-	-	-	-	460	-	-	***7.5***
BA2 RTP	FTB	0.76	0.14	69						
BA7	FTB	-	-	-	374	44	280	21	44	***2.5***
CA8-RTP	*FTC*	*0.93*	*0.15*	*67*	*989*	*58*	*346*	*13*	*47*	***2.1***

Thermogravimetry / Differential Thermal Analysis (TG/DTA).

When no TEA is added, after initial dehydration, the powders decompose above 500ºC in good agreement with previous reports [156]. In the case of TEA-containing inks, after ethanol elimination, an exothermal peak indicating reduction is observed at about 180ºC. At this point rapid mass loss is initiated and sustained until about 350ºC with little difference between air or argon atmosphere (Figure II-8.2a).
Above 500ºC this difference is substantial, attributed in air to selenide oxidation and evidenced by exothermal peak of F5T (absent in the argon-treated sample) (Figure 1b).

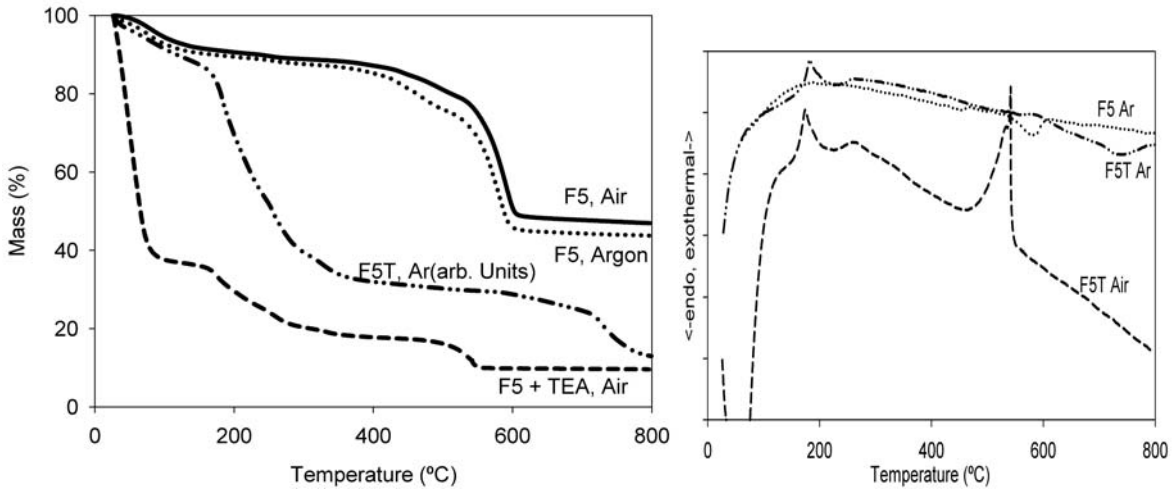

Figure II-8.2. TG/DTA air and argon at 10ºC/min of pure powders (F5) and TEA-containing inks (marked both as F5T, although the sample treated in argon contains less or no ethanol due to evaporation).

X-ray diffraction

XRD data indicated that the precursor powders were amorphous. Air pretreatment already yields Cu(In,Ga)Se_2 together with various secondary phases (Figure II-8.3). Rapid thermal processing yielded highly crystalline CIGS phase. In most samples with low performance we observed peak displacements and secondary peaks. Further analysis of XRD data is necessary in order to evaluate properly this asymmetry, as well as the presence of other phases evidenced by secondary peaks. In the higher performance samples, the patterns match $CuIn_{0,7}Ga_{0,3}Se_2$, JCPDS 35-1102 as shown in Figure II-8.3. The peak at 40.5º 2theta is due to the molybdenum substrate and the broad peaks at 31,4 and 52,9 may be due the formation of molybdenum selenides at the absorber/Mo interface ($MoSe_2$ JCPDS 40-0908) as observed by SEM.

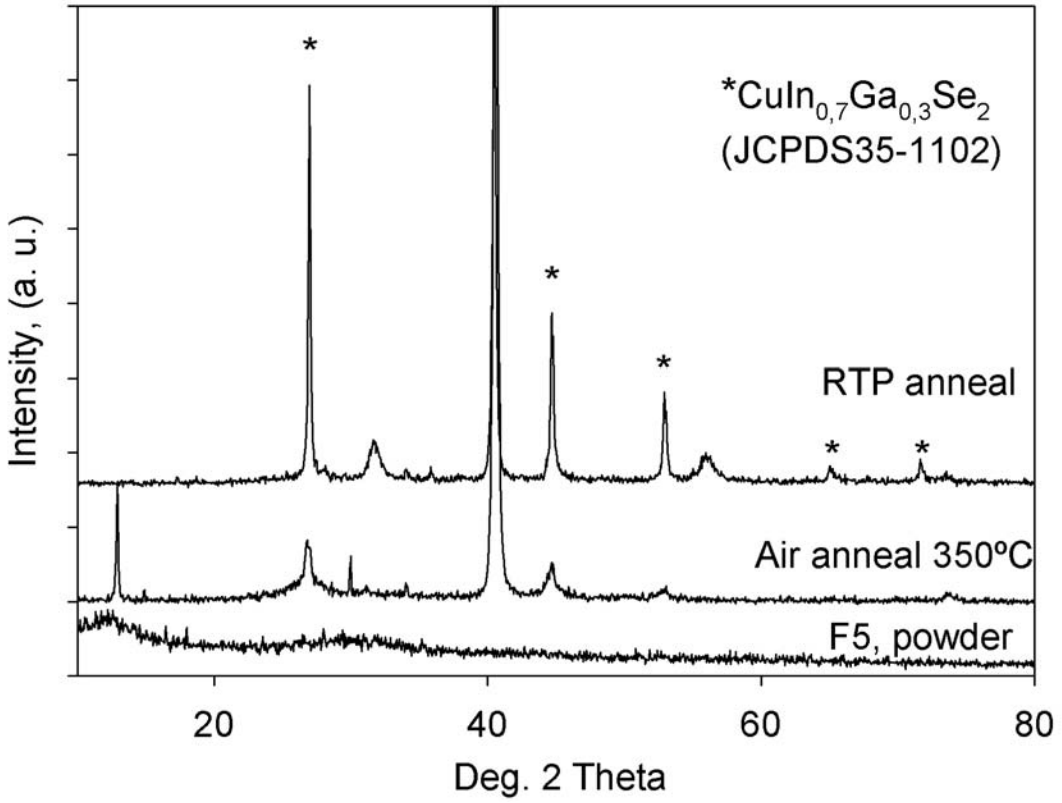

Figure II-8.3. XRD pattern of samples from F5 precursor at different treatment stages: precursor powder, printed film annealed in air at 350ºC and final rapid thermal processed absorber (F10-3).

Scanning Electron Microscopy

The amorphous powder precipitates contained nanoparticles with size less than 100nm (Figure II-8.4a). We could not establish if these particles were in fact agglomerates of even smaller particles, as may be inferred by the amorphous XRD patterns.

Films deposited on Mo-coated glass after air anneal at 350ºC had excellent adherence and uniformity (Figure II-8.4b). Following air anneal, the Rapid Thermal Treatment in Ar atmosphere, leads to the formation of larger crystallizations at the surface (Figure II-8.4c) while this effect was less pronounced in depth (Figure II-8.4d). Selenium excess during RTP selenization leads to the formation of a $MoSe_2$ underlayer with similar columnar morphology to the original Molybdenum contact, being the increased thickness after RTP an indication of its formation (Fig II-8.4b, d). This observation is supported by EDX microanalysis despite its low precision for cross sections.

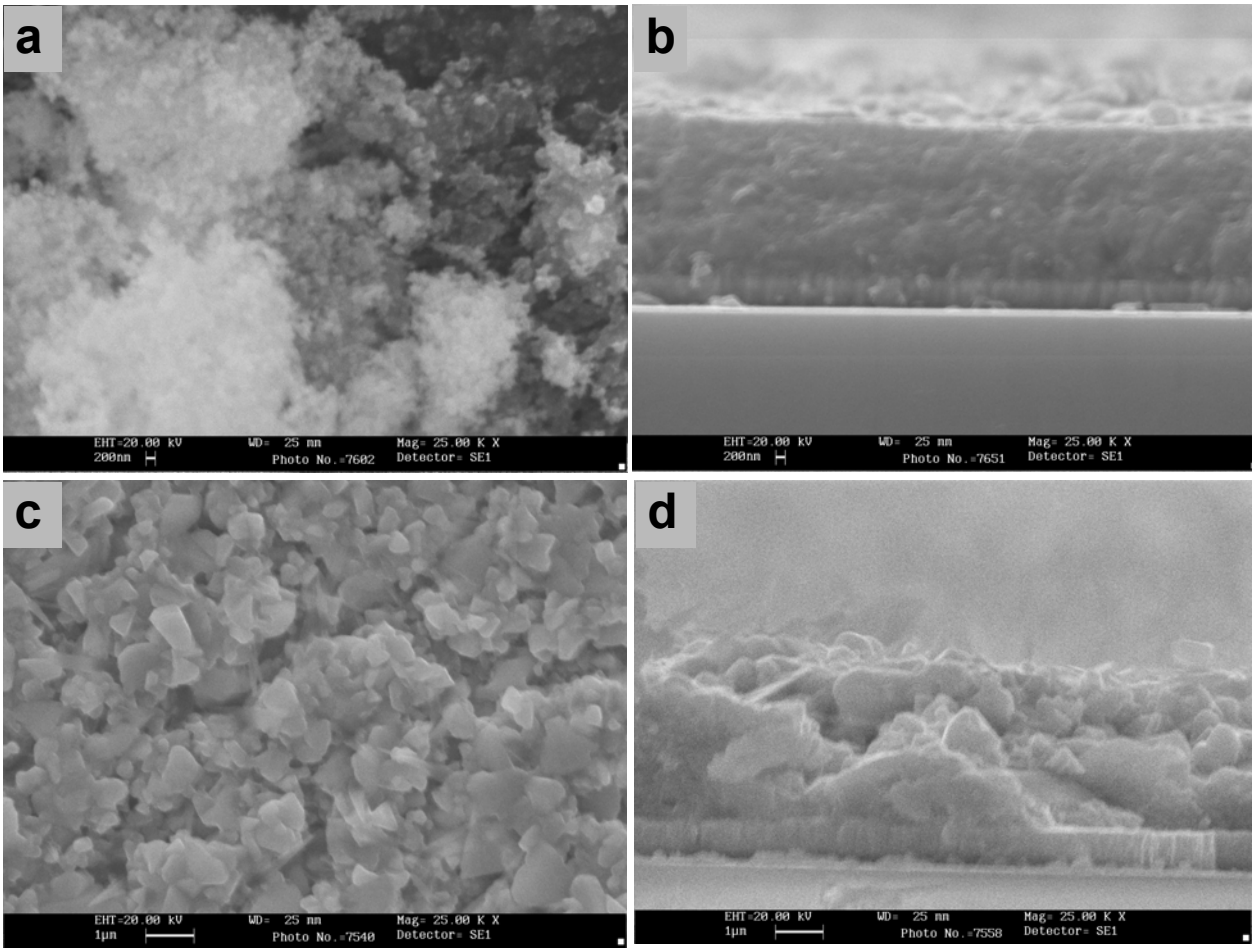

Figure II-8.4. Samples prepared at different stages of the study: precursor powder (a), cross section of a film pre-treated in air at 350ºC (b), rapid thermal treated film surface (c) and cross section (d).

Raman scattering

As discussed in the introduction, Raman scattering is an important technique for chalcopyrite characterization because of its sensitivity to the presence of undesired phases such as Cu-Au ordered phase [46-50]. In this study we did not detect the Cu-Au ordering except for one single case of Ga-free Cu-poor sample. While in different Ga-containing low-performance samples we observed secondary phases like Se and binaries (not shown), the Raman spectra of higher performance cells exhibit mainly the characteristic A1 mode frequency of Cu(InGa)Se_2. Figure II-8.5 shows the Raman spectra of sample 10-3. The peak at 176.3 cm^{-1} corresponds well to other reports (176-178cm^{-1}) [160].

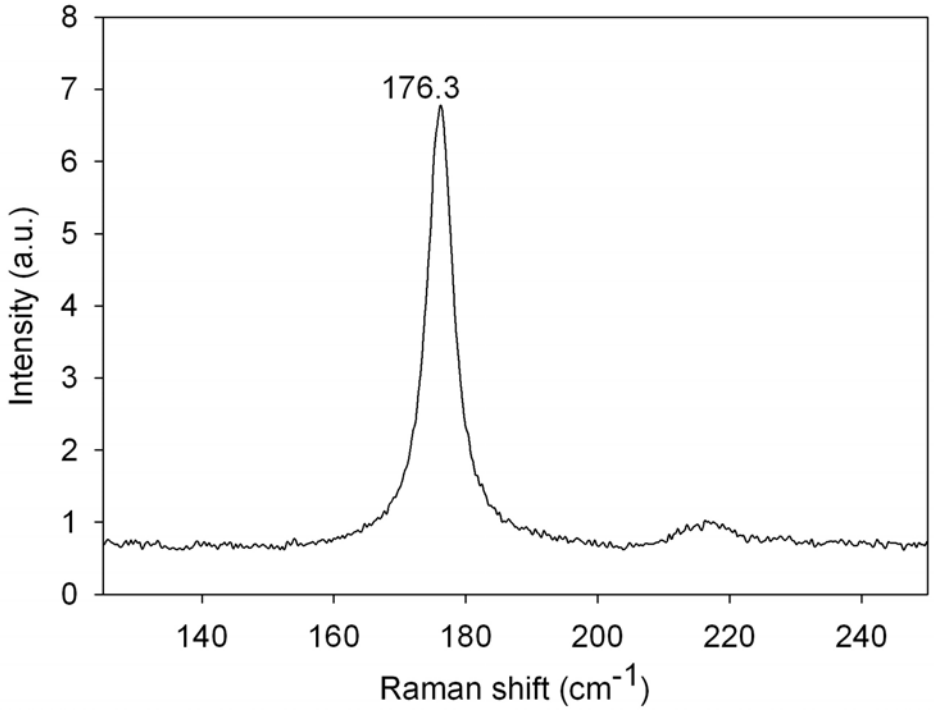

Figure II-8.5. Raman spectrum of sample 10-3, prepared from precursor F-5.

These values are higher than those for pure $CuInSe_2$ (173–174 cm^{-1}) since Ga is present in the desired phase. The A1 mode frequency increases linearly with the Ga content [162].

Cell performance:

Best cell parameters for each composition are given in Table II-8.II. Copper rich precursors did not reach efficiencies higher than 5.8% and the series F10-3, characterized in more detail above, yielded efficiency of 5,4%. The main limiting factor of these samples was low shunt resistance and fill factor which is an indication of recombination. This may be related to high conductivity of Cu-rich selenides and poor quality of the junction.

Improved cell parameters were observed with Cu-poor materials. Higher shunt resistance (2668 Ω) and 7.24% efficiency was obtained with Cu-poor sample AAX, prepared from precursor FTA (Figure II-8.6). A modified processing of the FTA precursor yielded even higher efficiency (7.5%). An investigation of the influence of all process parameters and additional sample characterization is being undertaken in order to determine the reasons for this increase and establish the route to further device improvement.

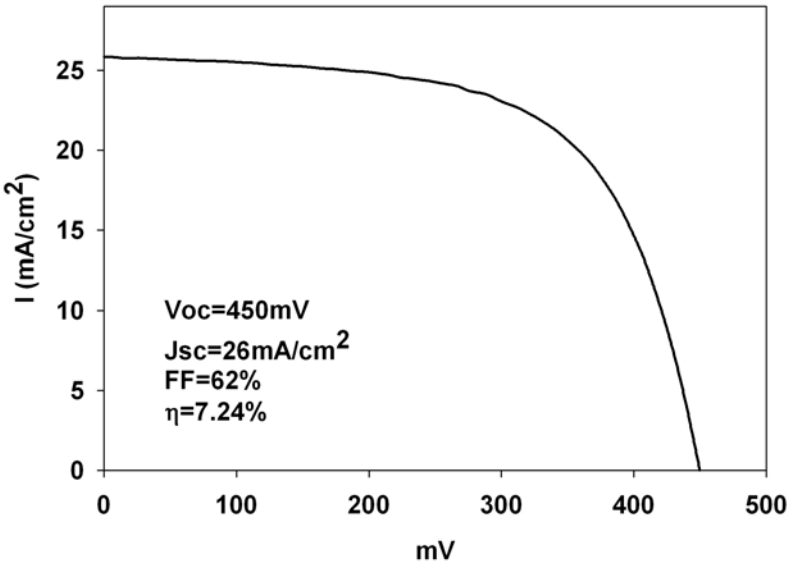

Figure II-8.6. I-V curve of cell AAX, prepared form precursor FTA.

The current density of AAX cell of 24.5mA/cm^2 determined by quantum efficiency measurements (Figure II-8.7) was close to the one observed from the J-V curve. The quantum efficiency (expressed in external values) is close to 75% in the short wavelength range, showing a good collection of the photogenerated electron holes pairs. The decrease of the quantum efficiency towards longer wavelengths indicates that the collection length (space charge width plus diffusion length of electrons) can be improved. The effective band gap determined from the spectral response was 1.12 eV which is another indication of substantial Gallium incorporation in the chalcopyrite film, close to the effective values of record performance devices, 1.14eV with 30% nominal Ga/(In+Ga) ratio [163].

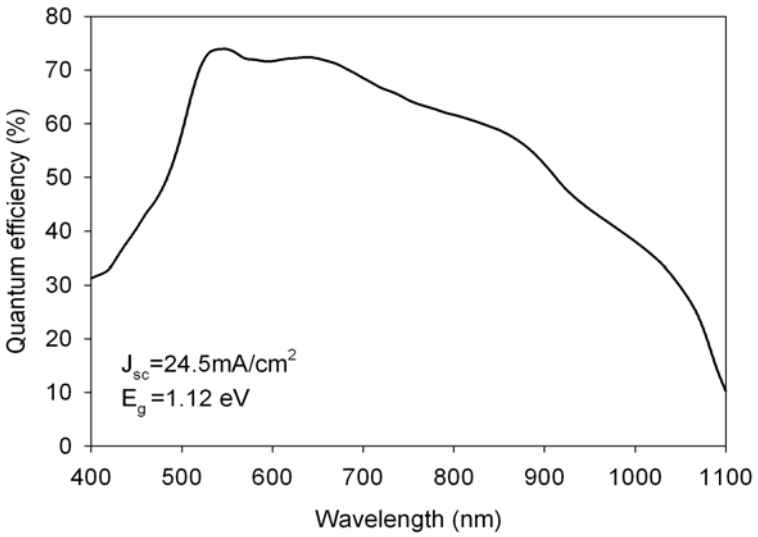

Figure II-8.7. Quantum efficiency of sample AAX prepared from precursor FTA.

II-8.4) Conclusions

- Nanometric precursor powders containing Cu-In-Ga-Se in desired ratio were obtained by a simple route.
- Pastes were deposited by printing method and subjected to Rapid Thermal Treatment yielding Cu(InGa)Se_2 with good crystallinity, as evidenced by X-ray diffraction and Raman spectroscopy.
- Cu-poor materials yielded better efficiency (7.5%) in comparison with Cu-rich compositions which suffered from very low shunt resistance.
- Quantum efficiency showed high carrier collection at short wavelengths and indicated that collection length can be further improved. The effective band gap of 1.12 eV confirmed the substantial Ga-incorporation observed by Raman spectroscopy and XRD.

GENERAL CONCLUSIONS OF THE THESIS

1) Different thin-films were obtained by use of two principal low-cost methods: spin-coating and printing.

2) Nanocrystalline TiO_2 films prepared by the sol-gel method showed high bactericidal activity but were too compact to be applied in dye cells.

3) Chalcopyrite films prepared in Part II showed superior performance in photovoltaic devices in comparison to mesoporous TiO_2 cells employing solid electrolytes.

4) Several of the promising absorber candidates for future photovoltaic production were obtained, most of them by novel approaches: $CuInS_2$, $Cu(In,Ga)Se_2$, $Cu(In,Ga)(S,Se)_2$, Cu_2ZnSnS_4.

5) In addition to absorber layers, alternative cadmium-free buffer layers for $CuInS_2$ devices were deposited by electro deposition.

6) Maximum photoelectric conversion efficiency of 7.5% was obtained by a novel printing method for $Cu(InGa)Se_2$.

7) Further optimization of several of the methods proposed is expected to yield even higher efficiencies.

LIST OF PUBLICATIONS:

JOURNALS:

1) T. Todorov, E. Cordoncillo, J.F. Sánchez-Royo, J. Carda, P. Escribano, *$CuInS_2$ Films for Photovoltaic Applications Deposited by a Low-Cost Method,* Chemistry of Materials 18 (2006) 3145

2) T. Todorov*, L. Oliveira, J. Carda, and P. Escribano, *Influence of treatment conditions on chalcopyrite films deposited at atmospheric pressure*, Physica Status Solidi, 11, (2008)3437–3440.

3) T. Todorov, J. Carda, P. Escribano, A. Grimm, J. Klaer, R. Klenk, *Electro deposited In2S3 buffer layers for CuInS2 solar cells*, Solar Energy Materials & Solar Cells 92 (2008) 1274– 1278

4) L. Oliveira, T. Todorov, E. Chassaing, D. Lincot, J. Carda, P. Escribano *CIGSS Films Prepared by Sol-Gel Route*, Thin Solid Films, Accepted for publication via E-MRS 2008, Strasbourg.

5) T. Todorov, M. Kita, J. Carda, P. Escribano, *Cu_2ZnSnS_4 Films Deposited by a Soft-Chemistry Method*, Thin Solid Films, Accepted for publication via E-MRS 2008, Strasbourg.

CONFERENCE PROCEEDINGS:

1) T. Todorov, E. Cordoncillo, F. Fabregat, I. Mora-Sero, H. Beltrán, V. Kozhukharov, J. Carda, *Effect of Preparation Methods and Conditions on Nanocrystalline Anatase Properties* , Proceedings vol.D, 10^{TH} International Ceramics Congress, CIMTEC 2002, Florence, Italy ISBN 88-86538-35-9 p 395.

2) T. Todorov, E. Cordoncillo, J. Carda, P. Escribano, *Characterization of $CuInS_2$ Films Deposited by a Low-Cost Method*, Proceedings 21-th European Photovoltaic Solar Energy Conference and Exhibition, Dresden, 4-8 sept. 2006, ISBN 3-936338-20-5, p.1969.

CONFERENCE CONTRIBUTIONS:

1) T. Todorov, E.Cordoncillo, F. Fabregat, J.B. Carda, Development of Sol-Gel Solid *Electrolytes for Dye-sensitised Solar Cells, NATO Advanced Study Institute: Organic Conductors, Cuperconductors and Magnets: From Synthesis to Molecular Electronics,* Corfu, Greece 29/04-11/05/2003

2) T. Todorov, E. Cordoncillo, F. Fabregat-Santiago, J.B. Carda, J. Bisquert, G. García – Belmonte, I. Mora *Dióxido de Titanio Nanoporoso Utilizado en Células Solares de Colorante*, VI Reunion Nacional de Electrocerámica y V Conferencia Iberoamericana, Castellón, España, 19-21/07/2003.

3) T. Todorov, E. Cordoncillo, P. Escribano, F. Fabregat, J.M. Pedra, J.B. Carda, *Sol-Gel Preparation of Nanocrystalline Films for Solar Cell and Bactericidal Applications*, European Congreso on Advanced Materials and Processes EUROMAT 2003, Lausanne, Switzerland 1-5/09/2003.

4) T. Todorov, J.B. Carda, Backed Up By the Past, Looking Into the Future: *Will New Materials Or New Technology Bring Photovoltaics to the People?*, Euroconference Photovoltaic Devices- EUROPV-2003, Granada, Spain, 7-12/11/2003

5) T. Todorov, J. Carda, E. Cordoncillo, P. Escribano, J. Klaer, R. Klenk, *Optimization Of Electro Deposited In_2S_3 Buffer Layers In $CuInS_2$ Cells*, Materials Research Society Spring Meeting-2007, Symposiym Y: Thin-Film Compound Semiconductor Photovoltaic, 9-13/04/2007 San Francisco, USA.

BIBLIOGRAFÍA PARTE I

[1] G. Centi, R. Santen, *Catalists for renewables: From Feedstock to Energy Production*, Wiley-VCH Verlag, Weinheim 2007, ISBN 978-3-527-31788-2.

[2] Energy Information Administration, U.S. Department of Energy, *Energy Outlook 2005*, www.eia.doe.gov/oiaf/ieo/index.html.

[3] Energy Information Administration, U.S. Department of Energy, *System for the Analysis of Global Energy Markets (2005), International Energy Annual 2002*,DOE/EIA-0219(2002) (Washington,DC,March 2004), www.eia.doe.gov/iea/.Projections:EIA.

[4] B. Goodfrey, *Renewable Energy Power for Sustainable future*, Oxford University Press, 1996.

[5] M. Asif, T. Muneer, *Energy supply, its demand and security issues for developed and emerging economies*, Renewable and Sustainable Energy Reviews
11 (2007) 1388–1413.

[6] P.G. Romero, *Aplicaciones energéticas de los nanomateriales*, VIII Ciclo de Conferencias Por Donde Va la Ciencia?, Castellón, 26.02.2004.

[7] C. Campbell & J. Laherrere, *The End of Cheap Oil*, Science, 281 (1998) 1128.

[8] J. Goldemberg, World Enegry Assessment: *Energy and the Challenge of Sustainability*, UNDP, New York, 2000.

[9] N. Lewis, J. Crabtree, *Basic Research Needs for Solar Energy Utilization: report of the Basic Energy Sciences Workshop on Solar Energy Utilization*, US Department of Energy, Office of Basic Energy Science, Washington, DC, 2005, www.sc.doe.gov/bes/reports/files/SEU_rtp.pdf

[10] H. Scheer, *The Solar Economy: Renewable Energy for a Sustainable Global Future*, Earthscan, London 2002. ISBN 1853838357.

[11] O. Morton, *Solar energy: A new day dawning?: Silicon Valley Sunrise*, Nature 443 (2006) 19-22.

[12] A. Simon, *Energy flow charts, Global Climate and Energy Project, Stanford University*, http://gcep.stanford.edu/research/exergycharts.html.

[13] L. Travis, *NASA International Satellite Cloud Climatology Project (ISCCP)*, http://isccp.giss.nasa.gov/

[14] S. Izquierdo, M. Rodrigues, Norberto Fueyo, *A method for estimating the geographical distribution of the available roof surface area for large-scale photovoltaic energy-potential evaluations*, Solar Energy 82 (2008) 929.

[15] *Libro Blanco de la Generación Eléctrica en España*, APPA, http://www.appa.es/descargas/APPA_LIBRO_BLANCO_2002_03_05.pdf

[16] K. Kurokava, K. Komoto, P. Vleuten, D. Faiman, *Energy from the Desert*, Earthscan 2007,ISBN:1844073637.

[17] Wissenschaftlicher Beirat der Bundesregierung Globale Umweltveränderungen, *Welt im Wandel: Energiewende zur Nachhaltigkeit*, Springer ISBN 3-540-40160-1

[18] T. Markvart, L. Castañar, (H.W. Schock) *Practical Handbook of Photovoltaics*, Oxford, 2003, ISBN 1856173909.

[19] Internacional Energy Agency, *Report IEA-PVPS T1-16:2007,* www.iea-pvps.org/products/download/rep1_16.pdf

[20] A. Goetzberger, H. Hebling, H.W. Schock, *Photovoltaic materials. History, status and outlook*, Materials Science and Engineering R 40 (2003) 1–46

[21] Best Research Cells, www.nrel.gov/pv/thin_film/docs/kaz_best_research_cells.ppt

[22] M. Green, K. Emery, Y. Hishikawa, W. Warta, *Solar Cell Efficiency Tables* (Version31) Prog. Photovolt: Res. Appl. 2008; 16:61–67.

[23] J. Hofstetter, J.F. Lelièvre, C. del Cañizo, A. Luque, *Acceptable contamination levels in solar grade silicon: From feedstock to solar cell*, Materials Science and Engineering: B, In Press, 2008.

[24] A. Luque, S. Hegedus, W. Shafarman, *Handbook of Photovoltaic Science and Engineering,* Wiley, Wienheim 2003, ISBN 0-47149196-9

[25] S. Tomasco, *IBM Research Unveils Breakthrough In Solar Farm Technology*, IBM Press Release, Armonk 2008.

[26] see [18]

[27] see [22]

[28] C. Riuz Herrero, *Modificación de las Propiedades Optoelectrónicas Por Medio del dopado con Bi en Células Fotovoltaicas Basadas en CdTe*, Tesis Doctoral, Universidad Autonoma De Madrid, 2007

[29] V. Fthenakis, H.Kim CdTe photovoltaics: *Life cycle environmental profile and comparisons*, Thin Solid Films, 515 (2007) 5961-5963.

[30] IBM, *Voluntary materials prohibitions and restrictions,* http://www.ibm.com

[31] see [22]

[32] K. Zweibel, *Thin film PV manufacturing: Materials costs and their optimization*, Solar Energy Materials & Solar Cells 63 (2000) 375-386.

[33] B. O´Regan, M. Grazel, *A Low-cost, High-efficiency Solar Cell Based on Dye-sensitized Colloidal TiO_2 Films*, Nature 353 (1991) 737

[34] Picture, www.epfl.ch

[35] U. Bach, Y. Tachibana, S. Haque, J. Moser, J. Durrant, M. Gratzel, D. Klug, *Charge Separation in Solid-State Dye-Sensitized Heterojunction Solar Cells*, J. Am. Chem. Soc.; 121(32) (1999) 7445-7446.

[36] F. Fabregat-Santiago, I. Mora-Seró, G. Garcia-Belmonte and J. Bisquert, *Cyclic Voltammetry Studies of Nanoporous Semiconductors. Capacitive and Reactive Properties of Nanocrystalline TiO_2 Electrodes in Aqueous Electrolyte*, J. Phys. Chem. B 107, 758 (2003).

[37] G. Boschloo, H. Lindström, E. Magnusson, A. Holmberg, A. Hagfeldt, *Optimization of dye-sensitized solar cells prepared by compression method* Journal of Photochemistry and Photobiology A: Chemistry 148 (2002) 11–15

[38] www.konarka.com

[39] J. Bisquert, G. García-Belmonte, F. Fabregat, Albert Compte, *Anomalous transport effect in the impedance of porous film electrodes*, Electrochemistry Communications 1(1999) 429-435.

[40] H. Tributsch, F. Willig, *Rate constants of interfacial electron transfer reactions: Current flow in nm-structured TiO2 electrodes,* Sol. Energy Mater. Sol. Cells 38 (1995) 355

[41] K. Kalyanasundaram, M. Graetzel, *Applications of functionalized transition metal complexes in photonic and optoelectronic devices,* Coordination Chemistry Reviews 77 (1998) 347–414

[42] G. Calogero, G. Di Marco, *Red Sicilian orange and purple eggplant fruits as natural sensitizers for dye-sensitized solar cells,* G. Solar Energy Materials and Solar Cells, 92-11 (2008)1341-1346.

[43] Murakami, M. Graetzel, *Counter electrodes for DSC: Application of functional materials as catalysts*, Inorganica Chimica Acta 361 (2008) 572–580

[44] B. Li, L. Wang, B. Kang, P. Wang, Y. Qiu, *Review of recent progress in solid-statedye-sensitized solar cells,* Solar Energy Materials & Solar Cells 90 (2006) 549–573

[45] K. Tennakone, V.P.S. Perera, I.R.M. Kottegoda, Grra. Kumara, *Dye-Sensitized Photoelectrochemical Cells Based on Porous SnO_2/ZnO Composite and TiO_2 Films with a Polymer Electrolyte*, J. Phys. D-Appl. Phys. 32 (1999)

[46] K. Tennakone, Grra. Kumara, A.R. Kumarasinghe, K.G.U. Wijayantha, P.M. Sirimanne, *A dye-sensitized nano-porous solid-state photovoltaic cell*, Semicond. Sci. Technol. 10 (1995) 1689

[47] V.P.S. Perera, K. Tennakone, *Recombination processes in dye-sensitized solid-state solar cells with CuI as the hole collector,* Sol. Energy Mater. Sol. Cells 79 (2003) 249

[48] Q.B. Meng, K. Takahashi, X.T. Zhang, I. Sutanto, T.N. Rao, O. Sato, A. Fujishima, H. Watanabe, T. Nakamori, M. Uragami, *Fabrication of an Efficient Solid-State Dye-Sensitized Solar Cell* ,Langmuir 19 (2003) 3572..

[49] Y.J. Ren, Z.C. Zhang, S.B. Fang, M.Z. Yang, S.M. Cai, *Application of PEO based gel network polymer electrolytes in dye-sensitized photoelectrochemical cells,* Sol. Energy Mater. Sol. Cells 71 (2002) 253.

[50] R. Komiya, L. Han, R. Yamanaka, A. Islam, T. Mitate, *Highly efficient quasi-solid state dye-sensitized solar cell with ion conducting polymer electrolyte*, J. Photochem. Photobiol. A-Chem. 164 (2004) 123

[51] M.K. Nazeeruddin, A. Kay, I. Rodicio, R. Humphrybaker, E. Muller, P. Liska, N. Vlachopoulos, M. Graetzel, J. Am. Chem. Soc. 115 (1993) 6382.

[52] Saito, N. Fukuri, R. Senadeera, T. Kitamura, Y. Wada, S. Yanagida, *Solid state dye sensitized solar cells using in situ polymerized PEDOTs as hole conductor*. Electrochem. Commun. 6 (2004) 71.

[53] Saito, T. Kitamura, Y. Wada, S. Yanagida, *Poly(3,4-ethylenedioxythiophene) as a hole conductor in solid state dye sensitized solar cells*, Synth. Met. 131 (2002) 185.

[54] West, *Solid State Chemistry and its Applications*, John Wiley & Sons Ltd., 1984.

[55] M. Koelsch, S. Cassaignon, C. Ta Thanh Minh, J.-F. Guillemoles, J.-P. Jolivet *Electrochemical comparative study of titania (anatase, brookite and rutile) nanoparticles synthesized in aqueous médium*, Thin Solid Films 451 –452 (2004) 86–92.

[56] H. Koo, J. Park, B. Yoo, K. Yoo, K. Kim, N. Park, *Size-dependent scattering efficiency in dye-sensitized solar cell*, Inorganica Chimica Acta 361 (2008) 677–683.

[57] Akira Fujishima, Tata N.Rao, *Journal of Photochemistry and Photobiology C: Reviews* 1 (2000)1-21.

[58] R.Cai, K. Hashimoto, Y.Kubota, A. Fujishima, *Photokilling of Malignant Cells with Ultrafine TiO 2 Powder*, Bull. Chem.Soc.Jpn.64(1991)1268-1273.

[59] A. Fujishima, Tata N. Rao, Donald A. Tryk, *Titanium dioxide photocatalysis*, Journal of Photochemistry and Photobiology C: Photochemistry Reviews, (2000) 1-21

[60] O.Legrini, E.Oliveros, *Photochemical processes for water treatment*, Chemical Reviews, 93, 671 (1993)

[61] V. Kozhukharov, P.Vitanov, *TiO_2-photocatalyzed oxidative water pollutants degradation: a review of the state-of-art*, Journal of Environmental Protection and Ecology 2, No1, 107-111 (2001)

[62] *Nanoparticles: Materials for the New Millennium*, www.altair.com

[63] A. Hagfeldt, M. Gratzel, *Light-Induced Redox Reactions in Nanocrystalline Systems,* Chem. Rev. 95 (1995), 49-68.

[64] E. Cordoncillo, J.B. Carda, M.A. Tena, G. Monros, P. Escribano, *Synthesis of Quantum-Size Cadmium-Zinc Sulfide Particle-Doped Glasses by the Sol-Gel Method*, Journal of Sol-Gel Science and Technology 8, 1043–1047 (1997)

[65] P. Escribano, B. Julián-López, J. Planelles-Aragó, E. Cordoncillo, B. Viana and C. Sanchez, *Photonic and nanobiophotonic properties of luminescent lanthanide-doped hybrid organic–inorganic materials*, J. Mater. Chem.18 (2008) 23 – 40.

[66] J. Bisquert, F. Fabregat-Santiago, I. Mora-Seró, G. Garcia-Belmonte, E. Barea, E. Palomares, *A review of recent results on electrochemical determination of the density of electronic states of nanostructured metal-oxide semiconductors and organic hole conductors*, Inorganica Chimica Acta, Volume 361, Issue 3, 15 February 2008, Pages 684-698

[67] A68 A. Zaban, *The Effect of the Preparation Conditions of TiO2 Colloids on Their Surface Structures*, J. Physical Chemistry B, 104 (2000), 4130-4133

[68] Beatriz Julián López, *Síntesis y Caracterización de Materiales Hibridos Siloxano-Óxido Dopados con Iones de Tierras Raras*, Tesis Doctoral con Mención Europea,
Universidad Jaume-I, Castellón, 17 octubre de 2003.

[69] L.E.Scriven. *Better Ceramics Through Chemistry III,* Mater. Res. Soc. Symp., Pittsburg, Pa., (1988) 717-729.

[70] A. R. West, *Solid State Chemistry and its application* Ed. John Wiley & Sons, 1996, page 174

[71] T. Todorov, E. Cordoncillo, F. Fabregat, I. Mora-Sero, H. Beltrán, V. Kozhukharov, J. Carda, *Effect of Preparation Methods and Conditions on Nanocrystalline Anatase Properties*, CIMTEC 2002, Florence, Italy, 14-19/08/2002ISBN 88-86538-35-9, sec.J, p39.

BIBLIOGRAPHY PART II

[1] A. Luque and S. Hegedus (Eds), *Handbook of Photovoltaic Science and Engineering,* John Wiley & Sons Ltd., 2003.

[2] M. A. Green, K. Emery, Y. Hishikawa and W. Warta, *Solar Cells Efficiency Tables (Version 31)*, Prog. Photovoltaics: Res. Appl. 16 (2008), p. 61.,

[3] Y. Tanaka, N. Akema, T. Morishita, D. Okumura, K. Kushiya, *Improvement of Voc upward of 600 mV/cell with CIGS-based absorber prepared by Selenization/Sulfurization*, Conf. Proceedings, 17th EC Photovoltaic Solar Energy Conference, Munich, October 2001; p. 989.

[4] H. Hahn, G. Frank, W. Klingler, A. Meyer and G. Storger, *Uber einige ternare Chalkogenide mit Chalkopyritstruktur*. Z. Anorg. u. Allg.Chemie, Vol. 271 (1953) p.153,

[5] S. Wagner, J. L. Shay, P. Migliorato and H. M. Kasper, *CuInSe2/CdS Heterojunction Photovoltaic Detectors*, Appl. Phys. Lett. Vol. 25 (1974) p. 434

[6] R. A. Mickelsen and W. S. Chen, *High Photocurrent Polycrystalline Thin-film CdS/CuInSe$_2$ solar cell*, Appl. Phys. Lett. Vol. 36, (1980) p. 371

[7] K. C. Mitchell, J. Ermer, and D. Pier, *Single and tandem junction CuInSe$_2$ cell and module technology*, Proc. 20th IEEE Photovoltaic Specialists Conf., Las Vegas, 1988 p. 1384.

[8] T. Markvart, L. Castañar, (H.W. Schock) *Practical Handbook of Photovoltaics*, Oxford, 2003, ISBN 1856173909.

[9] Haug, Franz-Josef, *Development of Cu(in,Ga)Se2 Superstrate Thin Film Solar Cells*. PhD Thesis. Zurich, 2001.

[10] T. Nakada, T. Kume, T. Mise A. Kunioka, *Superstrate- Type Cu(In,Ga)Se$_2$ thin Film Solar Cell*, Jpn. J. App. Phys. 37 (1998) L499.

[11] J. Yun, K. Kim, M. Kim, B. Ahn, S .Ahn, J. Lee, K. Yoon, *Fabrication of CIGS solar cells with a Na-doped Molayer on a Na-free substrate*, Thin Solid Films, Volume 515(2007), 5876-5879

[12] F. Kessler, D. *Rudmann, Technological aspects of flexible CIGS solar cells and modules*, Solar Energy 77 (2004), p. 685.

[13] T. Nakada, Y. Hirabayashi, T. Tokado, D. Ohmori, T. Mise*, Novel device structure for Cu(In,Ga)Se2 thin film solar cells using transparent conducting oxide back and front contacts,* Solar Energy 77 (2004), p. 739.

[14] D. Hariskos, S. Spiering, M. Powalla, *Buffer layers in Cu(In,Ga)Se2 solar cells and modules,* Thin Solid Films 480–481 (2005) p. 99.

[15] H.W. Schock, R. Noufi, *CIGS-based Solar Cells for the Next Millennium*, Prog. Photovolt. Res. Appl. 8 (2000), p. 151.

[16] R. Klenk, J. Klaer, D. Scheer, M. Lux-Steiner, I. Luck, N. Meyer, U. Ruhle, *Solar cells based on $CuInS_2$—an overview,* Thin Solid Films 480 - 481 (2005), p. 509.

[17] R. Klenk*, Characterisation and modelling of chalcopyrite solar cells,* Thin Solid Films 387 (2001), p. 135.

[18] N. A. Allsop, A. Schoenmann, H.-J. Muffler, M. Bar, M. C. Lux-Steiner and Ch.-H. Fischer, *Spray-ILGAR indium sulfide buffers for $Cu(In,Ga)(S,Se)_2$ solar cells*, Prog. Photovolt: Res. Appl. 13 (2005), p. 607.

[19] D. Hariskos, S. Spiering, M. Powalla*, Buffer layers in $Cu(In,Ga)Se_2$ solar cells and modules,* Thin Solid Films 480–481 (2005), p. 99.

[20] Ch. Kaufmann, *Chemical bath Deposition of Thin Semiconductor Films for Use as Buffer Layers in $CuInS_2$ Thin Film Solar Cells*, PhD Thesis, Queen´s College Oxford, Hilary, 2002.

[22] T. Nakada, K. Furumi, A. Kunioka, *High Efficiency Cadmium-free $CuIn,Ga)Se_2$ thin-film solar cells with chemically deposited ZnS buffer layers*, IEEE Trans. Electron Devices 46 (1999) 2093-2097.

[23] M. Bär, A. Ennaoui, J. Klaer, R. Sáez-Araoz, T. Kropp, L. Weinhard, C. Heske, H.-W. Schock, Ch.-H. Fischer,M.C. Lux-Steiner, *The electronic structure of the [Zn (S, O)/ZnS]/$CuInS_2$ heterointerface—impact of post-annealing,* Chem. Phys. Lett. 433 (2006), p. 71.

[24] Z. Djebbour, A. Darga, A. Migan Duboi, D. Mencaraglia, N. Naghavi, J.-F. Guillemoles, D. Lincot*, Admittance spectroscopy of cadmium free CIGS solar cells heterointerfaces,* Thin Solid Films 511 – 512 (2006), p. 320.

[25] S. Siebentritt, *Alternative buffers for chalcopyrite solar cells,* Solar Energy 77 (2004), p. 767.

[26] D. Gal, G. Hodes, D. Hariskos, D. Braunger, H.-W. Schock, *Size-quantized CdS films in thin film $CuInS_2$ solar cells,* Appl. Phys. Lett. 73 (1998), p. 3135.

[27] R.P. Wijesundera, W. Siripala, *Preparation of $CuInS_2$ thin films by electrodeposition and sulphurisation for applications in solar cells,* Solar Energy Materials & Solar Cells 81 (2004), p. 147.

[28] T. Todorov, J. Carda, P. Escribano, A. Grimm, J. Klaer, R. Klenk, *Electro deposited In2S3 buffer layers for CuInS2 solar cells,* Solar Energy Materials & Solar Cells 92 (2008) p. 1274.

[29] L. Groenendaal, F. Jonas, D. Freitag, H. Pielartzik, J. Reynolds, *Poly(3,4-ethylenedioxythiophene) and Its Derivatives: Past, Present, and Future*, Adv. Mater. 12, No.7 (2000), p. 481.

[30] C. Riuz Herrero, *Modificación de las Propiedades Optoelectrónicas Por Medio del dopado con Bi en Células Fotovoltaicas Basadas en CdTe*, Tesis Doctoral, Universidad Autonoma De Madrid, 2007

[31] Keh-moh Lin, Paijay Tsai *Parametric study on preparation and characterization of ZnO:Al films by sol–gel method for solar cells*, Materials Science and Engineering: B, 139, (2007) 81-87.

[32] J. Palm, V. Probst, F. Karg, *Second generation CIS solar modules*, Solar Energy 77 (2004) p. 757.

[33] K. Ramathan, proc. 2ndWorldConfPhoovoltaic energy Conversion1998

[34] R. Klenk, *Characterisation and modelling of chalcopyrite solar cells*, Thin Solid Films 387 (2001), p. 135.

[35] M. Green, K. Emery, Y. Hishikawa, W. Warta, *Solar Cell Efficiency Tables* (Version31) Prog. Photovolt: Res. Appl. 2008; 16:61–67.

[36] M. A. Contreras, B. Egaas, K. Ramanathan, J. Hiltner, A. Swartzlander, F. Hasoon, R. Noufi, *Progress toward 20% efficiency in Cu(In,Ga)Se2 polycrystalline thin-film solar cells,* Prog. Photov. 7 (1999), p. 311.

[37] H.W. Schock, R. Noufi, *CIGS-based Solar Cells for the Next Millennium*, Prog. Photovolt. Res. Appl. 8 (2000), p. 151.

[38] M. Contreras, M. Romero, R. Noufi, *Characterization of Cu(In,Ga)Se2 materials used in record performance solar cells,* Thin Solid Films 511-512 (2006) 51-54.

[39] A. Shah, J. Meier, A. Buechel, U. Kroll, J. Steinhauser, F. Meillaud, H. Schade, D. Domine, *Towards very low-cost mass production of thin-film silicon photovoltaic (PV) solar modules on glass,* Thin Solid Films 502 (2006), p. 292.

[40] B52-2008

[41] S. Nishivaki, S. Siebentritt, P. Walk, M. Ch. Lux-Steiner, *A stacked chalcopyrite thin-film tandem solar cell with 1.2 V open-circuit voltage,* Progress in Photovoltaics 11 (2003), p. 243.42)

[42] . Rusu, A. Rumberg, S. Schuler, S. Nishiwaki, R. Würz, S. M. Babu, M. Dziedzina, C. Kelch, S. Siebentritt, R. Klenk, Th. Schedel-Niedrig and M. Ch. Lux-Steiner, *Optimisation of the CBD CdS deposition parameters for ZnO/CdS/CuGaSe$_2$/Mo solar cells,* J. Phys. Chem. Solids 64 (2003), p. 1849.

[43] Yunbin He, CuInS2 *Thin Films for Photovoltaic: RF Reactive Sputter Deposition and Characterization*, Dissertation, Justus-Liebig-Universität, Gießen, May 2003.

[44] S. H. Wei, L. G. Ferreira, and A. Zunger, *First-principles calculation of the order-disorder transition in chalcopyrite semiconductors*, Phys. Rev. B 45 (1992), p. 2533.

[45] S. H. Wei, S. B. Zhang, and A. Zunger, *Effects of Na on the electrical and structural properties of $CuInSe_2$,* Phys. Rev. B 59 (1999), p. R2478.

[46] E. Rudigier, B. Barcones, I. Luck, T. Jawhari-Colin, A. Perez-Rodriguez, R. Scheer, *Quasi real-time Raman studies on the growth of Cu–In–S thin films,* J. Appl. Phys. 95 (2004), p. 5153.

[47] E. Rudigier, T. Enzenhofer, R. Scheer, *Determination of the quality of CuInS2-based solar cells combining Raman and photoluminescence spectroscopy*, Thin Solid Films 480–481 (2005), p. 327.

[48] L. Calvo-Barri, A. Pérez-Rodríguez, J. Alvarez-García, A. Romano-Rodríguez, B. Barcones, J.R. Morante, K. Siemer, I. Luck, R. Klenk, R. Scheer, *Combined in-depth scanning Auger microscopy and Raman scattering characterisation of $CuInS_2$ polycrystalline flms*, Vacuum 63 (2001), p. 315.

[49] J. Alvarez-Garcia, J. Marcos-Ruzafa, A. Pérez-Rodriguez, A. Romano-Rodriguez, J. R. Morante, R. Scheer, *MicroRaman scattering from polycrystalline $CuInS_2$ films: structural analysis,* Thin Solid Films 361-362 (2000), p. 208.

[50] B. J. Stanbery, S. Kincal, S. Kim, C. H. Chang, S. P. Ahrenkiel, G. Lippold, H. Neumann, T. J. Anderson, O. D. Crisalle, *Epitaxial growth and characterization of CuInSe2 crystallographic polytypes*, Appl. Phys. 91, No. 6 (2002), p. 3598.

[51] I. Konovalov, *Material requirements for CIS solar cells,* Thin Solid Films 451–452 (2004), p. 413.

[52] US Geological Survey Mineral Commodities Summaries 2005, available at: www.usgs.gov/minerals/pubs/commodity/

[53] A. Feltrin, A. Freundlich, *Material considerations for terawatt level deployment of photovoltaics*, Renewable Energy 33 (2008), p. 180.

[54] G. Phipps, C. Mikolajczak, T. Guckes, Indium and Gallium: long-term supply, Renewable Energy Focus, 9 (2008), p. 58.

[55] see 130

[56] S. Schorr, H. Hoeber, M. Tovar, *A neutron diffraction study of the stannite-kesterite solid solution series,* Europ. J. Mineral 19 (2007), p. 65.

[57] S. Siebentritt, *Wide gap chalcopyrites: material properties and solar cells*, Thin Solid Films 403-404 (2002), p. 1.

[58] L. L. Kazmerski, G. A. Sanborn, *$CuInS_2$ thin-film homojunction solar cells*, J. Appl. Phys. 48 (1977), p. 3178.

[59] R. Scheer, T. Walter, H.W. Schock, M.L. Fearheiley, H.J. Lewerenz, *$CuInS_2$ based thin film solar cell with 10.2% efficiency*, Appl. Phys. Lett. 63 (1993), p. 3294.

[60] R. Klenk, U. Blieske, V. Dieterle, K. Ellmer, S. Fiechter, I. Hengel, A. Jaeger-Waldau, T. Kampschulte, Ch. Kaufmann, J. Klaer, M.Ch. Lux-Steiner, D. Braunger, D. Hariskos, M. Ruckh, H.W. Schock, *Properties of $CuInS_2$ thin films grown by a two-step process without H_2S,* Sol. Energy Mater. Sol. Cells 49 (1997), p. 349.

[61] K. Siemer, J. Klaer, I. Luck, J. Bruns, R. Klenk, D. Braunig, *Efficient $CuInS_2$ solar cells from a rapid thermal process (RTP),* Sol. Energy Mater. Sol. Cells 67 (2001), p. 159.

[62] R. Klenk, J. Klaer, D. Scheer, M. Lux-Steiner, I. Luck, N. Meyer, U. Ruhle, *Solar cells based on $CuInS_2$—an overview,* Thin Solid Films 480 - 481 (2005), p. 509.

[63]N. Meyer, A. Meeder, D. Schmid, *Pilot production of large-area CuInS2-based solar modules*, Thin Solid Films 515 (2007), p. 5979.

[64] F. Hergert, R. Hock, A. Weber, M. Purwins, J. Palm and V. Probst, *In situ investigation of the formation of Cu(In,Ga)Se2 from selenised metallic precursors by X-ray diffraction—The impact of Gallium, Sodium and Selenium excess*, Journal of Physics and Chemistry of Solids 66 (2005), p. 1903.

[65] D. Lincot, J.F. Guillemoles, S. Taunier, D. Guimard, J. Sicx-Kurdi, A. Chaumont, O. Roussel, O. Ramdani, C. Hubert, J.P. Fauvarque, N. Bodereau, L. Parissi, P. Panheleux, P. Fanouillere, N. Naghavi, P.P. Grand, M. Benfarah, P. Mogensen, O. Kerrec, *Chalcopyrite thin film solar cells by electrodeposition* Solar Energy, Volume 77, (2004) 725-737

[66] U. Singh, W. Shafarman, R. Birkmire *Surface sulfurization studies of $Cu(InGa)Se_2$ thin film,*

Solar Energy Materials and Solar Cells, 90(2006) 623-630

[67] J. Bekker, V. Alberts, A. W. R. Leitch, J. R. Botha, *Properties of $CuIn(Se,S)_2$ thin films prepared by two-step growth processes*, Thin Solid 431-432 (2003), 116-121

[68] F. Hergert, S. Jost, R. Hock, M. Purwins, J. Palm, *A thermodynamical approach to the formation reactions of sodium-doped Cu(In,Ga)Se2,* Thin Solid Films 511 – 512 (2006), p. 147.

[69] D. Rudmann, *Effects of Sodium on growth and properties of $Cu(In,Ga)Se_2$ thin films and solar cells,* PhD Thesis, Swiss Federal Institute of Technology (ETH), Zurich, 2004.

[70] I. Oja, M. Nanu, A. Katerski, M. Krunks, A. Mere, J. Raudoja, A. Goosens, *Crystal quality studies of $CuInS_2$ films prepared by spray pyrolysis,* Thin Solid Films 480-481 (2005), p. 82.

[71] J. Hollingsworth, K. Banger, M. Jin, J. Harris, J. Cowen, E. Bohannan, J. Switzer, W. Buhro, A. Hepp, *Single source precursors for fabrication of I–III–VI_2 thin-film solar cells via spray CVD,* Thin Solid Films 431-432 (2003), p. 63.

[72] S. Weng, M. Cocivera, *Preparation of copper indium diselenide by selenization of copper indium oxide,* Journal of Applied Physics 74 (1993), p. 2046.

[73] M. Beck, M. Cocivera, *Thin-film copper indium diselenide prepared by selenization of copper indium oxide formed by spray pyrolysis,* Thin Solid Films 272 (1996), p. 71.

[74] S. Taunier, P. Grand, A. Chomont, O. Ramdani, N. Naghavi, C. Hubert, E. Mahe, O. Kerrec et al. *Cu(In,Ga)(S,Se)$_2$ solar cells and modules by electrodeposition*, Thin Solid Films 480–481 (2005), p. 526.

[75] R. Bhattacharya, J. Hiltner, W. Batchelor, M. Contreras, R. Noufi, J. Sites, *15.4% CuIn$_{1-x}$Ga$_x$Se$_2$-based photovoltaic cells from solution-based precursor films* Thin Solid Films 361 (2000), p. 396.

[76] O. Ramdani, J.F. Guillemoles, D. Lincot, P.P. Grand, E. Chassaing, O. Kerrec, E. Rzepka, *One-step electrodeposited CuInSe2 thin films studied by Raman spectroscopy*, Thin Solid Films 515 (2007), p. 5909.

[77] E. Chassaing, B. Canava, P.P. Grand, O. Roussel, O. Ramdani, A. Etcheberry, J.F. Guillemoles, D. Lincot, and O. Kerrec, *Electroless nucleation and growth of Cu-Se phases on molybdenum in Cu(II)-In(III)-Se(IV) solutions*, Electrochemical and Solid State Letters 10 (2007), p. C1.

[78] O. Ramdani, E. Chassaing, B. Canava, P.P. Grand, O. Roussel, M. Lamirand, E. Rzepka, A. Etcheberry, J.F. Guillemoles, D. Lincot, O. Kerrec, *Electrochemical cementation phenomena on polycrystalline molybdenum thin films from Cu(II)-In(III)-Se(IV) acidic solutions*, J. of Electrochemical Society 154 (2007), p. D383.

[79] G. Gonzales, M. Rosso, E. Chassaing, J.N. Chazalviel, *Experimental and theoretical study of the onset of the growth of an irregular metal deposit*, Electrochimica Acta 53 (2007), p. 141.

[80] O. Roussel, E. Chassaing, P.-P. Grand, O. Ramdani, M. Lamirand, A. Etcheberry, J. -F. Guillemoles, D. Lincot, *First stages of CIS electrodeposition from Cu(II)-In(III)-Se(IV) acidic solutions on polycrystalline Mo films,* J. of Electrochem. Soc. 155(2) (2008), p. D141.

[81] E. Chassaing, O. Ramdani, P.-P. Grand, J.-F. Guillemoles, D. Lincot, New insights in the electrodeposition mechanism of CuInSe2 thin films for solar applications, PhYsica Status Solidi (c) 5 (2008), p. 3445.

[82] S. Taunier, D. Guimard, D. Lincot, J. F. Guillemoles, P. Grand, Method of producint thin films of compound I-III-VI, promoting the incorporation of III elements in the film. US patent application 2006/015133A1.

[83] T. Todorov, E. Cordoncillo, J.F. Sánchez-Royo, J. Carda, P. Escribano, *CuInS$_2$ Films for Photovoltaic Applications Deposited by a Low-Cost Method*, *Chemistry of Materials* 18 (2006), p. 3145.

[84] T. Todorov, L. Oliveira, J. Carda, and P. Escribano, *Influence of treatment conditions on chalcopyrite films deposited at atmospheric pressure*, *Physica Status Solidi (c)* 5 (2008), p. 3437.

[85] L. Oliveira, T. Todorov, E. Chassaing, D. Lincot, J. Carda, P. Escribano, *CIGSS Films Prepared by Sol-Gel Route*, Thin Solid Films, Accepted for publication via EMRS 2008.

[86] T. Todorov, E. Cordoncillo, J. Carda, P. Escribano, *Characterization of $CuInS_2$ Films Deposited by a Low-Cost Method, Proceedings 21-th European Photovoltaic Solar Energy Conference and Exhibition*, Dresden, 4-8 sept. 2006, ISBN 3-936338-20-5, p.1969.

[87] D. Mitzi, M. Yuan, W. Liu, A. Kellock, A. Schrott, J. Chey, V Deline, L. Gignac, *New Solution-Based Deposition Route for High-Quality CIGS Absorber Layers,* EMRS 2008 Spring meeting, Strasbourg, 28 May 2008.

[88] M. Kaelin, D. Rudmann, A. Tiwari, *15.4% $CuIn_{1-x}Ga_xSe_2$-based photovoltaic cells from solution-based precursor films,* Solar Energy 77 (2004), p. 749.

[88] C. Eberspacher, C. Friedric, K. Pauls, J. Serra, Thin-film CIS alloy PV materials fabricated using non-vacuum, particles-based techniques, Thin Solid Films 387 (2001), p. 18.

[90] M. Kaelin, D. Rudmann, F. Kurdesau, H. Zogg, T. Meyer, A. Tiwari, *Low-cost CIGS solar cells by paste coating and selenization,* Thin Solid Films 480 (2005), p. 486.

[91] V. Kapur, A. Bansal, I. Asensio, *Non-vacuum processing of $CuIn_{1-x}Ga_xSe_2$ solar cells on rigid and flexible substrates using nanoparticle precursor inks,* Thin Solid Films 431 (2003), p. 53.

[92] U.S. Patent No. 6,127,202 "Oxide-Based Method of Making Compound Films and Making Related Electronic Devices" (2000).

[93] Nanosolar, Chalcogenide solar cells, International patent application WO2007065096A2.

[94] T. Todorov, J. Carda, P. Escribano, A. Grimm, J. Klaer, R. Klenk, *Electro deposited In2S3 buffer layers for CuInS2 solar cells*, *Solar Energy Materials & Solar Cells* 92 (2008), p. 1274.

[95] T. Todorov, M. Kita, J. Carda, P. Escribano *Cu_2ZnSnS_4 FILMS DEPOSITED BY A SOFT-CHEMISTRY METHOD*, *Thin Solid Films*, Accepted for publication via E-MRS 2008.

[96] A. R. West, *Solid State Chemistry and its application*, Ed. John Wiley & Sons, 1996.

[97] Princeton Instruments,http://content.piacton.com/Uploads/Princeton/Documents/

Library/UpdatedLibrary/Raman_Spectroscopy_Basics.pdf

[98] A. Oral, E. Mensur, M. Aslan, E. Basaran, *The preparation of copper(II) oxide thin films and the study of their microstructures and optical properties,* Materials Chemistry and Physics 83 (2004), p. 140.

[99] S.-Y. Lee, B.-O. Park, *CuInS2 thin films deposited by sol–gel spin-coating method,* Thin Solid Films 516 (2008), p. 3862.

[100] S.-Y. Lee, K.-H. Kim, B.-O. Park, *Oxidation effect on densification of CuInS2 absorber layer by paste coating*, Thin Solid Films 516 (2008), p. 4709.

[101] A. Kumbhar, K. Kishore, *Redox reactions of Cu(II)-amine complexes in aqueous solutions*, Radiation Physics and Chemistry 66 (2003), p. 275.

[102] K. Whitmire, J. Hutchison, A. Gardberg, C. Edwards, *Triethanolamine complexes of copper,* Inorganica Chimica Acta 294 (1999), p. 153.

[103] T. Emons, J. Li, L. Nazar, *Synthesis and characterization of mesoporous indium tin oxide possessing an electronically conductive framework*, Journal of the American Chemical Society 124 (2002), p. 8516.

[104] Kirilov, A.; Kopylovich, M.; Kirilova, M.; Haukka, M.; Guedes da Silva, M.; Pombeiro, A. Angewandte Chemie, 2005, 117, 4419.

[105] A. Ogwu, E. Bouquerel, F. Placido, *The Effects of Sputtering Conditions on the Optical Transmission and Wettability of Amorphous Copper Oxide Thin Films Prepared by Magnetron Sputtering,* Coating Materials News 13 (2003).

[106] Ch. Klopmann, J. Djordjevic, R. Scheer, *Real-time studies of phase transformations in Cu–In–Se–S thin films: 1. Intermetallic phase transformations* Journal of Crystal Growth 289 (2006), p. 113.

[107] F. Dhlamini, V. Alberts, *Synthesis of homogeneous pentenary chalcopyrite alloys with a classical two-step growth process,* Journal of Physics and Chemistry of Solids 66 (2005), p. 1880.

[108] M. Zouaghi, T. Nasrallah, S. Marsillac, J. Bernede, S. Belgacem, *Physico-chemical characterization of spray-deposited $CuInS_2$ thin films,* Thin Solid Films 382 (2001), p. 39.

[109] J. Qui, Z. Jin, J. Qian, Y. Shi, W. Wu, *Influence of post-heat treatment on the properties of $CuInS_2$ thin films deposited by an ion layer gas reaction (ILGAR),* Journal of Crystal Growth 282 (2005), p. 421.

[110] M. Krunks, O. Bijakina, T. Varema, V. Mikli, E. Mellikov, *Structural and optical properties of sprayed $CuInS_2$ films*, Thin Solid Films 338 (1999), p. 125.

[111] X. Hou, K. Choy, *Synthesis and characteristics of $CuInS_2$ films for photovoltaic application,* Thin Solid Films 480 (2005), p. 13.

[112] L. Brus, *Electron–electron and electron-hole interactions in small semiconductor crystallites: The size dependence of the lowest excited electronic state,* J. Chem. Phys 80 (1984), p. 4403.

[113] E. Cordoncillo, P. Escribano, G. Monrós, M. A. Tena, V. Orera, J. Carda, *The Preparation of CdS Particles in Silica Glasses by a Sol-Gel Method,* J. of Solid State Chem. 118 (1995), p. 1.

[114] J. Klaer, I. Luck, A. Boden, R. Klenk, I. Gavilanes Perez, R. Scheer, *Mini-Modules from a CuInS2 baseline process*, Thin Solid Films 431–432 (2003), p. 534.

[115] X. Hou, K. Choy, *Synthesis and characteristics of $CuInS_2$ films for photovoltaic application,* Thin Solid Films 480 (2005), p. 13.

[116] S. Kim, W. Jeong, G. Park, Y. Back, Y. Jeong, Y. Yoo, *Heat-treatment effect of chalcopyrite copper indium disulphide thin film growth,* Synthetic Metals 71 (1995), p. 1747.

[117] J. Klaer, R. Klenk, H-W. Schock, *Progress in the development of $CuInS_2$ based mini-modules,* Thin Solid Films 515 (2007), p. 5929.

[118] K. Whitmire, J. Hutchison, A. Gardberg, C. Edwards, *Triethanolamine complexes of copper,* Inorganica Chimica Acta 294 (1999), p. 153.

[119] J. E. Huheey, E. A. Keiter, R. L. Keiter, *Inorganic Chemistry. Principles of Structure and Reactivity*. 4th ed. Harper Collins College Publishers, 1993.

[120] M. Gossla, W. N. Shafarman, *Five-source PVD for the deposition of $Cu(In_{1-x}Ga_x)(Se_{1-y}S_y)_2$ absorber layers,* Thin Solid Films 480-481 (2005), p. 33.

[121] F. Dhlamini, V. Alberts, *Synthesis of homogeneous pentenary chalcopyrite alloys with a classical two-step growth process,* Journal of Physics and Chemistry of Solids 66 (2005), p. 1880.

[122] A. Neisser, I. Hengel, R. Klenk, Th.W. Matthes, J. AD Alvarez-Garcia, A. Perez-Rodriguez, A. Romano-Rodriguez, M.-Ch. Lux-Steiner, *Effect of Ga incorporation in sequentially prepared CuInS2 thin film absorbers,* Solar Energy Materials & Solar Cells 67 (2001), p. 97.

[123] R. Kaigawa, A. Neisser, R. Klenk, M.-Ch. Lux-Steiner, *Improved performance of thin film solar cells based on $Cu(In,Ga)S_2$*, Thin Solid Films 415 (2002), p. 266.

[124] F. Dhlamini, V. Alberts, *Synthesis of homogeneous pentenary chalcopyrite alloys with a classical two-step growth process,* Journal of Physics and Chemistry of Solids 66 (2005), p. 1880.

[125] C. Jensen, D. Tarrant, J. Ermer, G. Pollock in: R. J. Schwartz (Ed.), Proceedings of 23rd IEEE Photovoltaic Specialist Conference, Louisville, KY, USA, May 10 – 14, 1993, p. 577.

[126] J. Guillemoles, P. Cowache, A. Lusson, K. Fezzaa, F. Boisivon, J. Vedel, D. Lincot, *One step electrodeposition of $CuInSe_2$: Improved structural, electronic, and photovoltaic properties by annealing under high selenium pressure,* J. Appl. Phys. 79 (1996), p. 7293.

[127] K. Ito, T. Nakazawa, *Electrical and Optical Properties of Stannite-Type Quaternary Semiconductor Thin Films,* Jpn. J. Appl. Phys. 27 (1988), p. 2094.

[128] Th.M. Friedlmeier, N. Wieser, T. Walter, H. Dittrich, and H.W. Shock, Proceedings of 14th European Conference on Photovoltaic Science and Engineering and Exhibition (Barcelona, 1997), p. 1242.

[129] H. Katagiri, *Cu_2ZnSnS_4 thin film solar cellsThin,* Solid Films 480–481 (2005), p. 426.

[130] K. Jimbo, R. Kimura, T. Kamimura, S. Yamada, W. S. Maw, H. Araki, K. Oishi, H. Katagiri, *Cu_2ZnSnS_4-type thin film solar cells using abundant materials,* Thin Solid Films 515 (2007), p. 5997.

[131] N. Nakayama, K. Ito, *Sprayed films of stannite Cu_2ZnSnS_4,* Applied Surface Science 92 (1996), p. 171.

[132] N. Kamoun, H. Bouzouita, B. Rezig, *Fabrication and characterization of Cu_2ZnSnS_4 thin films deposited by spray pyrolysis technique,* Thin Solid Films 515 (2007), p. 5949.

[133] K. Moriya, J. Watabe, K. Tanaka, H. Uchiki, *Characterization of Cu_2ZnSnS_4 thin films prepared by photo-chemical deposition,* Phys. Stat. Sol. (c) 3, No. 8 (2006), p. 2848.

[134] K. Tanaka, N. Moritake, H. Uchiki, *Characterization of Cu_2ZnSnS_4 thin films prepared by photo-chemical deposition,* Solar Energy Materials & Solar Cells 91 (2007), p. 1199.

[135] J. Scragg, P. Dale, L. Peter, *Towards sustainable materials for solar energy conversion: Preparation and photoelectrochemical characterization of Cu_2ZnSnS_4,* Electrochemistry Communications 10 (2008), p. 639.

[136] SeJin Ahn, KiHyun Kim, KyungHoon Yoon, *Cu(In,Ga)Se_2 thin film solar cells from nanoparticle precursors*, Current Applied Physics 8 (2008) 766-769

[137] M. Kaelin D. Rudmann, F. Kurdesau, T. Meyer, H. Zogg, A.N. Tiwari, *CIS and CIGS layers from selenized nanoparticle precursors,* Thin Solid Films 431–432 (2003), p. 58.

[138] S. Schorr, V. Riede, D. Spemann, Th. Doering, *Electronic band gap of $Zn_{2x}(CuIn)_{1-x}X_2$ solid solution series (X = S, Se, Te),* Journal of Alloys and Compounds 414 (2006), p. 26.

[139] N. A. Allsop, A. Schoenmann, H.-J. Muffler, M. Bar, M. C. Lux-Steiner and Ch.-H. Fischer, *Spray-ILGAR indium sulfide buffers for Cu(In, Ga)(S, Se)2 solar cells*. Prog. Photovolt: Res. Appl. 13 (2005), p. 607.

[140] D. Hariskos, S. Spiering, M. Powalla, *Buffer layers in Cu(In,Ga)Se2 solar cells and modules*, Thin Solid Films 480–481 (2005), p. 99.

[141] Ch. Kaufmann, *Chemical bath Deposition of Thin Semiconductor Films for Use as Buffer Layers in CuInS2 Thin Film Solar Cells*, PhD Thesis, Queen´s College Oxford, Hilary, 2002.

[142] T. Nakada, K. Furumi, A. Kunioka, *High-efficiency cadmium-free Cu(In,Ga)Se2 thin-filmsolar cells with chemically deposited ZnS buffer layers*, IEEE Trans. Electron Devices 46 (1999), p. 2093.

[143] M. Bär, A. Ennaoui, J. Klaer, R. Sáez-Araoz, T. Kropp, L. Weinhard, C. Heske, H.-W. Schock, Ch.-H. Fischer, M.C. Lux-Steiner, *The electronic structure of the [Zn (S, O)/ZnS]/CuInS2 heterointerface–Impact of post-annealing*, Chem. Phys. Lett. 433 (2006), p. 71.

[144] S. Siebentritt, *Alternative buffers for chalcopyrite solar cells*, Solar Energy 77 (2004), p. 767.

[145] US patents: Electrolytic apparatus and process, 4687554; Dip type surface treatment apparatus and dip type surface treatment method 6610187, Apparatus for continuously producing a base for a printed circuit board 4883575.

[146] D. Gal, G. Hodes, D. Hariskos, D. Braunger, H.-W. Schock, *Size-quantized CdS films in thin film $CuInS_2$ solar cells,* Appl. Phys. Lett. 73 (1998), p. 3135.

[147] R.P. Wijesundera, W. Siripala, *Preparation of CuInS2 thin films by electrodeposition and sulphurisation for applications in solar cells*, Solar Energy Materials & Solar Cells 81 (2004), p. 147.

[148] B. Asenjo, A.M. Chaparro, M.T. Gutiérez, J. Herrero, C. Maffiotte, *Quartz crystal microbalance study of the growth of indium(III) sulphide films from a chemical solution*, Thin Solid Films 480–481 (2005), p. 151.

[149] S. Nakamura, A. Yamamoto, *Preparation of CuInS2 films with sufficient sulfur content and excellent morphology by one-step electrodeposition*, Solar Energy Materials and Solar Cells 49 (1997), p. 415.

[150] Ph. Mandin, C. Fabian, D. Lincot, *Importance of the density gradient effects in modelling electro deposition process at a rotating cylinder electrode*, Electrochimica Acta 51 (2006), p. 4067.

[151] J. Klaer, R. Klenk, D. Abou-Ras, R. Scheer, H.W. Schock, *Progress in mini-modules from a CuInS2 baseline process*, Proc. 21st European PVSEC, Dresden, 4-8 September 2006, p. 1801.

[152] I. Lauermann, M. Bär, I. Kötschau, P. Pistor, M.C. Lux-Steiner, *Synchrotron-based spectroscopy for the characterization of surfaces and interfaces in chalcopyrite solar cells*, Proc. of Thin-film Compound Semiconductor Photovoltaics: Symposium held March 29–April 1. 2005, MRS Spring Meeeting, San Francisco 2005, p. F2.1.1.

[153] J. Reichardt, M. Bär, A. Grimm, I. Kötschau, I. Lauermann, S. Sokoll, M. C. Lux-Steiner, and Ch.-H. Fischer, *Inducing and monitoring photoelectrochemical reactions at surfaces and buried interfaces in Cu(In,Ga)(S,Se)2 thin-film solar cells*, Applied Physics Letters 86 (2005), 172102.

[154] M. Bär, J. Reichardt, A. Grimm, I. Kötschau, I. Lauermann, K. Rahne, S. Sokoll, M. C. Lux-Steiner, and Ch.-H. Fischer, *Zn(O,OH) layers in chalcopyrite thin-film solar cells: Valence-band*, Journal of Applied Physics 98 (2005) 053702.

[155] M.G. Sandoval-Paz, M. Sotelo-Lerma, J.J. Valenzuela-Jáuregui, M. Flores-Acosta, R. Ramírez-Bon, *Structural and optical studies on thermal-annealed In2S3 films prepared by the chemical bath deposition technique*, Thin Solid Films 472 (2005), p. 5.

[156]-[159] Available upon authorization.

[160] W. Witte, R. Kniese, M. Powalla, *Raman investigations of Cu(In,Ga)Se_2 thin films with various copper contents*, Thin Solid Films (2008) in press

[161] H. Tanino, H. Deai, H. Nakanishi, *Raman spectra of $CuGa_xIn_{(1-x)}Se_2$,* Jpn. J. Appl. Phys. Suppl. 32 (1993), p. 436.

[162] W. Witte, R. Kniese, A. Eicke, M. Powalla, *Influence of the Ga Content on the Mo/Cu(In,Ga)Se2 Interface Formation,* Proceedings of the fourth IEEE World Conference on Photovoltaic Energy Conversion, Waikoloa, USA, May 7–12, 2006, p. 553.

ANNEX 1

ANALISIS CLINICOS
LABORATORI MICROBIOLOGIA
J.V. GALIANO

C/. Mayor, 56 Entresuelo (Edificio Simago)
Teléfono 964 23 74 08
12001 CASTELLON

LABORATORIO ASOCIADO A A.E.L.I. -NACIONAL- Y A U.I.L.I. -INTERNACIONAL-

ESTUDIO SOBRE MATERIAL CERÁMICO RECUBIERTO CON SUSTANCIA BACTERICIDA

Realizado por LABORATORIO DE MICROBIOLOGIA CASTELLONENSE S.L.
Director J. Galiano

Para
Dr. D. Teodor Todorov
Facultad de Químicas

Patrocinado por
ESMALTES S.A.

Fabrica de Esmaltes Cerámicos
Carretera Castellón – Alcora km. 82,5
ALCORA (Castellón de la Plana)
ESPAÑA

ANALISIS CLINICOS
LABORATORI MICROBIOLOGIA
J.V. GALIANO

C/. Mayor, 56 Entresuelo (Edificio Simago)
Teléfono 964 23 74 08
12001 CASTELLON

LABORATORIO ASOCIADO A A.E.L.I. -NACIONAL- Y A U.I.L.I. -INTERNACIONAL-

ESTUDIO DE LA ACTIVIDAD BACTERICIDA

Fundamento del estudio.-

El estudio consiste en ver la actividad bactericida que pueden tener diversas sustancias inorgánicas que cubren un azulejo cerámico procedente de una investigación patrocinada por ESMALTES S.A.
Se han analizado 7 muestras diferentes. Tres con superficie brillante (B-1, B-2, B-3) y cuatro con superficie mate (M-1, M-2, M-3, M-4). Las pruebas se realizaron bajo condiciones ambientales habituales y este es el resultado obtenido. Las muestras fueron recibidas en este laboratorio el 27 de julio de 2003 y los trabajos se hicieron durante el mes de agosto del mismo año.

Material. -

- Cultivo de *Escherichia coli* ATTC 35218. Cepas liofilizadas y recuperadas en medios específicos para cultivo microbiano.
- Líquido para la preparación de las suspensiones microbianas (Norma Francesa FT-72-190) Recomendada por el Instituto Pasteur de Paris. Solución fisiológica estéril de polisorbato 80 al 0,05%.
- Placas Petri de plástico de 9 cm. de diámetro en cuyo fondo se coloca un papel de filtro humedecido con 6 ml de agua destilada, todo estéril.
- 60 ul de la suspensión bacteriana de *E.coli* con una concentración bacteriana aproximada de 40 a 100 * 10^7 ufc / ml diluida a 1 / 10.000
- Iluminación con dos tubos fluorescentes (Philips TLD 36W / 33) de 1,20 cm de longitud y potencia de 36 W. Distancia de iluminación 100 cm.
- Tiempo de exposición a la iluminación: 60 minutos destapada la placa y de 6 a 8 horas tapada.
- Azulejos problema y azulejos control con la misma base de bizcocho y similar esmalte los controles sin sustancia bactericida

Método.-

El método utilizado es el investigado por el Dr. Galiano y que fue supervisado por el Instituto Pasteur al que se le añadieron ligeras modificaciones.

Las piezas cerámicas de un tamaño de 25 x 50 mm se introducen en la paca Petri ya preparada se le añaden 60 ul de la suspensión bacteriana ya diluida y se cubre con una lámina cubreobjetos de 24 x 50 mm.

Se iluminan 30 minutos con la placa destapada y luego de 6 – 8 horas con la placa tapada, luego se iluminan otros 30 minutos con la placa destapada.

ANALISIS CLINICOS
LABORATORI MICROBIOLOGIA
J.V. GALIANO

C/. Mayor, 56 Entresuelo (Edificio Simago)
Teléfono 964 23 74 08
12001 CASTELLON

LABORATORIO ASOCIADO A A.E.L.I. -NACIONAL- Y A U.I.L.I. -INTERNACIONAL-

Después de estar bajo iluminación esas horas, se saca el material a estudiar de la placa Petri y se introduce en una solución salina con Tween 80 según la Norme fracaise NF T 72- 190

Con cuidado y ya dentro del líquido se separa la lámina cubreobjetos y la pieza cerámica raspándose las superficies que estuvieron en contacto con la bacteria con una pipeta Pasteur con punta cerrada. Luego se agita unas diez veces manualmente por rotación y se colocan en un agitador rotativo durante 25 – 30 minutos.

Para el recuento de células utilizamos cultivos, en Agar Trypticasa Soja, de 5ml. y 10ml. del líquido (ambos por duplicado) así como de la pieza cerámica y de la lámina cubreobjetos, además se cuentan las bacterias que quedan en el líquido sobrante mediante filtración.

Después de numerosas experiencias vemos que aproximadamente quedan adheridas el mismo número de bacterias a la pieza cerámica y al cubreobjetos en el azulejo control y en el problema, todas ellas en un número despreciable si se realiza bien el raspado y la agitación, por ello en esta última prueba han sido despreciadas.

Al utilizarse solo 60 microlitros de la suspensión bacteriana, el número de bacterias colocadas sobre la superficie del azulejo oscila de 50 a 1500 según casos. El número de bacterias que se recuperan de esta superficie en el azulejo control después del periodo de iluminación es inferior a las colocadas en el azulejo, y si el azulejo problema tiene propiedades bactericidas todavía se recuperaran de él menor número de bacterias. La relación entre las bacterias colocadas y las recuperadas en ambos casos debe de ser desarrollada logarítmicamente para dar relaciones lineales.

Utilizamos la fórmula de la Norma Francesa antes aludida:

$$R = \log \frac{\text{Re}\,cuentoInóculo}{Y + X}$$

Y = Recuento de la lámina cubreobjetos y del bloque cerámico
X = Recuento del líquido de dilución

X = X1+ X2

X1 = Recuento por siembra de 5 ml (por duplicado) y por 10
X2 = Recuento por siembra de 10 ml (por duplicado) y por 5

ANALISIS CLINICOS
LABO Datos azulejo mate.- MICROBIOLOGIA
V. GALIANO
C/. Mayor, 56 Entresuelo (Edificio Simago)
Teléfono 964 23 74 08
12001 CASTELLON

fecha	CONTROL MATE			M- 1			Ufc/ml	colocados	recuperados		
	5 ml	10 ml	cu+ce	5ml	10ml	cu+ce		Ufc/60ul	LOG(Recuento inoculo/(Y+X))		
a	9	14		1	5		493000000	dil 1:10000	control	M- 1	incremento M-1
	10	18		2	6		550000000	2998,5	157,5	57,5	
b	6	9		2	5		456000000		19,038	52,1478	
	10	15		4	12		500000000		**1,279**	**1,717**	**0,437**
total	35	56	0	9	28	0	1999000000				
media	**8,75**	**14**	**0**	**2,25**	**7**	**0**	**499750000**				

fecha	CONTROL MATE			M- 2			Ufc/ml	colocados	recuperados		
	5 ml	10 ml	cu+ce	5ml	10ml	cu+ce		Ufc/60ul	LOG(Recuento inoculo/(Y+X))		
a	9	14		1	3		493000000	dil 1:10000	control	M- 2	incremento M-2
	10	18		3	8		550000000	2998,5	157,5	42,5	
b	6	9		3	5		456000000		19,0381	70,5529	
	10	15		1	2		500000000		**1,279**	**1,848**	**0,568**
total	35	56	0	8	18	0	1999000000				
media	**8,75**	**14**	**0**	**2**	**4,5**	**0**	**499750000**				

fecha	CONTROL MATE			M- 3			Ufc/ml	colocados	recuperados		
	5 ml	10 ml	cu+ce	5ml	10ml	cu+ce		Ufc/60ul	LOG(Recuento inoculo/(Y+X))		
a	10	18		3	8		665000000	dil 1:10000	control	M- 3	incremento M-3
	14	20		5	13		930000000	5409	221,25	75	
b	13	19		2	5		861000000		24,447	72,12	
	14	18		3	8		1150000000		**1,388**	**1,858**	**0,469**
total	51	75	0	13	34	0	3606000000				
media	**12,75**	**18,75**	**0**	**3,25**	**8,5**	**0**	**901500000**				

fecha	CONTROL MATE			M- 4			Ufc/ml	colocados	recuperados		
	5 ml	10 ml	cu+ce	5ml	10ml	cu+ce		Ufc/60ul	LOG(Recuento inoculo/(Y+X))		
a	10	18		4	9		665000000	dil 1:10000	control	M- 4	incremento M-4
	14	20		4	11		930000000	5409	221,25	66,25	
b	13	19		2	5		861000000		24,447	81,645	
	14	18		2	4		1150000000		**1,388**	**1,911**	**0,523**
total	51	75	0	12	29	0	3606000000				
media	**12,75**	**18,75**	**0**	**3**	**7,25**	**0**	**901500000**				

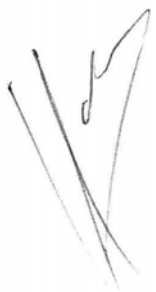

ANALISIS CLINICOS
LABORATORI MICROBIOLOGIA
J.V. GALIANO

C/. Mayor, 56 Entresuelo (Edificio Simago)
Teléfono 964 23 74 08
12001 CASTELLON

GERMENES RECUPERADOS REFERIDOS A LOS COLOCADOS SOBRE AZULEJOS CONTROL Y PIEZAS DE ESTUDIO (EN FASE LOGARÍTMICA)

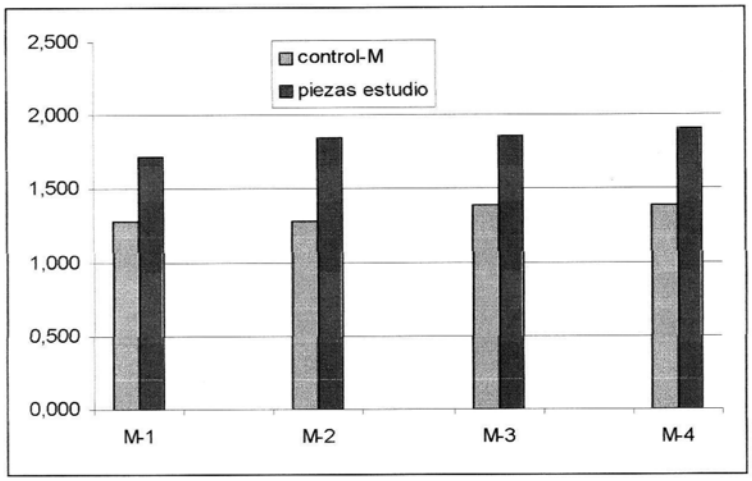

Incremento del poder bactericida del azulejo tratado

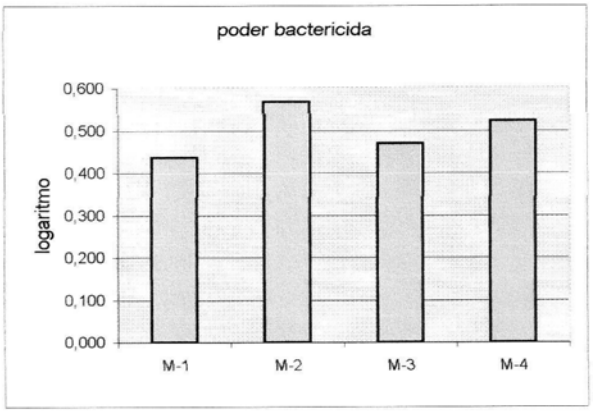

ANALISIS CLINICOS
LABORATORIO MICROBIOLOGIA
J.V. GALIANO

C/. Mayor, 56 Entresuelo (Edificio Simago)
Teléfono 964 23 74 08
12001 CASTELLON

LABORATORIO ASOCIADO A A.E.L.I. -NACIONAL- Y A U.I.L.I. -INTERNACIONAL-

Datos azulejo con brillo.-

fecha	CONTROL BRILLO			B- 1			Ufc/ml	colocados	recuperados		
19-ago-03	5 ml	10 ml	cu+ce	5ml	10ml	cu+ce		Ufc/60ul	LOG(Recuento inoculo/(Y+X))		
a	9	20		3	6		288000000	dil 1:10000	control	B- 1	incremento B-1
	14	24		1	2		306000000	1731	219	31	
b	11	19		1	3		500000000		7,91	55,39	
	12	20		1	2		60000000		**0,90**	**1,74**	**0,85**
total	46	83	0	6	13	0	1154000000				
media	**12**	**21**	**0**	**2**	**3**	**0**	**288500000**				

fecha	CONTROL BRILLO			B- 2			Ufc/ml	colocados	recuperados		
	5 ml	10 ml	cu+ce	5ml	10ml	cu+ce		Ufc/60ul	LOG(Recuento inoculo/(Y+X))		
a	9	20		2	6		288000000	dil 1:10000	control	B- 2	incremento B-2
	14	24		1	3		306000000	1731	219	34	
b	11	19		1	2		500000000		7,91	51,29	
	12	20		2	4		60000000		**0,90**	**1,71**	**0,81**
total	46	83	0	6	15	0	1154000000				
media	**12**	**21**	**0**	**2**	**4**	**0**	**288500000**				

fecha	CONTROL BRILLO			B- 3			Ufc/ml	colocados	recuperados		
	5 ml	10 ml	cu+ce	5ml	10ml	cu+ce		Ufc/60ul	LOG(Recuento inoculo/(Y+X))		
a	9	20		2	5		288000000	dil 1:10000	control	B- 3	incremento B-3
	14	24		1	2		306000000	1731	219	48	
b	11	19		1	7		500000000		7,91	36,44	
	12	20		3	10		60000000		**0,90**	**1,56**	**0,66**
total	46	83	0	7	24	0	1154000000				
media	**12**	**21**	**0**	**2**	**6**	**0**	**288500000**				

ANALISIS CLINICOS
LABORATORIO MICROBIOLOGIA
J.V. GALIANO

C/. Mayor, 56 Entresuelo (Edificio Simago)
Teléfono 964 23 74 08
12001 CASTELLON

Incremento del poder bactericida del azulejo tratado

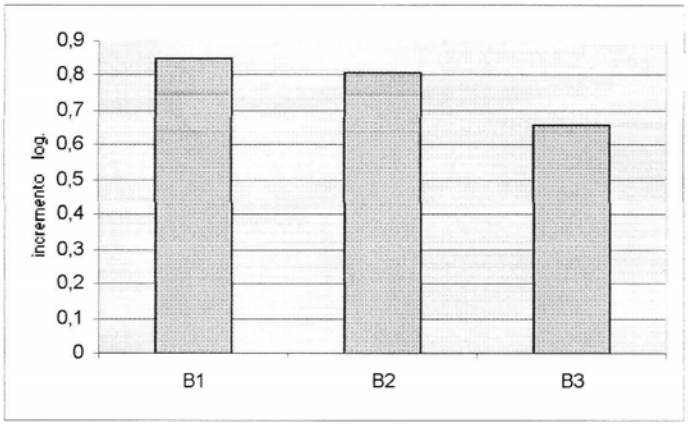

GERMENES RECUPERADOS REFERIDOS A LOS COLOCADOS SOBRE AZULEJOS CONTROL Y PIEZAS DE ESTUDIO (EN FASE LOGARÍTMICA)

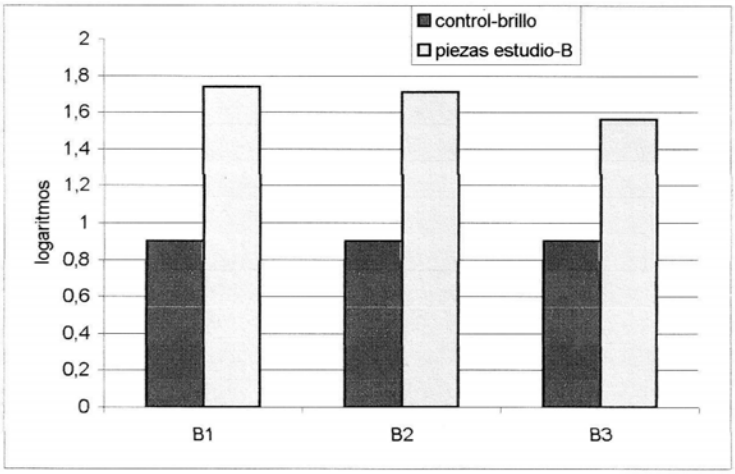

ANALISIS CLINICOS
LABORATORI MICROBIOLOGIA
J.V. GALIANO

C/. Mayor, 56 Entresuelo (Edificio Simago)
Teléfono 964 23 74 08
12001 CASTELLON

LABORATORIO ASOCIADO A A.E.L.I. -NACIONAL- Y A U.I.L.I. -INTERNACIONAL-

CONCLUSIONES :

Los datos parecen indicar que los materiales cerámicos M-1, M-2, M-3, M-4 tienen una actividad como bactericida bastante importante muy superior a las piezas cerámicas convencionales utilizadas como control, y parece que los resultados obtenidos con las piezas de brillo B-1, B-2, B-3 igualan y hasta superan a las anteriores. Pero debido al escaso número de pruebas realizado con cada una de las piezas estos resultados son solo provisionales y por ello no excesivamente fiables, haría falta un número de pruebas entre veinte y cuarenta con cada muestra para certificar estos resultados y comprobar que estadísticamente los resultados son correctos y no debidos al azar.

Fdo José Galiano
Microbiólogo
Director Técnico

Castellón 25 agosto 2003